

# Realization of a demonstrator slave for robotic minimally invasive surgery

***Citation for published version (APA):***

Bedem, van den, L. J. M. (2010). *Realization of a demonstrator slave for robotic minimally invasive surgery*. [Phd Thesis 1 (Research TU/e / Graduation TU/e), Mechanical Engineering]. Technische Universiteit Eindhoven. <https://doi.org/10.6100/IR684835>

***DOI:***

[10.6100/IR684835](https://doi.org/10.6100/IR684835)

***Document status and date:***

Published: 01/01/2010

***Document Version:***

Publisher's PDF, also known as Version of Record (includes final page, issue and volume numbers)

***Please check the document version of this publication:***

- A submitted manuscript is the version of the article upon submission and before peer-review. There can be important differences between the submitted version and the official published version of record. People interested in the research are advised to contact the author for the final version of the publication, or visit the DOI to the publisher's website.
- The final author version and the galley proof are versions of the publication after peer review.
- The final published version features the final layout of the paper including the volume, issue and page numbers.

[Link to publication](#)

***General rights***

Copyright and moral rights for the publications made accessible in the public portal are retained by the authors and/or other copyright owners and it is a condition of accessing publications that users recognise and abide by the legal requirements associated with these rights.

- Users may download and print one copy of any publication from the public portal for the purpose of private study or research.
- You may not further distribute the material or use it for any profit-making activity or commercial gain
- You may freely distribute the URL identifying the publication in the public portal.

If the publication is distributed under the terms of Article 25fa of the Dutch Copyright Act, indicated by the "Taverne" license above, please follow below link for the End User Agreement:

[www.tue.nl/taverne](http://www.tue.nl/taverne)

***Take down policy***

If you believe that this document breaches copyright please contact us at:

[openaccess@tue.nl](mailto:openaccess@tue.nl)

providing details and we will investigate your claim.

# **Realization of a Demonstrator Slave for Robotic Minimally Invasive Surgery**

Linda van den Bedem



This research is supported by the Dutch Technology Foundation STW, applied science division of NWO and the Technology Program of the Ministry of Economic Affairs.

A catalogue record is available from the Eindhoven University of Technology Library.

Realization of a Demonstrator Slave for Robotic Minimally Invasive Surgery / by  
Linda J.M. van den Bedem. – Eindhoven: Technische Universiteit Eindhoven, 2010  
Proefschrift. – ISBN: 978-90-386-2300-9

Copyright © 2010 by Linda J.M. van den Bedem.

This thesis was prepared with the pdfL<sup>A</sup>T<sub>E</sub>X documentation system.

Layout Design: Dennis Bruijnen, TU Eindhoven, the Netherlands.

Cover Design: Dirk de Kanter and Linda van den Bedem, Eindhoven, the Netherlands.

Reproduction: PrintPartners Ipskamp B.V., Enschede, the Netherlands.

# **Realization of a Demonstrator Slave for Robotic Minimally Invasive Surgery**

PROEFSCHRIFT

ter verkrijging van de graad van doctor  
aan de Technische Universiteit Eindhoven,  
op gezag van de rector magnificus, prof.dr.ir. C.J. van Duijn,  
voor een commissie aangewezen door het College voor Promoties  
in het openbaar te verdedigen  
op woensdag 22 september 2010 om 16.00 uur

door

Linda Jacoba Martina van den Bedem

geboren te Amersfoort

Dit proefschrift is goedgekeurd door de promotoren:

prof.dr.ir. M. Steinbuch

en

prof.dr. I.A.M.J. Broeders

Copromotor:

dr.ir. P.C.J.N. Rosielle

# Summary

## Realization of a Demonstrator Slave for Robotic Minimally Invasive Surgery

Robots for Minimally Invasive Surgery (MIS) can improve the surgeon's work conditions with respect to conventional MIS and to enable MIS with more complex procedures. This requires to provide the surgeon with tactile feedback to feel forces executed on e.g. tissue and sutures, which is partially lost in conventional MIS. Additionally use of a robot should improve the approach possibilities of a target organ by means of instrument degrees of freedom (DoFs) and of the entry points with a compact set-up. These requirements add to the requirements set by the most common commercially available system, the da Vinci which are: (i) dexterity, (ii) natural hand-eye coordination, (iii) a comfortable body posture, (iv) intuitive utilization, and (v) a stereoscopic '3D' view of the operation site.

The purpose of Sofie (Surgeon's operating force-feedback interface Eindhoven) is to evaluate the possible benefit of force-feedback and the approach of both patient and target organ. Sofie integrates master, slave, electronic hardware and control. This thesis focusses on the design and realization of a technology demonstrator of the Slave. To provide good accuracy and valuable force-feedback, good dynamic behavior and limited hysteresis are required. To this end the Slave includes (i) a relatively short force-path between its instrument-tips and between tip and patient, and (ii) a passive instrument-support by means of a remote kinematically fixed point of rotation. The incision tissue does not support the instrument.

The Slave is connected directly to the table. It provides a 20 DoF highly adaptable stiff frame (*pre-surgical set-up*) with a short force-path between the instrument-tips and between instrument-tip and patient. During surgery this frame supports three 4 DoF manipulators, two for exchangeable 4 DoF instruments and one for an endoscope.

The pre-surgical set-up of the Slave consists of a 5 DoF platform-adjustment with a platform. This platform can hold three 5 DoF manipulator-adjustments in line-up. The set-up is compact to avoid interference with the team, entirely me-

chanical and allows fast manual adjustment and fixation of the joints. It provides a stiff frame during surgery. A weight-compensation mechanism for the platform-adjustment has been proposed. Measurements indicate all natural frequencies are above 25 Hz.

The manipulator moves the instrument in 4 DoFs ( $\Phi$ ,  $\Psi$ ,  $\Theta$  and  $Z$ ). Each manipulator passively supports its instrument with a parallelogram mechanism, providing a kinematically fixed point of rotation. Two manipulators have been designed in consecutive order. The first manipulator drives  $\Psi$  with a worm-wormwheel, the second design uses a ball-screw drive. This ball-screw drive reduces friction, which is preferred for next generations of the manipulator, since the worm-wormwheel drive shows a relatively low coherence at low frequencies. The compact  $\Theta Z$ -manipulator moves the instrument in  $\Theta$  by rotating a drum. Friction wheels in the drum provide  $Z$ . Eventually, the drum will be removable from the manipulator for sterilization. This layout of the manipulator results in a small motion-envelope and least obstructs the team at the table. Force sensors measuring forces executed with the instrument, are integrated in the manipulator instead of at the instrument tip, to avoid all risks of electrical signals being introduced into the patient. Measurements indicate the separate sensors function properly. Integrated in the manipulator the sensors provide a good indication of the force but do suffer from some hysteresis which might be caused by moving wires.

The instrument as realized consists of a drive-box, an instrument-tube and a 4 DoF tip. It provides the surgeon with three DoFs additional to the gripper of conventional MIS instruments. These DoFs include two lateral rotations (pitch and pivot) to improve the approach possibilities and the roll DoF will contribute in stitching. Pitch and roll are driven by means of bevelgears, driven with concentric tubes. Cables drive the pivot and close DoFs of the gripper. The transmissions are backdriveable for safety. Theoretical torques that can be achieved with this instrument approximate the requirements closely. Further research needs to reveal the torques achieved in practice and whether the requirements obtained from literature actually are required for these 4 DoF instruments. Force-sensors are proposed and can be integrated.

Sofie currently consists of a master prototype with two 5 DoF haptic interfaces, the Slave and an electronic hardware cabinet. The surgeon uses the haptic interfaces of the Master to manipulate the manipulators and instruments of the Slave, while the actuated DoFs of the Master provide the surgeon with force-feedback.

This project resulted in a demonstrator of the slave with force sensors incorporated, compact for easy approach of the patient and additional DoFs to increase approach possibilities of the target organ. This slave and master provide a good starting point to implement haptic controllers. These additional features may ultimately benefit both surgeon and patient.

# Nomenclature

## Symbols

Symbol	Description	Unit
$\alpha$	coefficient of expansion	$10^{-6}/K$
$\Phi_0$	initial $\phi$ -rotation of the manipulator while being identified	$^\circ$
$\phi$	rotation in the plane tangent to the muscular layer	$^\circ$
$\phi$	rotation of the manipulator	$^\circ$
$\Psi_0$	initial $\psi$ -rotation of the manipulator while being identified	$^\circ$
$\psi$	rotation in the plane tangent to the muscular layer	$^\circ$
$\psi$	rotation of the manipulator	$^\circ$
$\theta$	rotation aligned with the center line of the instrument	$^\circ$
$\omega_{\phi, \psi, \theta}$	angular velocity in respectively $\phi, \psi, \theta$	rad/s
$\sigma_{Hz}$	Hertzian contact stress	N/m <sup>2</sup>
$\nu$	Poisson's ratio of a material	-
$A$	surface	m <sup>2</sup>
$a$	distance between point P and support A	m
$C$	circumference	m
$C_{1,2}$	controller of the system for either SISO ( $C$ ) or MIMO ( $C_{1,2}$ )	-
$c$	lateral stiffness	N/m
$c_{ax}$	axial stiffness	N/m
$c_{fixed}$	lateral stiffness at the instrument-tip when fixed at its top	N/m
$c_{tip}$	lateral stiffness at the instrument-tip	N/m
$c_{x,y,z}$	stiffness in respectively $x, y, z$ -direction	N/m
$D$	diameter	m
$D_{Fw}$	diameter of the friction wheel	m
$D_G$	diameter of curvature for the cable connected to the gripper	m
$D_{curv}$	diameter of curvature, either of the gripper or pulley	m
$D_i$	inner diameter of the instrument tube	m
$D_o$	outer diameter of the instrument tube	m
$D_{Wu}$	diameter of the pulley applied in the instrument-tip	m
$d\phi$	resolution in $\phi$	$^\circ$
$d\psi$	resolution in $\psi$	$^\circ$
$d\theta$	resolution in $\theta$	$^\circ$

Symbol	Description	Unit
$dL$	change in length	m
$dL_{max}$	maximum change in length	m
$dL_{min}$	minimum change in length	m
$dr$	displacement	m
$dT$	change in temperature	°C
$dz$	displacement in $z$ -direction	m
$dz_f$	virtual play in $z$ -direction due to friction	m
$E$	modulus of elasticity or Young's modulus of a material	N/m <sup>2</sup>
$e$	eccentricity	m
$e$	error signal	V
$F$	force	N
$F_{11,21}$	the force sensor output (MIMO)	-
$F_{curv}$	force allowed as a function of $D_{curv}$	N
$F_f$	friction force	N
$F_{f-tot}$	friction force, total	-
$F_{in}$	input force	N
$F_{max}$	maximum force	N
$F_{min}$	minimum force	N
$F_{out}$	output force	N
$F_{out-max}$	maximum output force	N
$F_{out-min}$	minimum output force	N
$F_p$	preload force	N
$F_{pb}$	preload force applied at the preload wheel block	N
$F_s$	static load	N
$F_t$	tangential force	N
$F_{tip}$	force at instrument tip	N
$F_{tip-max}$	maximum force at instrument tip	N
$F_w$	friction wheel of the Z-drive	-
$F_{zf}$	occurring friction (in hysteresis-loop)	N
$f_0$	first natural frequency of the mechanism	Hz
$f_{roll}$	rolling friction coefficient	-
$f_s$	sliding friction coefficient	-
$f_{x,y,z}$	frequency in respectively $x$ , $y$ , $z$ -direction	Hz
$G$	shear modulus of a material	N/m <sup>2</sup>
$g$	gravitational acceleration	m/s <sup>2</sup>
$H$	height	m
$I$	area moment of inertia	m <sup>4</sup>
$I_p$	polar area moment of inertia (against torsion)	m <sup>4</sup>
$I_t$	area moment of inertia of a tube	m <sup>4</sup>
$i$	actuation signal	V
$i$	transmission ratio	-
$i_{tot}$	total transmission ratio	-
$K_{b1,b2}$	bending stress factor to calculate bending stress in gears	-
$K_{c1,c2}$	Hertzian stress factor to calculate contact stress in gears	-
$k$	rotational stiffness	Nm/rad
$k_\phi$	rotational stiffness in $\phi$	Nm/rad
$k_\psi$	rotational stiffness in $\psi$	Nm/rad
$k_\theta$	rotational/torsional stiffness in $\theta$	Nm/rad
$k_t$	rotational stiffness $k_t(c_t)$	Nm/rad

Symbol	Description	Unit
$L$	length	m
$L_G$	length of the instrument gripper	m
$L_i$	incision length	-
$L_{ins}$	instrument inserted length, related to the muscular layer of the incision	m
$L_o$	instrument length	m
$L_{tip}$	instrument tip length	m
$LL$	left lateral rotation of the operating table	°
$m$	mass	kg
$m_s$	static load applied by means of mass	kg
$m_t$	tube mass	kg
$n$	number of friction surfaces or contacts	-
$P$ or $P_{ij}$	the process or system, with $P_{ij}$ one SISO term of the process	-
$P_{m11,m21}$	the force sensor process (MIMO)	-
$R$	radius	m
$R_e$	radial distance of elastic element e	m
$RL$	right lateral rotation of the operating table	°
$rT$	reverse Trendelenburg rotation of the operating table	°
$S$	safety factor	-
$S$	sensitivity	-
$T$	complementary sensitivity	
$T$	Trendelenburg rotation of the operating table	°
$T_a$	applied torque	Nm
$T_m$	measured torque	Nm
$T_{max}$	maximum torque	Nm
$T_{min}$	minimum torque	Nm
$T_{out-max}$	maximum (measured) torque related to point P	Nm
$T_{out-min}$	resolution of (measured) torque related to point P	Nm
$T_p$	preload torque	Nm
$T_{tip-max}$	maximum output torque at the instrument tip	Nm
$T$	temperature	°C
$t$	wall thickness (of the outer instrument tube)	m
$t$	thickness	m
$u_S$	measurement signal for sensitivity	V
$u_T$	measurement signal for complementary sensitivity	V
$v$	velocity (of the instrument-tip)	m/s
$v_z$	translational velocity in $z$	m/s
$x, y, z$	cartesian coordinates	m
$x_{in}$	$x$ -movement, in	m
$x_{out}$	$x$ -movement, out	m
$z$	translation of the instrument, aligned with the center line of the instrument	m

## Subscript

Symbol	Description
$E$	endoscope trocar
$e$	elastic element
$f$	friction
$i$	index number, can stand for several things
$max$	maximum
$min$	minimum
$O$	target organ
$o$	outer
$out$	defined at the kinematically fixed point of rotation P
$p$	preloaded
$Ri$	instrument trocar
$t$	tube
$tot$	total
$Wf$	friction wheel
$Wp$	preload wheel

## Acronyms

Acronym	Description
$\Phi, \Psi, \Theta$	DoF of the manipulator or instrument
$A_{1,2}$	assistant 1,2 at the operating table
$A_{i1,i2}$ or $\square$	retractor or assistant instrument trocar
ADC	analog-to-digital converter
Amp	amplifier
AZM	Academisch Ziekenhuis Maastricht
B	bevelgear (of the Z-drive)
CPU	central processing unit
D/A	digital-to-analogue
DAC	digital-to-analogue converter
DoF(s)	degree(s) of freedom
E or $\bigcirc$	endoscope trocar
EM	electro mechanical
Enc	encoder
H1	lower horizontal arm of the $\Phi\Psi$ -manipulator
H2	upper horizontal arm of the $\Phi\Psi$ -manipulator
J2	joint between H1 and V1
I/O	input / output
J4	joint between H2 and V2
L	large
l	left
l.m.l.	left midclavicular line
Mech	mechanical
MIMO	multiple input multiple output
MIS	minimally invasive surgery
No	number
OR	operating room or operating theater
PLC	programmable logic controller
point P	kinematically fixed point of rotation P or kinematic rotation pole or remote center of rotation of the manipulator
R	robot
$R_{i1,i2}$ or $\triangle$	robot instrument trocar
RA	rapidly adapting (receptors)
r.a.l.	right axillary line
S	small
S	surgeon
SA	slow adapting (receptors)
SISO	single input single output
TU/e	Eindhoven University of Technology
UMC Utrecht	Universitair Medisch Centrum Utrecht
V1	front vertical arm of the $\Phi\Psi$ -manipulator
V2	back vertical arm of the $\Phi\Psi$ -manipulator
$W_f$	friction wheel of the Z-drive
$W_p$	preload wheel of the Z-drive
$W_w$	worm-wormwheel
Z	DoF of the manipulator or instrument

## Medical Dictionary

The dictionary is based on information from [28], unless stated otherwise.

anthropometry	the study of determining the dimensions and proportion of the (human) body
axillary	armpit
axillary line	
anterior	a vertical line along anterior axillary fold
mid	a vertical line at mid point between anterior and posterior axillary line
posterior	along post axillary fold
CABG	coronary artery bypass graft: a surgical procedure, which involves replacing diseased (narrowed) coronary arteries with veins obtained from the patients lower extremities (autologous graft). During this procedure the patient is placed on a heart bypass machine (heart-lung machine) to allow the surgeon adequate time to perform surgery on the resting (nonbeating) heart [89]
cholecystectomy	the surgical removal of the gallbladder
clavicle	collar bone
colectomy	the surgical removal of the colon or part of the colon (partial colectomy, hemi-colectomy)
corpuscle	(1) a small mass or body, (2) a blood cell
hernia	the protrusion of a loop or knuckle of an organ or tissue through an abnormal opening
herniation	bulging of tissue through an opening in a membrane, muscle or bone
hiatal	relating to the hiatus: an aperture, opening, or foramen
hiatal      hernias	the protrusion of a loop or knuckled of an organ or tissue through an abnormal opening
(HHs)	
laparoscopy	a surgical procedure in which a tiny scope is inserted into the abdomen through a small incision. it is used for a variety of procedures and often to diagnose disease of the fallopian tubes and pelvic cavity
metastases	cancer that started from cancer cells from another part of the body
midclavicular line	a vertical line passing through the midpoint of the clavicle
mitral valve repair	surgical procedure to repair the valve between the left auricle and left ventricle of the heart [89]
mobilization	making movable
mucous      membrane	the lubricated inner lining of the mouth, nasal passages, vagina and urethra, any membrane or lining which contains mucous (slimy) secreting glands
myotomy	the dissection, or that part of anatomy which treats of the dissection, of muscles

---

Nissen fundoplication	treatment of reflux oesophagitis: by manipulating the lower oesophagus and stomach, a zone of increased pressure is created in the lower oesophagus. The increase in intraluminal pressure will discourage the reflux of stomach acid back into the oesophagus (which can lead to oesophageal inflammation)
obesity	an increase in body weight beyond the limitation of skeletal and physical requirement, as the result of an excessive accumulation of fat in the body
oesophageal	pertaining to the oesophagus
oesophagitis	inflammation of the oesophagus
oesophagus	that part of the alimentary canal between the pharynx and the stomach; the gullet
pharynx	the cavity at the back of the mouth. It is cone shaped and has an average length of 76 mm and is lined with mucous membrane. The pharynx opens into the oesophagus at the lower end
pneumoperitoneum	the abdominal cavity is inflated with CO <sub>2</sub> to create workspace for the surgeon
prolapse	the falling down or sinking of a part
proprioceptive	capable of receiving stimuli originating in muscles, tendons, and other internal tissues. Origin: L. Proprius, one's own, and capio, to take
prostatectomy	the surgical removal of the prostate gland
psychophysics	the science of the connection between nerve action and consciousness; the science which treats of the relations of the psychical and physical in their conjoint operation in man; the doctrine of the relation of function or dependence between body and soul
psychophysiology	the study of the physiological basis of human and animal behavior
rectopexy	surgical fixation of a prolapsing rectum
rectum	the last portion of the large intestine (colon) that communicates with the sigmoid colon above and the anus below
reflux	a backward or return flow
resection	excision of a portion or all of an organ or other structure
sclerotic	pertaining to (soft) tissue composed of cells either with the walls hardened or with the walls both hardened and thickened
supine	on the back
tendon	a fibrous, strong, connective tissue that connects muscle to bone
thoracoscopy	the use of a fiberoptic scope through a small incision in the chest wall for the purpose of directly observing the organs of the chest
thymectomy	removal of the thymus
Trendelenburg	German surgeon, 1844–1924
-position	a supine position on the operating table, which is inclined at varying angles so that the pelvis is higher than the head with the knees flexed and legs hanging over the end of the table; used during and after operations in the pelvis or for shock.

trocar	the trocar is a surgical device, which makes it possible to create incisions in a visceral cavity (i.e. thorax, abdominal cavity) and keeps it open with the aid of a tube [53]. Strictly speaking, a trocar is the cutting obturator within a cannula (through which an instrument enters the body cavity). In practice, the term trocar is commonly used by surgeons to describe the whole trocar-cannula apparatus [74]. The cannulas have a valve-system. The troicarts or trocars have their point of rotation at chest or abdominal level because they are fixed there [21]
uterectomy	the operation of excising the uterus, performed either through the abdominal wall or through the vagina
visuo-motor transformation	describes which muscles have to be stimulated and how far they have to contract to generate a desired hand movement to manipulate the instruments with respect to the retinal image, has been constructed in the surgeon's childhood but needs new programming, which requires training [16]

# Contents

<b>Summary</b>	<b>v</b>
<b>Nomenclature</b>	<b>vii</b>
<b>1 Robot Assisted Minimally Invasive Surgery</b>	<b>1</b>
1.1 Minimally Invasive Surgery . . . . .	1
1.2 Historical developments and current systems . . . . .	5
1.3 Problem formulation . . . . .	8
1.4 System overview and contents of this thesis . . . . .	9
<b>2 System Requirements</b>	<b>11</b>
2.1 Characteristics of performing MIS . . . . .	11
2.2 Characteristics of the human operator . . . . .	17
2.3 Requirements summarized . . . . .	19
<b>3 Pre-Surgical Set-up</b>	<b>21</b>
3.1 Pre-surgical set-up requirements . . . . .	22
3.2 Pre-surgical set-up concepts . . . . .	25
3.3 Platform-adjustment and platform . . . . .	28
3.4 Manipulator-adjustment . . . . .	40
3.5 Conclusion and recommendations . . . . .	46
<b>4 Manipulator for Instrument and Endoscope</b>	<b>49</b>
4.1 Manipulator design requirements and concepts . . . . .	49
4.2 Manipulator: $\Phi$ and $\Psi$ -DoFs . . . . .	56
4.3 Manipulator: $\Theta$ and $Z$ -DoFs . . . . .	71
4.4 Manipulator evaluation . . . . .	84
4.5 Conclusion and recommendations . . . . .	91
<b>5 Instrument</b>	<b>95</b>
5.1 Instrument requirements and concepts . . . . .	96
5.2 Instrument details . . . . .	102
5.3 Instrument evaluation . . . . .	118
5.4 Conclusion and recommendations . . . . .	118

<b>6</b>	<b>Sofie System-integration</b>	<b>121</b>
6.1	Interaction between surgeon and master . . . . .	121
6.2	Interaction between master and slave . . . . .	128
6.3	Conclusion and recommendations . . . . .	133
<b>7</b>	<b>Conclusion and Recommendations</b>	<b>135</b>
7.1	Introduction . . . . .	135
7.2	Conclusion . . . . .	136
7.3	Recommendations . . . . .	139
	<b>Bibliography</b>	<b>141</b>
<b>A</b>	<b>Minimally Invasive Surgery</b>	<b>151</b>
A.1	Advantages of conventional MIS . . . . .	151
A.2	Disadvantages of conventional MIS with respect to open surgery . . . . .	152
<b>B</b>	<b>Existing Robotic MIS Systems and Instruments</b>	<b>155</b>
B.1	Existing Systems . . . . .	156
B.2	Existing instrument-tips and accessories . . . . .	157
<b>C</b>	<b>Observed Procedures</b>	<b>159</b>
<b>D</b>	<b>Pre-Surgical Set-up</b>	<b>165</b>
D.1	Concepts for the pre-surgical set-up platform . . . . .	165
D.2	Mass of the platform-adjustment and platform . . . . .	166
D.3	Clamp $\Theta_1$ of the platform-adjustment . . . . .	167
D.4	Platform weight-compensation . . . . .	171
D.5	Measurement equipment used . . . . .	178
<b>E</b>	<b>Manipulator</b>	<b>179</b>
E.1	Manipulator drive-train characteristics . . . . .	179
E.2	Manipulator force sensors for $\Phi$ , $\Psi$ , $\Theta$ and $Z$ . . . . .	181
E.3	Manipulator eigenmodes 2 and 3 . . . . .	185
E.4	Manipulator identification measurement results . . . . .	186
<b>F</b>	<b>Instrument</b>	<b>189</b>
F.1	Calculations and data for the bevelgears used in the instrument-tip . . . . .	189
F.2	Cable-drive in the drive-box: gripper driven . . . . .	192
F.3	Drive-train characteristics . . . . .	193
	<b>Samenvatting</b>	<b>195</b>
	<b>Dankwoord</b>	<b>197</b>
	<b>Curriculum Vitae</b>	<b>199</b>

## Chapter 1

# Robot Assisted Minimally Invasive Surgery

Patients that experience conventional surgery are generally adequately mended regarding their actual disease or condition, but suffer from the large incision that accompanies this treatment. Minimally Invasive Surgery (MIS) is performed through small incisions and improves the patient's conditions. However, the surgeon then experiences disadvantages that can be overcome by using a robot. Such a robotic system generally consists of a master and slave. The surgeon controls the slave at the operating table by operating the master. This chapter presents background information on (robotic) MIS and historical developments in preparation to this thesis' scope and problem formulation: design and development of a slave for haptic enhanced robotic minimally invasive surgery with additional degrees of freedom (DoFs)<sup>1</sup>.

## 1.1 Minimally Invasive Surgery

Here, MIS is described regarding the conventional and robotic methods applied, and regarding the information available for surgeons performing MIS.

### 1.1.1 Conventional Minimally Invasive Surgery

With Minimally Invasive Surgery (MIS) the same therapeutic result is obtained as in conventional surgery, but with seriously reduced harm to the body. In

---

<sup>1</sup>partly based on [11]

conventional MIS or endoscopy the surgeon and possibly an assistant, perform surgery through small incisions of  $\approx 1$  cm. They obtain visual feedback from the body cavity with a scope plus camera and manipulate their long and slender instruments outside the patient. Within the field of MIS several disciplines can be distinguished. The name of the discipline depends on the body cavity in which surgery takes place, e.g. the area of work for the slave described in this thesis is laparoscopy and thoracoscopy, surgery performed in the abdominal and the thoracic cavity respectively. Performing surgery through small incisions (of approximately 1 cm) has proven advantages for the patient ([22] and mentioned references, Appendix Section A.1), mainly associated with the trauma related to accessing the area of surgery (Appendix A). However, it provides the surgeon with inconveniences and requires many hours of training ([96] and mentioned references, Appendix Section A.2). In short, these inconveniences include loss of natural hand-eye coordination and reduced dexterity, visual feedback and feedback on forces applied. Loss of the natural hand-eye coordination is the main reason [16, 17, 21, 109], which is caused by the eyes not being aimed at the hands (mislocation of the visible scene/monitor) and effects in the visible scene according to [16]. These effects consist of amplification, mirroring and misorientation between expected and observed tip movements. Misorientation is caused by a difference between the camera's line-of-sight and the surgeon's natural line-of-sight when looking directly into the abdomen. This seriously disturbs the visuo-motor transformation, because a hand movement does not result in a corresponding expected tip movement (on the retinal image). It requires extensive training to manipulate the instruments purposeful when performing MIS.

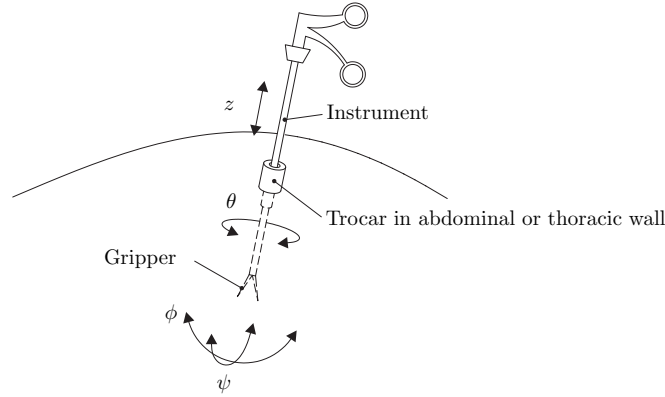


Figure 1.1: Conventional instruments used for endoscopic surgery allow instrument movements in  $\phi, \psi, \theta, z$  (with respect to the instrument trocar) and possibly provide a gripper action, resulting in five DoFs.

An incision reduces the number of available degrees of freedom (DoFs) to manipulate the instrument from the usual six or seven (if a gripper is applied) in open surgery to four movements  $\phi, \psi, \theta, z$  plus a fifth gripper DoF if applicable (Figure 1.1). This restricts the directions in which the target organ can be ap-

proached and the movements that the surgeon can make with the instrument-tip, thus limiting dexterity. In addition, manipulation of the surgical instruments, and visualization of the surgical field differ from that in open surgery [21]. The endoscope within, provides the visual feedback in MIS. It is often controlled by an assistant and visual feedback is generally limited to 2D despite the advances in endoscopic development. The first causes discomfort and orientation errors, while unstable camera control may compromise the smoothness of the procedure [108]. Furthermore, often the surgeon has to maintain an uncomfortable body posture. This may cause even physical complications in the long run.

In laparoscopy a pneumoperitoneum is created which means that the body cavity is inflated (8–12 mmHg) with carbon dioxide to create workspace. In thoracoscopy a lung is deflated which is sometimes supported with some additional gas. Plastic or metal cannulas (called trocars in the remainder of this thesis) with seals are placed in the incisions to protect the tissue, to simplify exchange of instruments and to keep the carbon dioxide inside the cavity. However, feedback on applied forces is limited due to friction between instruments and seals and can change during one procedure as the instrument becomes more wetted [37].

### 1.1.2 Robotic Minimally Invasive Surgery

The inconveniences for the surgeon that accompany MIS can be overcome by using a robotic master-slave operating system. In robotic minimally invasive surgery a robotic system is used to perform surgical procedures in a minimally invasive manner. The term robot is adopted because it seems to be a generally accepted name for the type of systems described below, in the medical/surgical community. Such a system consists of a slave at the operating table and a master, connected by means of a computer, electronics and control software. The slave at the operating table follows the path the surgeon specifies at the master. According to [19] it is not intended to replace a surgeon and perform tasks autonomously (which actually does not match with the definition of a robot given by [78, 109] and others<sup>2</sup>), since surgery is performed on human beings and not one patient is similar to the other. This requires direct control of the system by the surgeon. The intention is to physically separate the surgeon from the surgical site. The surgeon actually performs telesurgery (tele generally limited to 0.5–3 m), which can provide several advantages. A master-slave system allows the surgeon to perform surgery almost as if it was a conventional procedure. Additionally it provides possibilities of e.g. filtering tremor of the surgeon by applying a low-pass filter and scaling down hand and finger movements to a level where microvascular procedures are feasible (among others mentioned in [21, 108]). It can further extend human abilities<sup>3</sup> from relatively small/easy procedures possible while per-

<sup>2</sup>Generally a robot is seen as a machine that can replace a person, and is usually controlled by a computer [78], it performs its tasks autonomously without interference of a person [109] (here also called artificial intelligence (AI)).

<sup>3</sup>A master-slave system is based on intelligence amplification (IA) enhancing a human's own abilities [109], the system mentioned here is also called a medical robotic surgical-assistant

forming conventional MIS to technically challenging procedures (as mentioned in e.g. [21, 32, 80]). This does imply that the system provides at least six DoFs and preferably more, at the instrument-tip. The additional DoFs allow the surgeon to approach the target organ from more directions than originally granted by the incisions used. Preferably intuitive manipulation of these DoFs is provided at the master. In addition, an ergonomic design of the master can prevent surgeon's back and neck complaints that often occur when performing conventional MIS [21]. A teleoperated system can even be used to protect the surgeon from e.g. a harmful imaging environment, by allowing a safe distance between the slave and the master [101]. In addition, a master-slave system can extend the training possibilities by introducing the driving-school concept into the operating room (OR) when using two masters [6] and by training procedures beforehand on a master connected to a virtual environment.

In [107] (among others) several studies are presented that compare conventional MIS procedures and procedures performed with the da Vinci surgical system (see Table 1.1). It states, use of the system is considered to be safe and feasible, shows significant benefits in performing end-to-end anastomosis and aortic replacement in pigs, but is expensive, large, requires a relatively long set-up time and has a lack of force-feedback.

### 1.1.3 Obtaining information while performing MIS

The surgeon uses his or her senses, mainly sight, touch and hearing to obtain information while performing an open procedure. The information obtained from sight and touch is compromised while performing conventional MIS. The surgeon has direct sight on the target organ and surroundings in open surgery. In conventional MIS, the surgeon is generally provided with 2D visual information of (part of) the operative site on a screen. Current commercially available robotic MIS systems [63] provide the surgeon with stereoscopic visual information from the operative site. This information approaches the 3D visual feedback from open surgery if the surgeon is able to process stereoscopic feedback, which improves the 2D visual information provided when performing conventional MIS.

In open surgery, the surgeon directly senses forces exercised with and on his/her instruments. The surgeon has (more or less) direct contact with the target organ, he or she can palpate the organ to distinguish between healthy and inflamed tissue, or e.g. between healthy and sclerotic vessels. As stated, this haptic information from the operative site is reduced when conventional MIS is performed. An experienced surgeon derives the forces he or she executes while performing (robotic) MIS by observing the deformation of the tissue [19, 83, 96].

Haptic feedback consists of kinesthetic feedback and tactile information which roughly provides you with a sense of force and of surface structure respectively. Kinesthetic and tactile feedback give access to invisible structures and to manipulation or grasping forces [94]. Providing only three force levels on screen already

---

(whose surgeon extenders are operated directly by the surgeon and augment his/her abilities) in [120].

reduces the number of broken sutures, loose knots and applied peak forces [4] and therefore improves safety for the patient. However, by providing this force information haptically, another information channel than visual is used which reduces the visual load. This can reduce tiring the surgeon and improve the speed of the procedure since people react faster on force-input than on visual input [115]. It can even improve safety ([12] mentioned in [35]).

## 1.2 Historical developments and current systems

Inspecting body cavities to diagnose abnormalities of the bladder and gullet with a scope was done at the end of the nineteenth century already [22]. Gynaecologists performed relatively simple procedures like sterilization by looking directly through the scope and using one hand to perform the surgery, already in the 1950's [22]. The first laparoscopic cholecystectomy, performed on September 12, 1985 in Germany [102], is considered to be the first MIS procedure performed. In [38] (mentioned in [22]), a technique for laparoscopic cholecystectomy is presented that actually removed sceptis among fellow-surgeons. The surgeon got to use both hands when a camera was connected to the scope. A laparoscopic cholecystectomy was also the first (reported) operation that was performed with a robotic telemanipulation system (the 'Mona' from Surgical Intuitive) on 3 March 1997 at the St Pierre Hospital in Brussels, Belgium [60]. In the early 1990s, the first master-slave manipulator for surgery was developed at SRI International (originally Stanford Research Institute), supported by the US Federal Government. Its technology [14] (from [108]) was licensed to Intuitive Surgical in 1994 [108]. In 2000 the first laparoscopic procedure in the Netherlands was performed and robotic technology was introduced here [107]. Currently there are seven hospitals in the Netherlands that have a da Vinci system installed.

In 2001 the first transcontinental robot-assisted laparoscopic cholecystectomy was performed with a Zeus system on a patient situated in Strasbourg (France) by a surgeon situated in New York (USA) [85]. In 2003 a telerobotic remote surgical service with a Zeus system was set-up between a teaching hospital and a rural hospital to teach and assist the rural surgeons [6]. However, this is not strived for by [19, 83].

In [100, 120] and others, an overview has been presented on historical developments and existing medical systems which displays the above mentioned da Vinci system as well. This thesis is not intended to complete this overview, but some of the mentioned and some additional systems intended for laparoscopic and thoracoscopic robotic surgery are presented here in Table 1.1 and in Appendix Table B.1. An overview on instruments or instrument-tips is displayed in Table 1.2 and in Appendix Table B.2. This overview merely illustrates the variety of existing products and projects. The systems and instruments presented are subdivided in commercially available systems and systems that are developed and or used in laboratory.

Table 1.1: Pick from overview on robotic MIS systems.

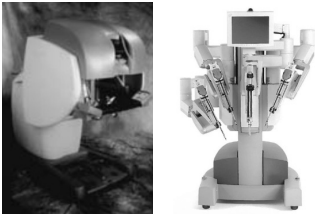
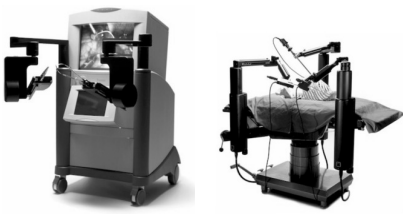

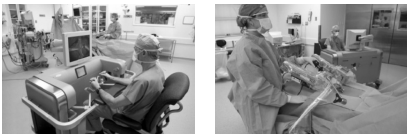
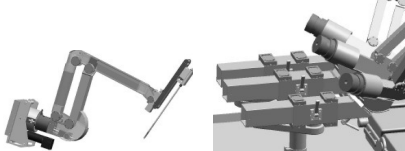


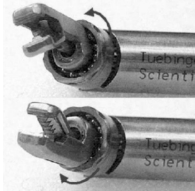

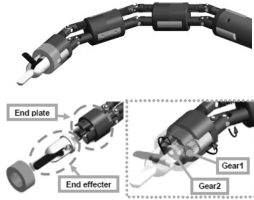
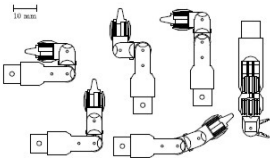
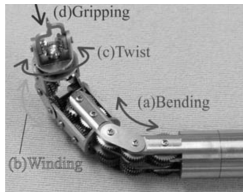
<b>Commercial: Laparoscopic / Thoracoscopic Robotic Systems</b>	
 <p>Intuitive Surgical Inc. (USA) has the da Vinci surgical system [49, 63] (based on [80, 81] and others) with a master (left) and floor mounted slave (right). It has 3-4 slave arms, with 4+3 (instrument) DoFs actuated each; passively supports the instrument in the incision; and no force-feedback.</p>	 <p>Intuitive Surgical Inc. (USA) has the Zeus [40] master-slave system since 7 March 2003 and took it out of production. It has table mounted slave manipulators with 4+2 gripper DoFs actuated each; does not support the instrument in the incision; and no force-feedback.</p>
<b>Research projects: Laparoscopic / Thoracoscopic Robotic Systems</b>	
 <p>Deutsches Zentrum für Luft und Raumfahrt (DLR, Germany) developed the MIRO: teleoperated surgery system for MIS [52, 53, 94, 95]. It has table mounted slave manipulators; 7 DoFs each; actively supports the instrument in the incision; and force-feedback.</p>	 <p>Hansen Medical Inc. (USA) with a cross-license with Intuitive Surgical [86] has the Laprotek surgical (master-slave) system [97] since April 4, 2005. It has table mounted slave manipulators; 7 DoFs each; instrument support in the incision is unknown; master capable of force-feedback.</p>
 <p>Biocybernetics Laboratory of the Heart Prosthesis Institute (Poland) developed the RobIn Heart slave [91, 92, 99]. It is floor mounted, has 3 arms on one standard, or two separate table mounted manipulators, 4+4 instrument DoFs each; passively supports the instrument in its incision; and no force-feedback.</p>	 <p>University of Washington (USA) developed the Raven [54, 55, 79]. It has two table mounted slave manipulators; 7 DoFs (Zeus instruments); passively supports the instrument in the incision; and no force-feedback.</p>

Table 1.2: Pick from overview on instrument-tips with either 3 or 4 DoFs.

Commercially available:	
 <p>Intuitive Surgical Inc. (USA) has the Endo-Wrist Instrument [117] operated with the da Vinci. It has 3 DoFs: pitch, yaw and gripper.</p>	 <p>Tuebingen Scientific Medical GmbH (Germany) has the Radius Surgical System [44], manually operated. It has 3 DoFs: pitch, roll and one gripper yaw.</p>
Research projects:	
 <p>DLR (Germany) has the MIRO instrument [53, 94, 95]. It has 3 DoFs: pitch, yaw and gripper. It includes a 6-DoF force sensor, a hexapod with strain-gauges.</p>	 <p>Kogakuin University (Japan) developed the Robotic Forceps Teleoperation System [70]. It has 4 DoFs: omnidirectional-bending/pitch, yaw, roll and one gripper yaw. Strain-gauges in the shaft measure forces.</p>
 <p>Biocybernetics Laboratory of the Heart Prosthesis Institute (Poland), developed the RobIn Heart instrument [99]. It has 4 DoFs: pitch, pitch, gripper and yaw.</p>	 <p>Waseda University (Japan) developed the Multi-DoF Forceps Manipulator [64]. It has 4 DoFs: bending, winding, twist, gripper (yaws are coupled).</p>

Some of the systems presented (da Vinci, RobIn Heart) have their slave mounted on the floor. In conventional (MIS) procedures, changing the orientation of the table is used by the surgeon e.g. to influence blood flow [83] or reposition the intestine. This can be facilitated by coupling the slave to the table. Table 1.1 shows systems which have each manipulator of the slave separately connected to the table. Others support it on the patient (Appendix Table B.1). Some systems do not provide instrument-support (e.g. Zeus from the table above

and UC Berkeley system Table B.1), while others support the instrument either actively (e.g. MIRO) or passively (e.g. da Vinci). Accuracy is highest for slaves providing instrument support, since they are independent of the variable support stiffness the incision tissue can provide. Systems providing instrument support are either designed for compliance and actively support the instrument (e.g. MIRO), or designed for stiffness with a passive kinematically fixed point of rotation to support the instrument (e.g. da Vinci). Compliant systems are stated to be inherently safe in case of collisions, e.g. with the team surrounding the table. A low stiffness or high compliance reduces the occurring collision force, however deteriorates the position accuracy significantly.

The RobIn Heart is the only slave providing eight DoFs. Its instrument presented in Table 1.2 has four DoFs, as well as some others. The RobIn Heart Instrument does not provide force-measurements, the MIRO instrument-tip does. The MIRO is the only system listed here providing force-feedback. A separate three-DoF force sensor is shown in Appendix Figure B.1.

### 1.3 Problem formulation

The most prominent commercially available robotic system for laparoscopy and thoracoscopy (da Vinci) provides the surgeon with advantages like an ergonomic position, natural hand-eye coordination, wrist dexterity and stereoscopic ('3D') visual feedback. However, additional features derived from the system overview presented above, would meet the surgeon's and hospitals wishes even more. These include:

1. connecting the slave to the operating table to ease adjustment of the table during surgery,
2. providing additional DoFs to the instrument-tip to extend organ approach possibilities,
3. providing the surgeon with force-feedback to reduce operating time and improve safety for the patient,
4. reducing the size of the system to ease approaching the patient and the field of surgery, and
5. reducing the costs and improve set-up time of the system.

Sofie (Surgeon's Operating Force-feedback Interface Eindhoven) is being developed<sup>4</sup> to integrate all features (focus on 1–4) mentioned above into one robotic MIS system for (general) laparoscopy and thoracoscopy. Its overall purpose is to evaluate the possible benefit of force-feedback and of additional DoFs.

Providing force-feedback requires (i) measuring forces at the slave to obtain the required information, (ii) actuating the two operator's joysticks (*master interfaces*), (iii) and providing haptic control (software). Good dynamic behavior and

<sup>4</sup>at Eindhoven University of Technology

limited hysteresis for both master and slave are very relevant in order to provide valuable force-feedback and good accuracy. Especially, since we chose to measure the forces outside the body cavity for safety of the patient, and to measure the movements of the instrument and surgeon's hand at the actuator of each DoF. This thesis focusses on the mechanical design and realization of a technology demonstrator of Sofie's slave (*the Slave*). The features and choices mentioned above will be integrated in the Slave, based on the following ideas:

- provide the endoscope and instrument manipulators with a single stiff frame near the field of surgery, which is connected to the table [106],
- place the force sensors to measure forces executed with the instrument-tip, at the manipulator and instrument outside the patient, and
- provide the instrument-tip with four DoFs.

These ideas will be implemented and evaluated, related to the features mentioned in this thesis.

## 1.4 System overview and contents of this thesis

This thesis primarily focusses on the Slave. Figure 1.2 shows a sneak-preview of the Slave with its main modules: the pre-surgical set-up, the manipulators and its endoscope and instruments.

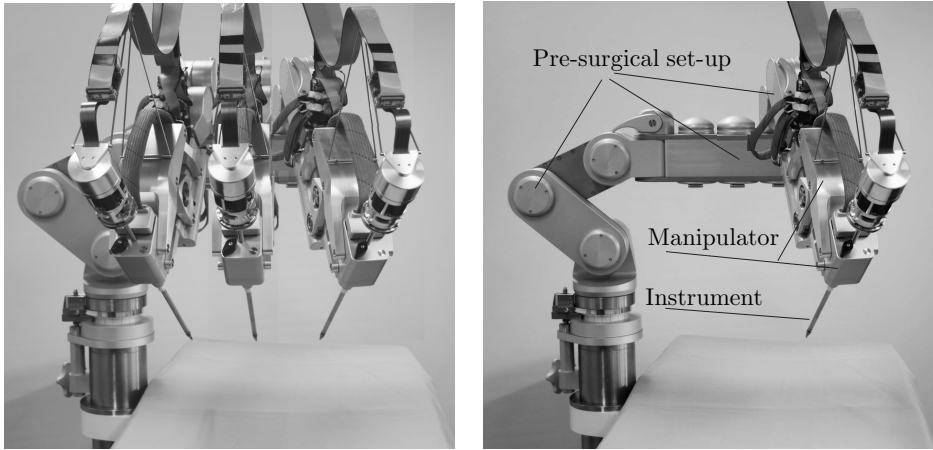


Figure 1.2: Modular layout of the Slave: one pre-surgical set-up (Chapter 3), three manipulators (Chapter 4) and two instruments (Chapter 5) and one endoscope. Left shows the Slave with its manipulator and instrument in three positions of the pre-surgical set-up, right shows the current status of the Slave as realized.

First, Chapter 2 discusses its requirements to integrate the features mentioned, incorporating the basic ideas. These requirements are based on a literature study on human characteristics regarding sensing forces and performing accurate movements, and on a field study in which MIS procedures are observed and discussed. This information will be merged into design and performance requirements. Chapters 3–5 will discuss the modules of the non-autonomous Slave as shown in Figure 1.2. These modules are a pre-surgical set-up (Chapter 3), one of three endoscope and instrument manipulators (Chapter 4) and a four-DoF instrument (Chapter 5). Each of these three chapters will discuss the requirements, the concepts, a detailed description on the design as realized (e.g. kinematics, drive-line, force sensors) and an evaluation pertaining to its respective module. Chapter 6 will discuss the Slave integrated within the framework of Sofie. This framework also includes a master (two are discussed), the electronics, and the (haptic) control-software. Design of one of the two presented masters and the haptic control are covered by two closely related projects. Conclusion and recommendations on the design and realization of the Slave for haptic enhanced robotic MIS with additional DoFs can be found in Chapter 7.

## Chapter 2

# System Requirements

The Slave is intended to be compact and connected to the table, provide additional degrees of freedom (DoFs), measure forces and improve set-up time (features mentioned in Section 1.3). This chapter presents the design and performance requirements of the Slave. The design requirements form the basis of developing the layout of the Slave. The performance requirements form the basis to actually detail the design and evaluate the system. Characteristics of performing minimally invasive surgery (MIS) and characteristics of the human operator will lead to these design and performance requirements of the Slave, respectively presented in Section 2.1, 2.2 and 2.3. The first characteristics are derived from literature and from both conventional and robotic MIS procedures we observed and evaluated afterwards with the surgeon [8, 9]. The second characteristics regarding the human operator are derived from literature. Useability related to the patient's safety, the OR room and human-machine-interfacing interweave the previously mentioned requirements. These points are mainly of concern when the system is commercialized, but will be taken into account if possible. Experience with the system will indicate whether the requirements proposed are proper set.

## 2.1 Characteristics of performing MIS

### 2.1.1 Performing MIS: patient and team position

Space in an operating room (OR) often is limited, especially around the operating table. One surgeon, two assistants at the operating table (one often in training), one scrub nurse, one OR nurse to help out the scrub nurse and one or two anesthesiologists are deployed around the operating table to perform (robotic) MIS, thus

a total of six to seven people. This number of people is also required for an open procedure. Appendix Table C.1 [8] displays a schematic overview of observed procedures with the positions of the surgeon, assistants and robot (if applicable). The anaesthesiologist, scrub nurse and OR nurse are not presented. However, note that the anaesthesiologist generally stays near the patient's head, one of the patient's arms protrudes from the operating table, and the scrub-nurse is located near the surgeon or the first assistant (in case of robotic MIS).

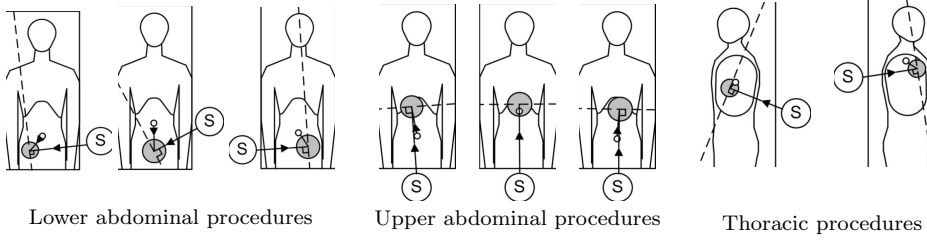


Figure 2.1: The surgeon (S) and endoscope trocar (small circle) generally remain at the same side of the surgical area (grey circle), based on [8].

Figure 2.1 shows that conventional procedures have the endoscope trocar and surgeon at the same side of the surgical area (from [8], describing procedures both witnessed and from literature). Ideally, the surgeon stands on the line through the target organ and the endoscope trocar (O'E in Figure 2.2) to make the conditions for instrument manipulation best. The torso of the surgeon would be perpendicular to the line O'E.

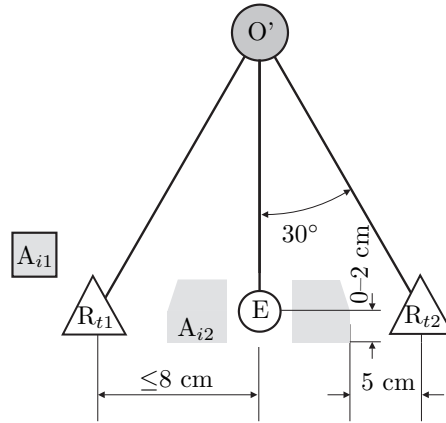


Figure 2.2: Picture from [19], is the point of departure for positioning trocars. O' is the (projection of the) target Organ, E the endoscope trocar, R<sub>t1,t2</sub> the robot instrument trocars, grey area the area for the assistant's trocars A<sub>i1</sub>, and A<sub>i2</sub> the liver retractor (in case of surgery in the upper abdomen).

These conditions are more easily met while performing conventional laparoscopy in the upper abdomen, the surgeon will stand between the patient's legs, or in thoracoscopy if the patient is in lateral position. However, often the surgeon has to depart this line resulting in an uncomfortable body posture, e.g. when surgery is performed in the lower abdomen (Appendix Table C.1). For robotic MIS this condition is met more easily regarding the Slave. The Slave replaces the surgeon at the operating table. It is positioned on line O'E, opposite the ideal position of the surgeon (to perform surgery from the same side as the surgeon would do in conventional MIS). The da Vinci slave has relatively long manipulators to be positioned on this line and reach the required trocars. The human arm length will be used as an indication for the length of the elements of the presented slave robot. Since the robot will provide movements similar to the movements of the surgeon. The first assistant takes the spot of the surgeon, see Appendix Table C.1. This spot is on the line O'E for surgery in the upper abdomen (e.g. a laparoscopic oesophageal myotomy). However, the assistant has to depart this line to perform surgery in the lower abdomen, e.g. a rectopexy. According to [83] the slave of the da Vinci would be located near the patient's left shoulder when performing a thymectomy, a CABG or a mitral valve repair in robotic thoracoscopic procedures. This coincides with a spot on the line O'E.

Appendix Table C.1 shows the patient in supine position when a laparoscopic procedure is performed. Sometimes a semi lateral position is used for procedures in the thoracic region and on the spleen, being performed from the abdomen [19]. This semi-lateral position is maintained by positioning the patient on a (vacuum) mattress filled with granule. [84] prefers a supine patient position when performing a thymectomy, a CABG, or a (mini) mitral valve repair with the da Vinci system. Appendix Table C.1 shows a lateral patient position for a oesophageal resection. In any case, the Slave should allow supine and lateral position of the patient for laparoscopy and thoracoscopy. During surgery the patient position relative to the table top is maintained. However, the table orientation is preferably variable. A procedure performed in the lower or upper abdomen generally starts with respectively a Trendelenburg or reverse-Trendelenburg position (max 30°) of the table. An additional lateral rotation can be used to increase the possibilities of positioning the organs. Basically, the table is tilted to move the other organs away from the target organ [19] or to influence the circulation and blood volume. This change has to be realized together with the anesthiologist(s). Applying the table with an additional flex provides extra space between the ribs [84].

### 2.1.2 Performing MIS: trocar placement

It needs to be possible to place the trocars anywhere in the thoracic or abdominal region. The torso length (seat-shoulder) of a person is about 70 cm. Crosswise, the boundaries are given by the shoulder and hip width<sup>1</sup>. The mean male shoulder width (50 cm [50]) is taken as a reference. The range of height of the trocars

<sup>1</sup>These values will probably not hold for obese patients.

(relative to the table-top) is indicated by the patient in supine position and in lateral position. In supine position the patient's abdomen indicates the height of the trocars. The minimum abdominal height is 20 cm, which will increase when inflated with carbon dioxide. In lateral position the thorax width is set as a reference. This width is adopted similarly to the shoulder width. So, it needs to be possible to place the incisions within an area of 70x50 cm and within 20–50 cm perpendicular to the table top.

Figure 2.2 shows the ideal position of the endoscope (E) and instrument ( $R_{t1,t2}$ ) trocars of the robot. The incisions of the robot trocars need to have a mutual distance of at least 8 cm, to prevent collision of the arms [19]. This figure corresponds to the description of a thymectomy [126] (and others), in which (i) a sufficient distance between and triangulation of the trocars is stressed to prevent this fencing or colliding, (ii) a  $180^\circ$  arc should contain these trocars to avoid mirror imaging, and (iii) a suitable distance between trocars and target organ is required, to provide space for manipulation. Appendix Table C.2 shows the observed trocar positions, which are defined with respect to the endoscope trocar (note that these are rather estimates than firm values). The robot instrument trocar positions are most relevant for design of the Slave. In robotic procedures in the upper and lower middle abdomen the robot instrument trocars remain within 5 cm of the endoscope trocar in  $x$ -direction and within 5–20 cm of the endoscope trocar in  $y$ -direction, with  $x$ -direction dictated by the line O'E (Figure 2.2). This approaches the numbers in Figure 2.2. The instrument or retractor trocars of the assistants ( $A_{i1,i2}$ ), are often placed between the robot instrument trocars, except for the liver retractor which is used in procedures in the upper abdomen. The retractor between the endoscope and right robot instrument trocar is placed at a distance of 1–5 cm of the endoscope trocar in  $x$ -direction and at a distance of 5–10 cm in  $y$ -direction.

### 2.1.3 Performing MIS: initial trocar orientation

The initial orientation of the instrument or endoscope trocar, is the direction between the target organ and the respective incision, before surgery starts. Figure 2.3 shows this initial orientation. Figure 2.3(a) shows the coordinate systems involved, with the global coordinate system with its origin in the corner of the table top. The coordinate systems (CS) of the target organ, endoscope and instrument trocar are indicated with respectively  $CS_{O,E,Ri}$ . The origin of each of these coordinate systems is placed in the target organ, with  $z$  perpendicular to the table-top. The initial orientation of the endoscope and (robot) instrument trocars consists of a  $\theta$  and  $\psi$  component. Figure 2.3(b) and 2.3(c) display  $\theta_E$  and  $\theta_{Ri}$ . The initial orientation  $\psi$  of the endoscope or instrument trocar is a rotation around respectively axes  $y_E$  and  $y_{Ri}$ .

Appendix Table C.3 displays the initial orientation angles of the instruments. The total angle  $\theta$  between the instrument trocars remains within  $150^\circ$ , with a maximum of  $\pm 75^\circ$  and a minimum of  $\pm 15^\circ$ . With robotic laparoscopy, the trocars

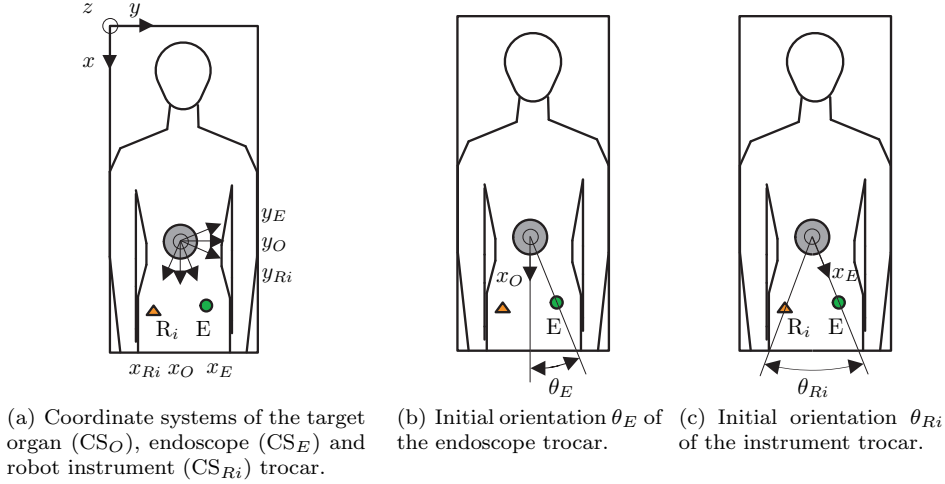


Figure 2.3: The initial orientation of the robot instrument ( $\Delta$ ,  $R_i$ ) and endoscope ( $\bigcirc$ ,  $E$ ) trocar, is the orientation of the trocars at the start of the surgical procedure, pointing towards the target organ (grey- $\bigcirc$ ). It has a  $\theta$  component with  $\theta_E$  and  $\theta_{Ri}$  shown in (b) and (c), and a  $\psi_E$ ,  $\psi_{Ri}$  component, the rotation around axes  $y_E$  and  $y_{Ri}$  (left figure).

enter the abdominal cavity with  $50^\circ < \psi < 75^\circ$  ( $75^\circ$  almost parallel to the table top). In thoracoscopic robotic procedures, this angle can be more perpendicular to the table top  $\psi \approx 30^\circ$ . In conventional procedures this can be even more extreme: the trocar lying in a plane parallel to the table top. The tension on the abdominal or thoracic wall should be minimal for the initial orientation of the trocars. However, in general this will not be the case since the trocar enters the body cavity (almost) perpendicular to the wall to limit the incision length. This direction often does not coincide with the initial orientation of the trocar, which is the case for both conventional and robotic procedures.

Thus ideally, the Slave should be adaptable to provide the surgeon with the required initial orientation of the trocars. The instrument diameter should be small, especially if they are to pass between ribs and to limit post-operative pain. It should at least be comparable with current instruments which range from 5 mm diameter to 13 mm diameter [74].

#### 2.1.4 Performing MIS: instrument movements

The observed instrument movements (Appendix Table C.4) are related to the required  $\phi$  and  $\psi$  of the instrument. The instrument movements are given relative to their initial orientation and expressed as rotations around the incision (again these values are rather estimates than firm). This table shows rather small angle variations in robotic surgery, up to  $40^\circ$  but generally about  $20$ – $30^\circ$ . In conventional MIS it can be even  $90^\circ$ . The instrument revolves  $\theta = \pm 270^\circ$  around its

$z$ -axis. Ideally (in conventional MIS), it is inserted 10–15 cm along its  $z$ -axis but generally more, up to 25 cm or even more when treating e.g. obese patients [19]. The observed robotic procedures show instrument-tip rotations of  $\pm 70^\circ$  for pitch and  $\pm 90^\circ$  for pivot, which is very advantageous in removing or applying stitches, according to [19]. These ranges exceed the human wrist movements. Stitching is done with a curved ( $90^\circ$ ) needle. The needle is grabbed in the middle, with the instrument axis perpendicular to the plane of the needle. By [83] and in [77] a preference for even more DoFs at the instrument-tip is expressed to allow more freedom of movement while performing surgery in the thoracic cavity. The rigid thoracic wall considerably limits the maneuverability at instrument angles greater than  $45^\circ$  [77]. The ribs restrict the freedom to position the trocars. According to [96] the desired accuracy when suturing blood vessels in cardiac surgery (a demanding task), is 0.1 mm for translation and  $0.5^\circ$  for rotation. To provide the surgeon with good manipulability a minimum velocity of 60 mm/s for translation and  $30^\circ/\text{s}$  for rotation is required. These will be implemented for large instrument-movements.

### 2.1.5 Performing MIS: executing forces

Requirements on forces that need to be executed with the instrument while suturing, are based on a literature study [36]. Tensile properties of sutures can give an indication of these loads when tying a suture, but the variance on their values are substantial [71]. Factors of influence are for instance: (i) type of suture (material used, suture caliber (diameter), spontaneous degradation, natural or synthetic composition, monofilament or multifilament structure used), (ii) rate of loading, (iii) presence of a surgical knot, and (iv) measurements performed (single suture versus multiple sutures in a sutured tendon). An analysis of publications with experimentally obtained load levels for instrument-tips used in endoscopy, establishes the following values:

- nominal needle driving and cutting of load 2.5 N while able to rotate the tip  $180^\circ$  in half a second (corresponds to the velocity set in [96]),
- nominal suture tying load of 5 N at standstill. In [113] it is stated that several Newtons are required to securely tie a suture, in [73] tying forces range from 1–5 N for various types of sutures,
- peak suture tying load of 10 N at standstill, which is based on a maximum force at the tip of 8.9 N in [80] and 6–7 N in [30], and
- nominal gripper load of 10 N, which should be able to securely hold a needle. The peak gripper load is set to 20 N, which lies between the maximum gripper force of 50 N in [80], of 40 N in [30] and 10 N in [113].

### 2.1.6 Performing MIS: safety

In [80] the following is stated regarding safety of the system, (i) removal of the Slave during the procedure should be easy e.g. in case of a conversion to conventional surgery, (ii) large DoFs of the Slave should be counterbalanced to limit the load on the person who sets up the system in combination with low inertia of the different elements, to reduce the stored energy in the system, (iii) DoFs should be redundantly equipped with e.g. sensors, brakes or clutches, (iv) some DoFs should be backdriveable to remove the corresponding part of the robot manually, and (v) sterilization is to be considered for parts that are directly or indirectly in contact with the patient. If the instrument is to be re-usable it has to be able to withstand the heat of an autoclave or chemical methods of sterilization [80]. In actual surgery all other slave robot parts are covered with a drape, this drape should not hamper its movement. Fail-safe operation is required for a commercial system, which requires a safety protocol for electrical hardware and software [80].

## 2.2 Characteristics of the human operator

The robotic system is operated by a surgeon. Therefore, it should match the characteristics of the human operator. It is not necessary to exceed these characteristics beyond the human capabilities (incorporating a scaling factor if applicable). The required bandwidth of the Slave strongly depends on the tasks the surgeon needs to perform. The tasks considered are controlling (output) and sensing tasks (input), respectively (i) executing accurate movements and applying forces to manipulate instruments, and (ii) obtaining haptic information from the (remote) environment. The input and output of people are asymmetric, they sense stimuli much faster than they can respond to them. In literature [25, 35] the control bandwidth refers to the rapidity with which people can respond, the sensing bandwidth refers to the frequency with which haptic stimuli are sensed.

### 2.2.1 Human performance in manipulating an instrument

Primarily, the operator needs to perform accurate voluntary movements with the Slave during surgical procedures. 99% of the frequency content of accurate motion by the surgeon is in the 0–2 Hz region [26, 54]. Whereas involuntary motion like tremor, is in the 8–10 Hz region [35, 114]. Ideally, the designed master-slave robot should be able to suppress these involuntary movements.

The accuracy of body movements strongly depends on human joint angle resolutions, which therefore are directly related to the fingertip position [119]. The shoulder joint ( $0.8^\circ$ ) has the best rotational resolution [119], and the best Cartesian resolution was found to be 1 mm [118] (from [25]). [56] suggests a four-times better resolution for the interface. This would require a  $0.2\text{--}0.5^\circ$  rotational res-

olution and 0.25 mm end-tip position resolution, similar to the recommendation made in [105] (from [25]). According to [104], the highest resolution a surgeon can position his hand with is 50  $\mu\text{m}$ .

According to ([115] and mentioned references) a single finger may exert 7 N without experiencing discomfort or fatigue [59], which is the same order as the values in Section 2.1.5. People can exert forces with their hand and fingers with a 5–10 Hz bandwidth [114].

### 2.2.2 Human performance and obtaining haptic information

Surgeons use their sense of touch to obtain information during a surgical procedure. This sense of touch (haptic sensing) can be subdivided into two categories: kinesthetic and cutaneous or tactile sensing. Within the haptic community [35] kinesthetic sensing incorporates the sensation of the body movements (proprioception) and force perception. It is based on receptors relatively deep inside the body, in muscles, tendons and joints. These sensors obtaining proprioceptive and force information are closely related, because also the sense of force plays a role in the sense of motion, as motion in free space compensates for one's limbs weight [35]. Kinesthetic sensing is mainly used to examine mechanical properties like stiffness, damping, geometry and weight. Cutaneous sensing, or tactile feedback, incorporates high frequent subtle information from receptors and nerve endings in the skin which indicate heat, pressure and texture [115]. According to ([23], from [114]) the force perception bandwidth is 20 Hz, the proprioceptive bandwidth is 30 Hz and tactile sensing has a bandwidth of 320 Hz. Vibrotactile stimuli can be perceived up to 1000 Hz. Initially, force-feedback is considered most relevant for the design of this slave. According to [23] (from [114]), the recommended control bandwidth is about 10 times the minimum necessary bandwidth required for a satisfactory performance of force-feedback. However in [25] several different recommendations are found: (i) in [105] a force feedback bandwidth of at least 50 Hz is recommended, (ii) in [103] a 15 Hz force feedback loop was used with good results, and (iii) in [62] study results are presented that show that even 8 Hz is sufficient, no significant advantages were observed when the force feedback bandwidth was increased to 32 Hz. Therefore, the required first natural frequency of the system is set to 20 Hz.

According to [80] the forces most valuable to the surgeon are the forces in the range up to 5 N. However, human beings have a (very) poor quantitative sense of force they apply, e.g. force sensation also depends on muscle fatigue. Fatigue increases the perceived force magnitude, even when the force actually produced by the muscle stays constant [69] (from [25, 35]). [68] (from [25, 35]) shows that the threshold by which a force variation can be detected depends on the initial force magnitude. This difference threshold equals 5–10% of the actual force level and holds for forces between 2.5 and 10 N [35]. The threshold deteriorates at lower levels. The threshold increases to 15–27% for forces below 0.5 N. The smallest force level that can be detected by hand equals 0.06 N.

In the field of laparoscopic and thoracoscopic surgery interaction will mainly take

place with soft tissue. People find a stiffness of 25,000 N/m indistinguishable from being rigid [119]. This value is relevant for instrument to instrument contacts rather than contact with soft tissue.

Humans are very sensitive to vibrations, sensitive to change in stimulus, but relatively insensitive to constant stimulus. Therefore, the system should be equally good in all directions regarding friction and inertia. Parasitic effects in the force signal like inertia and temperature should be compensated. Friction will be reflected back to the surgeon (e.g. in freespace-motion), scaled when a force scaling factor is used and contact forces below the frictional force will not be felt [80].

### 2.2.3 Human-machine interaction

Ideally, the surgeon should be able to enter the OR, install the system, connect the Slave to the trocars and start manipulating the instruments from the master without instructions beforehand. This means that it would provide an entirely ergonomic intuitive human-machine interface with a realistic (stereoscopic) impression of the surgical field and good contact with the people at the table. It should be possible to set-up the Slave easily since this reduces the OR preparation time. Besides, it should be possible to change instruments within a few seconds, for safety and to reduce the required operating time. Performing autonomous sub-tasks requires appropriate software and could make performing surgery on the heart possible, this does not fall within the scope of this project.

## 2.3 Requirements summarized

This section presents the design and performance requirements. These are derived from the characteristics just discussed. The design requirements typically incorporate the Slave's features and basic ideas from Section 1.3.

The design requirements should provide the Slave with:

- a single frame connected to the table (feature, basic idea and Section 2.1.1),
- easy setup (feature, Section 2.2.3) and removal (Section 2.1.6),
- high adaptability (Section 2.1.1, 2.1.2, 2.1.3),
- a compact design, occupy little space above and around the operating table and have a small motion envelope (feature, Section 2.1.1, 2.1.1 and 2.1.2),
- force-measurements outside the patient (feature and basic idea),
- instruments:
  - with a small diameter, at least comparable with a 5–13 mm diameter of current instruments (Section 2.1.3),
  - with four DoFs at the instrument-tip (feature, basic idea, Section 2.1.4),

- with the possibility to change within a few seconds (Section 2.2.3),
- safety by:
  - counterbalancing large DoFs (Section 2.1.6),
  - applying some DoFs with backdriveability (Section 2.1.6),
  - incorporating sterilization issues if applicable (Section 2.1.6), and
  - incorporating a safety protocol for the electrical hardware and software of a commercial system (Section 2.2.3).

The performance requirements of the Slave:

- provide the possibility to initially place and orientate the trocars:
  - within an area of 70x50 cm and within 20–50 cm perpendicular to the table-top (Section 2.1.2),
  - with a minimum distance of 8 cm between (lined up) endoscope and instrument trocars (Section 2.1.2),
  - with an additional (fine) adjustment of 5 cm in  $x$  and 12 cm in  $y$ , see Figure 2.2 for the definition of  $x$  and  $y$  (Section 2.1.2),
  - with an initial orientation  $\theta$  150° and  $30 < \psi < 75^\circ$  (Section 2.1.3),
- provide instrument movements:
  - a rotation of  $\pm 35^\circ$  in  $\phi$  and  $\psi$ , a rotation desirably more than  $\pm 180^\circ$  in  $\theta$  and translate 300 mm in  $z$  (Section 2.1.4), with an accompanying angular velocity  $\omega_{\phi,\psi}=0.5$  rad/s,  $\omega_\theta=4$  rad/s and velocity  $v_z=60$  mm/s,
  - a rotation of the instrument-tip of  $\pm 70^\circ$  for pitch and  $\pm 90^\circ$  for pivot (Section 2.1.4),
  - a resolution of 50  $\mu\text{m}$  should be strived for (Section 2.2.1), although 0.1 mm and  $0.5^\circ$  should be sufficient for suturing blood vessels in cardiac surgery (Section 2.1.4),
- provide application and measurement of forces:
  - a nominal needle driving, cutting load of 2.5 N while able to rotate the tip  $180^\circ$  in half a second and a peak load of 10 N at standstill for suture tying (Section 2.1.5), which corresponds to the 7 N a single finger may exert without experiencing discomfort or fatigue (Section 2.2.1),
  - a nominal gripper load of 10 N and a peak load of 20 N (Section 2.1.5),
  - a resolution of 0.06 N preferably (Section 2.2.2),
- provide (asymmetric input and output) bandwidths:
  - a 0–2 Hz input range for accurate motion by the surgeon (Section 2.2.1),
  - an 8–10 Hz input suppression for involuntary motion like tremor (Section 2.2.1),
  - a 5–10 Hz input for forces exerted with hand and fingers (Section 2.2.1), and
  - a 20 Hz (minimum) output range to obtain force-information for the master-interface (Section 2.2.2).

## Chapter 3

# Pre-Surgical Set-up

The complete slave robotic system consists of its pre-surgical set-up, three manipulators, an endoscope, and two instruments. In this chapter we will focus on the pre-surgical set-up, Figure 3.1.

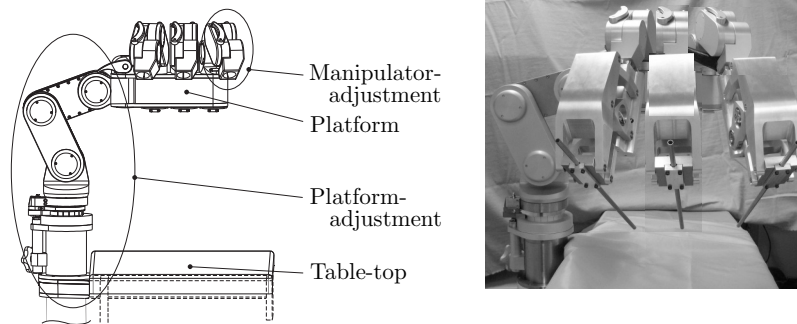


Figure 3.1: Left the pre-surgical set-up with its parts, right with its manipulators.

It consists of a single table connected platform-adjustment, platform and three manipulator-adjustments. The platform-adjustment is used to preoperatively position, orientate and fix the platform near the field of surgery. Subsequently, the three manipulator-adjustments are mounted. Each is used to initially position, orient and then fix its manipulator. The requirements and concepts of the pre-surgical set-up will be discussed in Section 3.1 and 3.2 respectively, followed with a detailed description of the design and evaluation of the platform-adjustment, platform in Section 3.3 and of the manipulator-adjustment in Section 3.4, with additionally a conclusion.

## 3.1 Pre-surgical set-up requirements

The requirements from Section 2.3 form the basis of the pre-surgical set-up requirements. A distinction is made between design (Section 3.1.1) and performance requirements (Section 3.1.2).

### 3.1.1 Design requirements

The design requirements include requirements based on the surgical procedure and on setting up the pre-surgical set-up prior to this procedure. These form the basis for the design of the layout of the pre-surgical set-up.

The pre-surgical set-up of the Slave should be connected to the operating table. This allows table adjustment, without the necessity to adjust the Slave as well. It increases flexibility in performing the procedure and reduces the time required. The pre-surgical set-up should avoid interference with the surgeon, assistants and anesthesiologists to enable approach and survey of the patient during the procedure. A compact design least hampers the team.

Figure 2.1 (Chapter 2) shows that the surgeon and endoscope trocar are at the same side of the surgical area for conventional procedures. More specifically, ideally the camera incision and orientation should coincide with the (projected) line connecting the surgeon's eyes and the surgical area (see again Chapter 2). This applies for robotic surgery as well. Here, the first assistant takes the place of the surgeon (who is operating the master). The least obstructive position for the Slave would then be on the other side of the table, opposite the first assistant and on the same line. In addition, the pre-surgical set-up should be surveyable. Among others this indicates that it ideally should remain below a height of 1.50 m, measured from the floor. A limited height gives a sense of control. As well as improves communication, since the team will be able to see each other across the system.

The pre-surgical set-up should provide a stiff frame during surgery, to allow for accurate instrument movements and force-measurements. A short force-path between instrument and patient and between instruments contributes to this, see Figure 3.2 on the next page and [106]. As shown in this figure, reducing the length of the force-path improves performing accurate movements (smaller deflections) and its dynamic behavior (increased first natural frequency). In addition, it makes the Slave less sensitive to disturbances from outside. The length of the force-path between instruments, consisting of the manipulator-adjustment and manipulator, does not have to exceed the length of a human arm to cover a similar range of motion. Here, the platform is seen as the surgeon's torso and the manipulator-adjustment with its manipulator as the surgeon's arms. This viewpoint on design for stiffness is one of the key contributions of this work, in relation to existing robots (see Table 1.1).

Prior to surgery the pre-surgical set-up has to fulfill some requirements as well. The platform-adjustment allows to position and orient the platform near and rel-

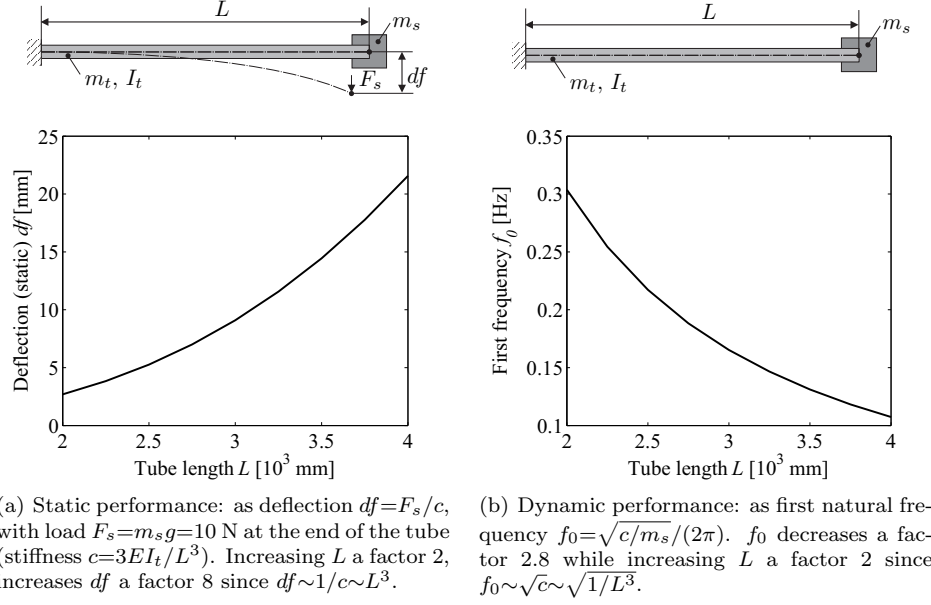


Figure 3.2: Example of the effect of change in force-path length=tube length ( $L$ ) on static (a) and dynamic performance (b) of a steel tube fixed at one end (top of the figure). The area moment of inertia ( $I_t$ ) of the tube is constant and its mass ( $m_t$ ) is assumed to be negligible. It has an initial outer diameter  $D_o=50$  mm and a wall-thickness  $t=1$  mm.

ative to the field of surgery. It should provide four (incremental) degrees of freedom (DoFs) for the platform-adjustment: three to position the platform near the field of surgery ( $x$ ,  $y$  and  $z$ ) and one to orient it along or across the patient, parallel to the table-top ( $\theta$ ). The platform should hold the manipulator-adjustments at a mutual pitch of 80 mm. This is the mean distance between the incisions of the trocars of the instrument and endoscope. Each manipulator should initially be positioned and oriented relative to its trocar. Five (continuous) DoFs are required for the manipulator-adjustment, see Figure 3.3.

Manual adjustment of the entire pre-surgical set-up is applicable, since positioning and orienting is required prior to the procedure. Ideally, the pose is maintained during the procedure. This implies a mechanical design, which avoids an actuator per DoF actuators that would only operate at setup and enables removing the system in case of an emergency (power shut down, evacuation). Fast manual operation reduces the stroke of handles to  $180^\circ$  and the actuation torque allowed. The design requirements of the pre-surgical set-up summarized:

- connect the Slave to the table,
- provide a single frame near the field of surgery for the manipulators,
- be compact to avoid interference with the team surrounding the operating table, enable approach and survey of the patient, provide a short force-path

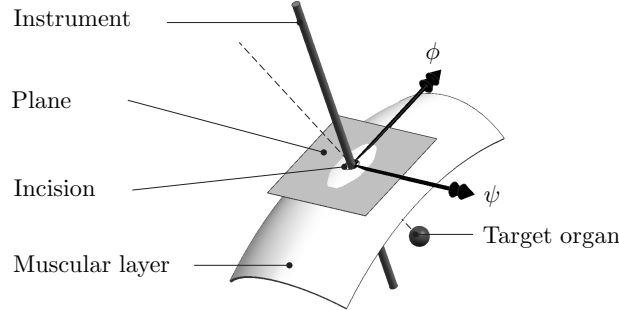


Figure 3.3: The manipulator-adjustment requires five DoFs to initially position and orientate the manipulator with its instrument. Positioning an instrument within its incision requires three DoFs. Adjustment of its orientation towards its target organ [—] requires  $\phi$  and  $\psi$  in the plane tangent to the (schematically shown) muscular layer in which the incision is set.

between instrument and patient and between instruments resulting in a stiff frame during surgery (locked joints),

- position and orient the platform near the field of surgery in respectively  $x$ ,  $y$ ,  $z$  and  $\theta$  (relative and parallel to the table-top),
- position and orient each manipulator (with its instrument) relative to its trocar in five DoFs:  $x$ ,  $y$ ,  $z$   $\phi$  and  $\psi$ ,
- provide the manipulator-adjustments with an inter-distance of 80 mm within the platform, and
- have a mechanical design that allows fast manual adjustment.

### 3.1.2 Performance requirements

The performance requirements for the pre-surgical set-up include its range of motion, resolution, stiffness and the platform load taken as a reference for the clamps of the joints. The range of motion and resolution are based on the patient size and proportions, anatomy and planned procedure.

The range of motion of the pre-surgical set-up is strongly related to the incision locations. It needs to be possible to place the trocars anywhere in the thoracic or abdominal region, within an area of 70x50 cm and within 20–50 cm in  $z$ -direction (perpendicular to the table top, Figure 2.3). The platform of the pre-surgical set-up is required to be above the incision-site, at least 10 cm. In addition, a  $\theta$  orientation of the platform should be provided. It allows orientating the platform approximately parallel to the incisions for the robot instruments and endoscope. It will be parallel to the dotted line in Figure 2.1. This  $\theta$  orientation reduces the required lengths of the manipulator-adjustment. Orientation should be possible along and transverse the table.

The range of motion of the manipulator-adjustments is based on anatomical differences between patients and can thus be small [11]: 5 cm in  $x$ -direction and 12 cm in  $y$ -direction relative to its mean position, Figure 2.2. Additionally, it should be able to cover the positioning resolution of the platform, and provide the initial trocar-orientation as well. The positioning resolution of the pre-surgical set-up is estimated to be 5 cm for the platform-adjustment and 1 mm for the manipulator-adjustment.

Table 3.1: Required stiffness  $c_{x,y,z}$  and rotational stiffness  $k_{\phi,\psi,\theta}$  of the platform supported by its platform-adjustment.

$c_x :$	$1 \cdot 10^6$	N/m	$k_\phi :$	$9 \cdot 10^4$	Nm/rad
$c_y :$	$1 \cdot 10^6$	N/m	$k_\psi :$	$9 \cdot 10^4$	Nm/rad
$c_z :$	$1 \cdot 10^6$	N/m	$k_\theta :$	$9 \cdot 10^4$	Nm/rad

Table 3.1 shows the required stiffness of the platform. This stiffness leads to a displacement of 0.3 mm of the platform if a person would push the platform in the same direction with a force of 300 N. This is within the set positioning resolution of the manipulator-adjustment. This stiffness should be met in the most extreme frequently used position of the platform. Dynamically it should result in a first natural frequency  $f_0$  preferably above 20 Hz.

The platform and connected manipulator-adjustments with manipulators are intended to be lighter than  $m_P=23$  kg, with  $F_P=m_P g$ . Therefore, each clamp should withstand a load of  $F_P S=450$  N at the platform, with  $S=2$  a safety factor. The performance requirements summarized:

- the range of motion of the platform is an  $xy$  area of 70x50 cm and a range of 30–60+ cm in  $z$ -direction (perpendicular to the table-top), a  $\theta$  orientation of the platform should be provided, along and transverse the table,
- the range of motion manipulator-adjustment is set to 5 cm in  $x$ -direction and 12 cm in  $y$ -direction relative to its mean position,
- the positioning resolution of the pre-surgical set-up is estimated to be 5 cm for the platform-adjustment and 1 mm for the manipulator-adjustment,
- the stiffness is given in Table 3.1,
- the platform-adjustment DoFs should withstand a load of 450 N at the platform, and
- the first natural frequency of the pre-surgical set-up should be above 20 Hz.

## 3.2 Pre-surgical set-up concepts

This section is divided into concepts on the platform-adjustment, on the platform, on the layout of the manipulator-adjustment and on considerations regarding the clamps fixating the joints of the pre-surgical set-up. The concepts chosen are presented.

### 3.2.1 Concepts on the platform-adjustment

Table 3.2: Concepts for the platform-adjustment connected to the table, used to position the platform (P) in  $x$ ,  $y$  and  $z$  near the field of surgery. With  $[-]$  position of platform and  $[- - ]$  a next position of the platform. The evaluation of the concepts is shown below the pictures. It includes criteria based on user-friendliness (one-sided support, compact height) and on technical characteristics (torsional stiffness and moving mass).

Portal structure of the platform-adjustment			
	Fixed 1	Fixed 2	Rail
Top view:			
Front view:			
<b>Evaluation criteria:</b>			
One-sided support	-	-	-
Compact height	-	-	-
Torsional stiffness	-	-	+
Moving mass	--	-	+
C-arm structure of the platform-adjustment			
	Rail & sliding	Fixed & sliding	Fixed & dyad
Top view:			
Front view:			
<b>Evaluation criteria:</b>			
One-sided support	+	+	+
Compact height	+	+	+
Torsional stiffness	+	+	+
Moving mass	+-	+-	+-

The design requirements (Section 3.1.1) form the basis of the layouts of the platform-adjustment in Table 3.2. Each layout presented in this table satisfies the following design requirements: the single platform-adjustment attaches the platform to the operating table, while allowing for its translation in  $x$ ,  $y$  and  $z$ -direction and a rotation  $\theta$  relative to the table-top. The layouts shown in Table 3.2 are either supported at two-sides (portal structure) or at one-side (c-arm structure) of the table and have been evaluated regarding user-friendliness and technical characteristics. The first criterium included access to the patient and area of surgery (one-sided support) and restricted height of the pre-surgical set-up. The technical characteristics comprise torsional stiffness and low moving mass. These four criteria were assigned a + or - value.

The three portal structures reduce the freedom to approach the patient and surgical area, since these are supported at two sides of the table. In addition these structures are less compact in height than the c-arm structures (front view in Table 3.2). The platform-adjustment with a portal structure layout makes it less user friendly than the c-arm structure.

Each layout will be subject to a torsional load. The center-of-mass of each instrument-manipulator will generally be at a distance from the  $yz$ -plane, described by the platform-adjustment frame. The portal structures 'fixed 1' and 'fixed 2' increase this distance even more. The Y-slide is stacked on the X-guidance. This brings the platform an amount  $x$  from the  $yz$ -plane. In addition, the X-guidance covers rather a large area above the operating table (top view in Table 3.2). The portal structure 'rail' provides the  $x$ -translation of the platform by rolling the platform-adjustment along the rail of the operating table<sup>1</sup>. The c-arm structures have a similar torsional load as the 'Rail' portal structure. Again the rail along the operating table can provide the platform with its  $x$ -translation, 'rail & sliding'. Using the rail as a guidance is in conflict with the limb-supports and other surgical and anaesthetic accessories that generally occupy the rails. Therefore, the c-arm will depart the table from a fixed position. The accompanying  $\theta$ -rotation provides for its  $x$ -translation, 'fixed & sliding' and 'fixed & dyad'<sup>2</sup>. Since the R-slide of the sliding construction extends with different lengths from the table and at different heights, it is harder to avoid than the dyad construction. Therefore, the 'fixed & dyad' construction has been chosen.

Several forms for the platform have been compared (Appendix Figure D.1). The least obstructive platform is the so-called 'line' platform (further on termed *platform*), its symmetry gives the possibility of working on either side of the platform. It holds the manipulator-adjustments at an inter-distance (the pitch) similar to the mean distance between the surgeon's instruments and the endoscope trocars for laparoscopic procedures (Figure 3.5(a)).

<sup>1</sup>The rails along the different operating table-tops in Europe, have a 25x10 mm cross-section.

<sup>2</sup>A dyad (the binary group) is a kinematic chain with two links and three full joints.

### 3.2.2 Concepts on the manipulator-adjustment

Each manipulator-adjustment fixates its manipulator to the platform, after providing it with an initial position besides and below the platform and providing an additional orientation (Figure 3.3). These DoFs are similar to the DoFs of the platform-adjustment with an additional rotation. Therefore its lay-out is similar.

### 3.2.3 Considerations on the clamp design

The joints of the platform-adjustment and manipulator-adjustment are locked during surgery to provide a stiff frame. The clamp-surface (either oriented tangential or axial) should be at the largest radius possible, since the rotational stiffness improves with the square of the radius. Manual operation restricts the stroke and force available to open and close the clamps. A transmission ratio is used to increase this actuation force up to the force required in the clamp. In addition, the clamp can either be form-closed or force-closed. A form-closed clamp generally reduces the required normal force, but at the same time it also reduces the flexibility in positioning. A force-closed clamp on the other hand is based on friction, which allows for continuous positioning, but requiring a larger normal force. This normal force and accompanying actuation torque can be reduced by increasing the friction coefficient or the number of friction-surfaces involved. This last option requires some space, which is limited.

## 3.3 Platform-adjustment and platform

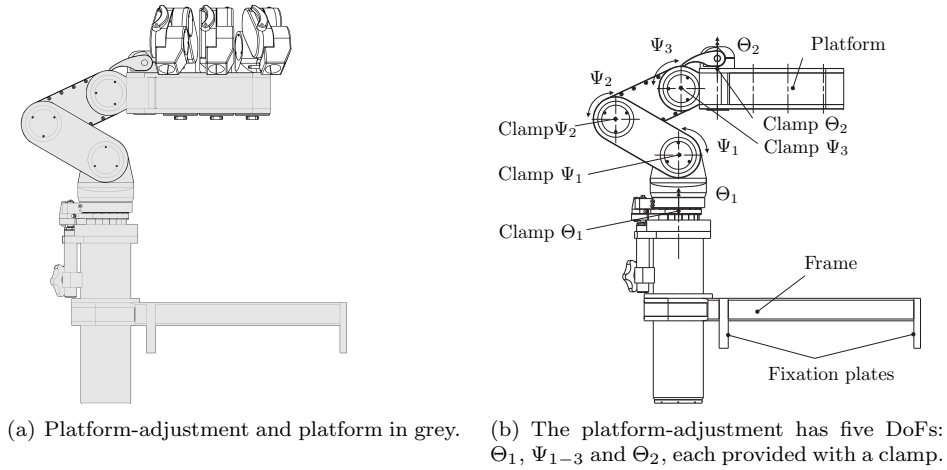


Figure 3.4: The fixed & dyad platform-adjustment with line platform.

Figure 3.4 shows the chosen fixed & dyad platform-adjustment and line platform. The fixation plates of the frame of the platform-adjustment are connected to the table on existing mounting points, see Figure 3.4(b), lower part. The platform-adjustment itself has five DoFs ( $\Theta_1$ ,  $\Psi_{1-3}$  and  $\Theta_2$ ) to position and orient its platform. These five DoFs are locked during surgery to provide a stiff frame. Two of these clamps (clamp  $\Theta_1$  and  $\Theta_2$ ) are continuous and three (clamp  $\Psi_{1-3}$ ) are discrete to reduce the required actuation force. The platform accommodates three manipulator-adjustments. Its length is indicated by the mutual pitch of these manipulator-adjustments. The platform-adjustment and platform will be discussed in this section regarding its kinematics, design, and analyses and measurements performed.

### 3.3.1 Kinematics of the platform-adjustment and platform

The DoFs to position and orient the platform are shown in Figure 3.5(a). These are three DoFs to position the platform ( $\Theta_1$ ,  $\Psi_1$  and  $\Psi_2$ ), one DoF to adjust its orientation parallel to the table-top ( $\Psi_3$ ) and one additional DoF to orient the platform along or across the patient ( $\Theta_2$ ). Its link length and resulting range of motion can be found in Figure 3.5(b) and 3.6.

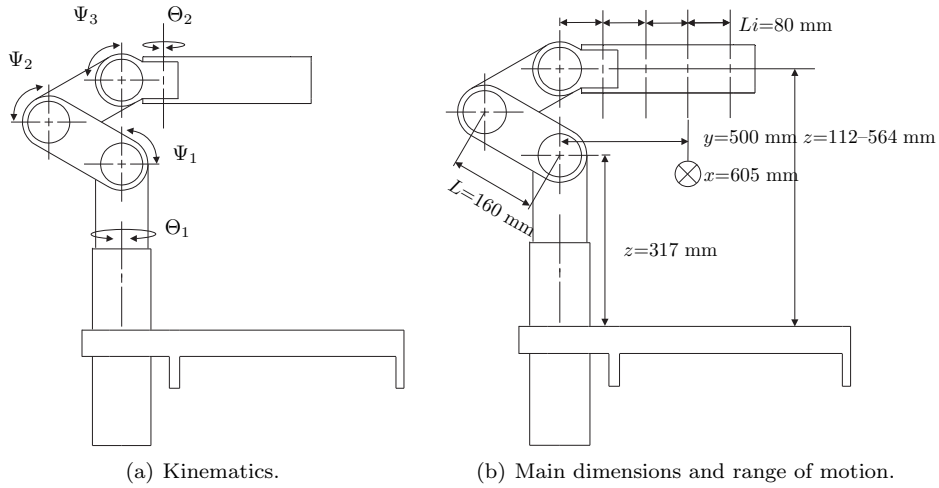
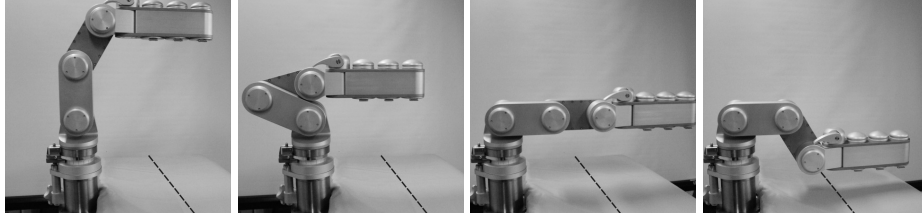
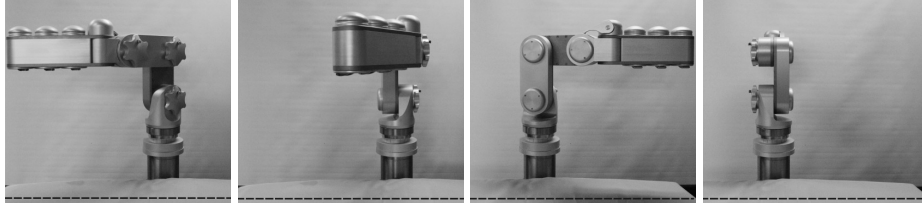


Figure 3.5: Kinematics of the platform-adjustment, link length ( $L$ ) and  $x$ ,  $y$  and  $z$  platform-range in resulting after realization (both side view). The individual manipulator-adjustments are located at a pitch  $L_i$  of 80 mm in the platform.



(a) Platform adjustable in height and across the table.



(b) Platform orientated along or across the table.

Figure 3.6: Pictures of the platform-adjustment in extreme postures, the dotted line indicates the longitudinal axis of the patient.

### 3.3.2 Design of the platform-adjustment and platform

The platform-adjustment and platform as realized are shown in Figure 3.7 on the next page. The frame supporting the dyad is connected to the table. The dyad consists of link 2 and 3 with a link-length ( $L$ ) of 160 mm each. The mass of link 1–4 of the platform-adjustment and the platform is reduced by milling chambers inside. The thus created open boxes are closed with covers to maintain the torsional stiffness of each link. The exterior of each link is kept smooth by fixating the bolts in the covers into inserts in the boxes. Each successive pair of links is fixed onto each other with the corresponding clamp. Discrete joint angles are allowed to position the platform near the field of surgery, since fine-positioning of the manipulators is done with the manipulator-adjustments. Clamp  $\Psi_{1-3}$  directly influences the stiffness of the platform-adjustment platform combination in  $z$ -direction. In addition the load on these clamps can occasionally increase if someone supports him or herself on this platform. For demonstration purposes only, this can be the weight of one person. The clamps are required to hold these additional loads as well to prevent the platform from undesired motion towards the patient. Clamp  $\Psi_{1-3}$  is therefore form-closed with teeth, because of axial space-restrictions to increase the number of friction-surfaces and the accompanying clamp-torque. Clamp  $\Theta_1$  and  $\Theta_2$  are constructed force-closed because additional load in this direction is more than three times less and continuous manipulator-adjustment is thereby still possible in spite of  $5^\circ$  incremental platform adjustment. The principles of continuous clamp  $\Theta_1$ , discrete clamps  $\Psi_{1-3}$  (steps of  $5^\circ$ ) and continuous clamp  $\Theta_2$  are subsequently given, each followed directly by its respective detailed description.

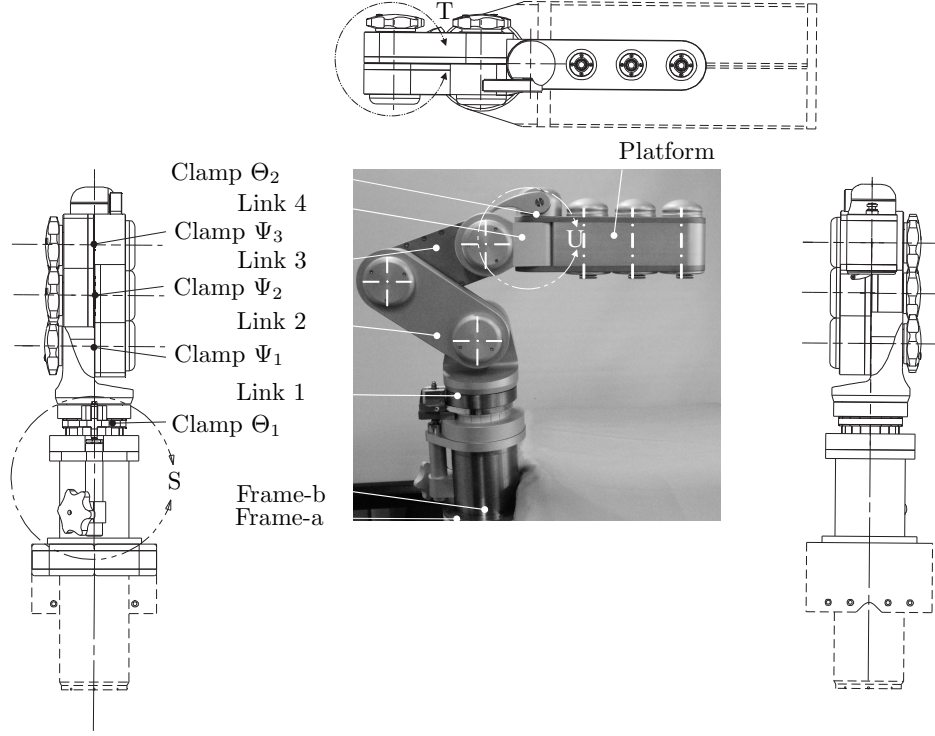


Figure 3.7: Platform-adjustment and platform of the pre-surgical set-up, as realized. Frame-b is connected to frame-a, which is mounted to the table on four existing mounting points, via a 200x50 mm rectangular tube transverse underneath the table cushions. Frame-a is an adapter, designed for the Maquet 1120 operating table. Different adapters can accommodate different tables.

### Clamp $\Theta_1$

Clamp  $\Theta_1$ , in Figure 3.8 on the next page fixates link 1 in  $\theta$  (and axially if lifted) by means of a collet chuck on frame-b. This continuous collet is actuated with a rolling wedge (1:50), being normally closed (i.e. held down) by means of a compression spring pulling down on a pull rod. The wedge and spring run parallel to frame-b (and  $\Theta_1$ ), which results in a slender construction. The wedge serving as a vertical to horizontal motion converter and providing a transmission ratio. The pull rod is actuated with a handle.

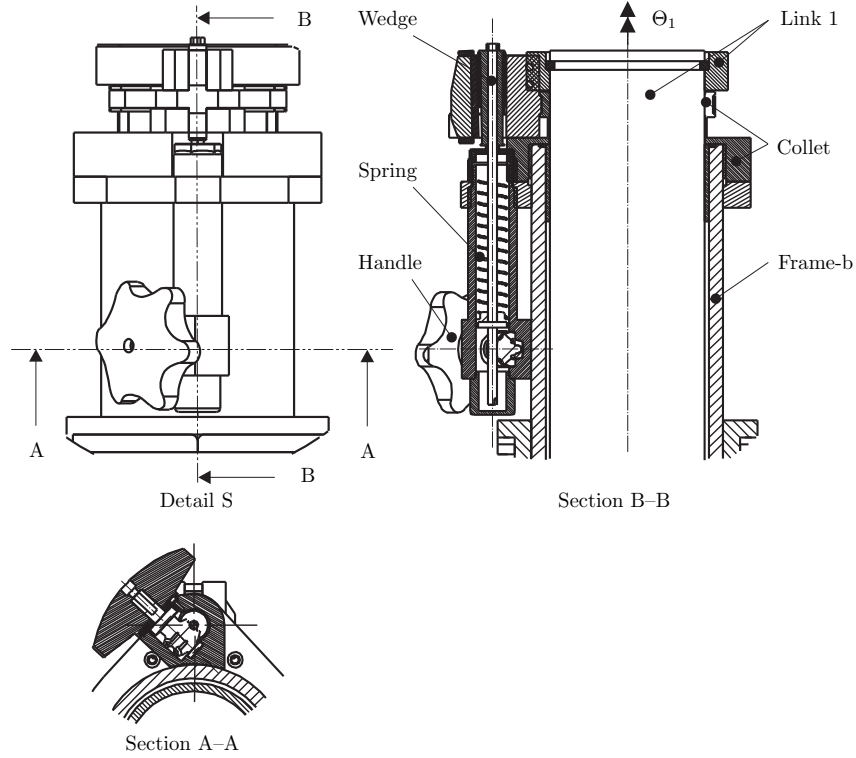


Figure 3.8: Clamp  $\Theta_1$ , with a cross-section of detail S in Figure 3.7.

Clamp  $\Theta_1$  in detail, also see Appendix D.3. The collet has a tangential friction-surface ( $D=90$  mm) to provide for radial and possibly axial adjustment and fixation of link 1. The radial normal force required (11 kN from Appendix D.3), results in a tangential force ( $F_t \approx 2250$  N assuming a friction coefficient  $f=0.2$ ). This force is similar to the brake-force in axial direction and results in a brake-torque of 100 Nm in  $\Theta_1$ . The required normal force in the contact between the collet and link 1 is provided by a spring steel strip that almost encircles the collet ( $250^\circ$ ). Both ends of the strip are mounted to the wedge-block shown in Figure 3.9. The wedge (1:50) runs on linear needle bearings between the wedge-block and the guidance-block. It is preloaded with a compression spring ( $\approx 120$  N), which holds the wedge-block in radially outward position and applies the required normal force to the collet. This normal force is removed by pushing the wedge against its pre-load along the wedge-block (up) with a (pull) rod. The rod runs through the spring and wedge. It has a nut on either side of the wedge and is connected at its lower end to a rotating handle. Rotating the handle then forces the rod up. Releasing the handle, automatically fixates link 1. The actuation torque of the handle is  $\approx 1.6$  Nm, which consists of two (calculated) tangential forces of 27 N at 30 mm radius on the handle.

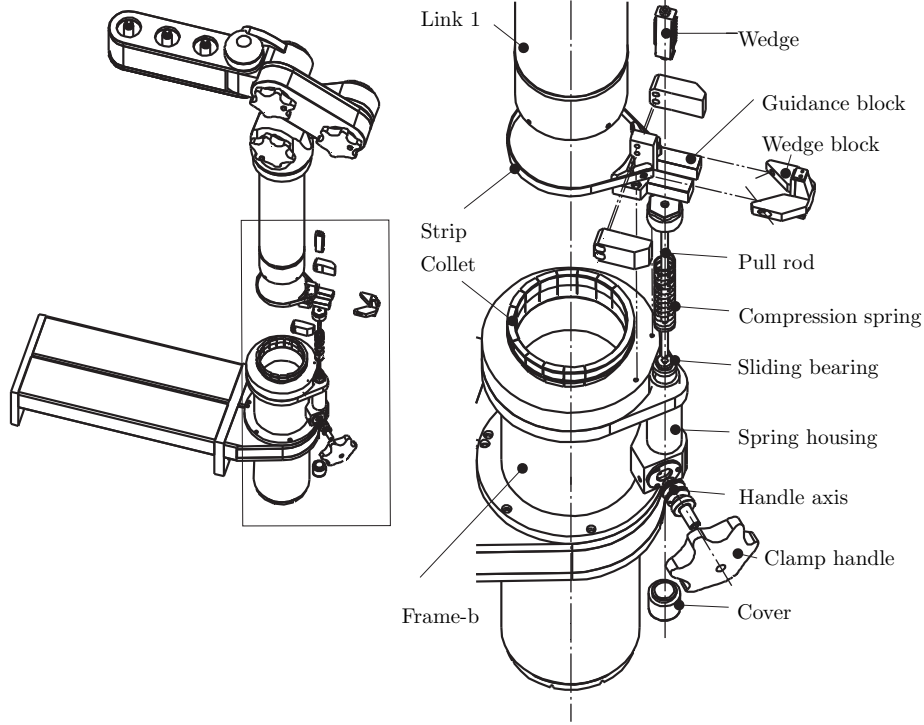


Figure 3.9: Clamp  $\Theta_1$ , exploded view. Link 1 is automatically fixated when the handle is released.

### Clamp $\Psi_{1-3}$

The  $\Psi_{1-3}$  DoFs of the platform-adjustment are fixated by means of similar clamps, Clamp  $\Psi_{1-3}$ . Clamp  $\Psi_2$  (described here) in Figure 3.10 locks link 2 and 3 in  $\Psi_2$ . The clamp is form-closed (incremental) as the required clamp force is high and the actuation force should be realized manually. The form-closed parts of these clamps are two engaged toothed rings. These rings are connected to link 2 and 3 and located at the middle plane of the platform-adjustment. The links are axially preloaded with a disc-spring. The clamp is opened by releasing the preload of the disc-spring and axially separating link 2 and link 3, to release the teeth. Link 2 axially translates on axis  $\Psi_2$ , which is connected to link 3, by unscrewing the bolt preloading the disc-spring. The bolt serves as a rotation to translation motion converter. Rotating the handle together with the nut, operates this bolt to open and to close the clamp. The green cover of the safety button of the handle indicates that the handle is locked and the clamp is closed.

Clamp  $\Psi_2$  in detail. The two toothed rings are bolted to each link. Each ring has a pitch diameter close to the height of the links. Its teeth are trapezium-shaped with a pitch of 4 mm, resulting in an increment of  $d\Psi=5^\circ$ . The sliding bearings of link 2 allow it to translate along and rotate around the axis  $\Psi_2$ , which is

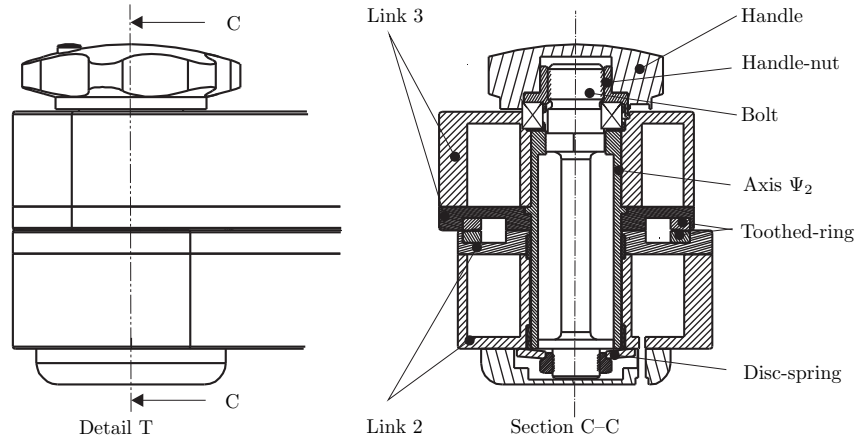


Figure 3.10: Clamp  $\Psi_2$  with basic components, with detail T from Figure 3.7. Clamp  $\Psi_1$  and  $\Psi_3$  are similar.

fixated to link 3. The bolt running through this axis  $\Psi_2$  preloads the disc-spring. Link 2 and 3 are axially preloaded with this disc-spring when the clamp is closed. Unscrewing the bolt releases the disc-spring from link 2, allowing the wave-spring to push link 2 from link 3. The preload of the disc-spring can be adjusted (during assembly) with the spring-nut. A small radial locking bolt running through the nut and into the bolt thread locks this spring-nut. The bolt itself can be discretely rotated inside its hexagon shaped guidance (Figure 3.11) to adjust the preload range even more, when required.

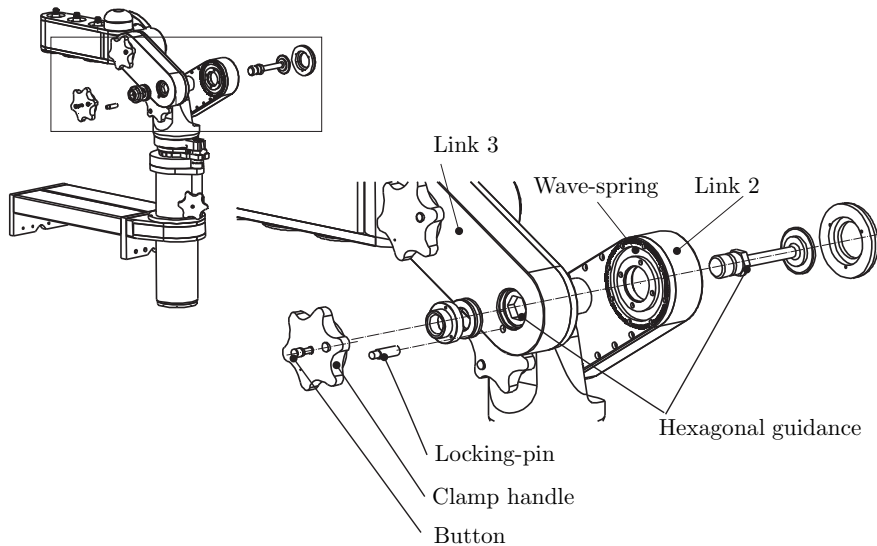


Figure 3.11: Clamp  $\Psi_2$ , exploded view.

Rotation of the bolt is prohibited by this hexagon shaped guidance inside the  $\Psi$ -axis, during normal operation of the clamp. Rotating the handle-nut with its connected handle then unscrews the bolt, releasing the teeth. Releasing the locking-pin by pushing the button of the handle (Figure 3.11) allows  $135^\circ$  rotation of the handle to open the clamp. The actuation torque of the handle is  $\approx 3.8$  Nm. This is similar to two (calculated) tangential forces of 47 N at a radius of 40 mm on the handle. The handles of the clamps are located all on the same side of the platform-adjustment, right since most people are right-handed. Left-handed can be provided when required.

### Clamp $\Theta_2$

Figure 3.12 shows the continuous force closed clamp  $\Theta_2$ . It fixates the platform in  $\Theta_2$ , with respect to link 4. The upper plate of the platform is clamped between link 4 and the clamp-head. The rod connected to an eccentric and actuated with the handle, applies the required normal force. Actuation of the handle releases and fixates the platform, as with clamp  $\Psi_{1-3}$ .

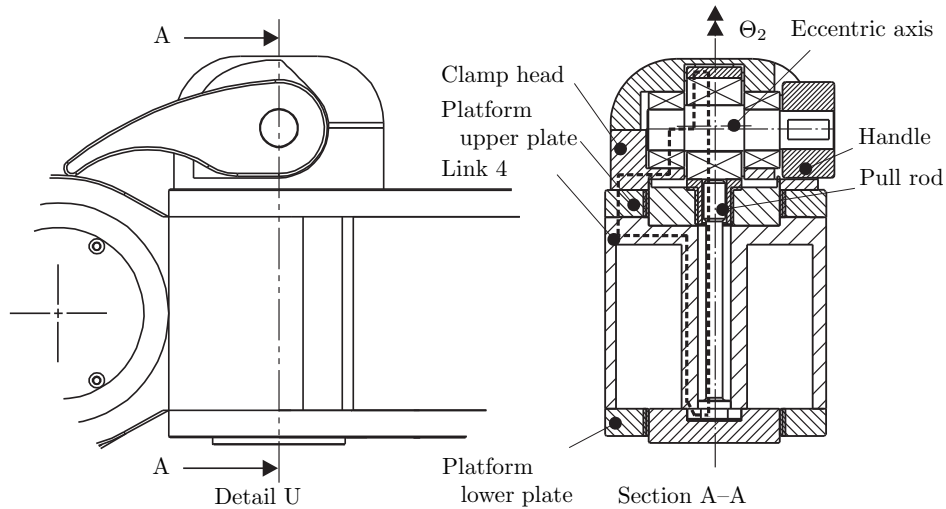


Figure 3.12: Cross-section of clamp  $\Theta_2$ , with its basic components and detail U from Figure 3.7. The clamping force-path is indicated with a dotted line.

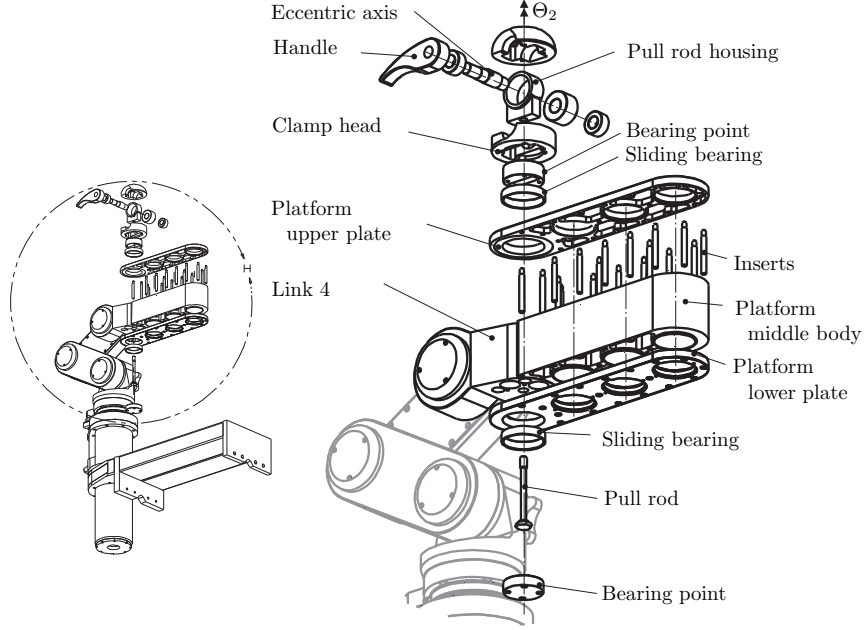


Figure 3.13: Clamp  $\Theta_2$ , exploded view. Continuous adjustment of DoF  $\Theta_2$  ( $\pm 60^\circ$ ).

Figure 3.13, shows clamp  $\Theta_2$  in detail with an exploded view. The clamped steel upper-plate and its lower counterpart, provide the aluminium middle body (with chambers to reduce weight) of the platform with bending stiffness and torsional stiffness. The high modulus of elasticity material (steel) is positioned furthest from the neutral bending line of the platform to increase bending stiffness. The plates close the open box of the middle body, which increases the rotational stiffness. The steel threaded inserts join the separate parts and realize a smooth surface. The plates are provided with bronze sliding bearings and allow the platform to rotate around and translate (a small distance) along its  $\Theta_2$ -axis bearing points that are connected to link 4. The  $\Theta_2$ -DoF of the platform is fixed by clamping its upper-plate between link 4 and the clamp head. The accompanying tangential friction force effects at the outer most radius possible (37.5 mm) of this upper-plate. The pull rod axially forces the clamp head towards link 4, which applies the required normal force on the upper plate. Screwing or unscrewing the pull rod into or from its pull rod housing adjusts the normal force (during assembly), the stretch of the pull rod. The pull rod housing runs on the eccentric axis, its needle bearing support reduces the actuation force. This eccentric axis ( $e=0.5$  mm) is rotated with the handle to lock and unlock  $\Theta_2$ , which requires a  $45^\circ$  rotation. The accompanying actuation torque of the handle is approximately 1.8 Nm. This is similar to a (calculated) tangential force of 34 N at a radius of 50 mm of the handle. Furthermore, the handle is oriented parallel to link 4 so it will protrude least from the platform-adjustment. Hence, the rectangular guidance of the upper bearing point of link 4 guiding the rectangular pull rod housing.

### Weight-compensation mechanism

The platform-adjustment weighs  $m=56$  kg (Appendix Table D.1), 38 kg for its static part (frame-a, frame-b and clamp  $\Theta_1$ ). Link 1 and clamp  $\Psi_1$  cover 8.2 kg, which does not add to the moving mass supported by the surgeon or assistant when installing the platform. The supported mass (link 2–4 and platform) ranges from 5.4–8 kg, depending on the DoFs arrangement and on which clamp is open. Here, the platform is supported near its center-of-mass. The weight-compensation mechanism [122] shown in Appendix D.4 compensates for the weight of the platform-adjustment, the platform and the mounted manipulator-adjustment with manipulators connected. This design can be added to the existing platform-adjustment and platform with a minimum of adjustments. A second mechanism presented in [122] can be integrated with the platform-adjustment and platform. This mechanism runs in the interior of the platform-adjustment, it requires a larger adjustment of the existing set-up.

### 3.3.3 Analysis of the platform-adjustment and platform

The platform-adjustment has been analyzed [10, 47] in three poses to find its performance in static (deflection) and modal behavior. The compact, tall and 3D pose (Figure 3.14) are expected extremes for use. The platform-adjustment has been simplified to analyze it with the finite element package Unigraphics NX Nastran. The main parts: frame-a, frame-b, link 1, link 2–3 and the platform have been included without any screw holes, clamps, etc. Meshmating was used to connect the parts, the meshsize was chosen 8 mm.

#### Stiffness

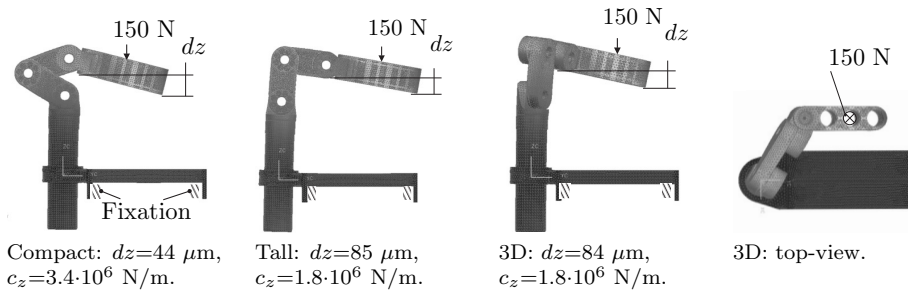
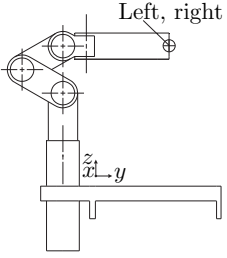
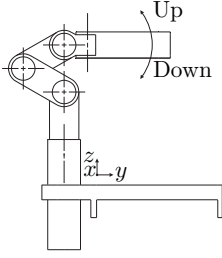
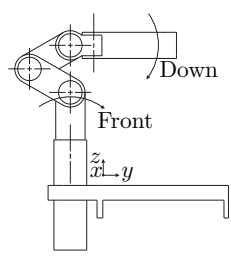


Figure 3.14: In a finite element analysis (NX Nastran) a force of 150 N is applied in  $z$ -direction ( $F_z$ ) to the platform-adjustment in three different postures: compact, tall and 3D. This results in a displacement  $dz$  and a calculated stiffness  $c_z$  of the platform-adjustment.

The stiffness of the platform-adjustment has been found in the three postures mentioned. The stiffness in  $z$ -direction is shown in Figure 3.14, it fulfills the set requirements. A modal analysis has been performed using the numerical models, on the three above mentioned postures. A dummy mass of 15 kg, resembling the mass of the manipulator-adjustments and manipulators is attached to the platform. For all postures the mode shape is similar, Table 3.3. All natural frequencies shown are well above the 20 Hz requirement set.

Table 3.3: Modal behavior of the platform-adjustment. The mode-shape is indicated for the compact posture, while the corresponding natural frequencies are displayed for all postures. Remarkable frequency values are found for the compact pose of the platform-adjustment, these were expected to be higher than the tall pose.

Pose	Mode 1 [Hz] platform( $x$ ) left-right 	Mode 2 [Hz] platform( $z$ ) up-down 	Mode 3 [Hz] column( $y$ ) front-back, platform( $z$ ) up-down 
Compact	40	61	114
Tall	56	83	120
3D	45	62	108

### 3.3.4 Experimental results of platform-adjustment and platform

Measurements have been performed on stiffness, hysteresis and first natural frequencies of the platform and platform-adjustment. These indicate the accuracy of positioning and possible design improvements if the results do not fulfill the requirements. The measurement results can be found below.

#### Stiffness

An indication of the stiffness in  $z$ -direction is shown in Table 3.4 on the next page, with displacement measurement and application of the mass at the middle manipulator-adjustment position of the platform (unless stated otherwise). Appendix D.5 shows an overview of the measurement instruments used. The stiffness of the platform-adjustment in  $z$ -direction approximates the required stiffness for the tall pose and satisfies the requirements for the other poses expected to be

used more frequently. The experimental values found are lower, this is attributed to simplifications in the finite element model. The contacts in the joints were modeled with mesh-mating conditions instead of bending and shear stiffness of the teeth and the connection stiffness of the toothed ring. In addition, the plates of the frame are fixed at the sides towards the table, instead of fixed at the connection holes.

Table 3.4: Stiffness of the platform-adjustment in  $z$ -direction ( $c_z$ ), obtained by applying a mass (15 kg) at the middle manipulator-adjustment position of the platform, and measuring the accompanying  $z$  displacement ( $dz$ ) at that same position (except for the 3D pose, measured at the outer edge of the platform).

Configuration	$dz$ [mm]	$c_z$ [N/m]
Compact	$102 \cdot 10^{-3}$	$1.4 \cdot 10^6$
Tall	$135 \cdot 10^{-3}$	$1.1 \cdot 10^6$
3D	$192 \cdot 10^{-3}$	$0.76 \cdot 10^6$

### Hysteresis

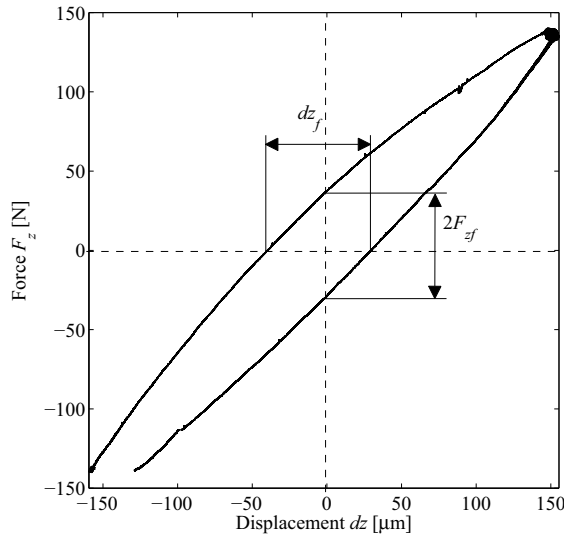


Figure 3.15: Hysteresis-plot of the platform-adjustment in tall pose, with the load applied in  $z$ -direction ( $F_z$ ) and measured displacement  $dz$ . The virtual play ( $dz_f$ ) found is  $70 \mu\text{m}$ , the friction in the construction is  $2F_{zf}=66 \text{ N}$  and the stiffness  $c_z \approx 1.0 \cdot 10^6 \text{ N/m}$ .

A hysteresis-measurement (for the equipment and set-up see Appendix D.5) in  $z$ -direction has been performed on the platform-adjustment in tall pose, by means of communicating vessels. A pre-load is applied to the platform, a vessel suspended

from a lever is slowly filled with water until its weight compensates for the pre-load and then slowly emptied again. Vessel and pre-load are connected to the set-up by means of springs to filter high frequency vibrations, low pass. The measurements result in the hysteresis-loop of Figure 3.15. The virtual backlash ( $dz_f$ ) found is  $70 \mu\text{m}$ , the friction force ( $F_{zf}$ ) in the construction is  $2F_{zf}=66 \text{ N}$  and the stiffness  $c_z \approx 1.0 \cdot 10^6 \text{ N/m}$ , equal to  $c_z$  shown in Table 3.4 as expected. The virtual backlash lies well within the positioning resolution set for the platform.

### Frequencies

The first natural frequencies of the platform supported by its platform-adjustment have been measured by connecting a 15 kg mass to the platform (resembling the mass of three manipulator-adjustments and three manipulators), applying excitation with a hammer and measuring the response with a laser vibrometer (Appendix D.5). Excitation and measurement have been performed in  $x$  and  $z$ -directions, on the platform. Table 3.5 shows the results, within specifications. In all platform-adjustment postures the first natural frequency occurs in the  $x$ -direction and the second in  $z$ -direction. This corresponds to the direction of the first two frequencies found in the modal analysis. The experimental values are lower than the theoretically obtained values, for similar reasons as described in Section 3.3.4.

Table 3.5: First natural frequencies  $f_{x,z}$  of the platform-adjustment and platform, measured with a laser vibrometer pointing at the platform. With  $x$  and  $z$  according to Table 3.3.

Configuration	$f_x$ [Hz]	$f_z$ [Hz]
Compact	23	31
Tall	27	39
3D	27	33

## 3.4 Manipulator-adjustment

The manipulator-adjustment provides the fine-adjustment to initially position the manipulator within the incision and realize its initial orientation towards the target organ. It is entirely mechanical, manually operated and its joints are fixated during surgery to provide a stiff frame in combination with the platform. The manipulator-adjustment will be discussed regarding its kinematics, design details and measurements performed.

### 3.4.1 Kinematics of the manipulator-adjustment

Each incision is provided with a trocar, through which an endoscope or instrument enters the body cavity. Three trocars are each connected to a manipulator. The invariant point P of the manipulator (next chapter) needs to be positioned in the incision, in the muscular layer to keep the post-operative pain limited. This requires three coordinates to be prescribed:  $x$ ,  $y$  and  $z$ . Two DoFs remain to orient the manipulator and its instrument towards the target organ, the  $\phi$  and  $\psi$  shown in Figure 3.3. The manipulator-adjustment provides and fixates these five DoFs as  $\Theta$ ,  $\Psi_{1-3}$  and  $\Phi$ , see Figure 3.16.

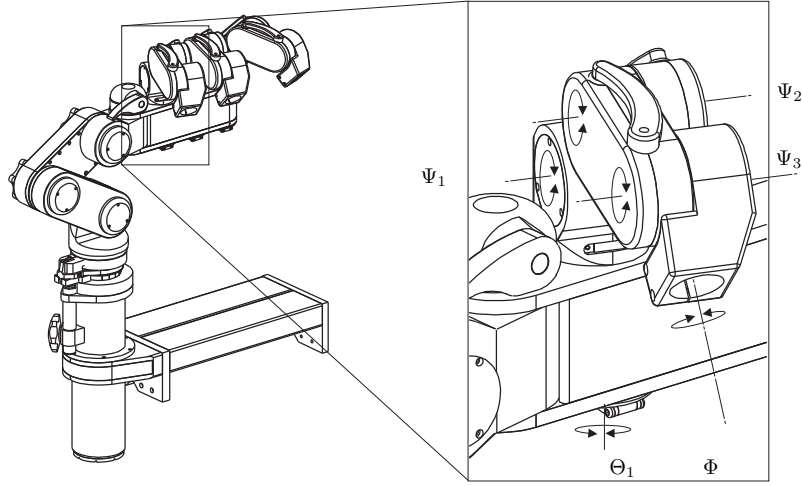


Figure 3.16: Kinematics of each manipulator-adjustment to position the invariant point P of the manipulator in the accompanying incision and provide its initial (neutral) orientation towards the target organ. The required five DoFs are provided as indicated.

### 3.4.2 Design of the manipulator-adjustment

The manipulator-adjustment is shown in Figure 3.17 on the next page. Its DoFs are fixated during surgery to provide a stiff frame. Clamp  $\Theta$  locks DoF  $\Theta$ , clamp 1 locks DoF  $\Psi_1$  and clamp 2 locks DoF  $\Psi_{2,3}$ , at any given value. DoF  $\Phi$  is locked within the manipulator. Each manipulator-adjustment ( $m=3.2$  kg each) is placed in its mounting spot within the platform (with its connected manipulator), after the platform is positioned near the field of surgery. After surgery the manipulator-adjustments and manipulators are removed from the platform. Therefore, the manipulator-adjustment requires a release mechanism. The release mechanism and clamps are discussed below.

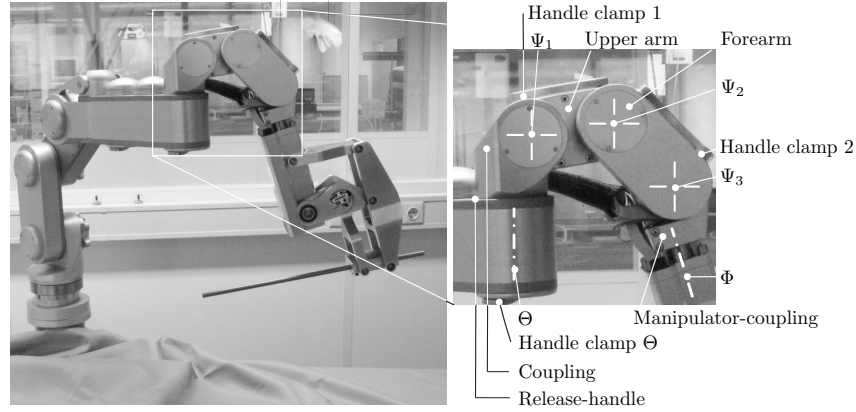


Figure 3.17: Kinematics of each manipulator-adjustment. Each arm-element (between two of its axes) has a length of 80 mm. The individual manipulator adjustments are located at a pitch of 80 mm in the platform (mean distance between trocars for the endoscope and the surgeon's instruments in laparoscopic procedures).

### Clamp $\Theta$ and the coupling release mechanism

Clamp  $\Theta$  and the release mechanism are integrated. Each mounting spot within the platform is provided with a platform-insert. This platform-insert interacts with the coupling of the manipulator-adjustment, see the left of Figure 3.18 on the next page. It attaches and fixates the coupling to the platform, the latter when clamp  $\Theta$  is activated. The pull rod of the platform-insert and the keyhole block of the coupling, mesh to couple the platform and coupling in  $z$ . Elongating the pull rod with an eccentric, applies a normal force between the coupling and platform. This normal force effects at a radius of 32 mm and provides a tangential friction-force, the force to fixate the manipulator-adjustment in  $\Theta$ . The manipulator-adjustment can be removed from the platform by releasing clamp  $\Theta$  and disconnecting the pull rod and keyhole block with the release-handle. Clamp  $\Theta$  and the release mechanism in detail, see the right of Figure 3.18. The pull rod is connected to the coupling of the manipulator-adjustment by means of a key-hole block. This block runs radially within the coupling. Its release-handle in open position allows the spring to push the circular hole of the keyhole block in central position. Then the coupling of the manipulator-adjustment can enter or depart the mounting-spot of the platform. Closing the release-handle forces the keyhole block radially inward. Then the keyhole block and pull rod of the platform-insert mesh. The clamping mechanism of clamp  $\Theta$  functions similar to clamp  $\Theta_2$  of the platform-adjustment. Although here, only one friction-surface is applicable. The pull rod can be elongated when it meshes with the keyhole block of the coupling. As in clamp  $\Theta_2$  of the platform-adjustment, it is elongated by rotating an eccentric axis that is connected to the handle of clamp  $\Theta$ . This results in a normal force between the manipulator-adjustment and platform upper-plate at a radius of 32 mm and a brake-torque of  $\approx 110$  Nm (assuming a friction coeffi-

cient  $f=0.2$ ). The calculated actuation force required is 145 N at a handle radius of  $R=35$  mm. The handle is locked in closed position.

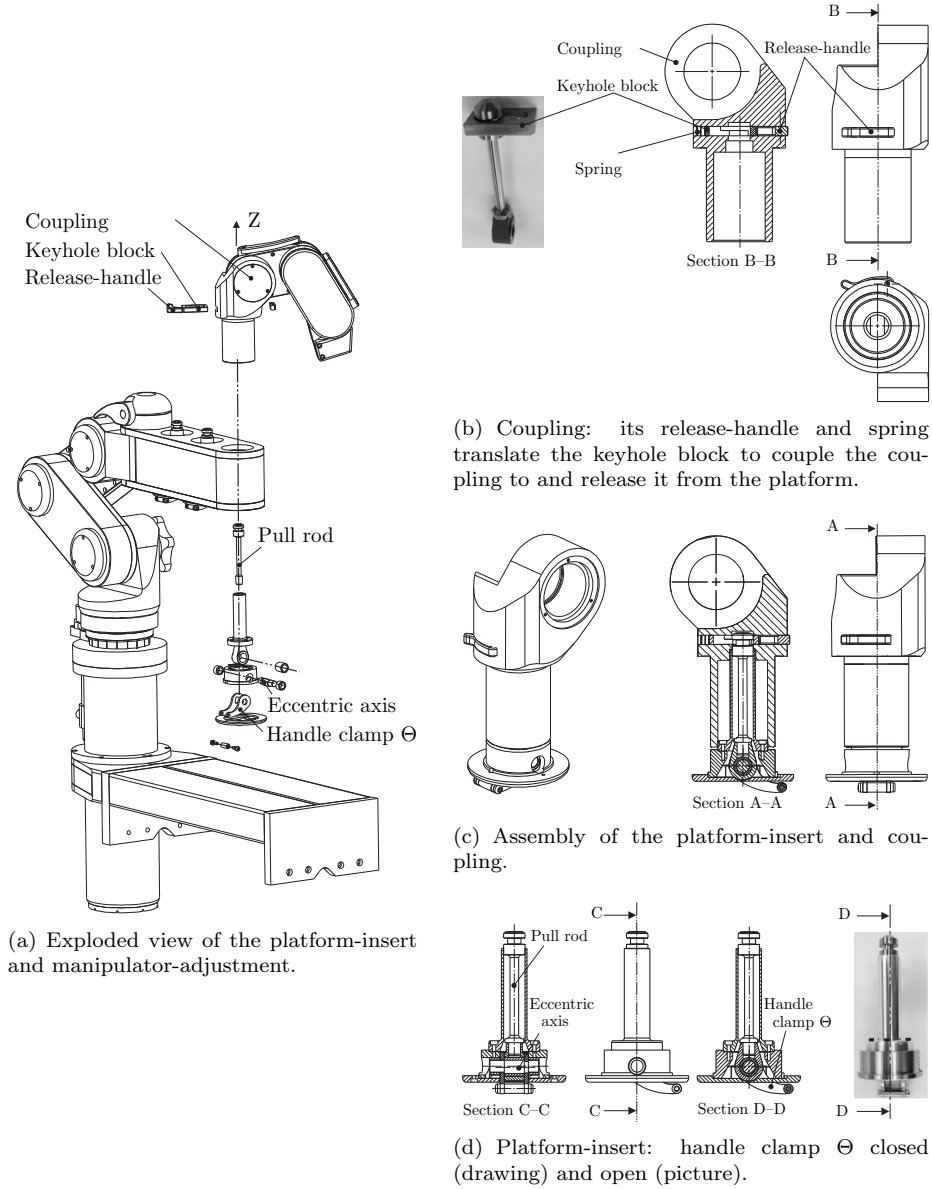


Figure 3.18: Manipulator-adjustment: clamp  $\Theta$  and the coupling release mechanism. The pull rod of the platform-insert and the keyhole block of the manipulator-adjustment coupling, mesh to couple the coupling and platform. Elongating the pull rod with the eccentric axis connected to the handle, provides the normal force to clamp the coupling onto the platform and fixate  $\Theta$ .

### Clamp 1 and 2 to fixate $\Psi_{1-3}$

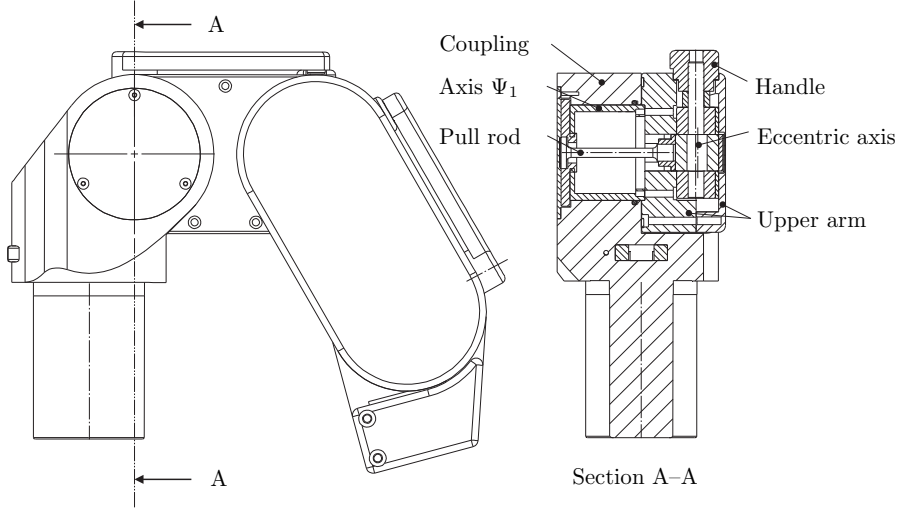
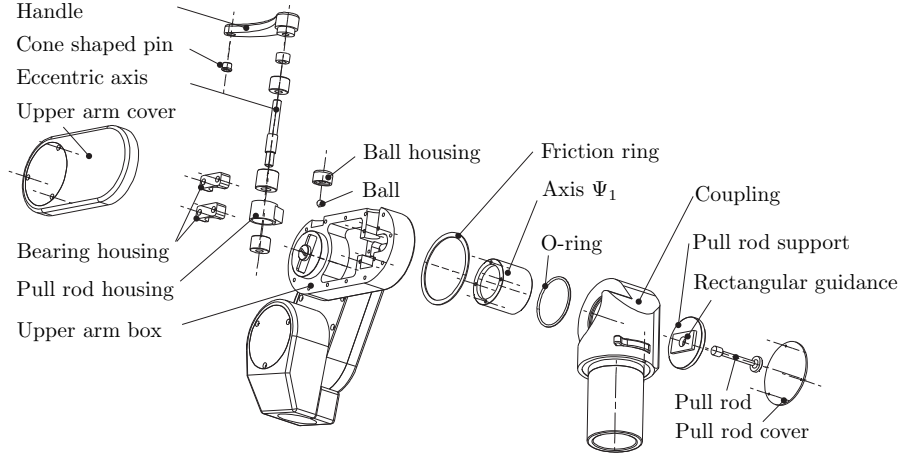
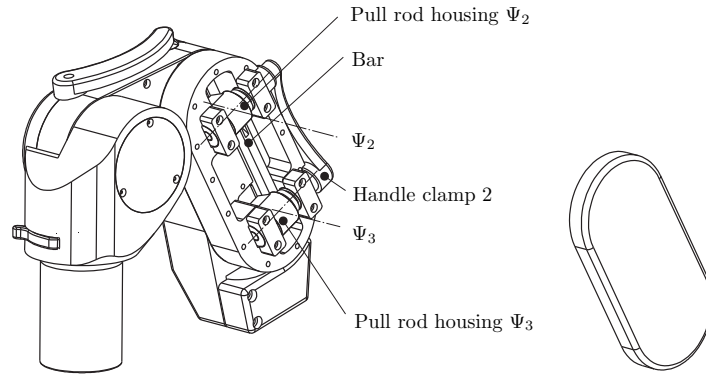


Figure 3.19: Manipulator-adjustment: clamp 1 fixates  $\Psi_1$ . Elongating the pull rod by rotating the eccentric axis with its handle, applies a normal force between the coupling and upper arm. This normal force results in a tangential friction force that fixates  $\Psi_1$ . Clamp 2 fixates  $\Psi_2$  and  $\Psi_3$  in a similar fashion.

DoFs  $\Psi_{1-3}$  are locked in a similar fashion as  $\Theta$ . The basic parts of clamp 1 are shown in Figure 3.19. Elongating the pull rod applies a normal force between the upper arm and coupling. This normal force effects at a radius, resulting in a tangential friction force that fixates  $\Psi_1$ . Actuation of the handle rotates the connected eccentric axis. This elongates the pull rod when closing the clamp or releases it when opening the clamp. Clamp 1 in more detail is shown in Figure 3.20(a) on the next page. The coupling and pull rod support axially sandwich the upper arm box. The upper arm box is supported by the hollow  $\Psi_1$ -axis, which is bolted to the coupling. This axis has a rectangular guidance, which aligns the tie-rod support with the coupling and increases the number of friction surfaces (and fixation torque). The tie-rod housing runs on the eccentric axis ( $e=0.5$  mm). Its needle bearing support reduces the actuation force. The eccentric axis is rotated with the handle. Closing the handle elongates the pull rod and applies the normal force at the radius of the friction ring (31 mm). This normal force can be adjusted (during assembly) by screwing the pull rod in or out of its housing. Applying or releasing this normal force requires a rotation of  $90^\circ$  and a (calculated) tangential force of 86 N at a radius of the handle of 50 mm. The handle is locked in its locking position by a pre-loaded ball, being pushed in a conical seat in the end of the handle. Locking and releasing  $\Psi_2$  and  $\Psi_3$  works in a similar fashion, except that only one handle is needed. Rotation of this handle, rotates the eccentric axis of  $\Psi_3$ . This rotation is copied to the eccentric axis of  $\Psi_2$  by means of the bar connecting both axes, shown in Figure 3.20(b).

(a) Exploded view clamp 1, locking  $\Psi_1$ .(b) Actuation of clamp 2 to fixate or release  $\Psi_2$  and  $\Psi_3$  with one handle. Both eccentric axes are connected with the bar shown.Figure 3.20: Manipulator-adjustment: clamp 1 fixates  $\Psi_1$ , clamp 2 works similar for  $\Psi_2$  and  $\Psi_3$ .

### 3.4.3 Experimental results of the manipulator-adjustment

Measurements on the manipulator-adjustment have been performed to obtain its performance in dynamic behavior. These results are presented below.

#### Frequencies

Figure 3.21 shows the (schematic) measurement set-up used to obtain first natural frequencies present in the manipulator-adjustment, in the directions indicated in the figure. The manipulator-adjustment is mounted in its platform (P). The platform itself is mounted on a slit-table, by supporting it onto two strips

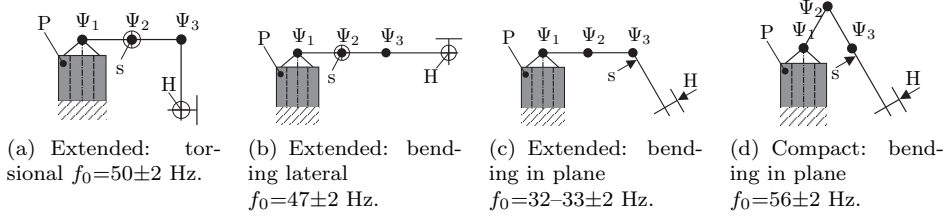


Figure 3.21: First natural frequencies of the manipulator-adjustment (joints  $\Psi_{1,2,3}$  are shown) held by its platform (P), which is fixated on a slit table. A dummy mass applied at the manipulator-coupling at joint  $\Psi_3$ , resembles the mass and location of the center-of-mass of one manipulator. An input is applied with a hammer (H), the response is measured with a displacement probe (s). The compact pose (Figure d) is expected to be used in general.

underneath its outer edges (at about 120 mm from its middle manipulator-adjustment mounting-point) and fixating it with a bolt supported through its middle manipulator mounting-hole. A dummy for the manipulator is suspended in the manipulator-adjustment, with its center-of-mass appropriately positioned at a similar point. The average position of the manipulator's center-of-mass has been taken, since it changes somewhat with the manipulator pose and with the entrance depth of the instrument. Measurements have been performed with a displacement probe  $s$  in contact with the manipulator-adjustment and a scope (Appendix Table D.7). An excitation was applied with a hammer (H). The obtained first natural frequencies are well within the specifications.

### 3.5 Conclusion and recommendations

The Slave is composed of its pre-surgical set-up, three manipulators, one endoscope and two instruments. The pre-surgical set-up consists of one five-DoF platform-adjustment connected to the table and one platform with three five-DoF manipulator-adjustments in line-up. It allows to initially position and orient each manipulator prior to surgery and then fixates this configuration. The platform-adjustment and platform connect all manipulators with a single frame to the table. This results in a small force path between two instrument-tips working together. It is compact to avoid interference with the surgical team and to provide a stiff frame during surgery. The platform can be positioned in  $x$ ,  $y$  and  $z$  near the field of surgery. An additional orientation places the platform parallel to the table-top and  $\theta$  can orientate the platform anywhere between longitudinal and transverse the table-top. The manipulator-adjustments and connected manipulators are mounted within the platform at a pitch of 80 mm. The length of each manipulator-adjustment and manipulator is comparable to the length of a human arm. Each manipulator-adjustment fixates its manipulator to the platform after

positioning the manipulator in its appropriate incision with an initial orientation pointing towards the target organ. Each manipulator-adjustment provides the required five DoFs. All DoFs of the pre-surgical set-up are locked during surgery to provide a stiff frame. The clamps are designed for the required load. The pre-surgical set-up is entirely mechanical. A wedge transmission (either translating or rotating) applied in all clamps reduces the actuation force, while keeping the required stroke of the handle limited. This results in the possibility of fast manual adjustment with a clamp handle rotation smaller than  $135^\circ$  and a limited required actuation torque. The proposed weight-compensation mechanism improves adjustment of the set-up even more.

The measured stiffness in  $z$ -direction of the platform and platform-adjustment fulfills the required stiffness of  $1 \cdot 10^6$  N/m. Its measured first natural frequency of approximately 27 Hz matches the requirements as well. The manipulator-adjustment itself exceeds this last requirement with a first natural frequency of approximately 45 Hz in tall pose and 55 Hz and in compact pose. This pose is expected to be used most in practice.

The range and accuracy of the platform-adjustment and range of the manipulator-adjustment satisfy the requirements. It is believed that the platform-adjustment range can even be smaller than stated in the requirements. This assumption has to be checked in a test-environment. The link-lengths can be reduced even more if these tests confirm this assumption, which is advantageous for the static and dynamic behavior of the pre-surgical set-up.

Scales can be applied at the joints of the pre-surgical set-up to provide information on its arrangement. Generally, the position and orientation of the platform-adjustment and manipulator-adjustment will be fixed during surgery. Therefore, the joint angles can be read and kept for reference. The obtained data in combination with information on type of surgery, anatomy and surgeon's preferences can eventually reduce the set-up time of the Slave.

The handles of the manipulator-adjustment are locked with closed clamps. A button should be added to the clamp handles to actually secure the handles in closed position.



## Chapter 4

# Manipulator for Instrument and Endoscope

The system provides the surgeon with one surgeon-controlled actuated endoscope and two surgeon-controlled actuated instruments. Each manipulator (discussed in this chapter) moves its endoscope or instrument in  $\phi$ ,  $\psi$ ,  $\theta$  and  $z$  during surgery, according to instrument movements shown in Figure 1.1. First the manipulator is discussed regarding its overall design requirements and the possible layouts of its DoFs. Subsequently the DoFs are discussed in pairs: the  $\Phi\Psi$  and the  $\Theta Z$  part of the manipulator. The part on the  $\Phi$  and  $\Psi$  DoFs discusses its specific design and performance requirements, followed with a description of the transmission and force sensor design details, and an evaluation of its force sensors. A similar discussion related to the  $\Theta$  and  $Z$  DoFs follows, with additionally an evaluation of its drive. The chapter closes with an evaluation (modal and identification measurements) of the four-DoF manipulator and a conclusion.

### 4.1 Manipulator design requirements and concepts

This section discusses the overall design requirements of the manipulator. These form the basis of the concepts as presented. Requirements relevant for detailed design, will be presented in the sections on the specific  $\Phi\Psi$ -manipulator and  $\Theta Z$ -manipulator.

### 4.1.1 Manipulator overall design requirements

The overall design requirements of the manipulator include specifications related to the patient. These are not specifically mentioned in Chapter 2 but are inherent to minimally invasive surgery (MIS):

1. limit post-operative pain,
2. move the instrument with respect to a center of rotation in  $\phi$ ,  $\psi$ ,  $\theta$  and through this center in  $z$ ,
3. allow for easy access, overview of port-sites and least obstruct the assistants at the table,

The post-operative pain can be kept low by allowing a small incision-length. The trocar-diameter is set to 10 mm, indicating that the instrument-diameter should be smaller (8.5 mm). This trocar-diameter is set as the defining dimension of the incision. An actual manipulator hinge can therefore not be applied here. Generally the incision will be placed perpendicular to the tissue. A 10 mm trocar-diameter results in an incision length of  $L_i \approx 16$  mm, or  $L_i \approx 12$  mm if a skin strain of 30% is incorporated. Old skin is assumed to be able to handle a strain of 30%, young skin 50%<sup>1</sup>. If the instrument enters the body cavity under an angle ( $\Psi=60^\circ$ ) with respect to its normal vector, its required circumference  $C=34$  mm. This results in an additional strain of 6%, which will be similar for any method: be it conventional or robotic MIS. This practice of keeping the strain low results in fast healing of the incisions. In addition to the small incision-length, support (forces) of the instrument should be provided by the manipulator instead of the muscular layer or ribs surrounding the incision-site to reduce post-operative pain. Two DoFs ( $x$  and  $y$ ) on the center-line of the instrument are prescribed by the incision. These need to be prescribed by the manipulator as well to provide the required support in these directions. Either two actuated DoFs in addition to the  $\Phi$ ,  $\Psi$ ,  $\Theta$  and  $Z$  actuated DoFs, or a passive support realizes this. The manipulator with passive instrument support in  $x$  and  $y$  is preferred above a six-DoF actuated manipulator for various reasons:

- the position of the hinge of the actuated six DoFs depends on the correct cooperation of the actuators,
- the structural stiffness of the two DoFs is more rigid in the passive case (mechanical support versus servo gains),
- the passive support has an inherent safety,
- the installation and removal can be performed electrically powerless, and
- the introduction of redundant actuators makes the system more complex and expensive.

<sup>1</sup>It is assumed that the muscular layer below the skin is most sensitive to these effects. Any fat and skin covering the muscular layer will follow the movements of the trocar. Strain on this tissue will be limited if the distance between the incisions is sufficiently large.

This passive layout does require that the manipulator is positioned correctly within the incision (with the manipulator-adjustment). Misplacement of the instrument would result in stirring movements in the incision site, increasing post-operative pain (also mentioned in e.g. [80]). Furthermore, movements caused by (artificial) respiration are considered limited. The abdominal and thoracic muscular wall will then remain stationary during surgery and do not alter their form, location and orientation with respect to the table top. This assumption is made since the thoracic muscular wall is provided with ribs that do not alter their form with reduced respiratory movements, and the abdominal wall is inflated ( $\approx 8\text{--}12\text{ mmHg}$ ) and tightened accordingly. In addition, the manipulator needs to be compact and light to fit with the last two design requirements.

#### 4.1.2 Manipulator concepts

As shown in Figure 1.1 the instrument rotates in  $\Phi$  and  $\Psi$  around its incision point. An actual hinge at this point to passively support the instrument would increase the incision-length. Therefore, this rotation point P is kinematically fixed instead of using an actual hinge. A mechanism remotely fixes the intersection of the  $\Phi$  and  $\Psi$  DoFs (point P) of the instrument: either with the segment mechanism or with the parallelogram mechanism (Figure 4.1 on the next page, also see [80]). During surgery this rotation point P has to coincide with the muscular layer of the incision.

The segment mechanism (top of the figure) has two segments 1 and 2, that rotate on their respective axes A and B. Both axes need to rotate to provide either  $\Phi$  or  $\Psi$  or a combination of both. The parallelogram mechanism (bottom of the figure) rotates around  $\Phi$ , while the parallelogram provides  $\Psi$ . In both cases the instrument is supported, which reduces support forces in the tissue and post-operative pain. The evaluation of these concepts is performed by means of the design requirements asking for a compact layout and compact motion envelope. Both concepts are compact in their layout. The parallelogram mechanism is more compact in its motion than the segment mechanism, indicated with the dotted lines in the right of both figures. Three manipulators on a row can more easily interfere with each other then.

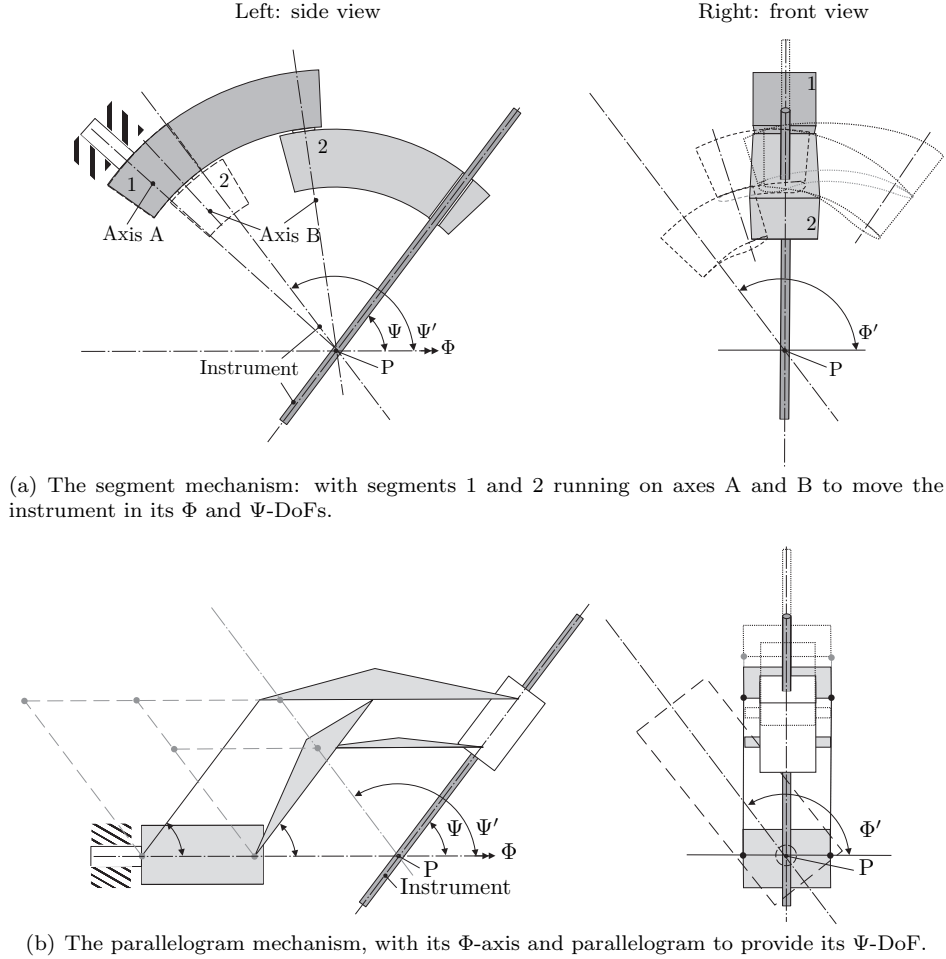
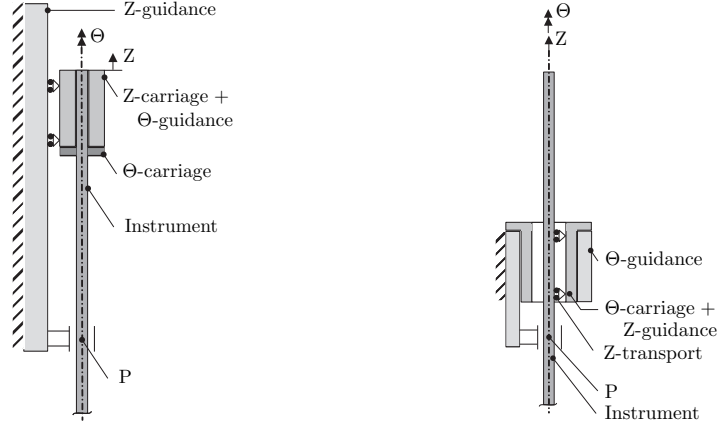


Figure 4.1: Concepts for the manipulator, to provide the instrument with its  $\Phi$  and  $\Psi$ -DoFs. The concepts facilitate in a kinematically fixed point of rotation P to keep the incision size restricted and in an instrument-support to reduce support forces in the tissue. Top: the segment mechanism. Bottom: the parallelogram mechanism. The  $\Phi$  and  $\Psi$ -DoFs of the instrument are shown, a next position  $\Phi'$  (front view) and  $\Psi'$  (side view) are shown with [—]. The neutral orientation for both  $\Phi$  and  $\Psi$  is in both right figures indicated with [...].

The parallelogram mechanism is chosen since the instruments and endoscope generally enter the body cavity close to each other, within a segment of  $90^\circ$ . A narrow motion-envelope is preferred then, which is hard to realize with the segment mechanism.



(a) Z $\Theta$ -mechanism: the Z-guidance is connected to the  $\Phi\Psi$ -manipulator. The instrument moves with its Z-carriage along its Z-guidance. The  $\Theta$ -guidance is integrated with the Z-carriage. The instrument is connected to the  $\Theta$ -carriage.

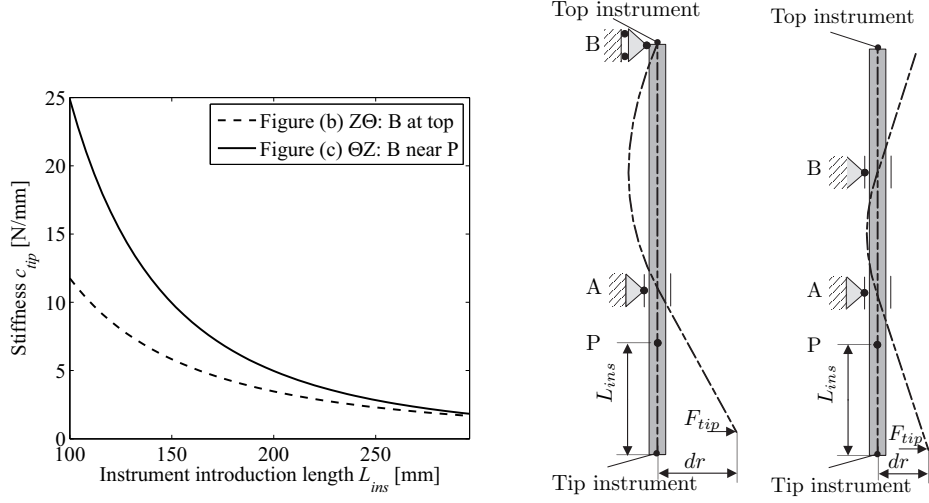
(b)  $\Theta$ Z-mechanism: the  $\Theta$ -guidance is connected to the  $\Phi\Psi$ -manipulator. The Z-guidance is integrated with the  $\Theta$ -carriage, which provides the instrument with  $\Theta$ . The instrument moves in  $z$  by means of its Z-transport.

Figure 4.2: Concepts for the manipulator, to provide the instrument with its  $\Theta$  and Z-DoFs through the kinematically fixed rotation point P of the manipulator.

The  $\Theta$ -DoF is most logically applied by revolving the instrument on its center line. The  $z$ -translation can either be provided by translating the instrument and its rotational mechanism with a mechanism or a guidance-carriage combination, see the Z $\Theta$ -mechanism in Figure 4.2(a). The other option is to translate the instrument in  $z$  from within its rotational mechanism. For example with friction-wheels, see the  $\Theta$ Z-mechanism in Figure 4.2 right. This figure displays the discussed layouts. Both layouts fulfill the design requirements regarding (reduced) post-operative pain and DoFs. The design requirements that ask for a compact layout and motion envelope are used to compare both concepts. The  $\Theta$ Z-mechanism (right of the figure) least obstructs the assistants at the table, since its layout is more compact than the Z $\Theta$ -mechanism. In addition, it offers most advantages to the assistants, since it reduces the required motion-envelope of the manipulator in comparison to the Z $\Theta$ -mechanism layout.

The layout for the  $\Theta$  and Z-DoFs determines also the mechanical support that can be provided to the instrument, and therefore the lateral stiffness at the instrument-tip. The Z $\Theta$ -manipulator of Figure 4.2(a) can support the instrument either by fixating its top to the carriage ( $c_{fixed}=1.1$  N/mm), which would result in unintended contact with the trocar, or it can simply support<sup>2</sup> the instrument (Figure 4.3(b)). The simply supported instrument would have one support point at its top on the carriage (B in this figure) with an additional support point near the patient (A). The  $\Theta$ Z-manipulator (Figure 4.2 right), can simply

<sup>2</sup>The supports of a simply supported beam provide only translational constraints: reaction forces no moments [41].



(a) Lateral stiffness ( $c_{tip}$ ) as function of the instrument inserted length  $L_{ins}$  and instrument support provided: Figure (b) ZΘ and Figure (c) ΘZ.

(b) ZΘ: B at top. (c) ΘZ: B near P.

Figure 4.3: The instrument lateral stiffness at the tip ( $c_{tip}=F_{tip}/dr$ ) when simply supported. The ZΘ-manipulator can provide B at the top (Figure b) and the ΘZ-manipulator can provide B near P (Figure c). Point P should be positioned within the incision.

support the instrument at two points (A,B) near the kinematically fixed point of rotation P and thus near the incision, Figure 4.3(c). The stiffness resulting from the support methods mentioned, is presented in Table 4.1. Simply supporting the instrument with both support points (A and B) near point P (and thus the incision) provides the highest stiffness, which confirms the choice of the ΘZ-manipulator (Figure 4.2(b)). The lateral stiffness at the instrument-tube tip can be increased by supporting the instrument(-tube) at more points. This is allowed if the instrument-tube has internal DoFs (its axial stiffness is two to three orders larger than its lateral stiffness). But it makes stresses present in the instrument more difficult to predict and the system more complex. Therefore, this is not considered further. The next step is to increase stiffness by choosing a material other

Table 4.1: Lateral stiffness of the instrument tube at the instrument-tip ( $c_{tip}=F_{tip}/dr$ ), depending on the instrument length being inserted into the patient and on the support provided. The instrument-tube has an outer diameter  $D_o=8.5$  mm, a wall thickness  $t=0.6$  mm, length  $L_o=412$  mm and material 316L stainless steel.

Simply supported instrument	Stiffness $c_{tip}$ [N/mm]
ZΘ-manipulator: support as in Figure 4.3(b)	2–12
ΘZ-manipulator: support as in Figure 4.3(c)	2–25

than stainless steel for the instrument-tube. Stainless steel however is commonly used because its extreme ductility avoids fracture even under abuse, and therefore chosen. Accordingly, the  $\Phi, \Psi, \Theta$  and Z-DoFs of the instrument are realized with the  $\Phi\Psi$  parallelogram and the  $\Theta Z$ -mechanism, see Figure 4.4. The manipulator should provide a stiffness an order of magnitude 1–2 above the instrument-stiffness (Table 4.2) for accurate movements and to achieve a first natural frequency above 20 Hz.

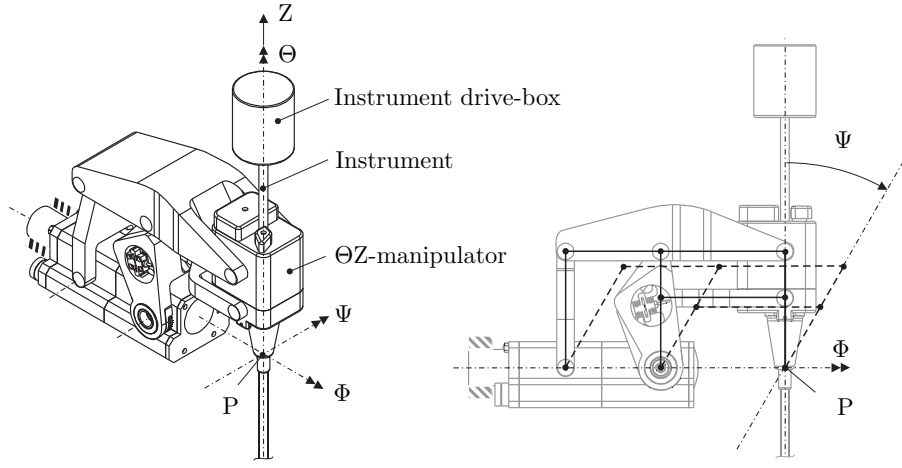


Figure 4.4: The instrument manipulator manipulates its instrument in  $\phi, \psi, \theta$  and  $z$ . Its double parallelogram (schematically given in the right figure with [—] neutral position, [---] another position) provides the  $\Psi$ -DoF at the kinematically fixed point of rotation P. In P this  $\Psi$ -DoF intersects with DoFs  $\Phi, \Theta$  and Z. P should coincide with the muscular layer of the incision during surgery.

Table 4.2: This table displays the stiffness of the outer instrument-tube. The lateral  $c_{tip}$  and rotational stiffness  $k_t(c_{tip})$  depend on the instrument support provided. The  $\Theta Z$ -manipulator simply supports the instrument according to Figure 4.3(c), with a mutual distance of 90 mm between point P and Support B. The instrument stiffness depends on the instrument's inserted length  $L_{ins}$ , with rotational stiffness  $k_t(c_{tip}) = k_\phi = k_\psi = c_{tip} L_{ins}^2$ .

Inserted length $L_{ins}$ [mm]		Instrument stiffness	
		$L_{ins}=300$	$L_{ins}=100$
Lateral stiffness $c_{tip}$	[N/mm]	2	25
Rotational stiffness $k_t(c_{tip})$	$[\cdot 10^5 \text{ Nmm/rad}]$	1.8	2.5
Axial stiffness $c_z$	$[\cdot 10^3 \text{ N/mm}]$	7.9	16
Torsional stiffness $k_\theta$	$[\cdot 10^4 \text{ Nmm/rad}]$	4.9	10

## 4.2 Manipulator: $\Phi$ and $\Psi$ -DoFs

This section discusses design and performance requirements of the  $\Phi$  and  $\Psi$ -DoFs, and details on their transmission and their force sensor. The force sensors are mentioned in the section on the transmission and discussed in further detail in Subsection 4.2.5. Evaluation of the manipulator can be found in Section 4.4.

### 4.2.1 Requirements of the $\Phi\Psi$ -manipulator

The design requirements of the  $\Phi\Psi$ -manipulator add detail to the overall manipulator design requirements given in Subsection 4.1.1. These are geared toward the parallelogram-mechanism:

- the manipulator should be as compact as possible (preferably not wider than 80 mm), to minimize the motion-envelope of the manipulator and maximize the motion envelope of the instrument,
- the force measurements will be performed outside the patient,
- the manipulator should be robust in use, among others fatigue of the electrical connections should be prevented by proper large radius routing,
- the  $\Phi$  and  $\Psi$ -DoFs are either locked or non-backdriveable when they are not controlled, for safety, and
- the  $\Phi\Psi$ -manipulator will not be in contact with the patient, therefore it is not required to be disposable or sterilizable. It should be safe in use.

Performance requirements of  $\Phi\Psi$ -manipulator are based on the instrument-tip at 300 mm inside the body (Section 4.1.1):

1. the range of motion in  $\phi$  and  $\psi$  is  $\pm 35^\circ$ ,
2. the resolution for positioning the instrument-tip results in  $d\phi=d\psi=9.5\cdot 10^{-3}^\circ$ ,
3. the angular velocity of the instrument gives  $\omega_\phi=\omega_\psi=0.5$  rad/s,
4. the range of forces applied and measured at the instrument-tip is up to 10 N,  $T_{out-max}=3$  Nm,
5. the resolution to measure forces at the instrument-tip is set to 60 mN,  $T_{out-min}=18$  Nmm,
6. the stiffness within the given dimensions (width=80 mm) should be as large as possible (a factor 1–2 above the values shown in Table 4.2), and
7. the first natural frequency  $f_0$  should be preferably above 20 Hz.

### 4.2.2 Transmission of the $\Phi\Psi$ -manipulator

The parallelogram frame of the manipulator with its  $\Psi$ -mechanism, revolves on its fixed  $\Phi$ -axis (Figure 4.5). This  $\Phi$ -DoF is driven with a drive-train coaxial

with the  $\Phi$ -axis. Placing the drive-train coaxially, reduces the moving mass of the manipulator. The  $\Phi$ -axis intersects with point P. The double parallelogram (schematically given in Figure 4.4) applies the  $\Psi$ -rotation in point P without a physical hinge in P to have minimal incision-size. Two layouts have been designed to drive the  $\Psi$ -DoF, see Figure 4.5. The first layout has been realized (first prototype). Insight in the characteristics and performance of this first prototype was the starting point to design the second layout, which is being realized. The first layout consists of a right-angled worm-wormwheel transmission, which places the drive-trains of both DoFs parallel to the  $\Phi$ -axis to limit the manipulator width. It preceded the second (preferred) layout, in which the  $\Psi$  is driven with a ball-screw drive located in the plane of symmetry of the manipulator. The manipulator dimensions near the patient are reduced even more. The forces executed with and on the instrument in  $\Phi$  and  $\Psi$  are measured near the output axis of each drive-train by means of an elastic element and displacement-sensor. Influence of the transmission between motor and outgoing axis is then prevented, the force signal from the instrument hereby is most accurate.

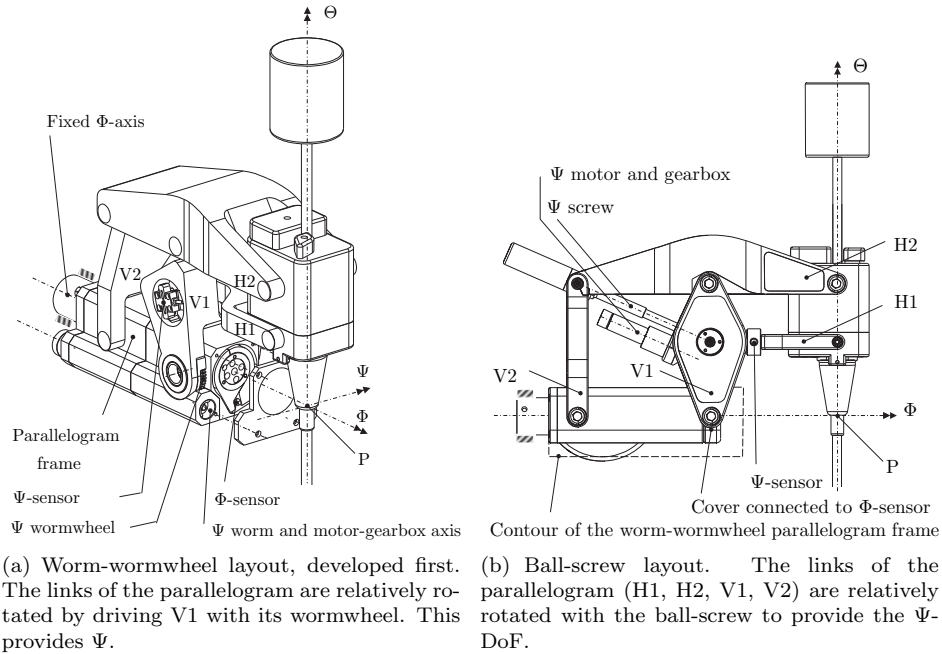


Figure 4.5: The  $\Phi$  and  $\Psi$ -DoFs of the manipulator. Two layouts for the  $\Psi$  drive-train have been developed in consecutive order, the worm-wormwheel (a) and ball-screw (b) layout respectively. The  $\Phi$  drive-train is similar for both cases.

### 4.2.3 Transmission $\Phi$ in detail

The hollow  $\Phi$ -axis is clamped by the manipulator-clamp of the manipulator-adjustment (Figure 3.17). The  $\Phi$ -axis supports the parallelogram frame (Figure 4.6) on three bearings. Two bearings in x-configuration on the left side near the manipulator-adjustment and one radial bearing on the right side of the hollow axis. The drive-train of the  $\Phi$ -rotation is placed and supported coaxially within its driven axis, see Figure 4.6.

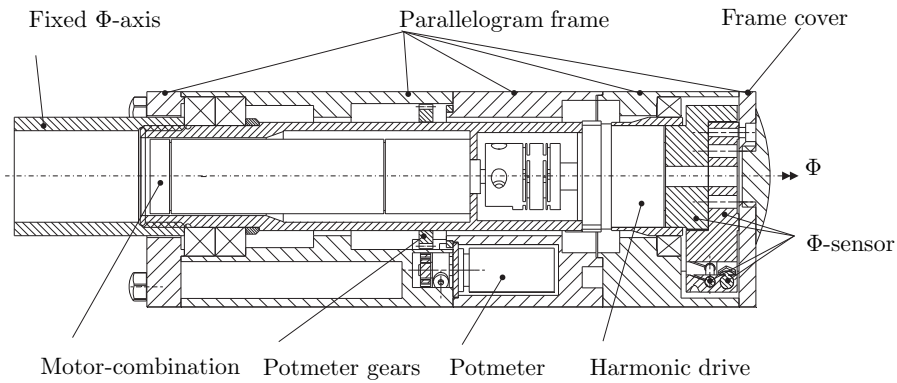


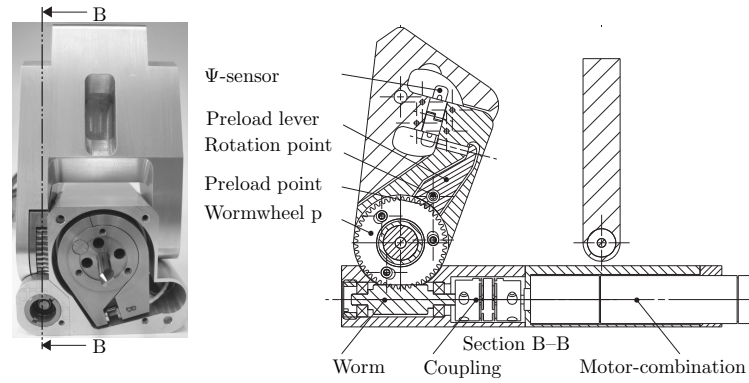
Figure 4.6:  $\Phi$ -DoF drive-train, cross-section of  $\Phi$ -axis and parallelogram frame. The motor-combination is connected to the  $\Phi$ -axis. The motor output axis drives the parallelogram frame in  $\Phi$ , by means of the intermediate harmonic drive and  $\Phi$ -sensor, which is connected to the cover of the parallelogram frame. The potmeter revolves with the parallelogram frame around the  $\Phi$ -axis. The gear connected to its outgoing axis rolls along the gear connected to the  $\Phi$ -axis, measuring the absolute  $\Phi$ -rotation of the parallelogram frame.

It includes a motor-combination (encoder-brake-motor-gearbox), which is connected with a flexible coupling to a harmonic-drive. The  $\Phi$ -force sensor couples the outgoing axis of this drive-train to the frame-cover of the parallelogram frame. The brake at the back of the motor locks the parallelogram frame in  $\Phi$  when the Slave is in manual operation mode. It can be released to adjust its initial  $\Phi$ -orientation, during operation it is released as well. The brake is included in the motor-combination since it is not used during surgery and fits within the fixed  $\Phi$ -axis. Furthermore, the motor is provided with an encoder. A multiturn potmeter, which is used as a reference signal and safety end-switch, provides the absolute  $\Phi$  angle of the parallelogram frame plane. It is mounted in the parallelogram frame, its outgoing axis is provided with a pinion that mates with a gear connected to the  $\Phi$ -axis. The hardware components and details of the  $\Phi$  drive-train of the ball-screw layout are similar to the  $\Phi$  drive-train of the worm-wormwheel layout. These components are presented in Appendix Table E.1 and E.2.

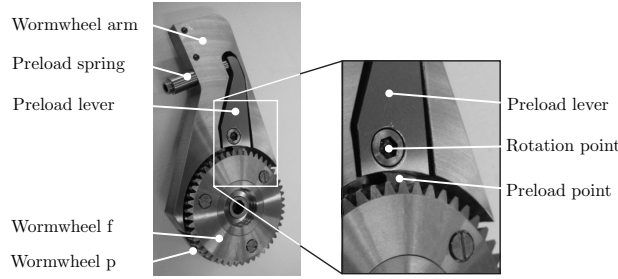
#### 4.2.4 Transmission $\Psi$ in detail

Two layouts have been developed for the  $\Psi$ -drive, the worm-wormwheel preceded the ball-screw layout. Each will be discussed with subsequently a comparison.

##### Worm-wormwheel layout



(a)  $\Psi$ -drive worm-wormwheel layout: worm support and connected drive-train, and preload mechanism of wormwheel p.



(b) Wormwheel arm with preloaded wormwheel.

Figure 4.7:  $\Psi$ -DoF worm-wormwheel support and drive-train.

Arm-V1 of the parallelogram (close to the instrument) is driven with a right-angled transmission, the worm-wormwheel drive, see Figure 4.7. The wormwheel of this drive is mounted to its wormwheel arm. This arm is connected to V1 with the  $\Psi$  force sensor, which transmits the torque from the wormwheel to V1. The wormwheel is composed of a fixed (f) and a preloaded (p) half. Wormwheel f is fixed to its wormwheel arm. Wormwheel p is preloaded on the worm to reduce backlash, with a spring through a preload lever (Figure 4.7(b)). The worm is positioned below the wormwheel in the parallelogram frame to keep the center-of-mass of the manipulator close to  $\Phi$ -axis. In addition it places the worm and its drive-train parallel to the  $\Phi$ -axis, which results in a slender layout of the parallelo-

gram frame. The worm itself is supported in two bearings. It is connected by means of a torsionally stiff otherwise elastic element to the gearbox of the motor. This transmission combination is not backdriveable so, with loss of power, the manipulator will remain in its position. The motor is provided with an encoder. The single-turn potmeter in element V1 provides an absolute angle for end-switch purposes, Figure 4.8. These hardware components of the drive-train just described are given in Appendix Table E.1. Accompanying details are given in Appendix Table E.2.

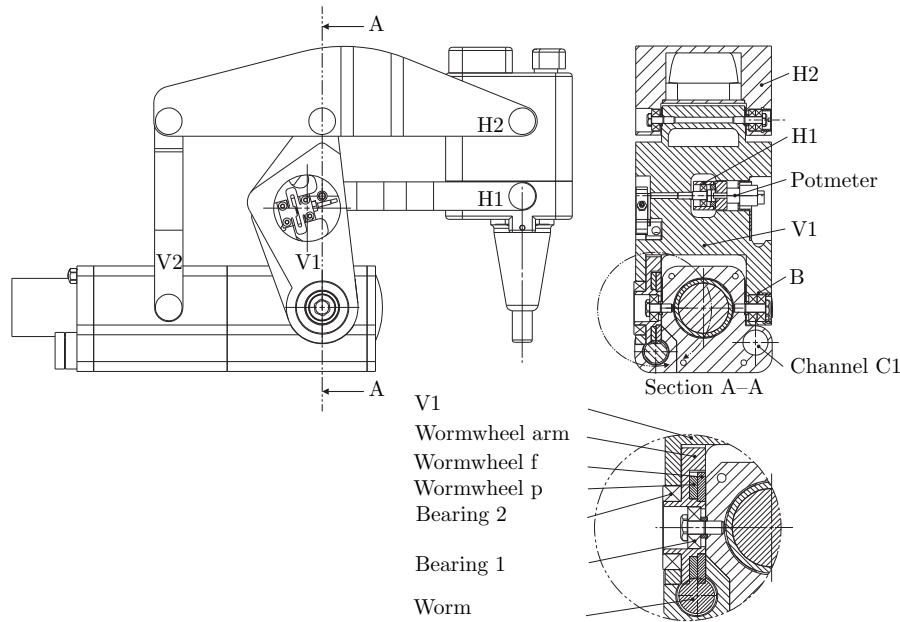


Figure 4.8: The worm drives the wormwheel combination. Wormwheel p is preloaded. Wormwheel f is connected to the wormwheel arm, which is supported by bearing 1, V1 is supported on the wormwheel arm with bearing 2 on one side and with two angular contact ball bearings in x-configuration at B on its other side.

### Ball-screw drive layout

The ball-screw drive layout is on display in Figure 4.9: it changes the distance between joint J2 and J4 of the parallelogram, controlling  $\Psi$ . The nut is fixed in its rotation and supported in J4 with a cardan joint (top view in Figure 4.9) that has its intersecting axes at the axis of J4. The screw shaft is supported in J2 with a similar cardan joint (cross-section in Figure 4.9). The additional bearings to allow for its rotation are placed as close to J2 as possible, see Figure 4.10. The screw shaft and nut can thus align, without the tendency to buckle.

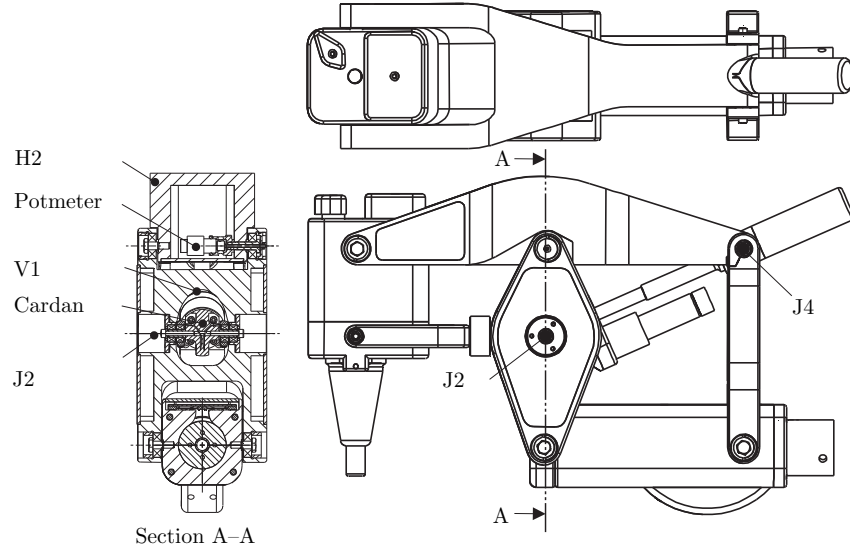


Figure 4.9:  $\Psi$ -DoF ball-screw drive, the cardan in J2 (and J4) allows the screw shaft to align with the nut, the potmeter provides an absolute angle.

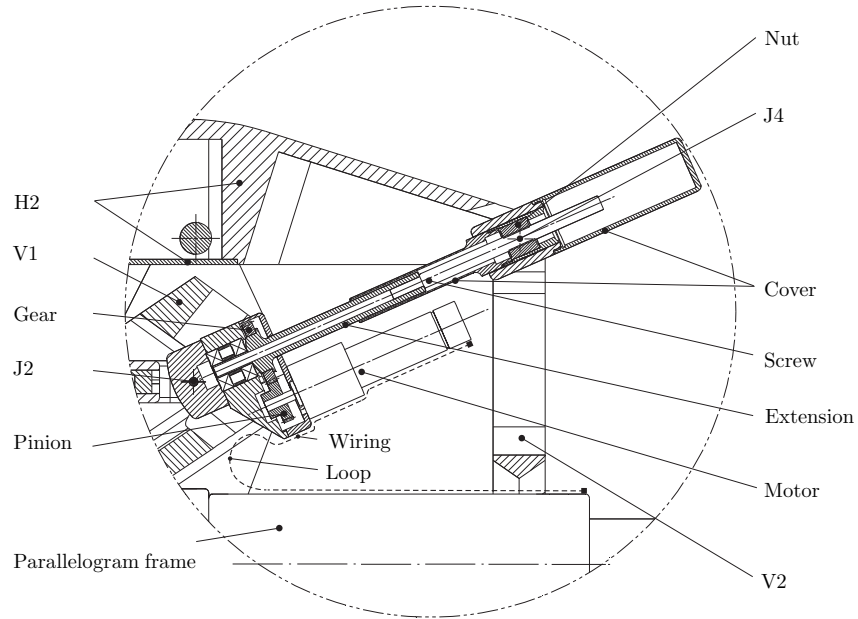


Figure 4.10:  $\Psi$ -DoF ball-screw drive, cross-section. Elements V1, V2 and H2 of the parallelogram are shown as well (partly). H2 is provided with closed chambers to reduce its mass significantly whilst maintaining its overall rigidity. The ball-screw drive wires for  $\Psi$  (its path indicated with [---]), run from its motor to the parallelogram frame. Its loop allows for the required movement between these parts.

The diameter of the screw shaft is limited to 6 mm to reduce the torque required. A ball-screw is chosen for the same reason, it reduces friction which leads to a smaller motor and lower overall mass. The ball-screw drive and its drive-train are placed in the plane of symmetry of the manipulator. The drive-train is located parallel and below the screw to keep the center-of-mass of the manipulator near the  $\Phi$ -axis. The lead prescribes the transmission ratio of the ball-screw drive. It is driven with a motor combination consisting of a reduced backlash gearbox, a motor with an encoder. The potentiometer in Figure 4.9 provides an absolute angle. The hardware components of the drive-train just described are given in Appendix Table E.1. The accompanying details are given in Table E.2.

### Comparison of the worm-wormwheel and ball-screw layout

The ball-screw layout succeeded the worm-wormwheel layout, based on ongoing insight. Both constructions are compared regarding construction and range of motion of the parallelogram and regarding their drive.

A comparison of the parallelogram construction is given in Figure 4.11 and below:

- the manipulator with the ball-screw drive has a larger distance to the patient compared to the manipulator with the worm-wormwheel layout: the bottom of the parallelogram frame lies  $h$  higher, the cover of the parallelogram frame lies  $q$  further and the circular distance is reduced with  $(D_v - D_w)/2$ ,
- the manipulator with its ball-screw layout has an increased distance between its parallelogram arms which improves the manipulator lateral and vertical stiffness quadratically:  $p$  between V2 of the ball-screw drive and V2 of the worm-wormwheel drive,  $(f-g)$  between H2 of the ball-screw drive and H2 of the worm-wormwheel drive. However, the worm-wormwheel manipulator can be equipped with arms of these dimensions as well,
- the mass of the ball-screw drive is reduced with  $\approx 1$  kg (21%) compared to the worm-wormwheel drive. Replacing V2 and H2 of the current worm-wormwheel layout with the corresponding arms of the ball-screw drive saves 0.1 kg,
- the parallelogram frame of the ball-screw drive has room to provide a channel for wires on top of the parallelogram frame,
- the  $\Psi$ -movement of both manipulator is  $\pm 35^\circ$  with respect to its neutral position, and
- the  $\Phi$ -movement of both manipulators is set to  $\pm 90^\circ$ .

A comparison of the worm-wormwheel and ball-screw drive is given below:

- the ball-screw drive is more rigid and more robust regarding load. Axial load in two directions (pull and compression) in H1, H2 and V1 versus bending in V1,
- the transmission of the ball-screw drive is realized through more contacts, the balls of the ball-screw and nut versus the teeth of the worm-wormwheel, which makes it more stiff,
- the ball-screw drive has rolling friction and a smaller and lighter motor, the worm-wormwheel drive has sliding friction,
- the ball-screw drive drives the  $\Psi$ -DoF from the plane of symmetry of the manipulator (Figure 4.11), which results in (axial) pull and compression load of the parallelogram arms versus additional torsion with the worm-wormwheel drive,
- the electrical wire motion of the  $\Phi$ -drive for both layouts is similar, and
- the electrical wire of the ball-screw  $\Psi$ -drive needs to allow limited motion between the parallelogram frame and its drive (Figure 4.10), the worm-wormwheel drive and wires for  $\Psi$  is fixed to the parallelogram frame.

The ball-screw drive is preferred. It has a smaller parallelogram frame which results in an increased distance relative to the patient and it is more stiff through its  $\Psi$ -drive symmetry and transmission. Now, the worm-wormwheel layout is intended for the endoscope and the ball-screw layouts to manipulate both instruments. Eventually, the robot will be provided with three similar ball-screw manipulators. This offers the possibility to proceed with the robotic procedure, even if one of the manipulators should fail. One additional similar back-up manipulator can then replace any of the manipulators used.

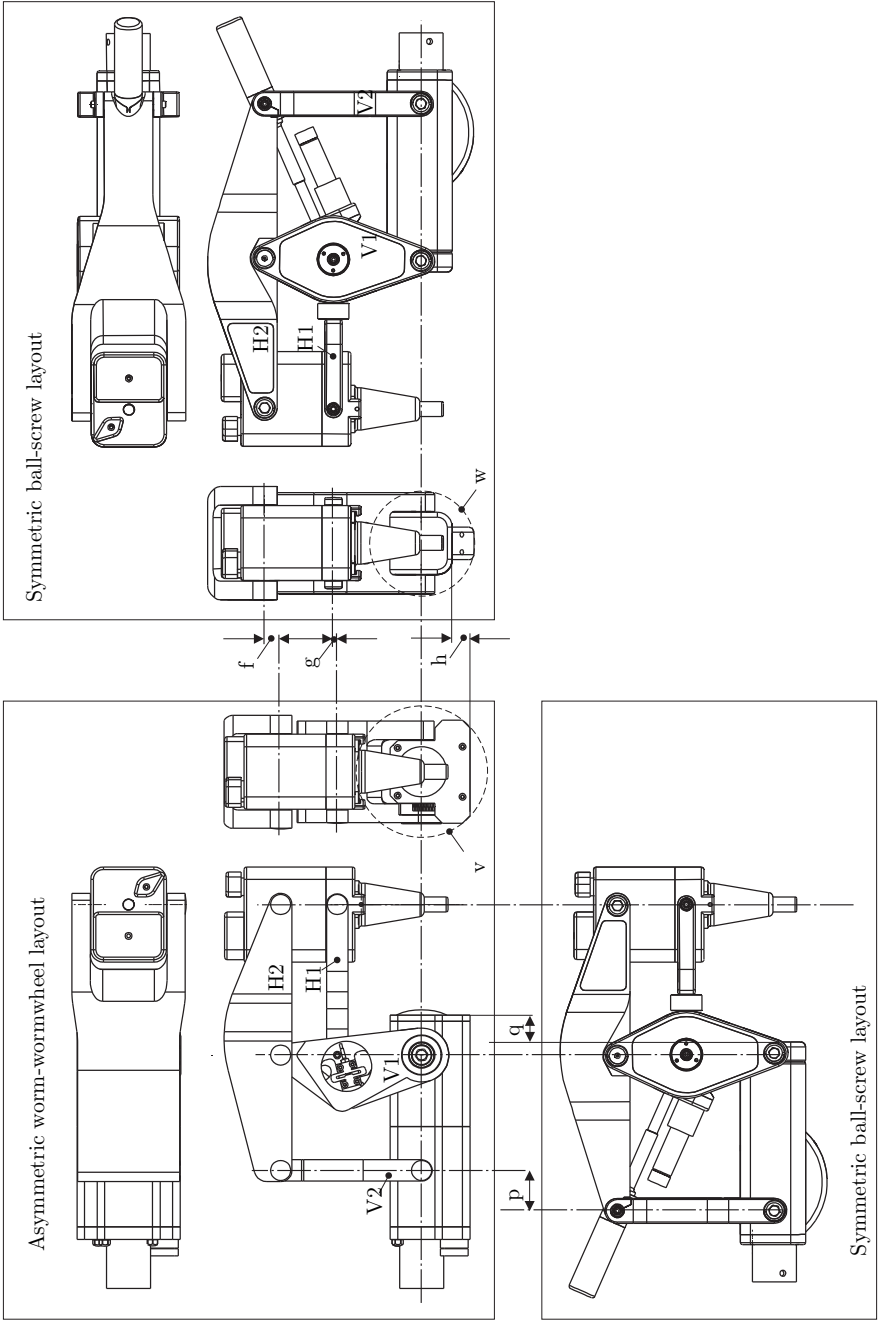
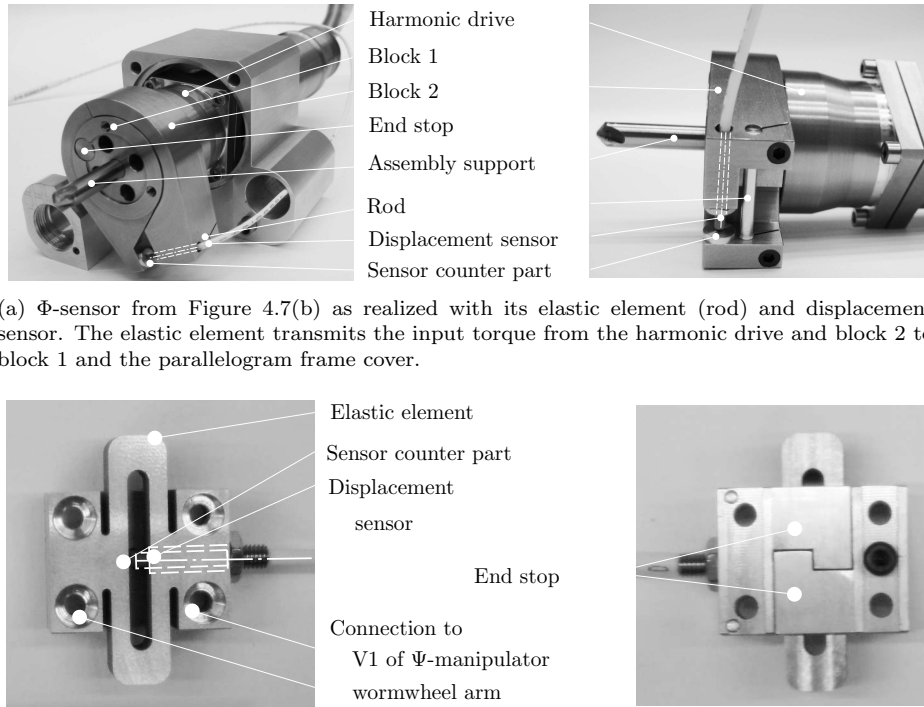


Figure 4.11: Comparison of the manipulator  $\Psi$ -drive for the worm-wormwheel and ball-screw layout.

### 4.2.5 Force-measurement of the $\Phi\Psi$ -manipulator

Forces executed with the instrument result in a  $\Phi$  and a  $\Psi$ -torque and are measured in the (external) manipulator to prevent bringing electronic signals within the patient. The forces are measured on the output shaft of each drive-train for accuracy, which prevents transmission friction from being introduced into the signal. For  $\Phi$ , the force sensor transmits the torque from the output shaft of the harmonic drive to the parallelogram frame (Figure 4.12(a)). For  $\Psi$ , the force sensor transmits the torque from the wormwheel to V1 (in case of the worm-wormwheel layout, Figure 4.12(b)). These forces are measured tangentially at a radius, by measuring the change in length of an elastic element (with stiffness  $c$ ) oriented in this tangential direction. This elastic element is placed at the largest radius ( $R$ ) possible, to increase transmission stiffness  $c(k/R^2)$  and make measurements of small changes in length possible. In addition, the stroke of the elastic element is mechanically limited with an end stop to prevent damaging the patient and manipulator when the elastic element would suffer overload. Construction details can be found in Figure 4.12.



(a)  $\Phi$ -sensor from Figure 4.7(b) as realized with its elastic element (rod) and displacement sensor. The elastic element transmits the input torque from the harmonic drive and block 2 to block 1 and the parallelogram frame cover.

(b)  $\Psi$ -sensor with its elastic element, displacement sensor and connection points. The left displays the front and right the back-side of the sensor.

Figure 4.12:  $\Phi$  and  $\Psi$  force sensors of the worm-wormwheel layout. The path of the displacement sensors is indicated with a  $[- -]$ .

### Force-measurement construction details

The force sensors are incorporated in the transmission and therefore influence the overall stiffness of the manipulator. Therefore, a stiff elastic element is used in combination with a high-end displacement sensor. For  $\Phi$  these components are mounted parallel and at a similar radius in two concentric blocks (Figure 4.12(a)). Block 2 is connected to the harmonic drive and block 1 is connected to the parallelogram frame. Since the parallelogram frame is fully supported by its bearings on the fixed  $\Phi$ -axis, this elastic element is a rod that transmits the tangential force resulting from the drive-train torque. Its change in length in two directions is measured with a displacement sensor, see Table E.3 and E.4 for details. This contactless displacement-sensor is calibrated with an offset to allow an overload. The end stop secures the displacement-sensor from contact with its counter part in case of an overload and the manipulator from uncontrolled movements if the rod should fail. This end stop consists of a pin connected to block 2, running within an oversize hole in block 1. The torque from the  $\Psi$  worm-wormwheel drive-train is transmitted by means of a tangential harmonic element, see Figure 4.12(b). The displacement of this elastic element (Appendix Table E.3 and E.4) is measured with a similar sensor as used for the  $\Phi$ -sensor. Here the end stop consists of two hook-shaped plates (Figure 4.12(b)) that interfere when the manipulator is overloaded. In the ball-screw layout the  $\Phi$ -force is transmitted in a similar manner as in the worm-wormwheel layout, Figure 4.13.

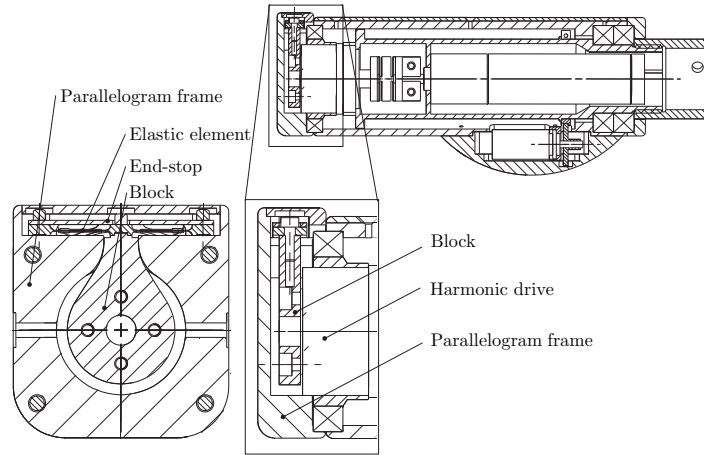


Figure 4.13: Ball-screw layout, the  $\Phi$ -sensor consists of an elastic element, strain gauges and an end-stop. Its elastic element couples the block connected to the harmonic drive and the parallelogram frame.

An elastic element transmits the torque of the drive-train by means of a tangential force at a radius, from the harmonicdrive to the parallelogram frame. A block is concentric with and connected to the harmonicdrive. In tangential direction one symmetric elastic element is connected in its middle to this block. At both

extensions it is connected to the parallelogram frame. The elastic element is a leaf-spring, parallel oriented tangential with respect to the  $\Phi$ -axis. Deformation of this leaf-spring (Table E.5) is measured with strain-gages. It is protected from overload by means of an end-stop. A commercially available strain-gage based force sensor in H1 measures the force of the  $\Psi$ -DoF, Figure 4.14.

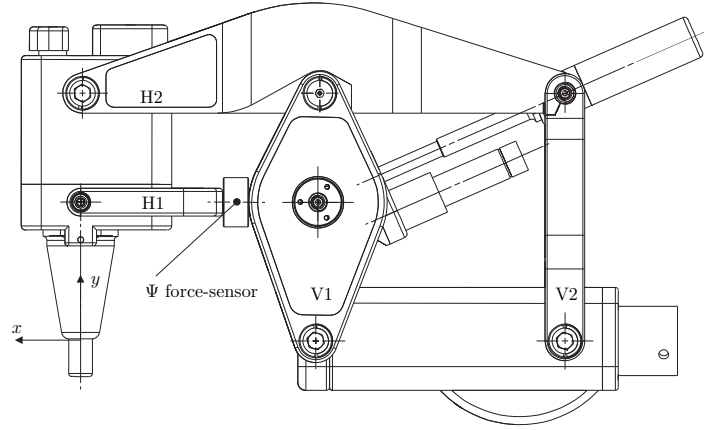


Figure 4.14: Ball-screw layout, with its commercial  $\Psi$  force sensor integrated in H1. H1 supports the  $\Theta$ Z-manipulator and instrument in  $x$ . H2 further provides support in  $x$ ,  $y$ ,  $z$ ,  $\phi$  and  $\theta$ . Together they provide  $\psi$ .

Support forces in H1 of the instrument are higher than in H2, which makes it appropriate for the sensor. The sensor should have overload capacity, which is set to two times the maximum load (Appendix Table E.5). Each  $\Phi$  and  $\Psi$  sensor measures the force executed with the instrument, temperature effects, manipulator weight and inertia, and externally applied forces. Temperature effects consist of a change in length of the elastic-element as a function of temperature ( $\alpha_{Al}=23.3 \cdot 10^{-6}/K$ ) and sensitivity of the sensor to temperature changes, and are compensated for by temperature-measurements. Information on the orientation of the manipulator, the  $z$ -position of the instrument and a model of the center-of-mass of the manipulator and instrument compensate for the manipulator weight. An inclination-sensor (connected to the parallelogram frame) indicates the initial orientation of the manipulator. The potmeter outputs provide additional orientation information during surgery. Compensation for the inertia asks for information on the distance between the center-of-mass (of the manipulator and instrument) and the axis under consideration. Compensation for the inertia around  $\phi$  requires  $\psi$  (relative to its neutral position) and  $z$  of the instrument. For the inertia around  $\psi$ ,  $z$  of the instrument is required. A distinction between forces executed with the instrument and externally applied forces (like contact with an assistant) is obviously hard to make.

#### 4.2.6 Wiring of the worm-wormwheel $\Phi\Psi$ -manipulator

Motor and encoder wires from the  $\Phi$  drive-train protrude from the  $\Phi$ -axis and are partly wrapped around the  $\Phi$ -axis and connected to the connector-block at the back of the parallelogram frame, Figure 4.15. This configuration allows for the  $\Phi$ -rotation between  $\Phi$ -axis and parallelogram frame. The  $\Phi$  and  $\Psi$ -potmeter wires and force sensor coax-cables run through channel C1 (Figure 4.8) of the parallelogram frame. The potmeter wires are directly connected to the connector-block, the coax-cables are collected at their electronic-box, its output cable is connected to the connector-block as well.

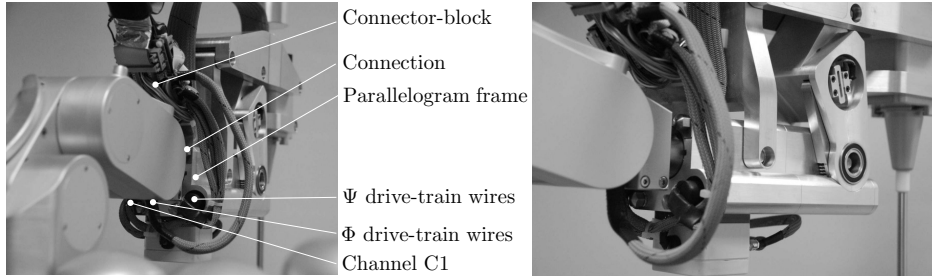


Figure 4.15: Wiring of the  $\Phi\Psi$ -manipulator with its worm-wormwheel layout.

#### 4.2.7 Evaluation of the $\Phi\Psi$ force sensors

This subsection presents the evaluation of the  $\Phi\Psi$  force sensors, each composed of an elastic element and a displacement sensor. The displacement sensors themselves are first calibrated to find a relation between input and output. Subsequently measurement results on the force sensors integrated in the manipulator are presented. These measurements indicate the accuracy of the force-sensors.

##### Evaluation of the $\Phi$ and $\Psi$ displacement sensors

The displacement sensor range, offset and preferred resolution required to perform the force-measurements, are shown in Table 4.3. A calibration [75] of the sensors is executed using equipment from [125] and described in Appendix E.2.3. An optical measurement setup with a nano-stepping piezo stage is used to move the sensor. For both sensors a fifth order polynomial is fit to the measurement data (Appendix Section E.2.3). The remaining errors are displayed in Figure 4.16(a) and 4.16(b). The range, resolution and output after calibration and fitting of the sensors is shown in Appendix Table E.8. With the applied method for calibration and the polynomial fit, the requested resolution of 30 nm is approximated closely for both the  $\Phi$  displacement sensor with a maximum error of 40 nm and

Table 4.3: Requirements of the SMU9000-2U inductive (eddy current) displacement-sensors used to measure the change in length of the elastic element of the  $\Phi$  and  $\Psi$  force sensors without contact. Displacement requirements and offset are based on the design of the manipulator (also see Appendix Table E.4), output requirements are set by the sensor.

DoF	Displacement range required [ $\mu\text{m}$ ]	Displacement range set [ $\mu\text{m}$ ]	Offset [ $\mu\text{m}$ ]	Displacement resolution set [ $\mu\text{m}$ ]	Output [V]
$\Phi$	$\pm 18$	$\pm 50$	250	0.03	$\pm 5$
$\Psi$	$\pm 38$	$\pm 50$	250	0.03	$\pm 5$

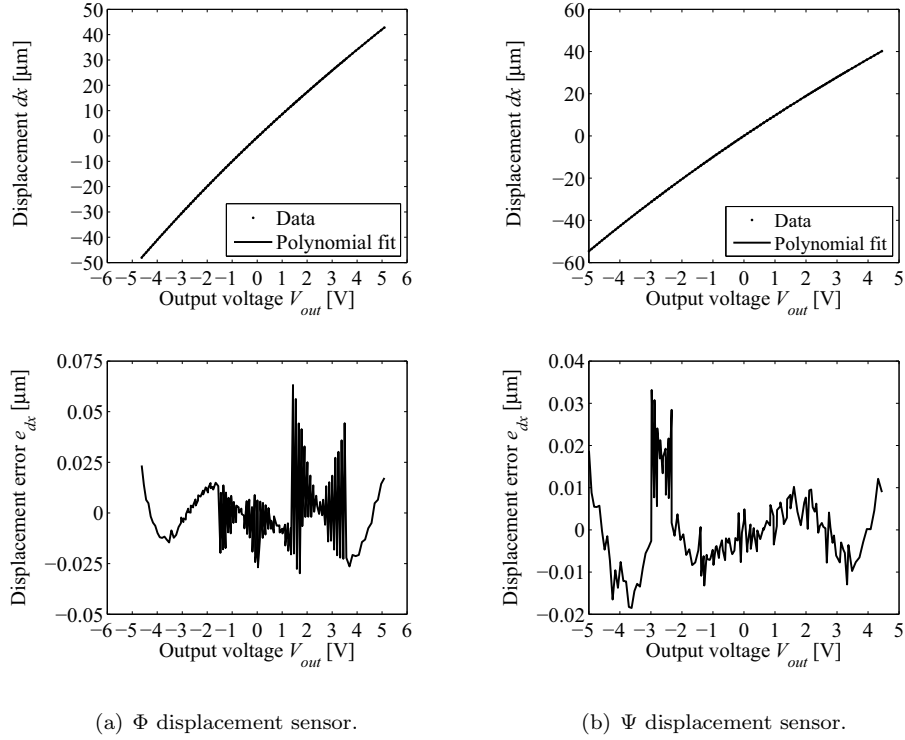


Figure 4.16: The worm-wormwheel manipulator has two Kaman SMU9000-2U displacement sensors as part of the  $\Phi\Psi$  force sensors. This figure displays results after measurement and calibration of these displacement sensors. Top: displacement data and polynomial fit. Bottom: displacement error as polynomial fit - data.

for the  $\Psi$  displacement sensor with 33 nm. So the force sensors themselves closely approximate the requirements to display the force resolution of 60 mN at the instrument-tip.

Table 4.4: Temperature measurements on the  $\Phi\Psi$  force sensors in the worm-wormwheel manipulator. Measurement 1: temperature presented at start (0 hr) and after 4 hr of running the manipulator on a sine. The temperature  $T$  and temperature change  $dT$  of the ambient and near surroundings of the  $\Phi$  and  $\Psi$  displacement sensors. Measurement 2: displays the change in output voltage of the displacement sensor as change in length  $dL$  of the elastic element of the  $\Phi$  force sensor subject to temperature change  $dT$  in a climate room.

	Measurement 1				Measurement 2		
	$T_{0hr}$ [°C]	$T_{4hr}$ [°C]	$dT=T_{4hr}-T_{0hr}$ [°C]	$dT-dT_{ambient}$ [°C]	$dT$ [°C]	$dL$ [μm]	$dL/dT$ [μm/°C]
Ambient	21	22	1	0	-	-	-
$\Phi$	20.5	23.2	2.7	1.7	14	5.4	0.39
$\Psi$	20.5	22.5	2	1	-	-	-

A temperature measurement has been done to deduce the sensitivity of the displacement sensors to the temperature. The temperature in an operating theater in the hospitals visited, is controlled to a set value  $\pm 1^\circ\text{C}$ . This set value ranges from  $19\text{--}21^\circ\text{C}$ . The temperature control of the operating theater takes into account the effect of its lights. A green light lights the entire operating theater, during the MIS procedures observed. The surgical lamps providing a spot light are switched off and will not influence the temperature of the Slave (and its sensors). The patient, the assistants and the motors driving the manipulators do affect the temperature of the Slave-robot. Performing a temperature measurement near the sensors, while the manipulator (with initial neutral position) moved with a mild sinus in  $\Phi$  and  $\Psi$  for four hours gave an indication of the motor influence on the sensor temperature, see Table 4.4. A temperature measurement in the climate room revealed the expected expansion of the elastic element of the sensor with the expansion coefficient of aluminium ( $\alpha_{Al}=23.3\cdot 10^{-6}/\text{K}$ ). The elastic element ( $L_0=15\text{ mm}$ ) is made of aluminium, which gives  $L_0\alpha_{Al}=0.35\text{ }\mu\text{m}/^\circ\text{C}$ . The difference between  $L_0\alpha_{Al}$  and the  $dL/dT$  from Table 4.4 can be caused by the displacement sensor. With a stiffness  $c=1.9\cdot 10^4\text{ N/mm}$  of the elastic element of the  $\Phi$  force sensor, a change in temperature of  $1^\circ\text{C}$  results in a change in force of  $cL_0\alpha_{Al}=6.7\text{ N}/^\circ\text{C}$  (at the instrument-tip). A temperature compensation is required.

A force, e.g. while tying a knot, is assumed to be applied within a relatively short period of time (a couple of seconds). The temperature is assumed to remain constant during this fast change of force and have little influence on this measurement. This assumption can be checked when the Slave is being used for comparable surgical tasks. In addition, people in general are good at noticing a fast change in force but bad at detecting a slow change, in addition to giving an absolute value. The sensitivity of the displacement sensors will be sufficient to account for this fast change. A temperature measurement can compensate for slow changes.

### Evaluation of the $\Phi$ and $\Psi$ force sensors in the manipulator

The  $\Phi$  and  $\Psi$  force sensors are being evaluated while integrated in the manipulator. A force is applied at the instrument-tip. A frame connected to the platform, provides the support of a digital force gauge sensor and of a preload. The force gauge sensor and preload, both are connected to the instrument-tip. The force is slowly increased, while the force sensor is being read. Figure 4.17(a) and 4.17(b) show the measurements results of respectively the  $\Phi$  and  $\Psi$  force sensor. These

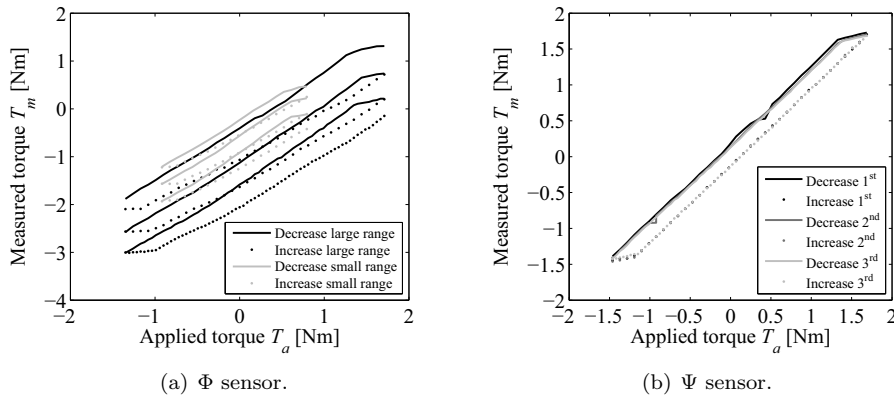


Figure 4.17: Results from evaluation of the  $\Phi$  and  $\Psi$  force sensor being integrated in its manipulator. The force applied at the instrument-tip and force measured at the force sensor are displayed as torque applied and measured at the kinematically fixed point of rotation P (Figure 4.1).

results show a reproducible behavior of the  $\Psi$  sensor. The measured torque is similar for three successive runs of increasing and decreasing the applied torque. For the  $\Psi$  sensor an uncertainty exists of 0.4 Nm at one torque applied. Friction in the measurement set-up and possibly the manipulator are suspected to contribute in this uncertainty. Further measurements with improved set-ups are required to determine the actual uncertainty of the sensor in combination with its manipulator. The drift of the  $\Phi$  force sensor displayed in Figure 4.17(a), is caused by a change of temperature, which can be compensated with a temperature measurement.

### 4.3 Manipulator: $\Theta$ and Z-DoFs

The  $\Theta$ Z-manipulator provides the  $\theta$  and  $z$  movement of the instrument. The Z-DoF will be realized by means of a friction wheel drive inside the  $\Theta$ -carriage. This section discusses the design and performance requirements of these  $\Theta$  and Z-DoFs, and details on their transmissions and force sensors. The next section presents the evaluation of the  $\Theta$ Z-manipulator.

### 4.3.1 Requirements of the $\Theta$ Z-manipulator

The design requirements of the  $\Theta$  and Z-DoFs add detail to the overall manipulator design requirements of Subsection 4.1.1:

- its height as compact as possible to keep sufficient space between manipulator and patient and keep the additional length of the instrument as small as possible,
- its width maximally 60 mm, to fit between the forks of H1 and H2,
- its motors mounted in the  $\Theta$ Z-housing to realize static wires which increases lifetime and reduces disturbing forces,
- its force sensors mounted in the  $\Theta$ Z-housing to realize static wires,
- its instrument-release mechanism should require one action to change an instrument with diameter 8.5 mm,
- its DoFs are either locked or non-backdriveable for safety, and
- its mechanism handling the instrument should prevent contamination in both directions and sterility should be taken into account.

The performance requirement of the  $\Theta$ Z-manipulator are derived for the instrument-gripper at a radius of 25 mm from the instrument tube:

- the range of motion in  $\theta$  is  $\pm 180^\circ$  and  $z=300$  mm,
- the resolution for positioning the instrument-tip is set to  $50 \mu\text{m}$  and results in  $d\theta=0.11^\circ$  and  $dz=50 \mu\text{m}$ ,
- the velocity of the instrument-tip is set to  $\omega_\theta=0-4$  rad/s and  $v_z=0-60$  mm/s,
- the range of forces applied and measured at the instrument-tip (at  $L_{tip}$  25 mm) results in maximally  $T_{out-max}=250$  Nmm for the  $\Theta$ -DoF and for the Z-DoF  $F_{out-max}=10$  N, a factor 2 applied in Z to take the instrument-mass into account makes  $F_{out-max}=20$  N,
- the resolution to measure forces is set to 60 mN,  $T_{out-min}=1.5$  Nmm for the  $\Theta$ -DoF and  $F_{out-min}=60$  mN for the Z-DoF,
- the stiffness should be sufficient to provide a 20 Hz bandwidth operation in  $\theta$  and  $z$ , target values can be found in Table 4.2.

### 4.3.2 Transmission of the $\Theta$ Z-manipulator

The  $z$ -movement of the instrument is provided by means of a friction-wheel drive. The instrument is supported and driven by two friction-wheels. The required normal force is applied by two preloaded wheels on the instrument per friction-wheel. The instrument can be removed from the  $\Theta$ Z-drive by lifting the preload wheels from the instrument (Figure 4.18). The friction-wheels are driven with a gear-set. Friction-wheels and gear-set are mounted in a drum. The Z-motor could be

mounted in the drum as well. This would increase the dimensions of the drum, which should be avoided to realize a compact construction in height. Therefore, the gear-set contains a Z-gear to allow motor-placement outside the drum, see Figure 4.19. The  $\Theta$  of the instrument is realized by rotating this drum with the connected  $\Theta$ -gear (Figure 4.19). The  $\Theta$  and Z-gear are driven with a pinion and motor-combination, mounted in the  $\Theta$ Z-housing. This constrains the maximum diameter allowed for each pinion and connected motor, and provides reduced wire-motion. In addition this realizes a separation between mechanical (drum) and electrical parts, which is advantageous for sterilization.

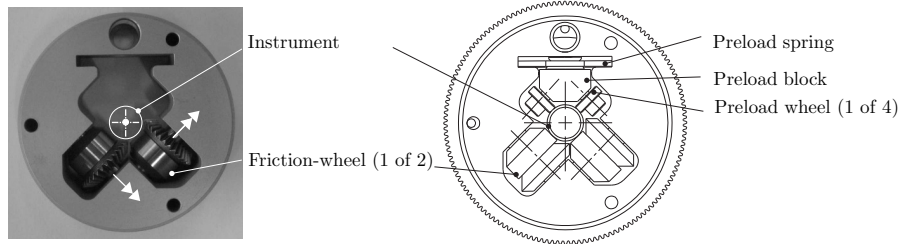


Figure 4.18:  $\Theta$ Z-manipulator: friction-wheels and preload wheels of the instrument Z-drive within the  $\Theta$ -drum.

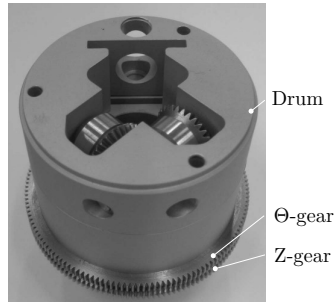


Figure 4.19:  $\Theta$ Z-manipulator: drum with gears of the  $\Theta$  and Z-drive.

### 4.3.3 $\Theta$ Z-manipulator in detail

The  $\Theta$ Z-drive and instrument release mechanism are described in detail here.

#### $\Theta$ Z-drive in detail

The  $\Theta$ Z-manipulator with friction-wheel drive makes the range of the instrument in  $\theta$  and  $z$  infinite. The  $z$ -stroke of the instrument is kept to the length of the

instrument and will be 300 mm. The  $\Theta$ -rotation can be infinite as well but is restricted to  $\pm 180^\circ$ . The required motor-torque directly depends on the friction-wheel diameter ( $D_{Wf}$ ) for Z and on the instrument-tip length for  $\Theta$  ( $L_{tip}$ ), in addition to the total transmission ratio ( $i_{tot}$ ) and efficiency ( $\eta_{tot}$ ). A high  $i_{tot}$  is desired to achieve a high stiffness, low motor-torque, a high rotational speed (high motor-efficiency) and a non-backdriveable transmission for safety. This results in a small motor which is advantageous for the total mass and dimensions of the  $\Theta$ Z-manipulator.

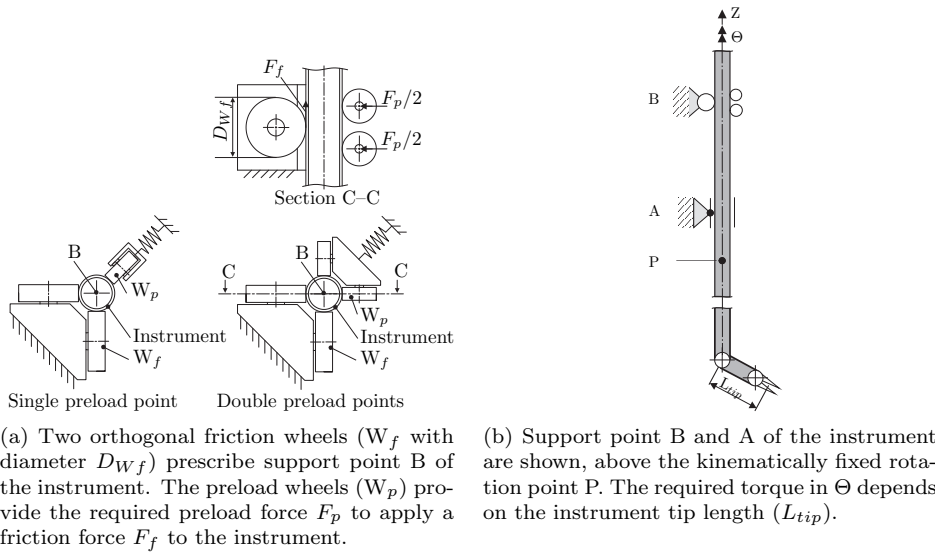


Figure 4.20: Instrument support. The friction-wheel drive for Z, provides support point B, support point A is applied below.

At the same time the required motor-torque depends on the friction force ( $F_f$ ) applied in the contact between the instrument and friction-wheel ( $W_f$ ) (Figure 4.20(a)). This friction-force can be influenced by the number of contacts ( $n$ ), the preload ( $F_p$ ) in normal direction and/or the sliding friction-coefficient ( $f_s$ ). The number of contacts between the instrument and friction-wheel drive is preferably two, provided with two orthogonal friction wheels (Figure 4.20(a)). This fixes one point on the center-line of the instrument-tube in  $x$  and  $y$ , support point B in Figure 4.20. The second support point of the instrument (A, in Figure 4.20(b)), required to prescribe the  $\Phi$  and  $\Psi$  as well, should be provided lower. The preload ( $F_p$ ) per contact is prescribed by the contact stress and allowable bearing load in the friction-wheels and preload wheels ( $W_p$ ). It can be provided in one contact point for both friction-wheels, left of Figure 4.20(a). This does increase the contact stress in the point where the preload is applied compared to the stress in the friction-wheel contacts. Therefore, each friction-wheel is provided with a preload in its plane of symmetry, right of Figure 4.20(a). This normal-force is applied with

two wheels above each other (top of Figure 4.20(a)) to reduce the space required, since the combination should fit within the drum ( $D=50$  mm). The preload wheels are preloaded with a leaf-spring (Figure 4.18). In principle this preload should prescribe only the normal-force. In this case however the leaf-spring also prescribes the tangential and  $z$ -location of the preload wheels on the instrument-tube. This keeps them in position relative to their respective friction-wheel. In addition, this tangential component increases  $T_\Theta$  that can be applied to the instrument. The orientation of the preload wheels on the instrument-tube is prescribed by the tube itself. The preload is set to 100 N per friction-wheel. Hertzian contact stress formulas do not apply, since the instrument-tube is relatively thin walled. A FEM analysis has been performed, to find an indication for the preload allowed. The wheels were modeled as cylinders (half). The instrument tube was modeled as a tube. A contact problem was defined and a preload of 100 N was applied per friction-wheel. The maximum occurring stress in the contact approximated  $430 \text{ N/mm}^2$ . This is well below the  $1500 \text{ N/mm}^2$  allowable Hertzian contact stress of steel-steel contact and therefore safe.

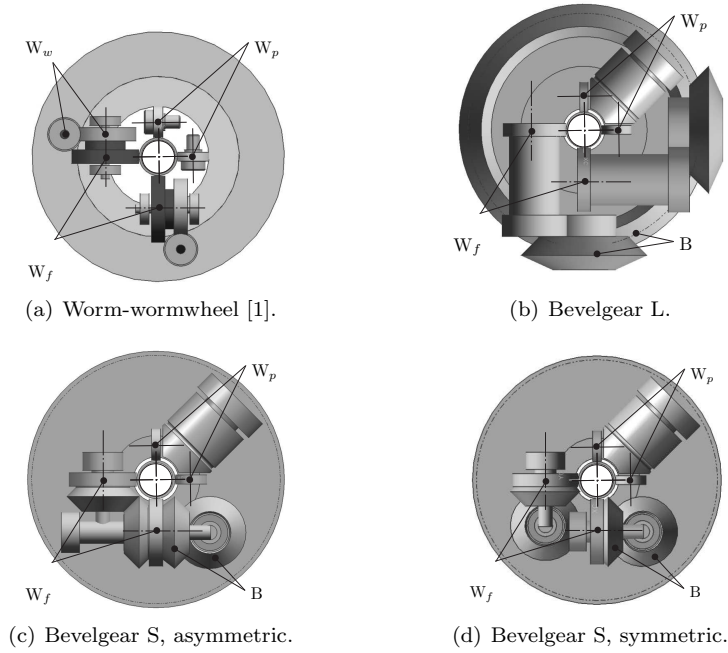


Figure 4.21: Friction-wheel drive concepts to translate the instrument in  $z$ . The friction-wheels ( $W_f$ ) are preloaded with the preloaded wheels (P) and driven with different gear-sets. In (a) a worm-wormwheel ( $W_w$ ) drive for both wheels is shown; in (b) a bevelgear (B) drive with large components protruding from the base-circle is shown; in (c) bevelgears with small components are on display, the first friction-wheel transmits the torque for the second friction-wheel; and (d) shows a symmetric bevelgear drive, each friction wheel has its own drive-train.

Figure 4.21 displays the gear-sets designed, providing for a right-angled transmission to drive the friction-wheels. Such a transmission allows orienting the motor parallel to the  $\Theta$  and  $z$ -axis. This is advantageous for the width of the  $\Theta Z$ -housing. The gear-set chosen is the symmetrical bevelgear transmission (Figure 4.21(d)). The worm-wormwheel drive (a) suffers more friction, the large bevelgear transmission (b) is less compact and more heavy. The symmetrical bevelgear transmission provides each friction-wheel with a similar force-path length and uses power-split (reduces the load on the gears) to drive the friction-wheels, compared to the asymmetric transmission (c). The out-going bevelgear of this transmission is connected to the friction-wheel (Figure 4.18). Each of the ingoing bevelgears is connected to a planet-gear (Figure 4.22).

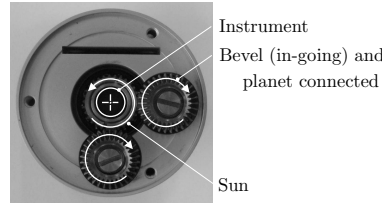


Figure 4.22:  $\Theta Z$ -manipulator: gear-set of the Z-drive, stacked below the friction-wheels and bevelgears of Figure 4.18.

The planet-gears are driven by the sun which itself is connected to the Z-gear (Figure 4.19 and 4.23). The Z-gear is driven by the Z-pinion, which is coupled to a gearbox-motor-set. A similar pinion-motor set-up is used to drive the  $\Theta$ -gear. Both gear-sets are driven with a gearbox, motor and encoder, see Appendix Table E.1 and E.2. The gear-set is assembled to minimize backlash, remaining backlash has to be measured. Preloading the gears to reduce backlash is rejected since it will double the load on the gears.

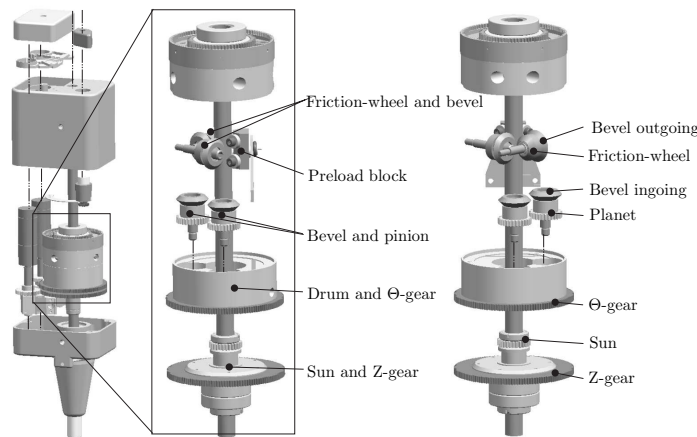


Figure 4.23:  $\Theta Z$ -manipulator: exploded-view of the  $\Theta Z$ -housing and of the drum.

### Instrument-release mechanism in detail

The instrument-tip should be free to pass the friction-wheel drive. Therefore, the pre-tension wheels are released from the instrument-tube while it is being inserted into or removed from the  $\Theta$ Z-drive. To this end the wheel-block is radially removed from the instrument-tube. This should be possible at any  $\Theta$  of the instrument, so at any  $\Theta$  of the drum and connected preload block. Radial translation of the preload block is realized with an eccentric mechanism that is driven by a gear-set. This gear-set is actuated with a handle on the  $\Theta$ Z-housing (Figure 4.25(c)), shown in detail in Figure 4.24.

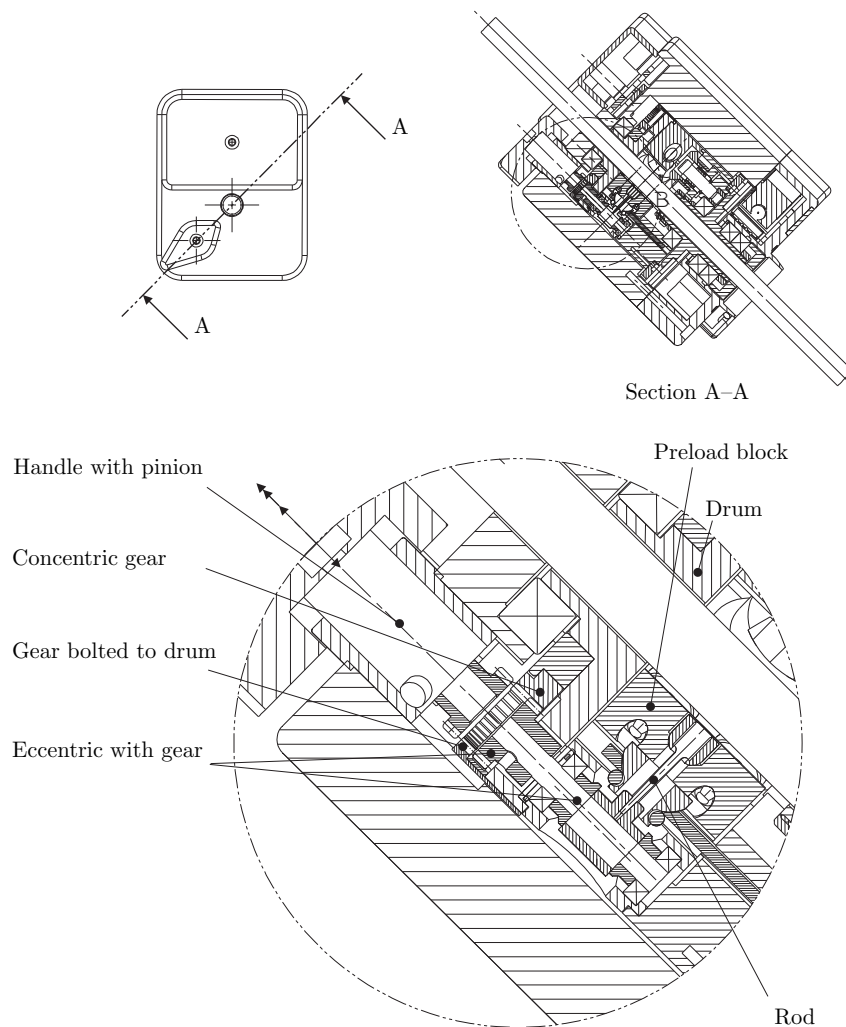


Figure 4.24:  $\Theta$ Z-manipulator instrument-release mechanism: gear-set to release the preload wheels from the instrument-tube.

Releasing the preload wheels starts with pressing the handle (see the figure above). This axially translates the handle pinion and results in meshing pinion and concentric gear. A subsequent rotation of the handle (the actuation torque is supported by the outer-gear bolted to the drum) rotates the concentric-gear and rotates the eccentric with connected gear. The rod that runs on this eccentric-axis then translates the preload-block outward. The position of the eccentric-gear depends on the  $\Theta$  of the instrument (and drum). This position never interferes with the fixed position of the button-pinion since they are located at different height levels.

#### 4.3.4 Force-measurement of the $\Theta$ Z-manipulator

The force-measurement should ideally be performed as close to the instrument as possible for accuracy, since this reduces e.g. the influence of friction. To realize a sensor that is mounted in the  $\Theta$ Z-housing, the first location possible is just outside the drum on each pinion. The pinion is directly coupled to the outgoing axis of each gearbox-motor-set. The tangential-force executed by the pinion is measured since this can be performed more easily than torque-measurement. To this end the pinion is supported in radial,  $z$  and  $\phi$  and  $\psi$ -direction by means of two leaf-springs. The force-measurement can then be performed either by executing the leaf-springs very stiff and measuring displacement, or by executing the leaf-springs less stiff and measuring the force with a force sensor. The latter construction is chosen because of the force sensor dimensions, see Figure 4.25(b). The motor-torque is not supported by the leaf-springs. The motor-torque support is given in Figure 4.25(c), it allows for motor-translation in its plane but prevents its out of plane rotation.

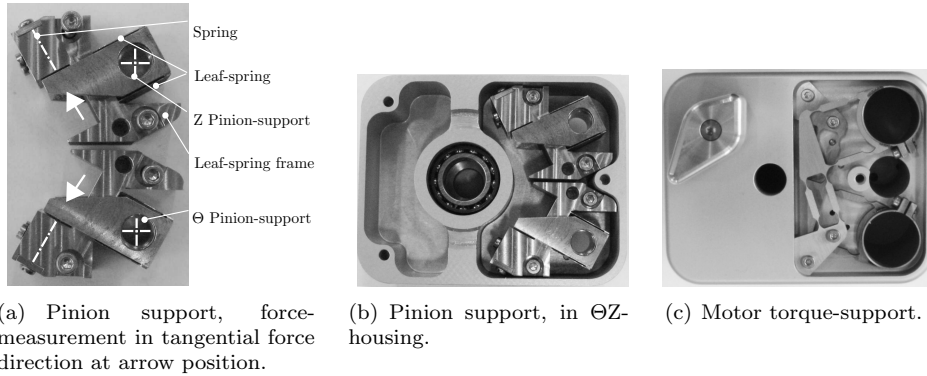


Figure 4.25:  $\Theta$ Z force measurement and motor support.

### Force-measurement construction details

The chosen force sensor is one directional and is pre-stressed with a spring to allow to measure forces in both directions. The support of the force sensor in the leaf-spring guidance of the pinion should be shimmed. The sensor should just contact the leaf-spring support before the preload is applied. This reduces the influence of the leaf-springs on the force-measurement. The signal of the force sensor is filtered and amplified to make it less susceptible to disturbances. This is done with the circuit in Appendix Figure E.1. Hardware is displayed in Appendix Table E.3, further information on the  $\Theta$ Z force sensors set-up is shown in Appendix Table E.6.

#### 4.3.5 Wiring of the $\Theta$ Z-manipulator

The wires of the force sensor electronics run through in between the motors in the  $\Theta$ Z-housing (Appendix Figure E.2). Underneath the cover, the wires from motor, encoder and force sensor electronics are connected to the flat-cable that runs from the  $\Theta$ Z-housing to the connector-block at the back of the parallelogram frame. This flat-cable is oriented with its cross-section parallel to the  $\Psi$ -axis, to limit disturbance forces on the  $\Psi$ -force measurement. The flat-cable is cast in a connector which is connected to the cover to relieve the cable-connections from changing load. This cover is as high as the height of the release-button to prevent loss of the instrument  $z$ -stroke.

#### 4.3.6 Evaluation of the $\Theta$ Z-drive

The  $\Theta$ Z test set-up in Figure 4.26 on the next page, is used to find an indication for the appropriate friction-wheel diameter by measuring the deformation of the instrument-tube (this directly influences the required torque and motor), the obtained sliding friction coefficient ( $f_s$ ), and the obtained roll friction coefficient ( $f_{roll}$ ). The set-up consists of the outer tube of the instrument, supported by four preload wheels on a preload wheel block, a friction-wheel block with two friction-wheels (can be exchanged for a block with different diameter wheels) connected with a cover to the guidance of the friction-wheels and a preload ( $F_{pb}$ ). The friction-wheel block is allowed to translate in  $x$ -direction, to find its position prescribed by the instrument and align with its cover. To this end the cover is supported by two guidance-balls. The center-line through the two guidance-balls and the center-line of the instrument lie in the same horizontal plane. As does the point in which the normals at the contact points of the friction-wheels on the instrument intersect. Measuring the diameter of the instrument-tube after applying and removing a preload of 1 and 10 kg at several positions on one tube circumference, did not show plastic deformation larger than 0.01 mm for any of the friction wheel diameters applied (12, 13 and 14 mm). A sliding calliper was

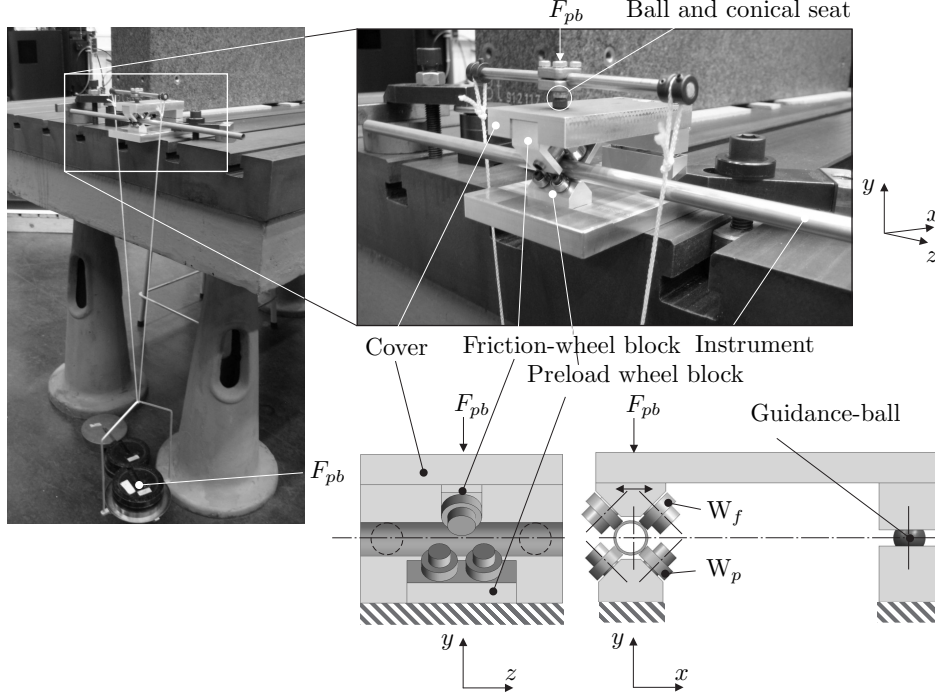


Figure 4.26:  $\Theta Z$  test set-up. The instrument-tube is supported by its preload wheels ( $W_p$ ) connected to their preload wheel block. The position of the friction-wheels ( $W_f$ ) and their friction-wheel block is defined by the center-line of the instrument-tube and by the cover and two guidance-balls. The preload ( $F_{pb}$ ) is applied by means of a yoke supported on a ball in a conical seat on the cover.

used to measure this diameter. This implies that the smallest friction wheel diameter used in the test can be applied in the  $\Theta Z$ -manipulator. A smaller diameter results in a reduced output torque and motors to provide the Z-DoF, compared to friction wheels with a larger diameter.

Figure 4.27 displays the sliding friction coefficient data ( $f_s$ ), indicating how well the wheel-combination transmits torque in  $\Theta$  to the instrument. The data is obtained by applying torque with a torque watch gauge on an adaptor at the end of the instrument-tube. This torque watch gauge is supported (on the rotating part to eliminate a support friction component in the measurement) as to keep the instrument aligned with its center-line. The torque indicated by the torque watch gauge when slip occurs is stored. Again the test is repeated at different positions on the tube. A linear fit on the data gives a friction coefficient of  $f_s=0.1$ . This friction coefficient results in a maximum torque transmitted in  $\theta$  of 125 Nmm with a preload  $F_{pb}=100$  N applied. This preload will be increased up to 141 N for the manipulator itself, resulting in  $T_{max}=170$  Nmm. Increasing the friction coefficient a factor 2, increases the maximum torque a factor 2 as well, which passes the set requirement.

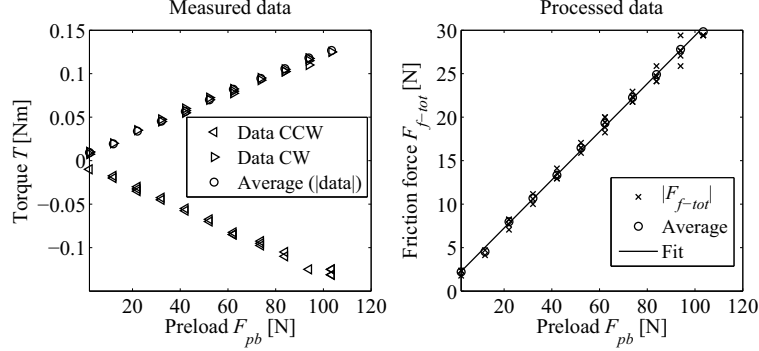


Figure 4.27:  $\Theta Z$  test set-up measurements to obtain  $f_s$ . A torque  $T$  is applied at the end of the instrument-tube in (C)CW (counter)clockwise direction. The torque applied when the instrument moves is stored, it is a function of preload  $F_{pb}$  and  $f_s$ . With  $f_s=0.1$  resulting from the fit  $F_{f-tot}=C_1+2.8f_sF_{pb}$  and  $C_1=1.7$ .

Figure 4.28 shows the roll friction coefficient data ( $f_{roll}$ ), obtained by applying an axial force at the height of the center-line of the instrument with a force watch gauge. An end-stop limits the speed of the instrument, since the force watch gauge should be released slowly. The force indicated by the force watch gauge when the instrument starts rolling is stored. The test is repeated with different preload levels and at different positions on the tube. A fit on the data gives  $f_{roll}=1.8 \cdot 10^{-3}$ . This  $f_{roll}$  results in a roll friction force of 0.72 N in z-direction (the 60 mN resolution can not be met), introduced by one support point of the instrument. It implies that the instrument should be provided with a rolling second support point as well. Additional tests need to be performed with the trocar provided with a seal.

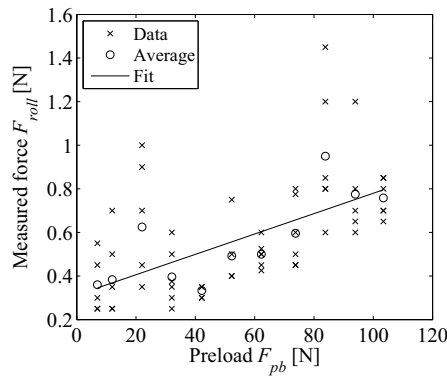


Figure 4.28:  $\Theta Z$  test set-up measurements to obtain  $f_{roll}$ . An axial force is applied at the instrument-tube at the height of its center-line. The force applied when the instrument starts rolling ( $F_{roll}$ ) is stored, it is a function of the preload  $F_{pb}$  and  $f_{roll}=1.8 \cdot 10^{-3}$ , resulting from the fit for  $F_{roll} = C_2 + 2.8f_{roll}F_{pb}$  ( $C_2=0.31$ ).

### 4.3.7 Evaluation of the $\Theta Z$ force sensors

The forces in  $\theta$  and  $z$ -direction are both measured with a Honeywell FSG15N1A force sensor. This subsection presents the evaluation of these force sensors. First a single sensor is tested to see if it fulfills the requirements and to find a relation between input and output. Then the accuracy of the sensors is tested while being integrated in  $\Theta Z$ -manipulator.

#### Evaluation of a single $\Theta Z$ force sensor

A single force sensor is calibrated, using the interface circuit in Appendix Figure E.1. A temperature sensor is integrated to compensate for temperature dependence of the force sensor. The required range for the  $\Theta$  force sensor is  $\pm 8.8$  N, this is  $\pm 4.6$  N for the  $Z$  force sensor. One sensor has been evaluated in the set-up in Figure 4.29, using its entire range.

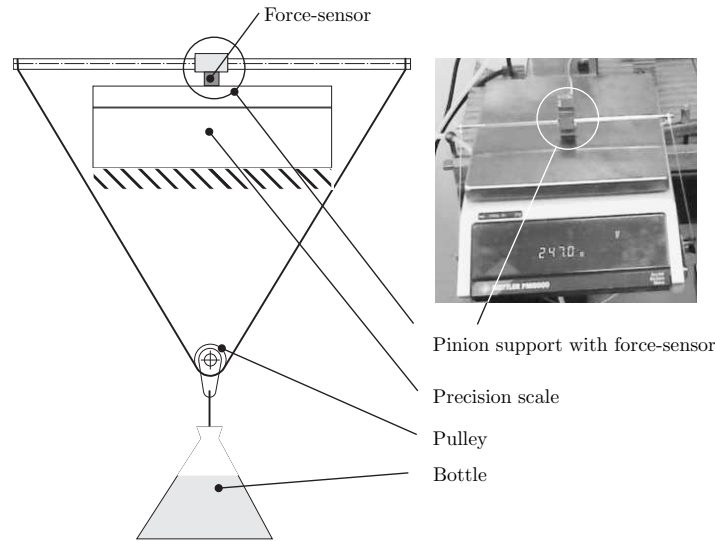
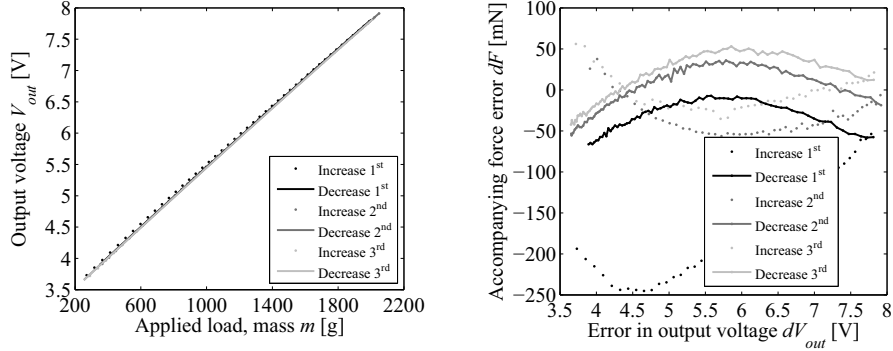


Figure 4.29:  $\Theta Z$  sensor test set-up. The sensor is mounted in its pinion support of the  $\Theta Z$ -manipulator (see Figure 4.25), without play in neutral position. This support is put on a precision scale to measure the applied load. It supports a rod that protrudes at two sides from the scale. Both rod-ends are provided with the ends of a string. This string supports a pulley (with bearing) from which a string with bottle is suspended. It allows the bottle to easily align and reduce parasitic loads on the sensor guidance. The bottle is slowly loaded and unloaded with water.



(a) Sensor output voltage  $V_{out}$  obtained by gradually adding water (mass  $m$ ) to and removing it from the bottle for three times.

(b) Error in output voltage  $dV_{out}$  between the measured data and a double averaged quadratic fit. All error data is within about 60 mN, except for the first increase curve.

Figure 4.30: Results from measurements on the  $\Theta$ Z Honeywell FSG15N1A force sensor.

The sensor is loaded and unloaded slowly by means of communicating vessels (one vessel being a bottle hanging below the sensor), the load applied is measured with the scale on which the sensor is put. The results are shown in Figure 4.30. The error between the data and the found polynomial (Appendix E.2.4) in Figure 4.30(b) shows that the sensor can be brought within its desired accuracy of 90 mN for  $\Theta$  and 60 mN for Z. It is assumed that behavior shown in the figures is similar for all sensors and that it will be constant in time. The sensor in its mechanical interface is temperature dependent. A change in output voltage of 20–40 mV is observed when heated from 35–40°C. The temperature sensor incorporated in the electronics circuit compensates for these temperature effects.

### Evaluation of the $\Theta$ Z force sensors in the manipulator

Evaluation of the  $\Theta$  and Z force sensors integrated in the  $\Theta$ Z-manipulator has been performed. A frame is connected to the platform. This frame supports the digital force gauge sensor, which applies a torque or force (respectively for  $\Theta$  and Z) to the instrument-tip. Again, a preload is used to constantly increase (and decrease) the load applied through the entire range. Unfortunately, the output of the Z force sensor is almost constant throughout its entire range. This gives the assumption that its pinion and pinion support are somehow obstructed in compressing it. Figure 4.31 shows measurements on the  $\Theta$  force sensor, with the results displayed as torque in  $\Theta$  on the instrument. The measured torque is not equal to the applied torque. There is quite a large uncertainty. The cover of the  $\Theta$ Z wires is thought to be the cause. It prevents the wires from moving freely and consequently might block the motor and connected pinion and introduce friction. Further research is required to correct this.

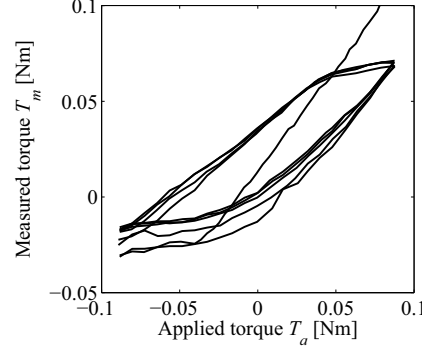


Figure 4.31: Results from evaluation of the  $\Theta$  force sensor being integrated in its manipulator. The torque applied at the instrument and force measured at the  $\Theta$  force sensor are displayed as torque on the instrument.

## 4.4 Manipulator evaluation

This section presents the modal and identification measurements performed on the manipulator with its  $\Phi$ ,  $\Psi$ ,  $\Theta$  and Z-DoFs. The modal measurements display the first natural frequencies and accompanying eigenmodes of the manipulator. These modes indicate points to improve the design if the obtained frequencies are not sufficient. The identification measurements display the dynamic behavior of the manipulator, indicating e.g. stiffness and friction.

### 4.4.1 Modal measurements of the manipulator

Modal measurements [2] have been performed on the Slave. During these measurements the Slave consists of its platform-adjustment, one manipulator-adjustment and one manipulator. These measurements provide insight in the dynamic behavior of the Slave. the Slave pose in Figure 4.32, is expected to be used frequently in the operating room and the basis for the modal measurements. A Kistler tri-axial acceleration sensor is placed at (38) predefined measurement points on the Slave. The sensor measures the response resulting from hammer impacts (hammer with impact sensor) applied at one point on the manipulator. Hammer impacts are applied in three directions at this point. Logging the data (sensor and hammer) starting at a trigger signal from the hammer, provides response phase information throughout the Slave. Figure 4.33 and Appendix Figures E.4 and E.5 present the first three eigen-modes at respectively 19, 25 and 31 Hz. This first natural frequency is caused by the rotational inertia of the manipulator in combination with the torsional stiffness of the harmonic drive. The second frequency shows a rotation  $\Psi$ , which is expected to be caused by the axial stiffness of the bearings supporting the worm. These values closely approximate the requirements set in



Figure 4.32: Pose of the Slave and its dummy instrument, used for modal measurements. This pose is expected to be used frequently during surgery. The 3D-acceleration sensor is put at several locations on the platform, manipulator-adjustment and manipulator.

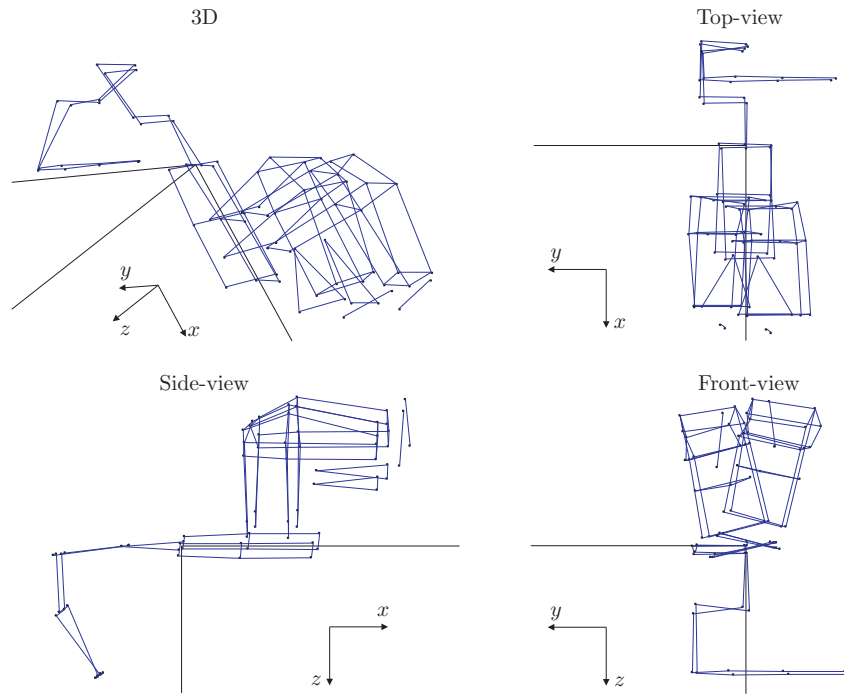
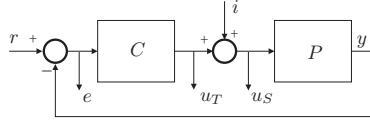


Figure 4.33: A rotation of the manipulator around the  $x$ -axis ( $\Phi$ -DoF) best seen in the front-view, is the first eigenmode occurring at 19 Hz.

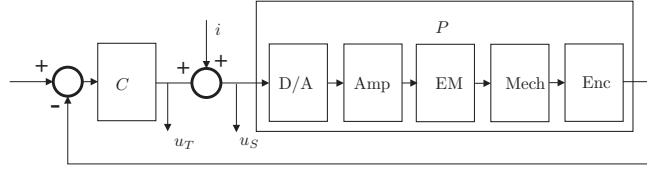
Chapter 2, which is sufficient to perform force-measurements. These frequencies are more fine regarding the position control of the manipulator. A surgeon performs accurate movements up to a frequency of 2 Hz.

#### 4.4.2 Identification of the $\Phi$ and $\Psi$ -DoFs

The manipulator has been evaluated as well by performing identification measurements [76], with the Slave pose similar to the one used for the modal analysis. To this end, closed-loop frequency response functions (FRF, sensitivity and complementary sensitivity measurements) have been performed, with a sample frequency of 4 kHz.



(a) Block-scheme for the single input single output (SISO) measurements, with  $C$  the controller,  $P$  the process,  $e$  is the error between reference signal  $r$  and output signal  $y$ ,  $i$  is the input signal,  $u_{S,T}$  is the output signal used to calculate respectively the sensitivity and complementary sensitivity.



(b) Block-scheme in more detail. The process consists the D/A converter, an amplifier and filter (Amp), the motor (EM), the mechanics of the manipulator (Mech) and the encoder (Enc).

Figure 4.34: The  $\Phi$  and the  $\Psi$ -DoF SISO measurements. Here,  $C$  is the control,  $P$  is the process or the appropriate  $\Phi$  and  $\Psi$ -DoFs (including their data-acquisition and processing time).

Figure 4.34 shows the blockscheme used for the single input single output (SISO) measurements of the  $\Phi$  and  $\Psi$ -DoFs. The actuation signal ( $i$ , in Volts) and the measurement signals ( $u_T$  and  $u_S$ , in Volts) are applied at and obtained near the summation point shown in Figure 4.34(b). The actuation signal consists of a multisine. In order to cancel effects of friction on the measurements, a low frequent jogging signal is added. The measurements provide the complementary sensitivity FRF as follows:

$$T(j\omega) = \frac{u_T(j\omega)}{i(j\omega)} = \frac{P(j\omega)C(j\omega)}{1 + P(j\omega)C(j\omega)} \quad (4.1)$$

Equation 4.2 shows the sensitivity FRF provided by the measurements:

$$S(j\omega) = \frac{u_S(j\omega)}{i(j\omega)} = \frac{1}{1 + P(j\omega)C(j\omega)} \quad (4.2)$$

Dividing the complementary sensitivity with the sensitivity results in the open-loop system. The applied control is divided out and time delay caused by zero order hold, the amplifier filter and computer calculation time are corrected for.

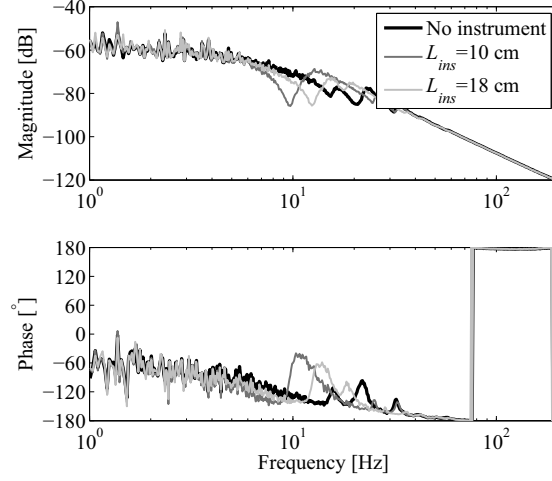


Figure 4.35: Bode-plot of the  $\Phi$ -DoF measured at an initial orientation  $\Phi_0=0^\circ$ . The Bode-plot (averaged data) is shown without an instrument to display the behavior of the manipulator itself and with a dummy-instrument inserted at  $L_{ins}=10$  and  $18$  cm. The dummy instrument increases inertia, indicated with the (anti)resonance peaks occurring at lower frequencies.

This results in the transfer function of the appropriate axis of the manipulator. Figure 4.35 displays the Bode-plot of the  $\Phi$ -DoF. This  $\Phi$ -DoF is initially identified in neutral orientation  $\Phi_0=0^\circ$  without an instrument and with instrument-dummy. The instrument dummy is inserted 10 and 18 cm relative to the kinematically fixed rotation point P (Figure 4.1). The magnitude plot seems to start at a slope -1 heading for -2 before the first anti-resonance (17.6 Hz). A slope of -1 indicates damping, which might be caused by (viscous) friction. Successively an anti-resonance (17.6 Hz) and resonance (19.4 Hz) indicate decoupling of mass. The magnitude curve is higher after the resonance than before: similar input results in an increased output (less mass to actuate). The first resonance shown in the modal analysis is equal and gives the physical explanation. An anti-resonance and resonance combination can be seen at 31 Hz, also found in the modal analysis. The phase is around  $-180^\circ$  indicating the system can be modeled as a mass here. The effect of adding an instrument to the manipulator and inserting it 10 or 18 cm (expected to be most frequently used) relative to point P, shows a shift in the position of the anti-resonance and resonance. The overall behavior is similar. Appendix Figure E.6 displays the open-loop resulting from a measurement performed up to 2 kHz. The coherence in the lower figures shows a dip at the first natural frequency at approximately 19 Hz and at 1735 Hz. This indicates the occurrence of a resonance. As expected, the behavior of the  $\Phi$ -DoF (process) is independent of its initial orientation ( $\Phi_0$ ), see Appendix Figure E.7. This figure also shows its resonance at 1735 Hz and an accompanying  $-180^\circ$  phase shift, typically seen because of decoupling of encoder shafts.

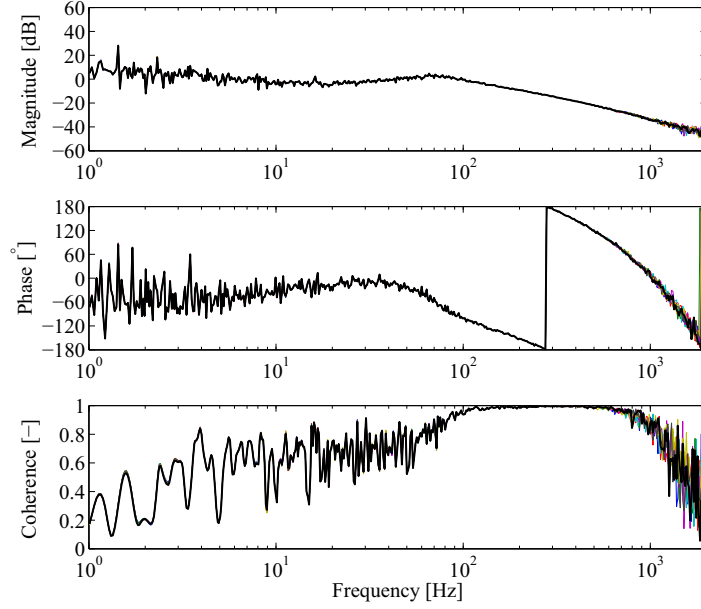


Figure 4.36: Open-loop measurement results (8 measurements) of identification of the  $\Psi$ -DoF, starting at an initial orientation of  $\Psi_0=0^\circ$ .

Figure 4.36, displays the measurement results on the  $\Psi$ -DoF of the manipulator with its worm-wheel drive. It shows a low coherence for low frequencies, which is the intended motion range of the manipulator. This is a relatively poor signal to noise ratio. It indicates either additional noise put into the process or (partly) non-linear behavior of the process. Non-linear behavior is caused by e.g. friction, large friction in this case. A relatively poor signal to noise ratio caused by friction, makes this worm-wheel drive less suitable for this application, since it requires good accuracy and low friction. The ball-screw drive is expected to solve this problem, since rolling friction applies here. As far as a low coherence allows explaining the process shown in Figure 4.37, some observations are presented (here, for the manipulator without an instrument). For low frequencies the slope of the magnitude plot seems to be -1, indicating damping. This damping might be caused by viscous friction. However, the low coherence suggests the presence of less predictable Coulomb friction as well. At approximately 25 Hz a change in slope from -1 to -2 occurs, indicating the presence of a pole. The frequency of 25 Hz shown in the modal analysis would occur as a pole pair. The relatively slow change of slope indicates damping, again.

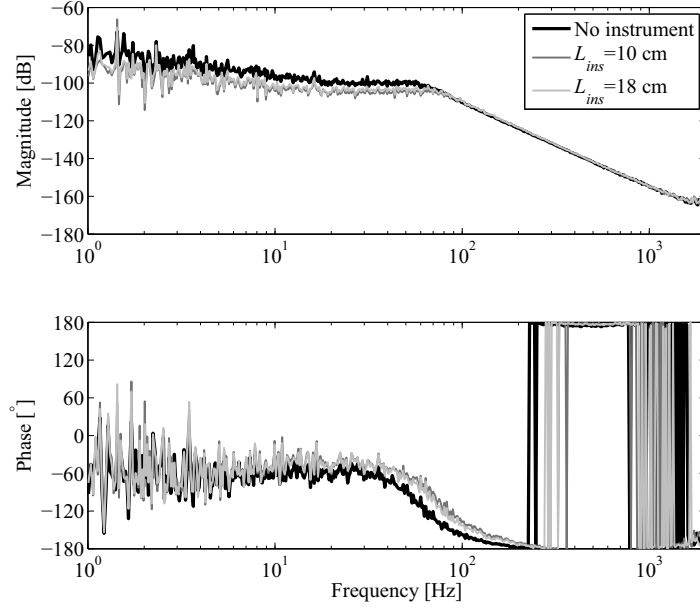


Figure 4.37: Bode-plot of the  $\Psi$ -DoF starting at an initial orientation of  $\Psi_0=0^\circ$ . The Bode-plot is shown without and with a dummy instrument inserted respectively  $L_{ins}=10$  and 18 cm.

#### 4.4.3 Identification of the $\Theta$ and Z-DoFs

Identification of the  $\Theta$  and Z-DoFs is performed in a multiple input multiple output (MIMO) manner, since the DoFs are coupled. Figure 4.38 shows the blockscheme applied. Appendix Figure E.9 shows the measurement results, including the resulting coherence. The coherence at low frequencies is acceptable. This means that the processes shown in Figure 4.39 and 4.40 are reliable. Both DoFs show signs of damping at the low frequency range (a -1 slope), whereas a -2 slope is shown for the high frequency range. The presence of a pole at approximately 30 Hz for Z and an anti-resonance and resonance at respectively 45 Hz and 64 Hz for  $\Theta$ , mark the breakpoints of these curves. The damping in both DoFs is probably caused by the friction in the gear transmission and in the motor transmission.

Cross coupling is present if the Z-DoF is driven, this can be seen in Appendix Figure E.10. The torque applied at the Z-gear to drive the friction wheels, has to be supported by the  $\Theta$  drum, which causes cross-coupling.

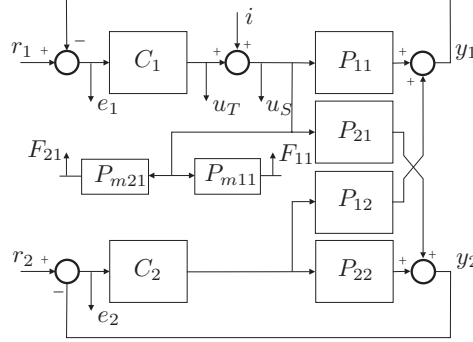


Figure 4.38: The  $\Theta$  and Z-DoFs are identified simultaneously in a multiple input multiple output manner. Here,  $C_{1,2}$  is the control,  $P_{11}$  and  $P_{22}$  are the appropriate  $\Theta$  and Z-DoFs and  $P_{12}$  and  $P_{21}$  the cross-terms (including the data-acquisition and processing time),  $e$  is the error between reference signal  $r_{1,2}$  and output signal  $y_{1,2}$ ,  $i$  is the input signal,  $u_{S,T}$  is the output signal used to calculate respectively the sensitivity and complementary sensitivity.  $F_{11,21}$  displays the force sensor output, while  $P_{m11,m21}$  displays the force sensor process.

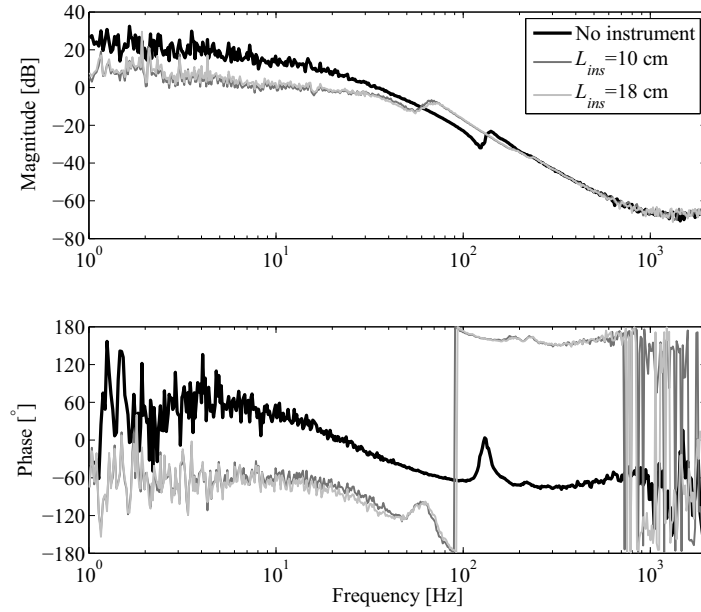


Figure 4.39: Process of the  $\Theta$ -Dof of the manipulator.

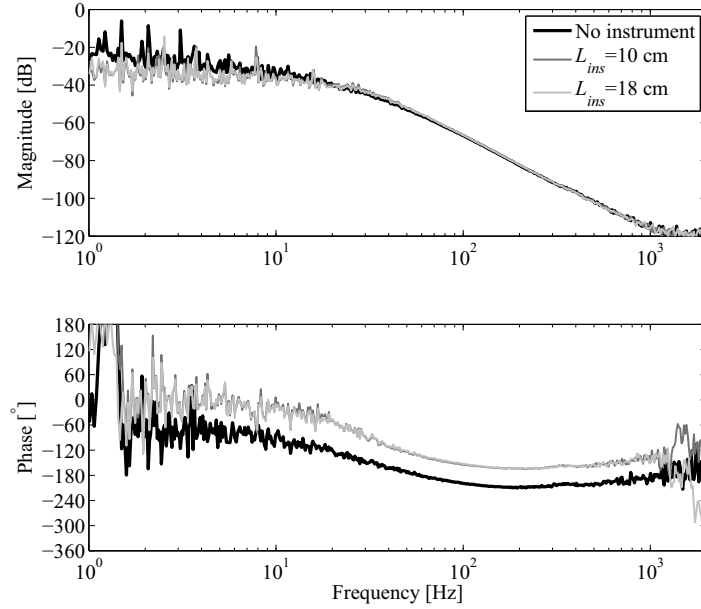


Figure 4.40: Process of the Z-DoF of the manipulator.

## 4.5 Conclusion and recommendations

### 4.5.1 Conclusion

The manipulator actuates the instrument and endoscope in  $\phi$ ,  $\psi$ ,  $\theta$  and  $z$  during surgery, relative to the incision in which it is initially positioned. It consists of a  $\Phi\Psi$ -manipulator with a parallelogram-mechanism and a compact  $\Theta Z$ -manipulator with a friction-wheel drive for  $z$ . The  $\Phi$  and  $\Psi$  are either non-backdriveable or provided with a brake. Force sensors measuring forces executed with the instrument, are integrated in the manipulator, to avoid all chance of electrical signals being introduced into the patient.

The  $\Psi$  parallelogram mechanism provides a kinematically fixed point of rotation located stationary within the incision during surgery. This avoids all lateral force loading of the tissue surrounding the incision and thereby reduces post-operative pain. This kinematic rotation pole at that location excludes the necessity of an actual hinge in the incision. The manipulator with a width of 80 mm, allows for easy access to and overview of the port-sites. It has a small motion-envelope and least obstructs the assistants at the table, while moving the instrument or endoscope.

Two  $\Phi\Psi$ -manipulators have been designed. The worm-wormwheel layout was

designed and realized prior to the design of the ball-screw layout. The name indicates the  $\Psi$ -drive, the  $\Phi$ -drive of both manipulators is similar. Modal measurements on the worm-wormwheel manipulator (without instrument applied), show a first natural frequency of 19 Hz in  $\Phi$ . This frequency is determined by the rotational stiffness of the  $\Phi$  harmonic drive and the rotational inertia of the manipulator. Identification of this axis revealed this frequency as well. The first natural frequency of the instrument overrules this first natural frequency and determines the dynamic behavior of the manipulator. The modal analysis indicated a frequency of 25 Hz in  $\Psi$ . Identification of the  $\Psi$  showed a limited coherence for low frequencies caused by friction, which indicates it is not reliable to control in this range. The ball-screw drive reduces friction and improves stiffness. It is expected to perform better. In addition, the manipulator dimensions near the patient are reduced even more.

The  $\Theta Z$ -manipulator (60 mm width), supports the instrument. It provides the instruments with a  $\theta$  and  $z$  movement, respectively by means of a rotating drum for  $\theta$  and friction wheels there in for  $z$ . The instrument is removed from the  $\Theta Z$ -manipulator with one action. The drum of the  $\Theta Z$ -manipulator will eventually be removable to sterilize this part of the manipulator. The electronical parts of the  $\Theta Z$ -manipulator are integrated with the  $\Theta Z$ -housing and will not be sterilized. Wire movements are limited as much as possible to realize a robust system.

Forces executed with the instrument in  $\phi, \psi, \theta$  and  $z$  are measured in the manipulator as close to the trocar as possible. The  $\Phi$  and  $\Psi$  forces are corrected for the manipulator mass, its inertia and temperature influences. These force sensors display almost linear behavior. Integrated in the manipulator they do suffer from some hysteresis which might be caused by moving wires. The  $\Theta$  and  $Z$  force sensors do not show the expected linear behavior and further research is needed here. The performance of the manipulator is summarized in Table 4.5. It fulfills the requirements set, except the accuracy of the force-sensors integrated in the manipulator requiring further research.

### 4.5.2 Recommendations

The ball-screw layout of the  $\Phi\Psi$ -manipulator is being realized and can be evaluated in the near future. A second design of the  $\Theta Z$ -manipulator should provide separate instrument support and  $\Theta$  and  $Z$  drive, making the drive independent of the reaction forces of the instrument. The instrument support provided in the trocar should contain rolling parts to reduce the friction in the driving direction and improve the force-measurements. At the same time the height of the manipulator can be reduced, e.g. by applying extra-thin-section deep groove ball bearings for the drum-support. This reduces the weight and rotational inertia of the manipulator, the required length of the instrument, and improves the dynamic behavior. The wiring of the  $\Theta Z$ -motors should be improved to reduce hysteresis and disturbance forces on its force sensors.

Table 4.5: Performance of the different DoFs of the worm-wormwheel manipulator, based on the design and specifications of the components applied. With the manipulator range, encoder resolution (res.), angular velocity ( $\omega$ ) and torques the instrument can apply ( $T_{tip-max}$ ). The first natural frequency ( $f_0$ ) obtained from identification measurements on the DoFs, are displayed for the neutral position with  $L_{ins}=18$  cm. The force sensors required range ( $T_{max}$ ) and resolution ( $T_{min}$ ) are displayed, with the accuracy  $dT$  obtained from the measurements performed. This accuracy is expected to display friction present in the measurement set-up as well, which requires further investigation. All manipulator and force measurement values are given with respect to the kinematic rotation pole P.

DoF	Manipulator					Force sensors		
	Range [°]	Res. [°]	$\omega$ [rad/s]	$f_0$ [Hz]	$T_{tip-max}$ [Nmm]	$T_{max}$ [Nmm]	$T_{min}$ [Nmm]	$dT$ [Nmm]
$\Phi$	$\pm 35$	$1.8 \cdot 10^{-3}$	0.5	19	$3 \cdot 10^3$	$9 \cdot 10^3$	18	400
$\Psi$	$\pm 90$	$7 \cdot 10^{-4}$	0.5	25	$3 \cdot 10^3$	$9 \cdot 10^3$	18	400
$\Theta$	$\pm 180$	$16 \cdot 10^{-3}$	4	64	170	250	1.5	50
	Range [mm]	Res. [mm]	$v$ [mm/s]	$f_0$ [Hz]	$F_{tip-max}$ [N]	$F_{max}$ [N]	$F_{min}$ [N]	$dF$ [N]
	300	$1.9 \cdot 10^{-3}$	60	-	20	20	$60 \cdot 10^{-3}$	-



## Chapter 5

# Instrument

The instrument of the Slave is manipulated with the manipulator and can be exchanged during surgery. It consists of a four-DoF tip (including a gripper), connected with a long and slender instrument-tube to a drive-box, see Figure 5.1.

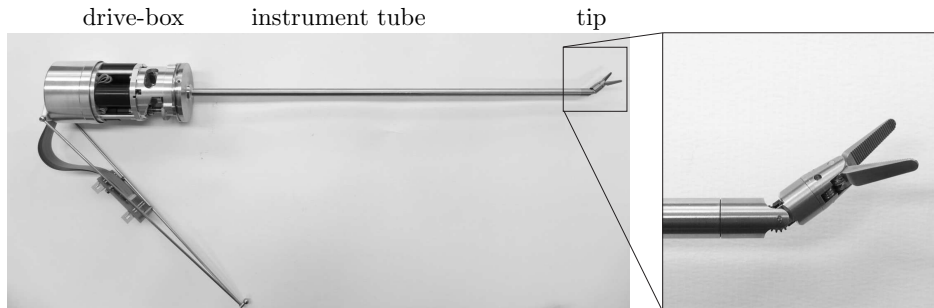


Figure 5.1: The instrument (as realized) consists of a drive-box, connected with a long and slender tube to its four-DoF tip: pitch, roll, pivot and close to move its gripper.

These pitch, roll, pivot and close-DoFs at the end of the instrument-tube, allow surgeons to work at the backside of an organ, approach organs from more than one angle (conventional MIS) and perform complex movements like stitching. The transmission of this tip runs through the instrument-tube and is driven in the drive-box. The drive-box holds four motors, one for each DoF. Force sensors are designed to measure forces executed with and on the instrument-tip as close to the tip as possible. This chapter discusses the requirements of the instrument; options for the layout of the tip DoFs and concepts on the transmission. The design of the concept chosen is treated in detail. The DoFs with a similar transmission (pitch-roll and pivot-close) are discussed in pairs, finishing with a conclusion.

## 5.1 Instrument requirements and concepts

The requirements are separated in design and performance requirements. The design requirements form the basis for the layout of the four DoFs and associated transmissions. The performance requirements are initially specified as a function of the task performed. Then the performance requirements are converted into specifications per DoF, based on the layout chosen.

### 5.1.1 Requirements of the instrument

Design requirements of the instrument:

1. the number of DoFs is four so the surgeon can work around an organ and have dexterity while suturing,
  - the first DoF should be transverse to the instrument-tube to move away from the relatively inflexible instrument-tube - DoF 1,
  - the remaining three DoFs should contain:
    - a roll for ease of needle manipulation (Figure 5.2) and an additional transverse axis for approach flexibility, variations on the order of these two DoFs are shown in the layout overview, and
    - a closing and opening movement of the gripper to actually hold the needle - DoF 4.
2. the DoFs in the tip should be backdriveable to be able to remove the instrument from the trocar in case of an emergency,
3. the  $z$ -stroke of the instrument is 300 mm (Section 4.1.1), an indication for the length of the instrument,
4. the forces should be measured in all DoFs,
5. the instrument transmission should be stiff for accuracy and force measurements performance,
6. the diameter of the instrument-tube is 8.5 mm, which is in line with common practice in laparoscopy and intra rib, offering enough freedom to keep the incision length limited (13.3 mm). A smaller diameter size can be developed later for special applications ( $D_o=6$  or  $D_o=5$  mm),
7. the drive-box diameter should be maximally 60 mm to fit between the fork of manipulator arm H2 and small for a reduced motion envelope in the presence of the assistants,
8. the instrument is intended for multiple use based on the anticipated accuracy requirements and accompanying manufacturing effort. Therefore, it needs to be sterilizable (eventually),
9. the outside surface should be smooth to reduce the risk of sutures that might get stuck, and
10. the instrument should be rapidly exchangeable during surgery.

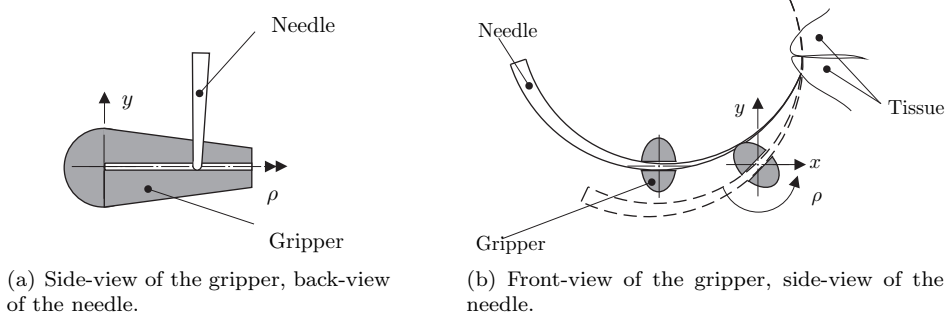


Figure 5.2: Stitching. Left: the curved needle is ideally grasped in its middle, with the gripper perpendicular to the plane of the needle. Right: stitching is realized while rolling ( $\rho$ ) the gripper and needle through the tissue and translating it slightly in  $x$  and  $y$ . With [—] indicating the initial position of the needle and [---] a subsequent position.

The performance requirements are set per task, except for the range of motion and positioning resolution:

- the range of motion is set to:  $\pm 70^\circ$  for the first transverse axis,  $\pm 90^\circ$  for the second transverse axis and roll and  $45^\circ$  to open and close the gripper jaws ( $90^\circ$  in total), with the angles given relative to their neutral orientation (instrument-tip aligned with its instrument-tube and closed gripper),
- the resolution for positioning the gripper is set to  $50 \mu\text{m}$ ,
- the maximum angular velocity  $\omega$  depends on the task at hand, see Table 5.1,
- the applied and measured force ( $F$ ) depends on the task as well (Table 5.1),
- the length between the first transverse axis and the gripper-axis ( $L_A$ ) is set to 15 mm. The length of the gripper ( $L_G$ ) is set to 10 mm. This (in combination with the task related forces from Chapter 2) leads to the torques ( $T$ ) that have to be transmitted, see Table 5.1, and
- the drive-box should be light (approximately 500 g) to provide a first natural frequency above 20 Hz when the instrument is inserted 18 cm. .

Table 5.1: The performance requirements of the instrument-tip are defined per task here, as angular velocity ( $\omega$ ) and force ( $F$ ) from Section 2.1.

Task	$\omega$ [rad/s]	$F$ [N]
Nominal needle driving, cutting	6.5	2.5
Suture tying	0.5	5.0
Max suture tying	0.5	10
Fine manipulation	0.5	0.06
Nominal gripper	0.5	10
Max gripper	0.5	20

### 5.1.2 Instrument concepts

The instrument consists of a tip with four DoFs, a connecting tube ( $D_o=8.5$  mm) for translation in and out of the patient, a multi-DoF transmission running through with a typical long center distance and a drive-box.

#### Tip layout concepts

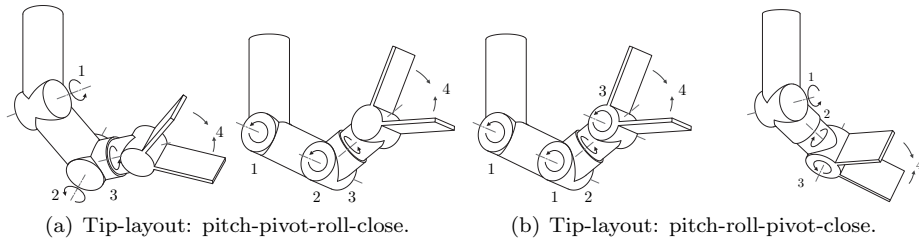


Figure 5.3: Layouts of the four DoFs (1, 2, 3, 4) of the instrument-tip, based on freedom to approach the organ and to stitch (pictures from [36]).

These four DoFs of the instrument-tip can be composed as on display in Figure 5.3. These instrument-tip DoFs are stacked. Options that include multiple hinges per DoF are not taken into account whenever possible, it reduces the experienced stiffness. For layout Figure 5.3(a) the second transverse axis (DoF 2) is placed before the roll (DoF 3), for layout Figure 5.3(b) this order is switched. The resulting target organ approach possibilities with the four DoFs from Figure 5.3 are shown in Figure 5.4 on the next page. The instrument-tube is required to move around and provide different starting points for different approach angles. It positions the first transverse axis (1) at any position  $(x(\psi), y(\phi))$  and  $z$  of the manipulator) on the circle C (with a variable diameter and  $z$  coordinate, Figure 5.4 middle). In addition, the manipulator provides an initial orientation  $\Theta$  of the gripper. This  $\Theta$  orientates axis 1 preferably tangentially to this circle, to point the tip towards target organ O. The additional transverse axis (DoF 2 in the left and DoF 3 in the right) allows more subtle approach changes. And the roll provides ease of stitching. This results in three positioning DoFs to position the first transverse axis, four DoFs to orient the gripper and one DoF to close and open the gripper. These DoFs are driven by their respective transmission running through the long and slender instrument-tube. Preferably, for each DoF the transmission ratio  $i \leq 1$  for high output stiffness, accurate movements, reduced transmission load and small motors (low mass, reduced power and current). Figure 5.5 (on the next page) illustrates the transmission ratio of e.g. a gripper at the end of an instrument-tube. The consequence of a relatively large gripper applied at the end of a small diameter instrument tube is that the achieved transmission ratio  $i > 1$  in many cases. The same holds when adding DoFs between tube end and

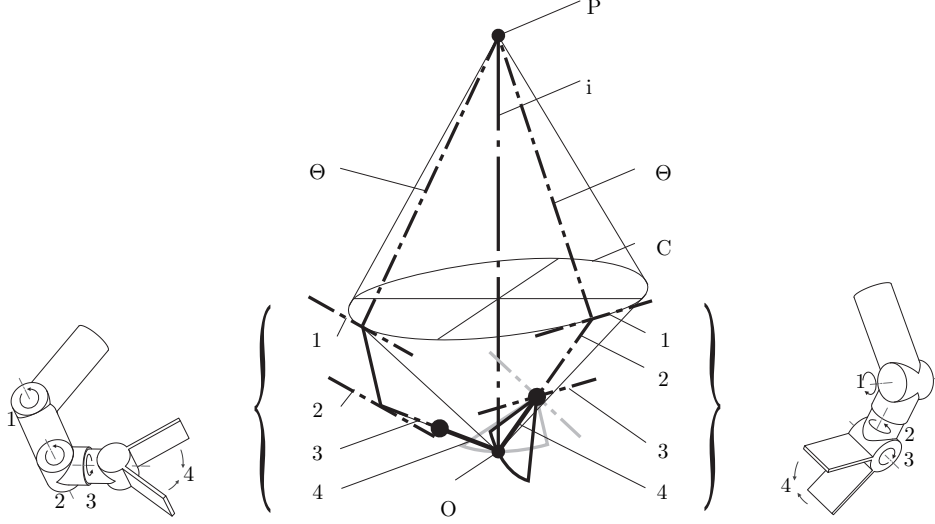


Figure 5.4: Approach possibilities of the tip-layouts proposed. Here, the variable  $i$  is the instrument-shaft used for conventional MIS,  $P$  is the entry point and  $O$  is the target organ. Left shows the approach for the pitch-pivot-roll-close tip and right the pitch-roll-pivot-close tip.

gripper. Increasing the tip-length (for more range) increases the transmission ratio. This enlarges the load ( $F_{in}$ ) on the transmission in the joints, since also  $i \sim F_{in}/F_{out}$ . The force and torque requirements set for the instrument-tip might just conflict with the technical feasibility of the applicable transmission (due to the space constraints). Exotic materials for the transmission might provide a solution if required.

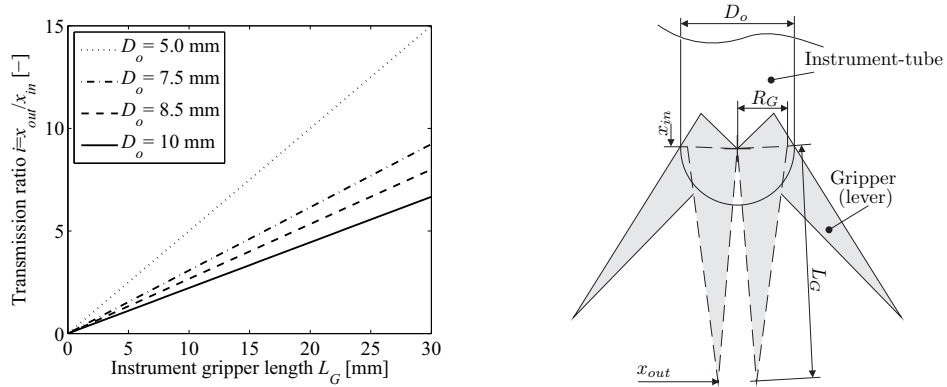


Figure 5.5: Transmission ratio  $i$  of any instrument-tip with a gripper at the end of a small diameter instrument tube (diameter  $D_o$ ). The gripper (right) acts as a lever with  $i = x_{out}/x_{in} \approx L_G/R_G$ , with  $[-]$  the initial gripper position and  $[- -]$  a next position.

### Transmission concepts

Therefore, the space within this instrument-tube should be used as to most optimally transmit the required torques and forces. A steel transmission is preferred, since the stiffness of a cylinder filled with steel is larger than the stiffness of a similar cylinder filled with water (or air). Torque is transmitted most optimally with concentric tubes at the largest radius possible, since  $k = GI_p/L$  and  $I_p \sim D^4$ . An axial force can then be transmitted by a tube/rod/cable near the center axis of the instrument (in case both torque and forces are transmitted), since  $c_{ax} = EA/L$  and  $A \sim D^2$ . Whether torque or force is transmitted depends on the tip-layout chosen and accompanying transmission. Several transmissions have been investigated, see Figure 5.6.

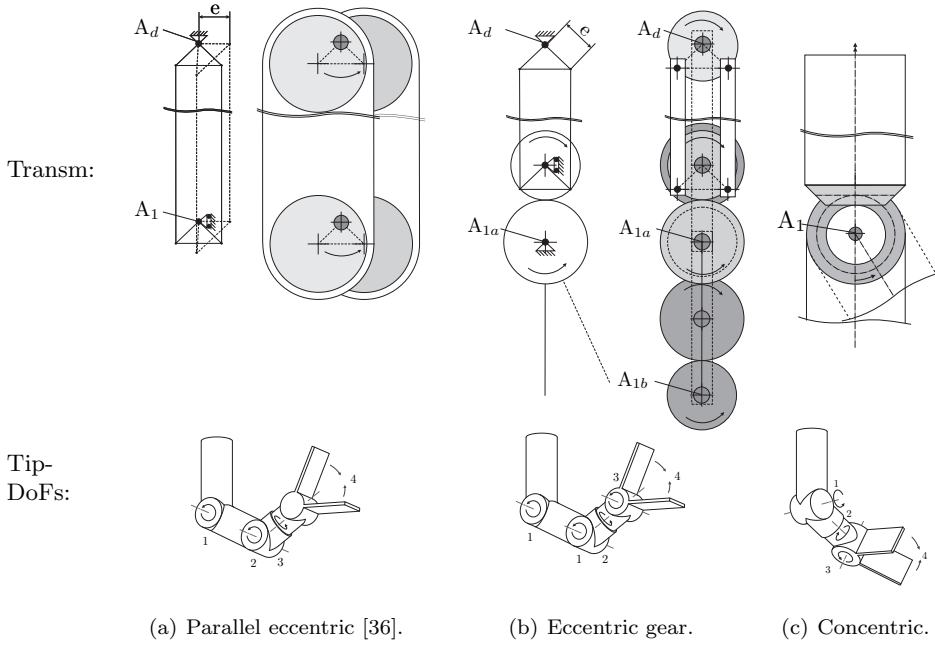


Figure 5.6: Two four-DoF tip-layouts (Tip-DoFs) with their designed transmissions (Trans) are presented: (a) shows the parallel eccentric drive to drive the pitch-pivot-roll-close tip (right of Figure 5.3(a)) and (b) and (c) show respectively the eccentric gear and the concentric transmission to drive the pitch-roll-pivot-close tip (right of Figure 5.3(b)). More specifically, the transmission of DoF 1 is displayed. In (a) and (c) DoF 2 is driven with a similar transmission as shown. Not shown here, are the cable drive of DoF 2 in (b) and of DoF 3 and 4 of all concepts.

The parallel eccentric drive (NSUmax, [36]) accompanies the right pitch-pitch-roll-close tip layout in Figure 5.3(a) and transmits force. The axes of DoFs 1 and 2 are parallel. This makes it suitable for the NSUmax layout. Both DoFs are driven

with an eccentric (radius for eccentricity  $< D_i/2 = 3.8$  mm) and each eccentric is driven with two parallel rods, which results in a compact transmission. A belt and a gear transmission are proposed for this tip-layout as well [36]. These were disregarded respectively because of allowable bending stress and transmission of the torque by the belt; and backlash and occurring stress in the gears. The eccentric gear drive accompanies the pitch-roll-pivot-close tip layout, Figure 5.3(b) right. This eccentric is driven with rods and a train of gears, transmitting force as well. This eccentric transmission requires DoF 1 to be split in two to increase its range. Finally, the tip layout in Figure 5.6(c) is accompanied with the concentric transmission. Since DoF 1 is succeeded with a DoF that requires roll of the instrument, both DoFs are most logically applied with a torque transmission: concentric tubes. DoFs 3 and 4 are driven with cables in all cases. The design requirements regarding the four DoFs with two transverse, one roll and one close-DoF are fulfilled for all concepts shown in Figure 5.3. The smallest backlash at the instrument tip, which is advantageous for the tip-accuracy, is achieved with (a); followed by (c); and then (b) because of its gear-train. The friction in the transmission is smallest for (c); followed by (b); and then (a). Concepts (b) and (c) will be backdriveable, concept (a) turned out not to be backdriveable.

### Chosen concept and resulting performance requirements

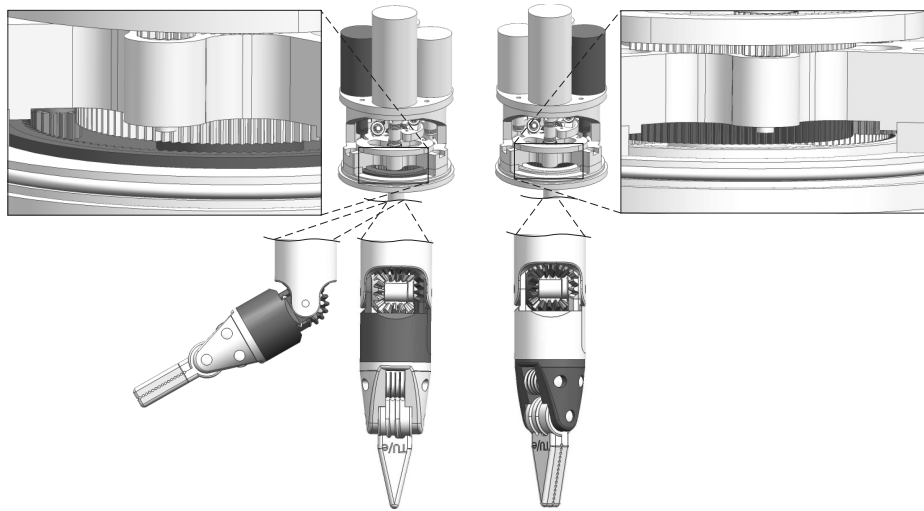
The pitch-roll-pivot-close with accompanying concentric transmission is chosen. Its friction is lower than the parallel eccentric drive and its backlash smaller than the eccentric gear drive. Its accompanying performance requirements are given per DoF in Table 5.2. These are based on the task requirements from Table 5.1.

Table 5.2: The performance requirements for instrument-tip DoFs are on display. The range of movement relative to its neutral orientation, the angular velocity  $\omega$  and the force  $F$  are shown. The positioning resolution (res.) and torque  $T$  are related to the length of the tip ( $L_{tip}=25$  mm) for pitch, and to the gripper length ( $L_G=10$  mm) for roll, pivot and close.

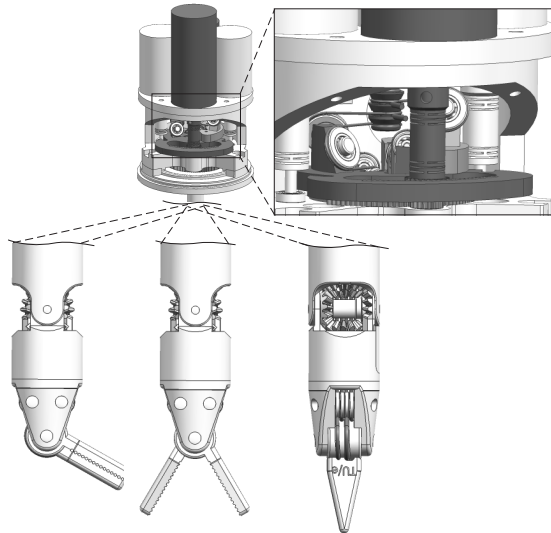
DoF	Range [°]	$\omega$ [rad/s]	$F$ [N]	$L_{tip,G}$ [mm]	Res. [°]	$T$ [Nmm]
Pitch nominal	$\pm 70$	6.5	2.5	25	0.11	62.5
Pitch max		0.5	10	25		250
Roll nominal	$\pm 90$	6.5	2.5	10	0.29	25
Roll max		0.5	10	10		100
Pivot nominal	$\pm 90$	6.5	2.5	10	0.29	25
Pivot max		0.5	10	10		100
Close nominal	45	0.5	10	10	0.29	2x100
Close max		0.5	20	10		2x200

## 5.2 Instrument details

Figure 5.7 shows an overview of the four-DoF tip (pitch, roll, pivot and close) with its concentric drive.



(a) Pitch (left) and roll (right).



(b) Pivot (left), close (middle) and cables (right).

Figure 5.7: Overview of the four DoFs of the instrument-tip with their respective drives. The appropriate parts participating in the drive are grey.

Pitch and roll are driven by concentric tubes in the instrument-tube. Pivot and close are driven with a cable transmission running through the concentric tubes of pitch and roll. The pitch (Figure 5.7(a) left) is driven with a right-angled bevel-gear transmission, connected to the outer concentric tube. The output bevelgear then rotates the tip. The roll-DoF is driven with the inner concentric tube. An additional bevelgear is provided to cross the pitch axis. These gears are smaller than the pitch-bevelgear transmission to fit within. The drive-box actuates the concentric tubes. The actuation in the drive-box is realized with respectively an internal and external gear-set connected to the appropriate motors. The pivot and close-DoFs of the gripper are driven with a cable-drive (Figure 5.7(b)). The cables pass through the inner concentric tube to be actuated in the drive-box. The motor-combinations in the drive-box are placed parallel to the instrument tube, to result in small dimensions. The drive-box diameter is limited to 60 mm to remain between the manipulator fork of H2. The forces are measured in the instrument drive-box. This prevents delicate wires and electronic signals from being brought into the patient. To eliminate friction of the transmission in the drive-box on the force-measurement data, forces are measured as close to the tip as possible. A detailed description of the DoFs, accompanying transmission and drive is given below. The description is divided in three parts: the pitch and roll are similar and described together, as well as the pivot and close, the third part is a description of the drive-box with its force sensors.

### 5.2.1 Pitch and roll

Pitch and roll are both driven with right-angled bevelgear transmission, schematically displayed in Figure 5.8.

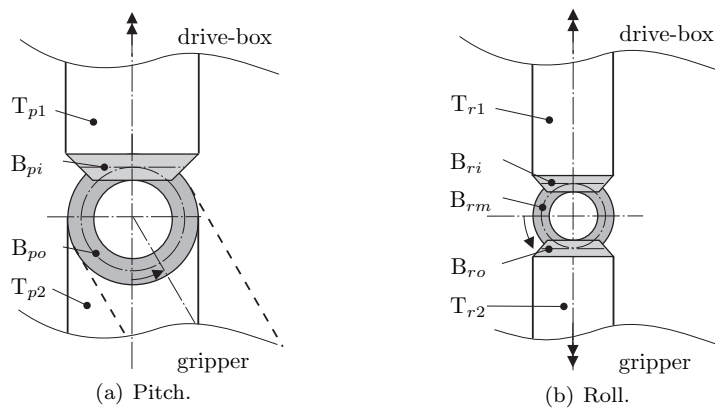


Figure 5.8: Pitch (left) and roll (right) of the instrument-tip are displayed. Tip movement for pitch are indicated as current position [—] and next position [—].

The input bevelgear of pitch ( $B_{pi}$ ) is connected to the actuated concentric tube  $T_{p1}$ . Its output bevelgear ( $B_{po}$ ) is fixed to  $T_{p2}$ . The roll-DoF is driven with a similar bevelgear transmission, of which its input bevelgear  $B_{ri}$  is connected to actuated tube  $T_{r1}$ . An additional step is provided to cross the pitch axis. Its intermediate bevelgear ( $B_{rm}$ ) is supported by the pitch axis. This meshes  $B_{rm}$  with its input and output ( $B_{ro}$ ) bevelgear while the pitch is being actuated. This output bevelgear is connected to tube  $T_{r2}$ , which rolls the gripper. The roll gears are smaller than the pitch-bevelgear transmission to fit within. Both transmissions are intended to have coinciding 'cone points' to realize smooth movements of pitch and roll. The actual set-up of the pitch and roll-DoFs is on display in Figure 5.9.

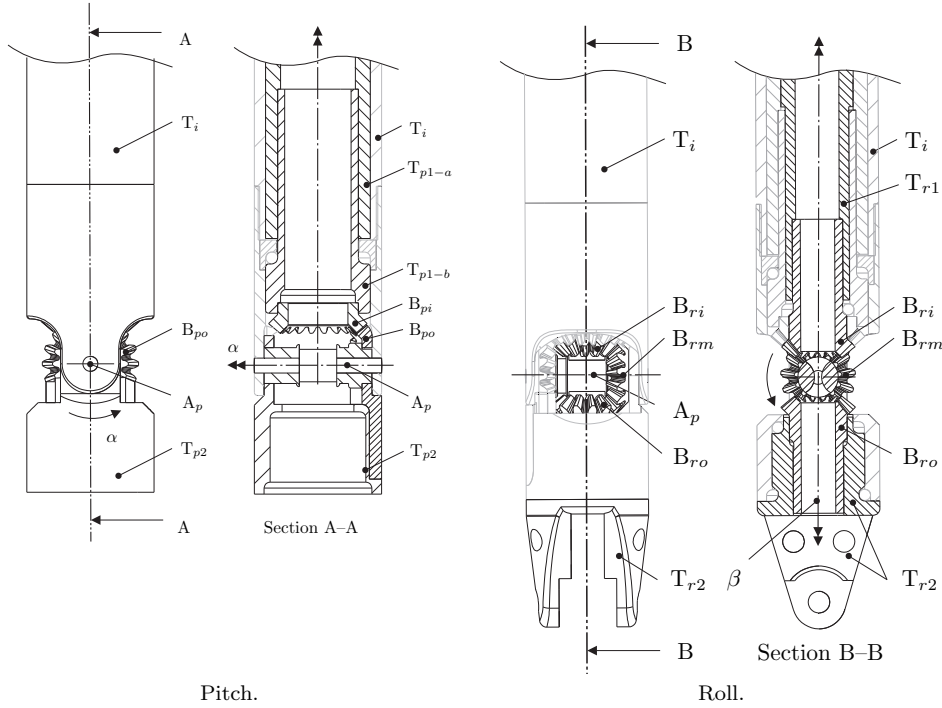


Figure 5.9: Pitch and roll bevelgear transmission at the instrument-tip.

The aim is uniformity to reduce the number of different products and manufacturing tools required. This eases assembly. To this end each gear has a similar module. The roll-gears and connecting axes have a similar form. In Figure 5.10 the support of the gear-tubes is shown. The support is provided by means of ball bearings whenever possible, to reduce friction. The bearing layout of the tip consists of an angular contact ball bearing  $S_{r3}$  with its 'cone-point' (intersection of line  $L_3$ ) at the gripper axis and a radial bearing  $S_{r2}$ . The gripper-cables provide pre-load in axial direction. Support of  $T_{p1}$  and  $T_{r1}$  is provided by an angular contact ball bearing at the instrument-tip side, respectively  $S_{p1}$  and  $S_{r1}$ . The

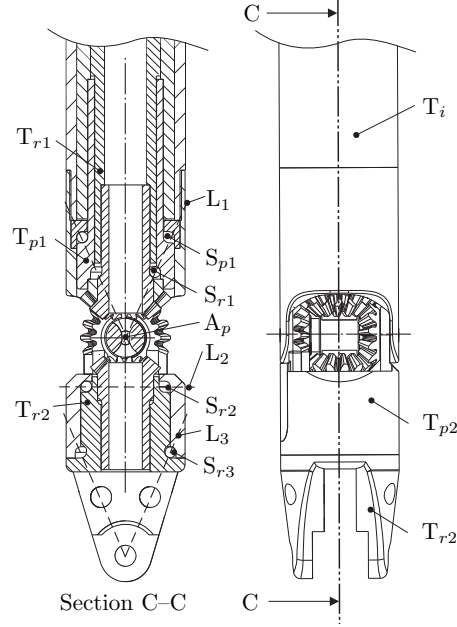


Figure 5.10: Pitch and roll support. With respectively  $S_{p1}$  supporting  $T_{p1}$  in  $T_i$ ,  $S_{r1}$  supporting  $T_{r2}$  in  $T_{p1}$  and  $S_{r2,r3}$  supporting  $T_{r2}$  in  $T_{p2}$ . The contact normals are indicated with lines  $L_{1-3}$ .

load on the bevelgears for both pitch and roll is larger than the load required on the tip, since for both DoFs  $i > 1$ . Stresses in the teeth of the gear can be split in bending stress in the root of the teeth and contact stress (Hertz). The allowable load depends on gear dimensions, type of load applied (load factors) and the applied material. It can be increased by increasing pitch-diameter of the gear  $D_b$ , increasing the modulus  $m$  and increasing the tooth width  $b$ . The gear dimensions are restricted by the diameter of the instrument-tube and can therefore be varied little. The dimensions are shown in Table 5.3.

Table 5.3: Dimensions of the bevelgears (Figure 5.9) used for the pitch and roll of the instrument-tip, with transmission ratio  $i=1$ .

DoF	Diameter $D$ [mm]	Module $m$ [mm]	Width $b$ [mm]	No of teeth $z$ [-]
Pitch:	5.4	0.3	0.9	13
Roll:	3.9	0.3	1.2	18

The diameter is given (space restrictions) and an involute tooth-profile is desired to realize a smooth run. The module is set to 0.3 mm for both sets. This module requires a minor profile shift (coefficient  $x^*=0.0247$  [72]) to prevent the teeth of the roll-bevelgear from being undercut. This module indicates the diameter of

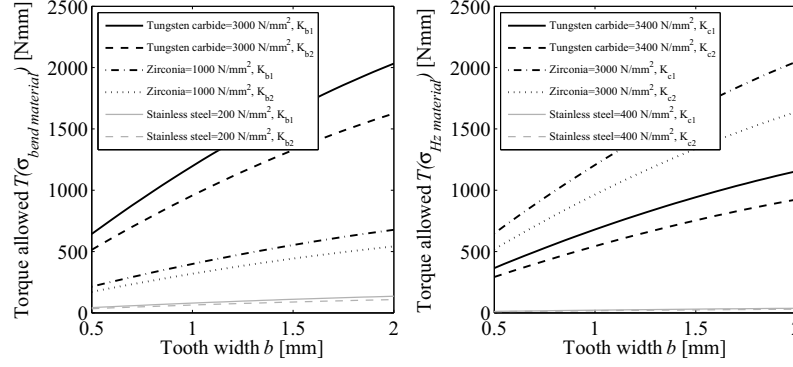
manufacturing tool as well<sup>1</sup>. Gears with these dimensions are not commercially available and are custom made. The material influences the allowable torque in the gears as well. The materials that can be used for gears are shown in Table 5.4.

Table 5.4: Mechanical properties of the materials applicable for the (bevel)gears are shown. Data on austenitic stainless steel (X10CrNiS18 9) and hardened steel (16MnCr5) from [82]. Data on alumina ( $\text{Al}_2\text{O}_3$ ), zirconia ( $\text{ZrO}_2$ ), silicon nitride ( $\text{Si}_3\text{N}_4$ ) from [43]. The ceramic poisson's ratio is given for  $20^\circ$  in [27]. Bending strength is based on a 4-point bending test.

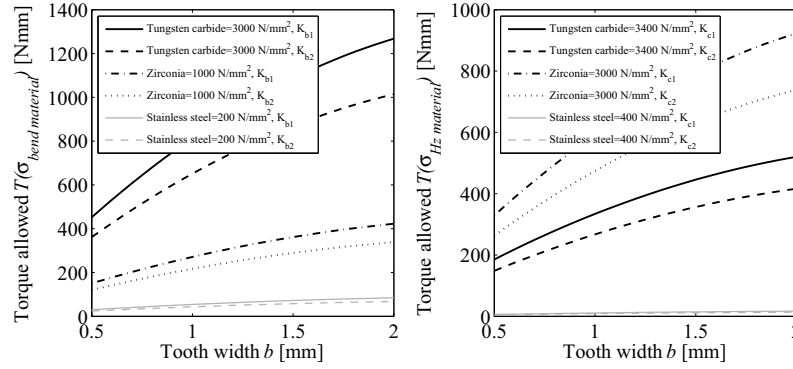
Specification		Metal			Ceramics		
		Stainless steel	Steel	Tungsten carbide	Alumina	Zirconia	Silicon nitride
		1.4305		BT-40	99.9%	$\text{Y}_2\text{O}_3$	-
Elasticity module	[GPa]	200	210	510	390	200	300
Poisson's ratio	-	0.3	0.3	0.27	0.22	0.31	0.28
Bending strength	[MPa]	200	400	3000	400	1000	750
Compressive strength	[MPa]	400	1630	3400	3900	3000	2500
Bio-compatible	y/n	y	n	?	y	y	y

Figure 5.11(a) and 5.11(b) on the next page, display the torque allowed on the bevelgears for respectively pitch and roll. The presented maximum allowable torque either is determined by the maximum allowable bending stress (Appendix Equation F.1) in the material, or by the maximum allowable Hertzian stress (Appendix Equation F.3). Which of both formulas applies, depends on the material and application constants (also shown in Appendix Section F.1) chosen. Calculation results on stainless steel and zirconia are displayed since these materials are bio-compatible. Tungsten carbide is displayed because of its good mechanical properties. The material chosen is the ceramic zirconia, since it performs better than stainless steel. This material and accompanying manufacturing process [43] is suitable for large series and mass production. Generally the manufacturing process starts with injection moulding (CIM) the powder, consisting of ceramic granules and bonding material. This gives the product in its green shape. The next step is debinding the green shape product, removing the bonding material and making the product very brittle. Subsequently the product is sintered. Sintering bonds the ceramic granules and removes the porosity. Finally, the product is polished resulting in the end-product. This manufacturing process can be applied when the instrument is realized with large numbers. For this prototype the bevelgears have been realized, starting milling each gear from an existing product in its green shape. A five-axis milling machine has been used. Each gear is worked on

<sup>1</sup>Wire EDM is considered and put aside since it could introduce cracks in the surface on this small scale.



(a) Allowable pitch-bevelgear torque  $T$ . The pitch-bevelgear as designed has pitch diameter  $D_1=D_2=5.4$  mm, module  $m=0.3$  mm and tooth width  $b=0.9$  mm.



(b) Allowable roll-bevelgear torque  $T$ . The roll-bevelgear as designed has pitch diameter  $D_1=D_2=3.9$  mm, module  $m=0.3$  mm and tooth width  $b=1.2$  mm.

Figure 5.11: Allowable bevelgear torque  $T$ , as a function of tooth width  $b$ , material (bending stress ( $\sigma_{bend}$ ) and Hertzian stress  $\sigma_{Hz}$ ) and calculation coefficients  $K_{b1}=1$ ,  $K_{b2}=0.8$  for bending stress and  $K_{c1}=1$ ,  $K_{c2}=0.8$  for Hertzian stress used (Appendix Section F.1).

preliminary with a 2.5 mm cutter. The teeth are then pre-worked with a 0.4 mm diameter cutter. The process is finished with a 0.2 mm diameter milling cutter (Figure 5.12) for a smooth surface. Figure 5.13 presents the resulting products.

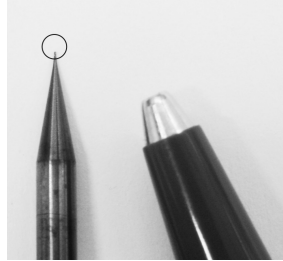
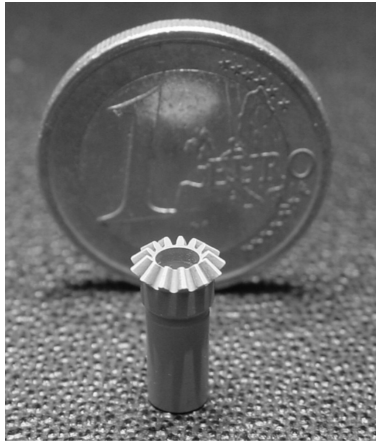
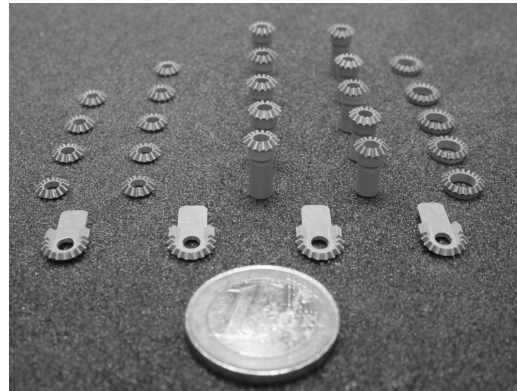


Figure 5.12: The circled cutter with a 0.2 mm diameter tool-tip, is used for finishing the bevelgears. The ballpoint tip next to it indicates the size of the tool-tip.



Roll bevelgear.



Products as realized.

(a) Bevelgears for pitch and roll in green-phase.



Green shape and end-product.

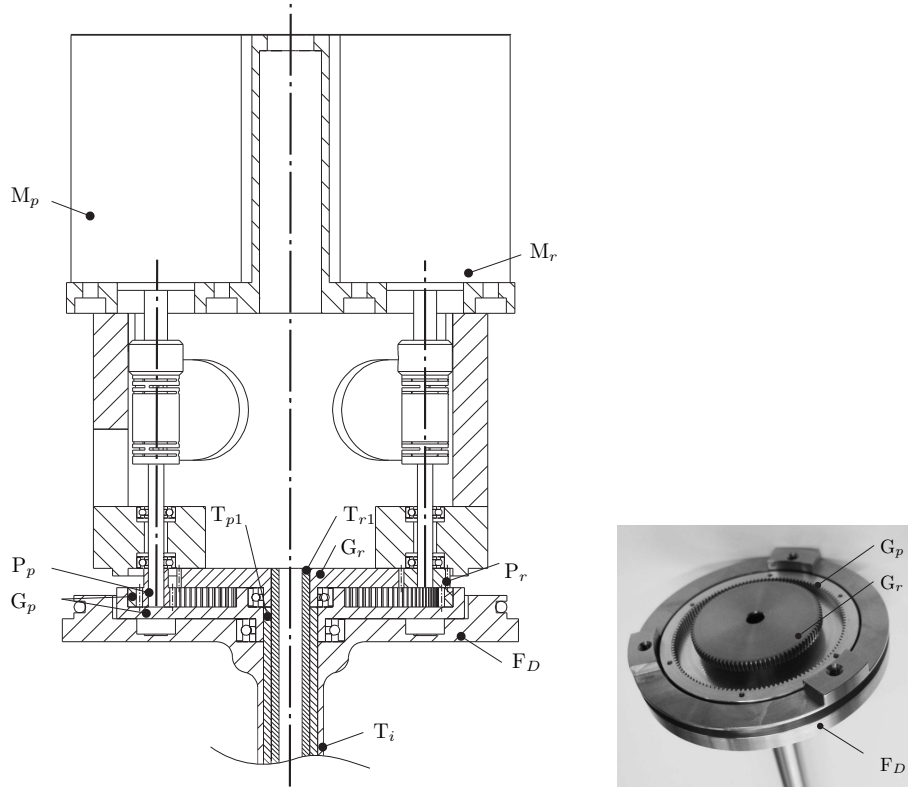


Bevelgear set for one instrument.

(b) Bevelgears for pitch and roll, end-product after debinding and sintering.

Figure 5.13: Bevelgears for pitch and roll.

The input and output bevelgears are pressed into their respective mounting tubes, since ceramics are well capable to withstand pressure. A pinion-gear combination connected to  $T_{p1}$  and  $T_{r1}$  for respectively pitch and roll, drives the input bevelgears for both DoFs. The torque required for pitch is higher than the torque required for roll. Therefore, the pitch-transmission is realized with an internal gear and spur-pinion, see Figure 5.14(a). This increases the transmission ratio (resulting in a reduced required motor-torque) and reduces backlash at the outgoing axis of the gear caused by play between the teeth. A spur-gear and pinion (Figure 5.14(a)) realize the roll-transmission, to have minimal transmission height and optimal efficiency. Both gears are realized from aluminium and hard-anodized (Figure 5.14(b)), while the pinions and axes are realized from high-grade steel. Motors  $M_p$  and  $M_r$  direct drive the respective pinions. Motors  $M_p$  and  $M_r$  direct drive the respective pinions.



(a) Driving pitch: concentric tube  $T_{p1}$  and annular gear ( $G_p$ ) are fixed. This combination is driven by pinion  $P_p$ , which is connected to motor  $M_p$ . Driving roll: concentric tube  $T_{r1}$  and spur gear  $G_r$  are joined and driven by meshing pinion  $P_r$ . This pinion is connected to motor  $M_r$ . (b) The gears for pitch ( $G_p$ ) and roll ( $G_r$ ) are mounted on the drive-box frame  $F_D$ .

Figure 5.14: The transmission of pitch and roll in the instrument drive-box consists of gear-pinion sets. The frame of the drive-box ( $F_D$ ) supports these gear-pinion sets and accompanying motors.  $F_D$  is fixed to instrument tube  $T_i$ .

### 5.2.2 Pivot and close

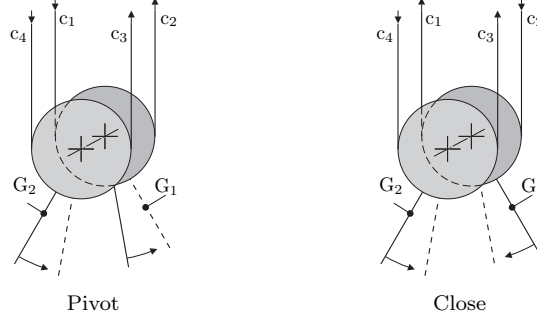
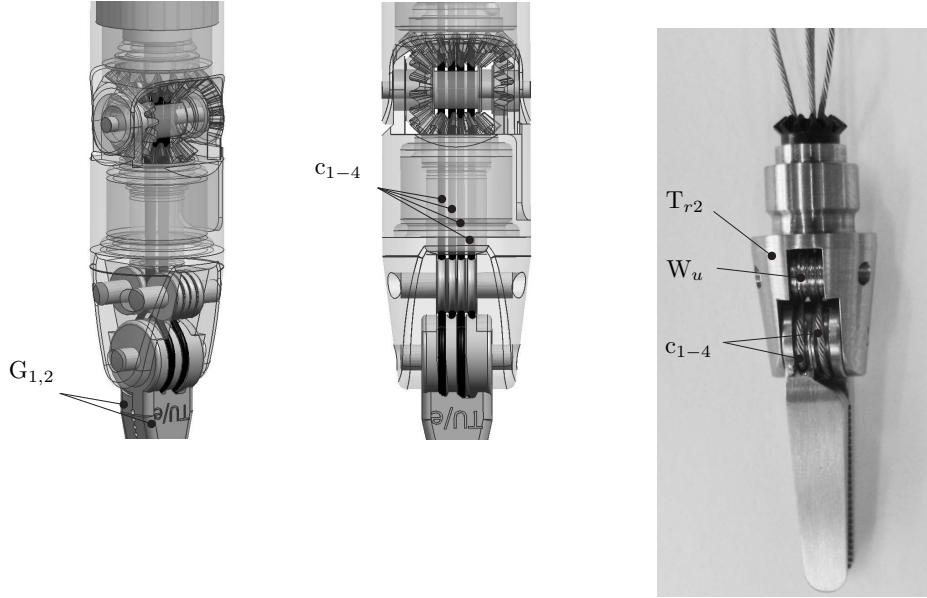


Figure 5.15: Pivot (left) and close (right) of the gripper (gripper jaw  $G_1$  and  $G_2$ ) and required cable ( $c_1$ ,  $c_2$ ,  $c_3$ ,  $c_4$ ) motion indicated with arrows. Movement of gripper jaws  $G_1$  and  $G_2$  is indicated as current position [—], next position [---].

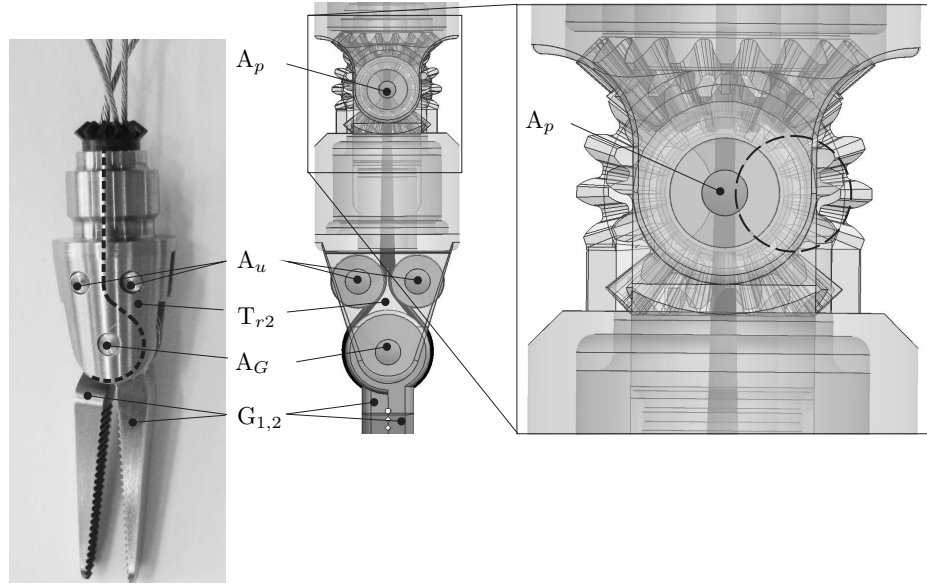
Each gripper is provided with two cables departing at opposite sides of its axis, since cables can only pull and the gripper is required to rotate in two directions. The cable motion to perform a pivot or close/open action (further mentioned as close) is shown in Figure 5.15. The actual gripper design with its cables is on display in Figure 5.16 on the next page. The cable course is transmitted from the outside of the gripper towards the center of the inner concentric tube driving roll ( $T_{r2}$ ) by means of pulleys ( $W_u$ ). Thereby, undesirable gripper motion caused by mere activating pitch or roll are kept small. The pulleys that shift the cable course (Figure 5.16), have a diameter  $D_{W_u}=3$  mm. This small pulley radius requires a small cable diameter yet many strands to curve on small radii, whereas the cables need to transmit large forces as well. A cable force of 80 N is required to close the gripper. This force is derived from the torque required to close the gripper (200 Nmm Table 5.2) and the cable curvature radius on the gripper ( $D_G=5$  mm). The possible cables are shown in Table 5.5. Dyneema ( $E=110$  GPa) was considered because it is superior to a steel wire regarding its stiffness. In addition it has thin filaments and can be used on a small diameter pulley. It is abandoned because its end fixation requires a larger construction than fixation of the steel cables.

Table 5.5: Possible cables, chosen on diameter ( $D_{cable}$  and  $D_{wire}$ ) and allowed load ( $F_{break}$  and  $F_{max}$ ). Both cables are made of 316 stainless steel. The effect of the diameter of curvature (pulley diameter Figure 5.16  $D_{W_u}=D_{curv}$ ) on the wire rope strength is accounted for by efficiency ( $\eta$ ). This efficiency is a function of  $A$  with  $A=D_{curv}/D_{cable}$  [48]. The resulting wire rope strength ( $F_{curv}$ ) is shown. The 7x19 cable is integrated in the design, since it curves more easily.

	Type	$D_{cable}$ [mm]	$D_{wire}$ [mm]	$F_{break}$ [N]	$F_{max}$ [N]	$D_{curv}$ [mm]	$A$	$\eta$ [%]	$F_{curv}$ [N]
1	7x7	0.54	0.06	240	180	3	5.6	77	139
2	7x19	0.45	0.03	156	117	3	6.7	80	94



(a) Instrument-tip with two gripper jaws  $G_{1,2}$  and two cables per gripper  $c_{1-4}$ . Right: the gripper as realized, with its cables  $c_{1-4}$  on gripper cable wheels and cable-pulleys ( $W_u$ ,  $D_{W_u}=3$  mm).



(b) The gripper jaws ( $G_{1,2}$ ) with connected cables run on axis  $A_G$  and supported by  $T_{r2}$ . The cable course is transmitted towards the center of  $T_{r2}$  with the cable-wheels running on axes  $A_u$ . The cables intersect axis  $A_p$  on its center line and are guided on a circular path (indicated with  $[-]$ ). Left: the gripper as realized with both gripper jaws  $G_{1,2}$  and cable-run  $[-]$ .

Figure 5.16: The cables ( $c_i$ ) provide the gripper jaws ( $G_{1,2}$ ) with pivot and close. The cable-run is shown.

The cable course intersects the pitch axis (Figure 5.16(b)) and continues through  $T_{r1}$ , to be actuated in the drive-box. Two courses of action are open to apply the cable motion within the drive-box: either drive each gripper or drive each DoF, respectively see Gripper-combination and DoF-combination in Figure 5.17.

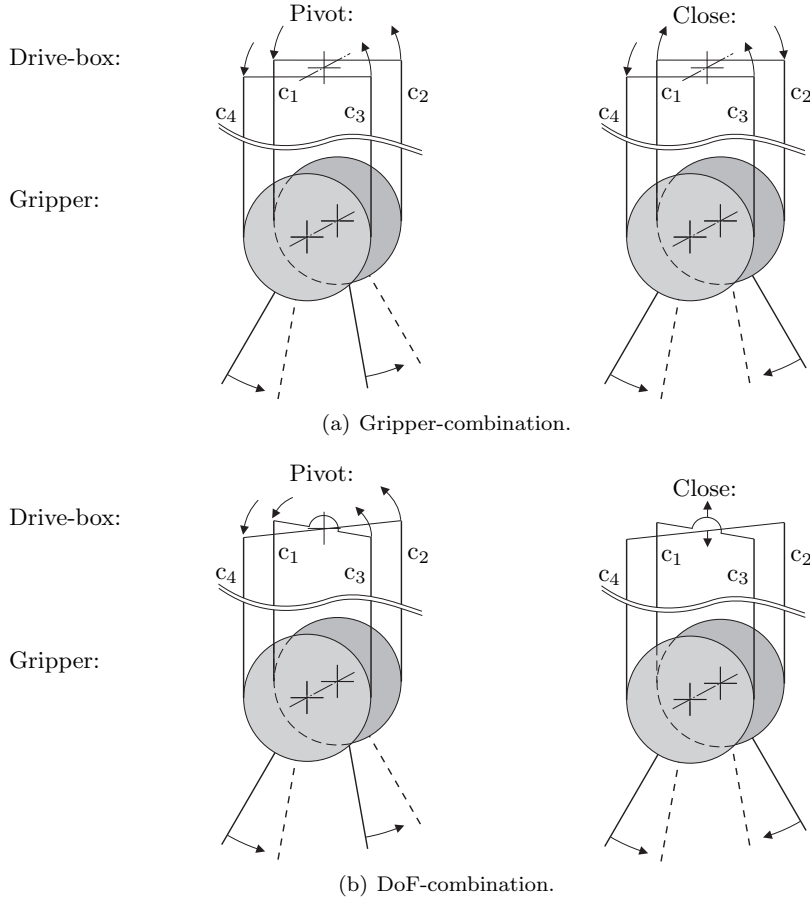


Figure 5.17: Two different sets of cable-pairs in the drive-box can perform pivot and close of the gripper. Either each pair of cables ( $c_{1-4}$ ) drives one gripper (a) or each pair of cables drives one DoF (b). Movement of the bar connecting the cables of a pair and the resulting gripper movement (left pivot, right close) are shown.

In the first case (Figure 5.17(a)) the cables departing from each gripper are connected in the drive-box to form a pair. Each pair is coupled to one motor driving one gripper, Appendix Figure F.1. In the second case (Figure 5.17(b)) the cable-pairs in the drive-box combine the DoFs. Either path entered requires two motors. The second option is chosen to prevent opposing the gripper motors while closing the gripper jaws. A schematic representation of the drive to close and pivot the gripper is shown in Figure 5.18.

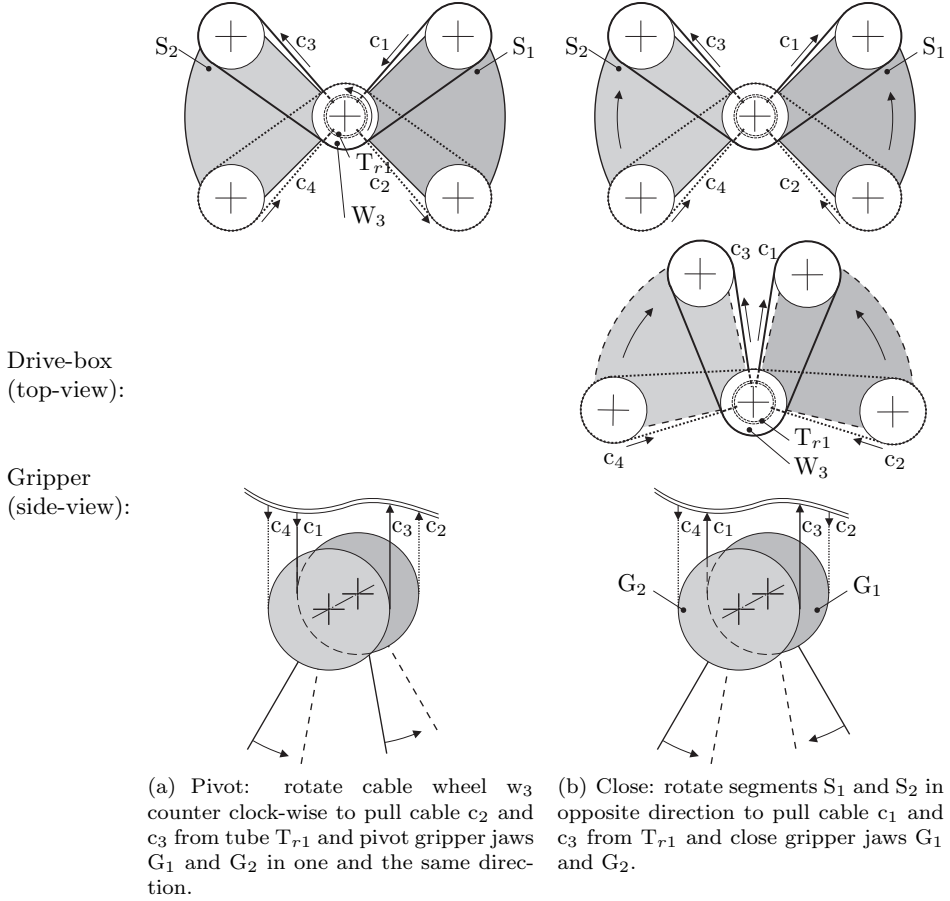
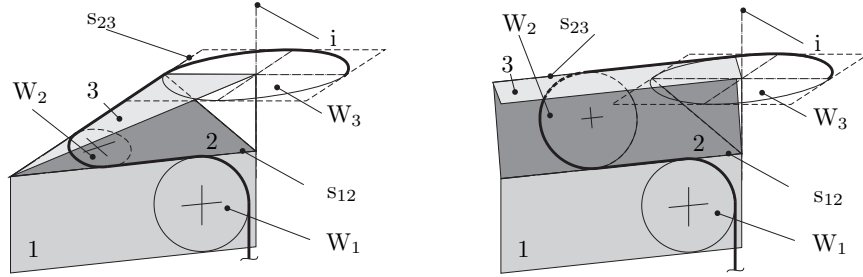


Figure 5.18: Schematic representation of the cable-drive in the drive-box, driving the gripper. The cable pairs formed drive the pivot and close-DoFs.

Each gripper is linked to one cable segment ( $S_1$ ,  $S_2$ ) in the drive-box. Rotating the segments in opposite directions results in closing and opening of the gripper, see Figure 5.18(b). These segments are placed parallel to the pitch and roll gears to realize a reduced height of the drive-box. The cables axially departing from the inner concentric tube driving roll ( $T_{r1}$ ) are radially re-routed to the segment planes. Here, each cable winds its segment-wheel  $180^\circ$  and departs the segment towards the instrument center-line again. Each cable is connected to its accompanying pivot cable-wheel ( $W_3$ ) near this center-line, see Figure 5.18(a). The four pivot cable-wheels are stacked. Figure 5.18(a) shows that rotating this stack of wheels results in pivot of the gripper. During assembly, the wheels can be rotated relative to each other to pre-load the cables.



(a) The intersecting curve  $s_{12}$  of plane 1 and 2, intersects with intersecting curve  $s_{23}$  of plane 2 and 3. (b) The intersecting curves  $s_{12}$  and  $s_{23}$  are parallel.

Figure 5.19: The path of the cable (fat black line) is determined by the orientation of wheels  $W_{1-3}$  and by the diameter of  $W_3$ . The wheels should lie tangent to the intersecting curves ( $s_{12}$ ,  $s_{23}$ ) of their planes of symmetry (respectively 1–3) for a smooth cable-run.

Figure 5.19 shows one of the four cables running along its cable wheel ( $W_1$ ), segment wheel ( $W_2$ ) and pivot cable-wheel ( $W_3$ ). These wheels are the components of the wheel-set of this single cable. A proper choice of orientation and diameter of these components provides a smoothly curved path. This allows the cable to stay in the wheel track, which reduces stress and wear of the cable and improves reliability.

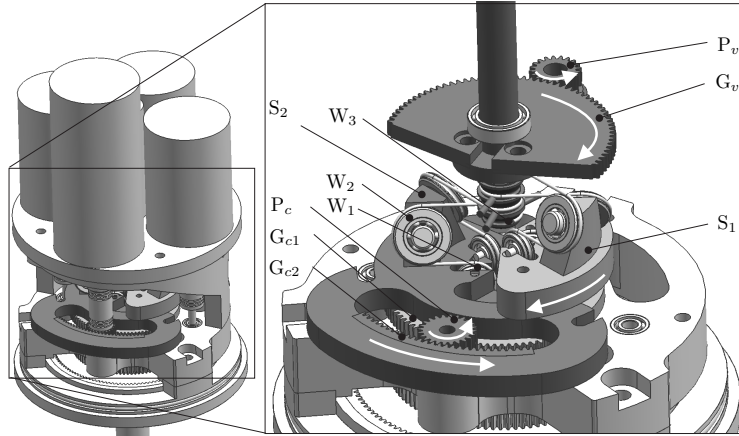


Figure 5.20: The cable-drive in the drive-box to pivot and close the gripper-jaws. Rotating gear  $G_v$  with its connected pivot cable-wheels ( $W_3$ ), pivots the gripper. Pinion  $P_v$  drives this combination. The gripper-jaws are closed by rotating the cable segments ( $S_1$  and  $S_2$ ) in opposite directions. To this end pinion  $P_c$  meshes with an annular gear ( $G_{c2}$ ) and a spur gear ( $G_{c1}$ ) each joined with respectively segment  $S_2$  and  $S_1$ . Each segment is linked to the cables departing from one gripper jaw. The cable-wheels ( $W_1$ ) and segment-wheels ( $W_2$ ) of both cables are part of the accompanying segment.

The cables connected to one gripper jaw both are linked to one segment to close the gripper. Each segment has a gear connected (Figure 5.20 and 5.21), one is provided with an internal, the other with an external gear. One pinion combination consisting of two stacked and connected pinions drives both gears. Rotating this pinion combination then rotates the segments in opposite directions to close the gripper. The transmission ratio of both segment pinion-gear sets is similar to realize the same rotation. This requires a slightly different diameter of the stacked pinions. The gripper can pivot by rotating the gear ( $G_v$ ) connected to the stacked pivot cable-wheels, with its meshing pinion ( $P_v$ ), see Figure 5.20.

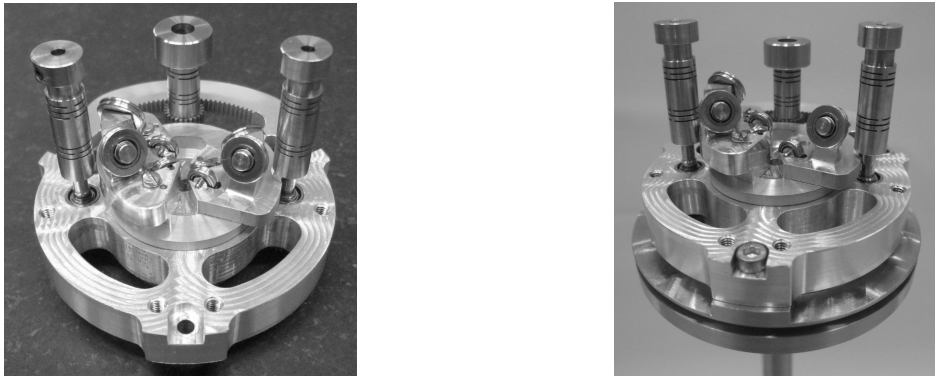


Figure 5.21: The segments of the cable-drive in the drive-box as realized.

### 5.2.3 Drive-box of the instrument

As stated, the drive-box has an outer diameter of 60 mm. Four motors are required to drive each DoF. These motors are placed parallel to the center line of the instrument-tube, at the corners of a rectangle. The maximum motor diameter allowed is 24 mm. The length of the diagonal is set to  $2 \times 17.4$  mm. The details on the transmissions and motor-combinations described in the previous subsections are shown in Appendix Table F.4 and F.5. The motors plus their mounting-flange weigh 320 g in total, the total drive-box weighs approximately 750 g. The instrument is intended for multiple-use and needs to be sterilized. The end-product will be provided with a separation between the mechanical part of the drive-box (the cables can then keep their pre-load) and the electrical part. The electrical part includes the motors on their mounting-flange, the sensor electronics and the wiring. An adaptor should be developed to couple the sterile and non-sterile part and the electrical-part of the instrument should be externally covered. The forces are measured in the drive-box as close to the tip as possible. Concepts to perform these force-measurements are on display in Figure 5.22.

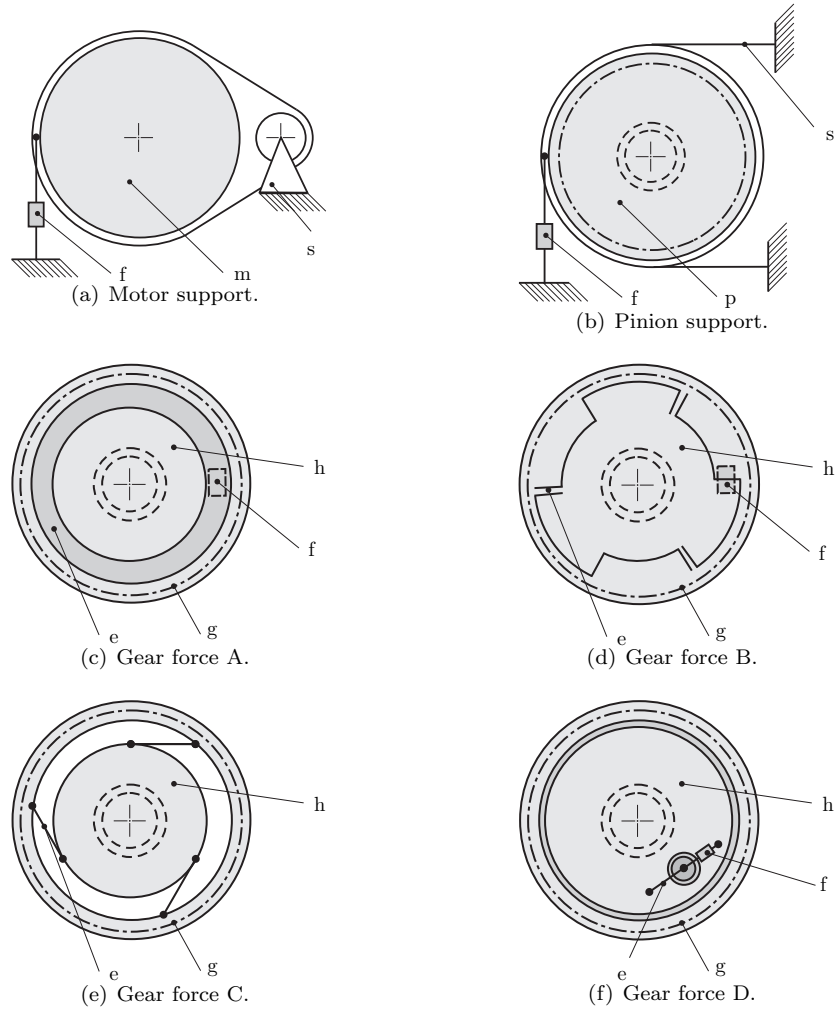


Figure 5.22: Concepts to measure the forces of each DoF. With motor (m); support (s); pinion (p); gear (g); and force sensor (f) consisting of either an elastic element (e) with stiff force sensor or a stiffer element (e) with displacement sensor.

The reaction force of the motor on the drive-box can be measured, as well as the reaction forces of the pinion and transmitted force within the gears. The force-measurement can best be performed in the gear of each DoF, close to the output of the drive-box. Gear force D incorporates limited wire-motion, measurement of the strain in the right direction resulting in a high sensitivity and a physical end-stroke for safety. This concept does include electronics in the mechanical part of the drive-box, which makes the separation between the mechanical and electrical part difficult. Since three out of four DoFs are driven without a motor-transmission, the reaction motor-torque can be measured as well. Therefore, the

motor-support option will be implemented in the near future. For now the motor-current will be measured to provide an idea on the motor-torque.

The instrument wires for the motors and force sensors move along with the instrument. These wires need to allow movements in  $\theta$  and  $z$  relative to the  $\Theta Z$ -manipulator, without being loaded too much (risk of fatigue) and getting entangled with neighboring instruments. In addition the wires should be compliant to reduce the influence on the force-measurements and mass should be low to reduce the load on the manipulator-drive. Therefore, the wiring (W) between the electronics-box (E) of the manipulator and the instrument drive-box (D) is executed as flex-foils (Figure 5.23). Flex-foils are light and flexible allowing movements but no torque. To this end the  $\theta$  and  $z$ -movements of the flex-foils are separated. Disconnection box R holds its flex-foils rolled up, allowing the instrument to perform a  $\theta$ -rotation. It does not perform a  $\theta$  itself, flex-foil part W therefore only has to allow a  $z$ -translation. The left of Figure 5.23 shows the rotation disconnection box (R) integrated with the  $\Theta Z$ -manipulator ( $M_{\Theta Z}$ ) and the wires guided on top of the parallelogram-frame ( $P_F$ ) of the manipulator. This would increase the height of the  $\Theta Z$ -manipulator (and the length of the instrument). The right of Figure 5.23 displays the rotation disconnection box (R) applied on top of the instrument drive-box (D) in a drum. A mechanism ( $M_R$ ) on arm H2 of the manipulator prevents rotation of the drum and provides a guidance of the wires (W).

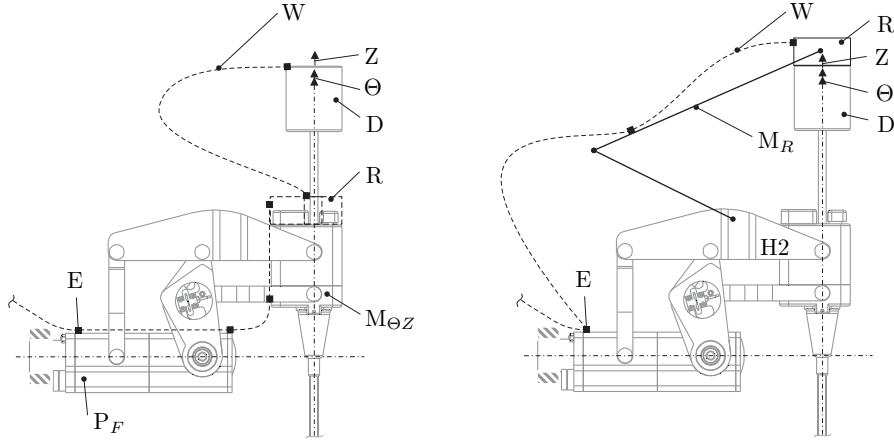


Figure 5.23: Wiring (W) of the instrument executed as flex-foils. The wires between the instrument drive-box (D) and manipulator electronics-box (E) need to allow  $\theta$  and  $z$  of the instrument. These movements are separated with the rotation disconnection box (R) to reduce the load on the wires. The rotation disconnection box can be integrated with the  $\Theta Z$ -manipulator ( $M_{\Theta Z}$ ) or with the instrument drive-box (D). The last requires a mechanism ( $M_R$ ) to prevent rotation of the rotation disconnection box.

## 5.3 Instrument evaluation

The instrument has been realized (Figure 5.1). Currently tests are set up and performed to first move the gripper. These tests will be followed by measurements to check the range, measure hysteresis to get insight in the friction present in the instrument and on the positioning accuracy, and identify the process to develop the proper controllers. Then it can be coupled to a master, to verify the benefit of these four DoFs and implement haptic control. This will initially be based on current used by the motors to drive the DoFs.

## 5.4 Conclusion and recommendations

### 5.4.1 Conclusion

The instrument consists of a four-DoF tip, connected with a long and slender instrument-tube to the drive-box of the tip. The instrument-tip can be used 300 mm from its trocar inside the body, stating the length of the instrument-tube. The four DoFs move the gripper in pitch (first transverse axis), roll, pivot (second transverse axis) and close. It allows surgeons to work at the backside of an organ, approach organs from more than one angle and perform complex movements like stitching. These DoFs are backdriveable, which allows the instrument to be removed from the trocar in case of an emergency. The tip and gripper length and the diameter of the instrument-tube determine the transmission ratio in the tip that can be achieved maximally. Ideally this transmission ratio  $i < 1$ , for accurate movements, reduced transmission loads and small motors. However, this compromises the reach of the instrument-tip. Torques on the pitch and roll transmission in the tip are substantial due to its transmission ratio. To this end, the transmission for pitch and roll is provided with zirconia bevelgears that are driven with concentric tubes inside the instrument-tube (outer diameter of 8.5 mm). The cables driving pivot and close pass through the inner concentric tube, close to the center line. The drive-box with diameter 60 mm, contains four motors to drive each of the tip DoFs. The current used by these motors will initially indicate the forces at the tip, friction needs to be compensated for. The theoretical performance of the instrument-tip is shown in Table 5.6. The range, angular speed, theoretical resolution and torques that can be achieved with this instrument approximate the requirements closely. These requirements are derived from literature, in which the forces are measured with conventional MIS instruments. The forces required to manipulate needles and tissue with instruments that move more subtle might be (much) smaller. Tests need to reveal whether this assumption is true.

Table 5.6: The performance of the different DoFs of the instrument-tip (defined at their output axes), is based on the design and specifications of the components applied. The range of movement relative to its neutral orientation, the positioning resolution provided by the encoder (res.), the angular velocity ( $\omega$ ) and the torque ( $T_{max}$ ), are shown.  $T_{max}$  is the maximum torque that can be applied by the tip, which depends on the limiting factor applicable for the zirconia bevelgears ( $K_{b2,c3}$  Appendix Section F.1) and on the cable preload ( $T_p$ ) applied. The force ( $F$ ) is related to the length of the tip ( $L_{tip}=25$  mm) for pitch and to the gripper length ( $L_G=10$  mm) for roll, pivot and close.

DoF	Range [°]	Res. [°]	$\omega_{max}$ [rad/s]	$T_{max}$ [Nmm]	$L_{tip,G}$ [mm]	$F$ [N]
Pitch	$\pm 75$	0.07	$> 6.5$	290 ( $K_{b2}=0.8$ ) 55 ( $K_{c3}=0.05$ )	25	11.6 2.2
Roll	$\pm 90$	0.15	$> 6.5$	249 ( $K_{b2}=0.8$ ) 34 ( $K_{c3}=0.05$ )	10	25 3.4
Pivot	$\pm 90$	0.15	$> 0.5$	235 ( $T_p=0T_{max}$ ) 118 ( $T_p=0.5T_{max}$ )	10	24 12
Close	37	0.03	$> 0.5$	235 ( $T_p=0T_{max}$ ) 118 ( $T_p=0.5T_{max}$ )	10	24 12

## 5.4.2 Recommendations

A more extensive evaluation of the zirconia bevelgears regarding the Weibull flaw statistics should be performed. The cables for pivot and close are preloaded during assembly to ensure each cable winds its wheels. Preloading cables reduces the load allowed. Replacing the cable with Dyneema can improve this load, but requires design of a compact fixation method. Further experiments and measurements should reveal the appropriateness of this four-DoF tip, its transmission and force measurements. Force-sensors integrated with the motor-support of the instrument drive-box can be applied to verify (and improve) the force measurements. Experiments should include finding the forces required by the surgeon, performing surgery (or dummy experiments) with this tip layout. If smaller forces apply, smaller motors can be used, which leads to a (required) mass reduction of the drive-box. Hysteresis measurements should provide insight in positioning accuracy and design improvements. Identification measurements provide this (last) information as well, in addition to the possibility to design controllers.

The mechanical part of the instrument and drive-box will be separable from the electromechanical part of the drive-box for sterility, in the next design. After evaluation of the instrument, expansion of the assortment of end-effectors at the instrument tip is required.



## Chapter 6

# Sofie System-integration

The Slave is part of Sofie (Surgeon's Operating Force-feedback Interface Eindhoven): the robotic surgical system. The surgeon uses Sofie to operate on the patient in a minimally invasive manner. Sofie consists of a master, electronics and software, and a slave. The surgeon operates the two haptic joysticks of the master, controlling the two instruments of the Slave and (using a mode switch) the endoscope. The interaction between surgeon/operator and master, and the interaction between master and slave (software and electronics) will be discussed in this chapter, with additionally a system evaluation.

### 6.1 Interaction between surgeon and master

The surgeon performs surgery while operating the Master. The Master should provide surgical information, the two joysticks or haptic interfaces to operate the Slave and the possibility to adapt the system to the surgeon's needs (operator control panel). Two masters are discussed here, the first master (called Master Device One) was developed first by Grasman and Hendrix [59]. It is intended for a different type of Minimally Invasive Surgery (MIS) than thoracic and abdominal surgery: vitreo-retinal eye-surgery. It is developed parallel to and in a similar time schedule as the Slave and will also be used for Sofie, to test manipulation of the Slave instruments and force-feedback. Based on ongoing insight, a second master is being designed (Master Device Two [51]). This master is intended for MIS in the thorax and abdominal region. First, the surgeon's information will be discussed, then the haptic interfaces of Master Device One and of Master Device Two; and subsequently the operator control panel.

### 6.1.1 The surgeon's information

First of all the surgeon needs information to perform MIS with a robotic system: surgical and system information, both provided at the master. The first is constructed from information of the surgical area and the team surrounding the table:

- visual feedback from the surgical area should be provided with a stereoscopic system ([42] and users [19, 83]) since it improves the perception of the environment and makes endoscopic surgery easier. Additionally, according to [26] stereoscopic vision improves surgical performance. Shadow and multi-spectral vision can improve the visual feedback [93]. Multi-spectral vision incorporates information on e.g. underlying blood vessels,
- force-feedback to feel how much force is exerted on the tissue. This force-information should not burden the surgeon's visual information channel (displayed) but be provided as a sense of touch, by means of the haptic interfaces of the master, and
- communication between the surgeon and the team surrounding the table should be reinforced since the surgeon is physically separated from the table. An open master close to the operating table, and/or using e.g. headsets can attempt to do that.

### 6.1.2 Master Device One

Master Device One is developed by Grasman and Hendrix [59] see also [11], within the scope of vitreo-retinal eye-surgery. It can be used for the Slave for laparoscopy and thoracoscopy as well. Both vitreo-retinal eye-surgery and laparoscopy/thoracoscopy use small entry points to the field of surgery. Relatively long and slender instruments are used and these instruments require a similar range of instrument angular motion. The Master provides five DoFs per instrument:  $\Phi$ ,  $\Psi$ ,  $\Theta$ ,  $Z$  and a gripper. The three DoFs of the Slave instrument-tip additional to its gripper need to be provided for. Master Device One is equipped with motors for force feedback.

#### Layout of Master Device One

The requirements for this master, setup by Hendrix [59], are summarized here if they are relevant to control the Slave for laparoscopy and thoracoscopy. These requirements are divided into design and performance requirements. The design requirements discussed in [59] are: (i) provide the surgeon with an ergonomic position, (ii) provide intuitive manipulation of the instruments by means of the handles, (iii) provide five DoFs to manipulate an instrument in four DoFs relative to its incision and actuate the instrument gripper of the instrument as DoF

five, and (iv) provide displacement information to the Slave and return force-information to the surgeon. This force-feedback can be magnified. Additional design requirements implemented are low inertia of moving parts allowing fast and precise gripper control, short force-path to achieve a high stiffness for force-feedback, and force-feedback as direct as possible, to reduce backlash, friction and loss of stiffness. A more intuitive working environment is created by virtually placing the hands of the surgeon inside body cavity in which surgery is performed. The accompanying performance requirements are: (i) instrument movements of  $\pm 45^\circ$  in  $\Phi$  and  $\Psi$  direction,  $360^\circ$  for  $\Theta$  and 30 mm in  $z$ -direction, (ii) resolution at the tip should be equal to or higher than the resolution a surgeon can position his hand with ( $50 \mu\text{m}$ ) [104], and (iii) continuous and maximum force levels are set to 3 and 10 N respectively. These values are based on literature and experiments. [115] states that an index finger can exert 7 N and a middle finger 6 N without experiencing discomfort or fatigue. [59] performed experiments with a one-DoF experimental set-up showing continuous forces up to 3 N and a maximum of 10–15 N. These experiments indicate the range of forces, which depends on the stiffness of the contact. These requirements match with the expected requirements for a master used to operate the Slave for laparoscopic and thoracoscopic surgery.

#### Master Device One as realized

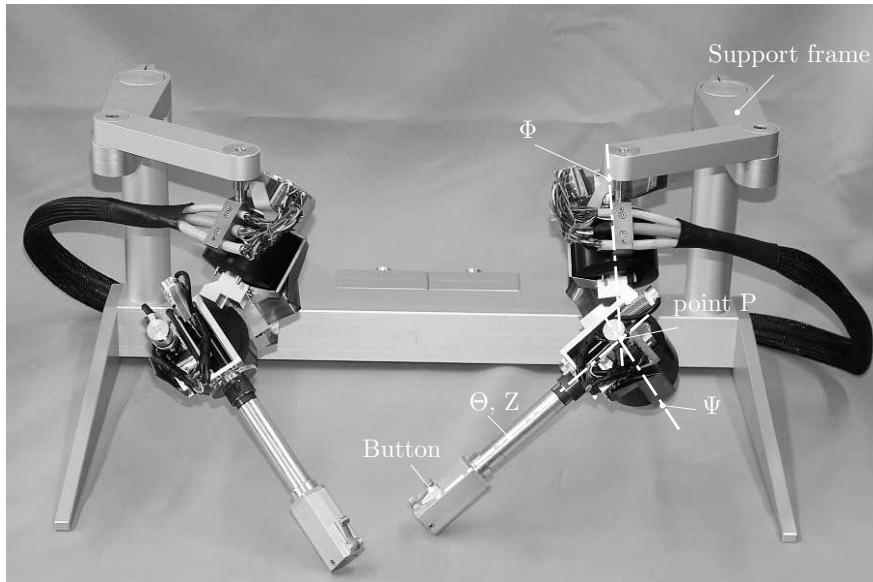


Figure 6.1: Master Device One with two 5-DoF haptic interfaces connected to their support frame [58]. The DoFs of one interface are shown. Point P is the intersection of the  $\Phi$ ,  $\Psi$  and  $\Theta$  axis. The support frame (an initial test version) allows translation and provides fixation of the position of point P to deal with different entry points. Each DoF of the 5-DoF haptic interfaces has a motor connected to provide force-feedback.

Grasman and Hendrix [59] developed the master consisting of a support frame with two 5-DoF haptic interfaces (Figure 6.1), one for each hand. The image of each instrument should be parallel to its 5-DoF haptic interface for intuitive operation. Adjustment of the frame prior to surgery, places and orientates each 5-DoF haptic interface parallel to its instrument and allows to deal with different positions of entry points. The 5-DoF haptic interface is based on a serial layout. As depicted in Figure 6.1 four parts can be distinguished:  $\Phi$  and its housing,  $\Psi$  and its housing, a  $\Theta$ -Z part and a button to control a gripper. The  $\Theta$ -Z part of the 5-DoF haptic interface has a parallel layout. All five DoFs are actuated with motors. Encoders are used to measure the rotation of the motor shafts. The length of the interface between rotation point P (intersection point of the  $\Phi$ ,  $\Psi$  and  $\Theta$  axis) and its tip is set empirically to  $\approx 150$  mm. With this length, the rotation point is placed above the wrist joint of the operator. This layout is very comfortable for a movement in  $\Phi$  and  $\Psi$  direction. To maintain this configuration during operation, the  $z$ -range is limited. A jogging mode will be implemented to control the instrument in its whole  $z$ -range. The  $\pm 90^\circ$   $\Theta$  rotation of the 5-DoF haptic interface, allowed by the operator's wrist is increased by implementing a jogging mode as well.

## Evaluation and performance

Table 6.1: Properties for the different DoFs of the 5-DoF haptic interface as realized [11, 59]. These properties are derived from the design and specifications of its components. With \*in practice restricted.

	$\Phi$	$\Psi$	$\Theta$	Z	Button
Range	$\pm 90^\circ$	$-88^\circ/45^\circ$	$\pm 175^\circ$	$\pm 8$ mm	5 mm
Resolution	$35 \mu\text{m}$	$35 \mu\text{m}$	0.1 mrad	$1.8 \mu\text{m}$	$25 \mu\text{m}$
Continuous force/torque	3 N	3 N	0.049 Nm*	2.4 N	1.9 N
Maximum force/torque	10 N	10 N	0.65 Nm*	32 N*	3.9 N

As indicated in Table 6.1, the resolution at the tip is higher than the resolution a surgeon can position his hand with ( $50 \mu\text{m}$ ) [104]. The range in  $\Phi$  and  $\Psi$  direction is made as large as possible and fulfills the requirements for eye surgery as well as laparoscopy and thoracoscopy. The limitation of  $-88^\circ$  in  $\Psi$ -direction is set to prevent alignment of the  $\Phi$  and  $\Theta$  axes. The  $\Theta$ -range is slightly smaller than the required range. It will be operated in jogging mode to increase the range. The  $z$ -stroke will be operated in jogging mode as well, to imitate a stroke of 300 mm. The continuous and maximum force levels also comply with the forces during endoscopy as can be seen in the requirements for the Slave for laparoscopy and thoracoscopy. The three DoFs of the Slave that are not implemented in this master are thought to be provided by switching control from coarse to fine manipulation. This to control coarse placement of the instrument-tip and ad-

ditionally fine-manipulation of its DoFs. Or an adaptor with additional DoFs should be developed. Master Device One and the Slave will be implemented in Sofie to test their cooperation and implement force-feedback.

### 6.1.3 Master Device Two

This section presents the design of the 8-DoF haptic interface of the Master Device Two [51] providing eight DoFs per hand. It controls the manipulators and instruments of the Slave for laparoscopic and thoracoscopic surgery. Each of the 8-DoF haptic interface DoFs has a motor connected, providing the surgeon with force feedback.

#### Basic layout of Master Device Two

The design requirements of this master are similar to the design requirements in Section 6.1.2. With in addition, three additional DoFs to be integrated to provide an 8-DoF haptic interface. Now the performance requirements and subsequently the designed 8-DoF haptic interface are presented. The performance requirements regarding the resolution at the tip and the continuous force-levels are similar to the requirements proposed in Section 6.1.2. With in addition:

- a smaller gripper force-feedback than the required force for the instrument gripper, because a surgeon normally uses a forceps while suturing. This forceps has a transmission ratio smaller than 0.25, which reduces the force the surgeon exerts, and
- a similar range of orientation of the gripper as the instrument on the Slave. However, the 8-DoF haptic interface is not required to provide the same angles. Scaling factors and speed control (jogging mode) can be applied to extend ranges and/or increase accuracy.

The basis for the design of Master Device Two is to measure the position and orientation of the surgeon's hand in the best possible way. This information should be converted to the required resulting position and orientation of the instrument-tip inside the patient. To this end, a mechanical coupling between the surgeons hand and fixed world is proposed. Master Device Two consists of a frame and two 8-DoF haptic interfaces, one for each hand. Each 8-DoF haptic interface consists of a parallelogram (Figure 6.2(a)), supported at one joint S. Point A of this parallelogram can be moved in  $x$ ,  $y$  and  $z$ , see Figure 6.2. A cardanic joint at point A of the parallelogram provides the required orientational DoF to control the instrument-tip. The surgeon operates the handle, which provides two additional DoFs and is connected to this cardanic joint. The 8-DoF haptic interface has rotating parts only. Its rotating encoders and actuators provide for angle measurement and force-feedback.

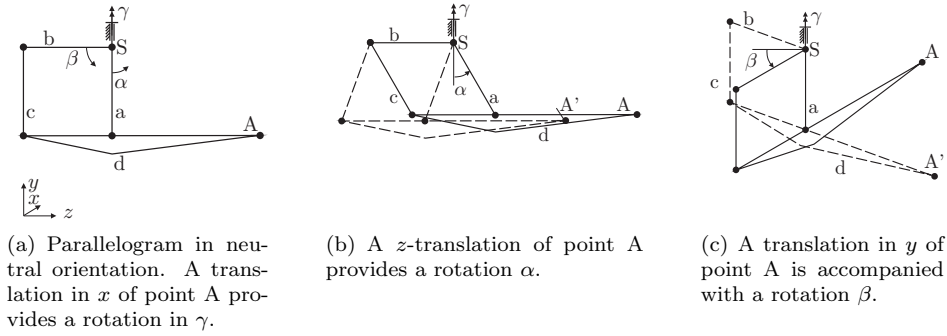


Figure 6.2: The 8-DoF haptic interface has a parallelogram supported at joint S as basic structure. This parallelogram provides measurement of and force-feedback in  $x$ ,  $y$  and  $z$  of point A. Left shows the neutral position, middle and right show the rotation resulting from the movement applied in point A, a next position is indicated with [—].

### 8-DoF haptic interface as designed

Figure 6.3 on the next page, displays one of two 8-DoF haptic interfaces. Frame f will be connected to the main frame of the Master. It supports fork e and a high-torque motor driving the fork. This motor drives the fork in  $\gamma$  by means of a capstan drive. The capstan drive provides a transmission ratio without backlash and is suitable for short strokes. The motor-encoder measures the rotation with increased resolution compared to an encoder located directly between frame a and fork e. Fork e provides support axis S to the parallelogram (similar to joint S in Figure 6.2). Parts a, b, c,  $d_1$  and  $d_2$  in this figure, form the parallelogram of Figure 6.2. Fork e supports arm b and a as to allow their independent rotation. It holds two high-torque motors, each actuating one arm via a capstan drive as well. Arms b and a (aluminium), each have a middle rib, because both arms are milled from two sides. The front arm (a) is larger, since it also transmits torsional loads. Additional glued plates close the open box, to provide torsional and bending stiffness. Rod c holds arm  $d_{1,2}$ , while arm a provides the main support point. Part  $d_1$  and  $d_2$  form the first axis  $\theta$  of the cardanic joint, with point A at the end of  $d_2$ . Part  $d_1$  consists of a large diameter cylinder with bearings at its ends, supporting the thin walled cylinder  $d_2$ . A motor inside  $d_1$  actuates rotation of  $d_2$ . Two additional motors, perpendicular to the  $\theta$  axis, actuate  $\phi$  and  $\psi$ , the second and third axis of the cardanic joint (i), by means of a cable transmission. Point A is the intersection point of the three axes  $\theta$ ,  $\phi$  and  $\psi$ . A handle (h) is connected to point A. The weight of the three motors mounted in  $d_1$ , acts as a counter-balance of the cardanic joint (i) and the handle (h). The handle provides a thumb actuated button to close the gripper and an index finger actuated wheel to apply the instrument gripper's yaw movement. Motors providing force-feedback to this button and wheel will be integrated in the handle. Further refinement of the design will be followed by realization and tests, but is left for future research.

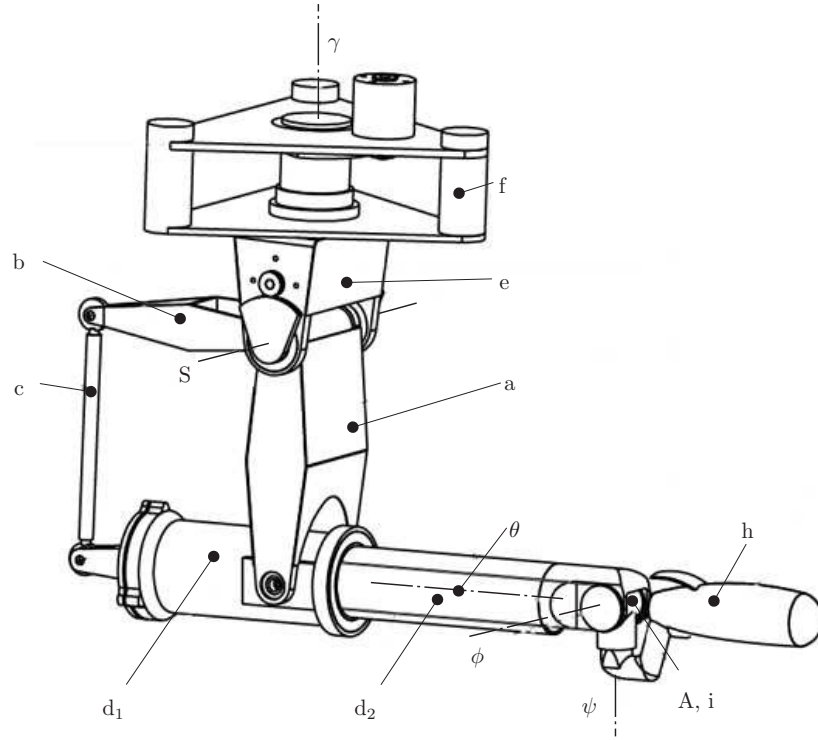


Figure 6.3: One 8-DoF haptic interface of Master Device Two.

#### 6.1.4 Operator control panel

The operator control panel presented in this section is intended for the commercial-product. This operator control panel allows the surgeon to obtain (basic) system-information, set-up the system and adjust its parameters during surgery. The commercial-product should have this operator control panel integrated in the master. Figure 6.4 displays the functions of the buttons (touch control) and indication lights. The left of this figure shows general system information and required actions. Here the surgeon can start and stop the system with the appropriate buttons. The surgeon assigns each haptic interface to a slave instrument-manipulator, and assigns one of the haptic interfaces to manipulate the Slave endoscope-manipulator, see Figure 6.5 for an illustration. The system status is indicated with lights, as well as problems that need attention. A service light should indicate when maintenance is required. The right of this figure shows the operator control panel used during surgery. It consists of a part occasionally used and a part frequently used. The first gives the possibility to scale the movements (and forces) during surgery, to switch force-feedback on or off, and to calibrate the camera. The frequently used operator control panel (possibly pedals) provides for: taking a break, clutching the master pens to reorient them

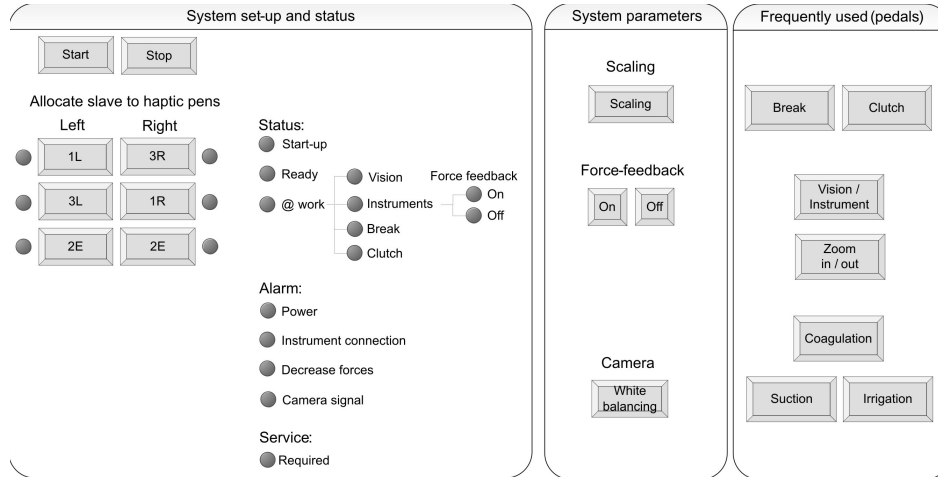


Figure 6.4: Example of a surgeon's operator control panel. Left shows the initial robot set-up (buttons) and its status (lights), the middle is more frequently used during surgery (buttons) and the right of the operator control panel is frequently used, possibly by means of pedals.

when required, switch between manipulation of the endoscope-manipulator and instrument-manipulator, zoom of the endoscope, coagulation of the appropriate instrument (if required), and control of suction and irrigation.

The system needs to be user-friendly. It should be intuitive to allow using the system with just a short learning curve. The training should include setting-up and using the system. It should cover procedures to solve common problems that might occur, like loss of camera-sight. A more extensive training should be followed to perform maintenance. A second operator control panel allows people trained for maintenance to check and test the system.

## 6.2 Interaction between master and slave

The Master is being operated by the surgeon and controls the Slave, performing surgery at the operating table. The Master and Slave are both connected to an electronic hardware cabinet. This cabinet is the interpreter between the Master and Slave. The PC is coupled to the hardware cabinet for development purposes. It is used to adjust the control-software (implement different controllers), perform measurements and observe the behavior of the system, based on signals.

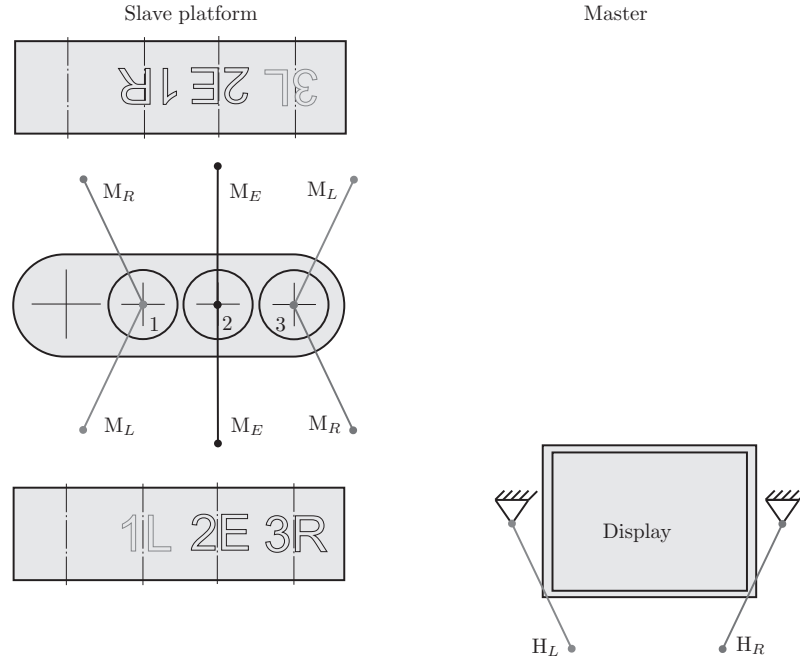


Figure 6.5: The number-letter combination shown on the platform (left) is used to assign the appropriate slave manipulator ( $M_L$ ,  $M_E$ ,  $M_R$ ) positioned in the platform (in 1, 2 or 3) to the appropriate haptic interface of the master ( $H_L$ ,  $H_R$ ), right. Here  $L$  indicates the left hand,  $R$  the right hand and  $E$  the endoscope.

### 6.2.1 Electronic hardware

For the current prototype version of Sofie the Master, electronic hardware cabinet and PC with control-software are separate systems. The electronic hardware cabinet in Figure 6.6 shown on the next page, couples the Slave and Master Device One. The Slave has 3x4 manipulator DoFs to be controlled, in addition to 3x4 instrument DoFs and 42 analogue sensor signals to be measured. These analogue signals consist of 24 force sensor signals, 12 absolute angle signals (for reference and homing), 3 gravitational signals and 3 temperature signals. Master Device One requires 2x5 haptic interface DoFs to be controlled. Each of the slave and master DoFs has one motor to be controlled and one encoder to be read.

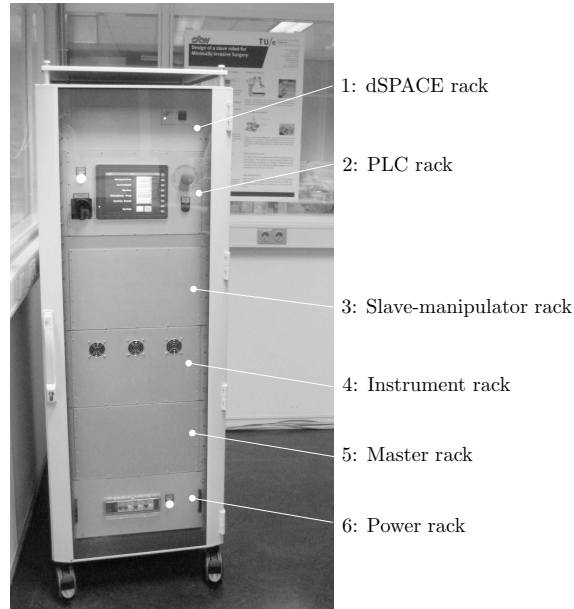


Figure 6.6: Electronic hardware cabinet.

The electronic hardware cabinet contains six racks, each with a separate function to make adjustments relatively easy when required. These racks are:

1. dSPACE rack, this dSPACE real-time simulation system performs data-acquisition and processing of the 34 encoders and 42 analogue sensor signals, and implements the controller developed on the PC. It contains one CPU (stand-alone Central Processing Unit) implementing the uploaded controller, 40 encoder, 64 ADC, 64 DAC channels, 48 digital I/O channels and several connector panels. It was chosen because it allows many in- and outputs, is easy to adjust, fast support is ensured and most students and researchers at TU/e are familiar with this system,
2. PLC (Programmable Logic Controller) rack for first line safety of the robot. The PLC monitors vital functions of the robot like the availability of supply voltages, the state of the safety buttons, the amplifier states and the availability of heartbeat signal from the dSPACE controller. Further machine safety is discussed in the safety section below,
3. slave manipulator rack with 12 power amplifiers for the actuators of the Slave,
4. instrument rack with 12 power amplifiers for the actuators of the instruments,
5. master rack with 10 power amplifiers for the force feedback actuators of the Master, and
6. power rack with a power supply for the various components.

### 6.2.2 Software

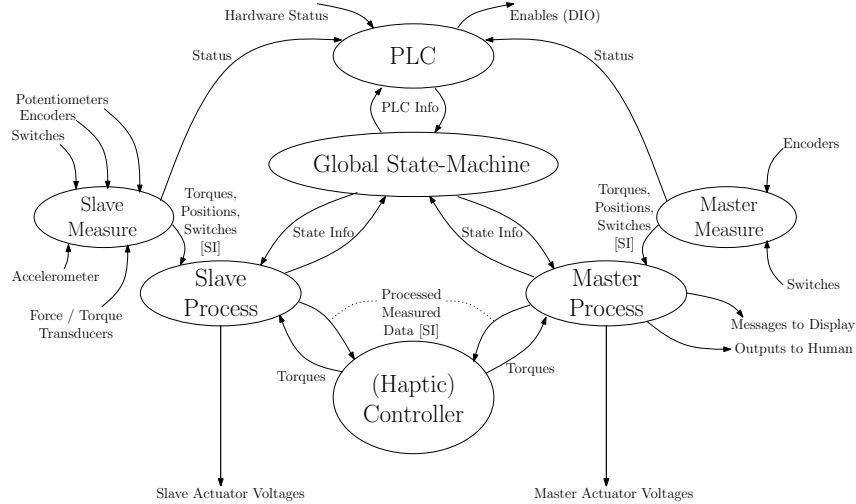


Figure 6.7: Structure of the software. It shows the processes running in the software and the information flow between these processes [116].

The software creates a platform for implementing haptic controllers and experimenting with these controllers. The software is built up of seven processes [116]: PLC, Global State Machine, Slave Measure, Slave Process, Master Measure, Master Process and (Haptic) Controller (Figure 6.7). All processes run on the dSPACE processor, except for the PLC process.

- **PLC:** takes care of all safety decisions, start up and stop of the machine based on hardware observations and state transitions of the rest of the system. It also brings the machine into a safe state when a failure is detected.
- **Global State Machine:** after clearing from PLC, it initializes the other processes and brings the system in operational state. It informs PLC of state changes and exchanges state information with Master and Slave Process.
- **Slave Measure:** reads switches and measures sensors like potentiometers, encoders, accelerometers and distance/force/torque sensors. It takes care of scaling and offset corrections and provides the sampled inputs (from dSPACE A/D converters) as signals with a physical meaning, like torques (in [Nm]) and angles [rad] related to the invariant point P. It checks whether sensor inputs are within expected ranges and informs PLC in case of malfunction.
- **Slave Process:** takes the sampled input data from Slave Measure and transfers these values to Haptic Controller. Furthermore, it processes sampled data into other signals like gravity compensation torque. It takes torques from the Haptic Controller process and takes care of sending it to the appropriate driver.

- Master Measure: has the same function as Slave Measure but now at the master side.
- Master Process: has the same function as Slave Process but now at the master side. Also takes care of presenting messages in human readable form.
- (Haptic) Controller: implements the controller(s) for the machine (in different states), actually coupling the master and Slave.

Several conventions are defined. The names and positive direction of these DoFs of the Master and Slave are defined. These DoFs or axes are coded related to whether they belong to the Master or Slave and to which manipulator they belong. With three manipulators/instruments available for the Slave and two for the master. Accordingly, the variables have a naming convention as well, and are required to be unique and meaningful. The signal type is part of this name, as well as the unit. This makes software written for e.g. one Slave manipulator easily adaptable for the other manipulators as well. The signals and blocks used for the software have a similar naming convention. All parameters are collected in one file to easily change values when required. The software is developed using Matlab, Matlab Simulink and State Flow.

### 6.2.3 Safety of the system

The Slave manipulators and Master are protected from performing unexpected movements by two safety layers. The first line safety is provided by the PLC. Without a confirmation from the PLC the system will cease from start-up. In addition, it will bring the system into a safe state in case of a detected failure during operation. The amplifier group (a group consists of the amplifiers belonging to one manipulator, one instrument or one 5-DoF haptic interface) with the detected failure is switched off, by disabling the outputs. The power supplies of the amplifiers is maintained. In case of an error in the Slave manipulator group, first the brake of the phi-axis is activated. In case of an emergency stop, all outputs and power supplies of the amplifier racks are disabled. An alternating heartbeat signal between PLC and dSPACE checks whether the other system is alive. The control software running on the dSPACE system provides the second safety line of the system. More specifically, the part of the system control restricting the range of movements, the maximum velocity etc. The maximum allowable torque executed by the motors, is set by the maximum allowable current on the motor amplifiers.

## 6.3 Conclusion and recommendations

### 6.3.1 Conclusion

Sofie (Surgeon's Operating Force-feedback Interface Eindhoven) consists of Master Device One, an electronic hardware cabinet and the Slave discussed in previous chapters. The surgeon controls the Slave at the operating table while operating the master. Two master's have been presented. The Master Device One has been developed first, within the scope of vitreo-retinal eye-surgery. It has a similar range of angular movements and forces required to operate the Slave for laparoscopy and thoracoscopy. It provides the surgeon with two five-DoF haptic pens to manipulate the Slave manipulators and obtain force-feedback. The remaining three DoFs of each manipulator and instrument combination can be controlled by switching the mode from coarse (manipulator) to fine manipulation (instrument-tip). The design of Master Device Two is proposed to provide the surgeon with two 8-DoF haptic interfaces. The electronic hardware cabinet actually couples Master Device One and the Slave. It performs data-acquisition and processing of the signals and implements the (haptic) control (dSPACE); provides a first system safety layer; houses amplifiers for the master, Slave manipulators and Slave instruments and provides the required power supply. This electronic hardware cabinet is not integrated with the master for development purposes. A separate PC is coupled to the hardware cabinet to implement different controllers, perform measurements and observe the behavior of the system (based on signals). The commercial product would omit a PC. It would have an operator control panel to set-up the system, obtain information on its status and change the robot parameters. This operator control panel would be integrated with the master. Just as the electronic hardware cabinet and the system providing the surgeon with surgical information. This information should consist of (stereoscopic) visual feedback and tools to improve communication with the team when required.

### 6.3.2 Recommendations and discussion

In this chapter we described the first prototype of Sofie. In the future a commercial version should have a master providing its two haptic interfaces. In addition, it will have the surgical information feedback; the operator control panel; and the electronic hardware for the Master, Slave and instruments integrated. This requires a smaller real time simulation system. The control-software will be implemented by this real time simulation system as well. The number of wires can be reduced by choosing brushed motors on the Slave manipulator and e.g. local amplification, signal conditioning and control of the manipulator and instrument axes. Eye-surgery is performed with four or five DoFs while laparoscopy/thoracoscopy is ideally performed with six or seven or even more DoFs at the instrument tip.

Master Device One is being provided with two 5-DoF haptic interfaces. Two or three DoFs of the Slave remain to be controlled. This can be realized by using the same DoFs of the Master in different control modes (e.g. coarse and precise range); or by development of an extension that should be applied to the 5-DoF haptic interface if used for laparoscopy/thoracoscopy. First the multi-mode alternative will be implemented.

The angle information of the manipulator adjustments (see again Section 3.5) can be used to orient the 5-DoF haptic interfaces according to the instruments and to use control to prevent collisions of the manipulators. However, we believe that the surgeons can use visual feedback to orient and prevent collision of the manipulators.

The master-slave system could also be used in semi-autonomous mode, if e.g. the manipulators follow the movements of the heart and the surgeon performs his/her manipulation on top of these automated movements. The heart would then appear to be stationary, this application of motion compensation is mentioned in e.g. [53] as well. The Slave should be able to perform these actions, since the required degrees of freedom are already actuated, but dedicated controls need to be developed.

Master-slave systems provide the surgeon with an improved body posture and more dexterity in performing surgery. A study should be performed on the long-term effect on surgeons using a master-slave systems. Besides, the influence on patient-safety while using robotic systems with and without force-feedback can be studied.

## Chapter 7

# Conclusion and Recommendations

### 7.1 Introduction

With Minimally Invasive Surgery (MIS) long, slender instruments and a video endoscope enter the body cavity through small incisions (1 cm). MIS has many advantages for the patient. However, performing conventional MIS requires extensive training, experience to determine the force executed on the tissue based on visual feedback mainly (as seals reduce force-feedback), and often an uncomfortable body posture. Consequently MIS is mainly used for relatively simple procedures, except by the specialist surgeon. Robotic MIS provides surgeons with intuitive natural hand-eye coordination, scaled movements to increase accuracy, additional degrees of freedom (DoFs) providing wrist dexterity, often stereoscopic ('3D') visual feedback and an improved body posture allowing more complex MIS. The type of robotic surgical systems discussed here, have a master operated by the surgeon, controlling the slave performing surgery by means of an electronic hardware cabinet. The overview of existing systems made at the start of this project indicated the features required additional to the features of the most common commercially available system (the da Vinci) as presented above. A field study (observed MIS procedures) performed, indicated similar additional features:

- connecting the slave to the table to ease table adjustment during surgery,
- providing additional DoFs to the instrument-tip to extend organ approach possibilities,
- providing the surgeon with force-feedback to reduce operating time and improve safety for the patient,

- reducing the size of the system to ease approaching the patient and the field of surgery, and
- reducing the costs and improve set-up time of the system.

These features are intended to be integrated in Sofie (Surgeon's Operating Force-feedback Interface Eindhoven). It is a robotic master-slave system being developed for laparoscopic and thoracoscopic surgery. It is a development set-up to implement haptic control and to evaluate the possible benefit of force-feedback, in addition to the benefit of additional DoFs. This thesis focus is on the design and realization of a demonstrator slave (*the Slave*) for Sofie. The ideas forming the basis to integrate the features mentioned above, into the Slave are:

- provide the endoscope and instrument manipulators with a single stiff frame near the field of surgery, which is connected to the table,
- integrate the force sensors in the manipulator and instrument, outside the patient,
- provide the instrument-tip with four DoFs.

The Slave as realized and presented in this thesis consists of:

- a pre-surgical set-up frame connected to the table, consisting of one platform-adjustment, one platform and three manipulator-adjustments (one currently realized) each fixating its instrument or endoscope manipulator to the platform thus realizing a short force-path between the instrument-tips,
- a four-DoF manipulator (three are required for surgery) with integrated force-sensors, to move its instrument or endoscope in  $\phi$ ,  $\psi$ ,  $\theta$  and  $z$  with respect to the incision and perform force-measurements, and
- a four-DoF instrument (at least two are required for surgery) to improve approach possibilities, provide dexterity while performing complex movements like suturing and perform force measurements.

In this chapter conclusions and recommendations regarding the design and realization of the Slave as presented above, and the system integration of Sofie with its electronic cabinet, software and master are presented.

## 7.2 Conclusion

### 7.2.1 Design and evaluation of the pre-surgical set-up

The pre-surgical set-up is connected to the table and provides the manipulators with a single frame near the field of surgery. It is compact to avoid interference

with the surgical team and highly adaptable. It consists of a five-DoF platform-adjustment at one side of the table, a platform, and three five-DoF manipulator-adjustments (the fifth being integrated in the manipulator). These are held by the platform in line up at an 80 mm pitch. The platform allows surgery to be performed at both of its sides. The platform-adjustment fixates the platform after the platform is being positioned (in  $x$ ,  $y$  and  $z$ ) near the field of surgery, parallel to and orientated along or across ( $\theta$ ) the table-top. The proposed weight-compensation mechanism improves adjustment of the platform. The manipulator-adjustments fixate each manipulator to the platform, after positioning it in its appropriate incision with an initial orientation towards the target organ. The combined length of each manipulator-adjustment and manipulator is comparable to the length of a human arm. This compact design results in a short force-loop between the instrument-tips.

The pre-surgical set-up is entirely mechanical. Its links are closed boxes to reduce weight and provide torsional stiffness. Its joints are locked during surgery to provide a stiff frame. The joint locking surfaces are located at the outer most radius to realize stiffness ( $k \sim R^2$ ) and reduce the required normal force. A wedge transmission (either translating or rotating) applied in all clamps reduces the actuation force, while keeping the required stroke of the handle limited. This results in the possibility of fast manual adjustment with a clamp handle rotation smaller than  $135^\circ$  and a limited required actuation torque.

The platform-adjustment and its platform as installed on a Maquet 1120 surgical table, provide the required range and have a first natural frequency with a lateral mode at  $\approx 27$  Hz (measured). The manipulator-adjustment has its (measured) first natural frequency with an in plane bending mode at  $\approx 45$  Hz in tall configuration and  $\approx 55$  Hz and in compact configuration (expected to be used most in practice) of the manipulator-adjustment. This fulfills the requirements.

### 7.2.2 Design and evaluation of the manipulator

The manipulator actuates the endoscope or instrument in  $\phi, \psi, \theta$  and  $z$  during surgery. It consists of a  $\Phi\Psi$ -manipulator with a parallelogram for  $\psi$  and a  $\Theta Z$ -manipulator with friction wheels for  $z$ , to manipulate the instrument and endoscope. Force sensors measuring forces executed with the instrument, are integrated in the manipulator instead of at the instrument tip, to avoid all chance of electrical signals being introduced into the patient.

The  $\Psi$  parallelogram provides a kinematically fixed point of rotation located stationary within the incision during surgery. This avoids all lateral force loading of the tissue surrounding the incision and thereby reduces post-operative pain. The kinematic rotation pole at that location excludes the necessity of an actual hinge in the incision. The manipulator (width 80 mm) allows for easy access to and overview of the port-sites. It has a small motion-envelope and least obstructs the assistants at the table, while moving the instrument or endoscope in its required range.

Two  $\Phi\Psi$ -manipulators have been designed in consecutive order. The worm-

wormwheel layout was designed and realized prior to the design of the ball-screw layout. The  $\Phi$ -drive of both manipulators is similar, the name indicates the  $\Psi$ -drive. Modal measurements on the worm-wormwheel manipulator (without instrument applied), show a first natural frequency of 19 Hz in  $\Phi$ . This frequency is determined by the rotational stiffness of the  $\Phi$  harmonic drive and the rotational inertia of the manipulator. Identification by a multisine input of this DoF revealed the same frequency. The first natural frequency of the instrument overrules this first natural frequency and determines the dynamic behavior of the manipulator. Identification of the  $\Psi$  showed a limited coherence for low frequencies caused by friction, which indicates it is not reliable to control in this range. The ball-screw drive reduces friction and improves stiffness. It is expected to perform better. In addition, the manipulator dimensions near the patient are reduced even more. The  $\Theta$ Z-manipulator (width 60 mm) supports the instrument. It provides the instrument with the required  $\theta$  and  $z$  movement, respectively by means of a rotating drum and friction wheels there in. Due to a partly parallel mechanism, some cross coupling exists between  $\Theta$  and  $Z$ . The instrument is removed from the  $\Theta$ Z-manipulator with one action. The drum of the  $\Theta$ Z-manipulator will eventually be removeable to sterilize this part of the manipulator. The electronical parts of the  $\Theta$ Z-manipulator are integrated with the  $\Theta$ Z-housing and will not be sterilized. Wire movements are limited as much as possible to realize a robust system. Forces executed with the instrument in  $\phi, \psi, \theta$  and  $z$  are measured in the manipulator as close to the trocar as possible. The  $\Phi$  and  $\Psi$  forces are corrected for the manipulator mass, its inertia and temperature influences. These force sensors display almost linear behavior. Integrated in the manipulator they do suffer from some hysteresis which might be caused by moving wires. The  $\Theta$  and  $Z$  force sensors do not show the expected linear behavior and further research is needed here.

### 7.2.3 Design and evaluation of the instrument

The instrument consists of a four-DoF tip, connected with a long and slender instrument-tube (outer diameter of 8.5 mm) to the drive-box of the tip. The 4 DoFs move the gripper in pitch, roll, pivot and close. It allows the surgeon to work at the backside of an organ, approach organs from more than one angle and perform complex movements. These DoFs are backdriveable, which allows the instrument to be removed from the trocar in case of an emergency. The transmission ratio in the tip is preferably smaller than one, for high output stiffness, accurate movements, reduced transmission load and small motors. However, this compromises the reach of the tip. The tip-transmission for pitch and roll is provided with zirconia bevelgears that are driven with concentric tubes inside the instrument-tube. Zirconia allows higher transmission loads than stainless steel, which is required for the high pitch and roll transmission ratio. Cables provide the gripper with pivot and close. The drive-box (60 mm diameter) contains four motors to drive each of the tip DoFs. The current used by these motors will initially indicate the forces at the tip. The range of motion and theoretical torques

that can be achieved with this instrument approximate the requirements closely.

#### 7.2.4 Sofie system-integration

Sofie consists of Master Device One, an electronic hardware cabinet, a PC and the Slave just discussed. It is a development set-up, to test cooperation of this master and slave, implement haptic control software and evaluate the possible benefit of haptic feedback and additional DoFs at the instrument-tip. The surgeon controls the Slave at the operating table while operating the Master. Two master's have been presented. The first, Master Device One, has been developed within the scope of vitreo-retinal eye-surgery. It provides surgical information (visual feedback) and two 5-DoF haptic interfaces to operate the Slave. These 5-DoF haptic interfaces provide the surgeon with the range of motion required to manipulate the Slave manipulators intended for laparoscopy and thoracoscopy. Its DoFs are actuated and provide force-feedback. The remaining three DoFs of each manipulator and instrument combination can be controlled by switching the control mode from coarse (manipulator) to fine manipulation (instrument-tip). The design of the second master, Master Device Two is proposed to provide the surgeon with two 8-DoF haptic interfaces.

The electronic hardware cabinet actually couples Master Device One and the Slave. It performs data-acquisition and processing of the signals and implements the (haptic) control. For commercialization, the Master requires its two haptic interfaces and the surgical information (visual feedback). This master should incorporate the following parts: (i) the electronic hardware cabinet, as far as control is not implemented locally, (ii) an operator control panel to set-up the system, obtain information on its status and change the robot parameters, (iii) and a system to improve communication with the team. This integration reduces the required space in the operating theater.

### 7.3 Recommendations

It is believed that the range of the pre-surgical set-up can even be smaller than stated in the requirements. This assumption has to be checked. The link-lengths can be reduced even more if these tests confirm this assumption, which is advantageous for the static and dynamic behavior (as first natural frequency present) of the pre-surgical set-up.

Scales applied at the joints of the pre-surgical set-up, in combination with information on type of surgery, anatomy and surgeon's preferences can eventually reduce the set-up time. Theoretically, the angle information of the manipulator adjustments can be used to orient the haptic pens or haptic interfaces of the master, according to the instruments and to use control to prevent collisions of the manipulators. However, most of the surgeons use visual feedback to orient and prevent collision of the manipulators.

The ball-screw  $\Phi\Psi$ -manipulator should be evaluated. A second design of the  $\Theta Z$ -manipulator should provide separate instrument support and  $\Theta$  and  $Z$  drive, making the drive independent of the reaction forces of the instrument. The instrument support should contain rolling parts to reduce the friction in the driving direction and improve the force-measurements. At the same time the height of the manipulator might be reduced. This reduces the weight and rotational inertia of the manipulator and it increases the useable length of the instrument. Wiring of the manipulator should be reconsidered to reduce the hysteresis in the force measurements. Flex foils might reduce experienced stiffness, relative movements between wires should be prevented.

The instrument has four DoFs. Two of these DoFs are driven with zirconia bevelgears. A more extensive evaluation of the zirconia bevelgears regarding the Weibull flaw statistics should be performed. The cables for pivot and close are preloaded during assembly to ensure each cable winds its wheels. Preloading cables reduces the load allowed. Replacing the cable with Dyneema can improve this load, but requires design of a compact fixation method. Further experiments and measurements should reveal the appropriateness of this four-DoF tip layout, its transmission and force measurements. How well the forces executed with/on the instrument can be sensed at the motor and felt at the controls will be tested (the new Master Device Two design should be refined and realized). Force-sensors integrated with the motor-support of the instrument drive-box can be applied to verify (and improve) the force measurements. Experiments should include finding the forces required by the surgeon, performing surgery (or dummy experiments) with this tip layout. If smaller forces apply, smaller motors can be used, which leads to a (required) mass reduction of the drive-box. The mechanical part of the instrument and drive-box will be separable from the electromechanical part of the drive-box for sterility, in the next design. After evaluation of the instrument, expansion of the assortment of end-effectors at the instrument tip is required.

Currently, Sofie has a master, a slave, an electronic hardware cabinet and (high-level) control software. This clears the way to further test the system in setting it up, manipulating a needle with additional tip DoFs (on a dummy), implementing haptic control and evaluating the resulting force-feedback. In the future, Sofie could be used in semi-autonomous mode even, if e.g. the instruments follow the movements of the heart and the surgeon performs his/her manipulation on top of these automated movements. The Slave is able to perform these actions, since the required degrees of freedom are already actuated. However, dedicated control software needs to be developed. A study should be performed on the long-term effect on surgeons using a master-slave systems. This study should check whether the more comfortable body posture and dexterity while performing MIS improves the long term as well. Additionally, the influence on patient-safety while using robotic systems with and without force-feedback can be studied.

We believe this project contributed to a further development of slave robots with force sensors and dexterity, and will benefit both the surgeon and the patient.

## Bibliography

- [1] R.J.T. van Aaken. Design of a 4 dof instrument manipulator for minimally invasive robotic surgery. Master's thesis DCT 2007.143, Technische Universiteit Eindhoven, 2007.
- [2] R. van der Aalst. Mirs slave modal analysis. Measurement report CST 2010.036, Eindhoven University of Technology, April 2010.
- [3] S. Aiono, and Soim B. Gilbert, J.M., P.A. Finlay, and A. Gordon. Controlled trial of the introduction of a robotic camera assistant (endoassist) for laparoscopic cholecystectomy. *Surgical Endoscopy*, 16(9):1267–1270, 2002.
- [4] T. Akinbiyi, C.E. Reiley, S. Saha, D. Burschka, C.J. Hasser, and and Okamura A.M. Yuh, D.D. Dynamic augmented reality for sensory substitution in robot-assisted surgical systems. In *Proceedings of the 28<sup>th</sup> IEEE EMBS Annual International Conference*, pages 567–570, 2006.
- [5] D. Amroch and G.B. Chiara. Pitfalls in laparoscopic cholecystectomy, how to fix them. In *The 21st International Conference of Society for Medical Innovation and Technology*, page 31. Society for Medical Innovation and Technology, October 2009. [www.smit2009.com](http://www.smit2009.com).
- [6] M. Anvari, C. McKinley, and H. Stein. Establishment of the worlds first telerobotic remote surgical service for provision of advanced laparoscopic surgery in a rural community. *Annals of Surgery*, 241(3):260–264, March 2005.
- [7] M. Balázs, H. Feussner, G. Hirzinger, K. Omote, and A. Ungeheuer. A new tool for minor-access surgery: Replacing mechanical joints in laparoscopic forceps with elastic beams for improved pressure control and sensitivity. *IEEE Engineering in Medicine and Biology Magazine*, 17(3):45–48, May/June 1998.
- [8] L.J.M. van den Bedem. Study on procedures in minimally invasive surgery. Literature study DCT 2006.126, Technische Universiteit Eindhoven, August 2006.

- [9] L.J.M. van den Bedem, P.C.J.N. Rosielle, and M. Steinbuch. Design of a slave robot for laparoscopic, thoracoscopic surgery. In *The 20th International Conference of Society for Medical Innovation and Technology*, page F.016. Society for Medical Innovation and Technology, 2008.
- [10] L.J.M. van den Bedem, J.C. Groen, P.C.J.N. Rosielle, and M. Steinbuch. Design of a slave robot for minimally invasive surgery. In *The 21st International Conference of Society for Medical Innovation and Technology*, page 52. Society for Medical Innovation and Technology, October 2009. [www.smit2009.com](http://www.smit2009.com).
- [11] L.J.M. van den Bedem, R. Hendrix, P.C.J.N. Rosielle, M. Steinbuch, and N.M. Nijmeijer. Design of a minimally invasive surgical teleoperated master-slave system with haptic feedback. In *Proceedings of the 2009 IEEE International Conference on Mechatronics and Automation*, pages 60–65, Changchun, China, 8–12 August 2009.
- [12] W.A. Bemelman, J. Ringers, and de Wit C.W.M. Meijer, D.W., and J.J.G. Bannenberg. Laparoscopic-assisted colectomy with the dexterity<sup>TM</sup> pneumo sleeve. *Diseases of the Colon & Rectum*, 39(10):S59–S61, October 1996.
- [13] P.J. Berkelman, P. Cinquin, J. Troccaz, J.-M. Ayoubi, and C. Létoublon. *Medical Image Computing and Computer-Assisted Intervention*, volume 2488/2002 of *Lecture Notes in Computer Science*, chapter Development of a compact cable-driven laparoscopic endoscope manipulator, pages 17–24. Springer Berlin/ Heidelberg, 2002.
- [14] J.C. Bowersox, A. Shah, J. Jensen, J. Hill, P.R. Cordts, and P.S. Green. Vascular applications of telepresence surgery: Initial feasibility studies in swine. *Journal of Vascular Surgery*, 23(2):281–287, February 1996.
- [15] P. Breedveld and S. Horose. Development of steerable endoscopes to improve depth perception during laparoscopic surgery. *Journal of Mechanical Design*, 126:2–5, 2004.
- [16] P. Breedveld and M. Wentink. Eye-hand coordination in laparoscopy an overview of experiments and supporting aids. *Minimally Invasive Therapy and Allied Technologies*, 10(3):155–162, 2001.
- [17] P. Breedveld, H.G. Stassen, D.W. Meijer, and J.J. Jakimowicz. Manipulation in laparoscopic surgery - overview of impeding effects and supporting aids. *Journal of Laparoendoscopic and Advanced Surgical Techniques*, 9(6): 469–480, 1999.
- [18] P. Breedveld, H.G. Stassen, D.W. Meijer, and J.J. Jakimowicz. Observation in laparoscopic surgery - overview of impeding effects and supporting aids. *Journal of Laparoendoscopic and Advanced Surgical Techniques*, 10(5):257–267, 2000.

- [19] I.A.M.J. Broeders. General surgeon, private communication, umc utrecht, August 15th 2006.
- [20] I.A.M.J. Broeders. Observed procedures, 2006–2007.
- [21] I.A.M.J. Broeders. Robottechnologie bij endoscopische chirurgie. *het Nederlands Tijdschrift voor Geneeskunde*, 8(1):10–11, March 2005. Dutch.
- [22] I.A.M.J. Broeders, J. Bonjer, and Th.J.M.V. van Vroonhoven. *Moderne patiëntenzorg in Nederland*, chapter Implementatie van laparoscopische chirurgie in Nederland: langzaam maar zeker voortschrijdend, pages 44–51. Elsevier gezondheidszorg, Maarssen, the Netherlands, first edition, 2002. Dutch.
- [23] T.L. Brooks. Telerobotic response requirements. In *Proceedings of the IEEE International Conference on Systems, Man, and Cybernetics*, pages 113–120, Los Angeles, CA, November 1990.
- [24] G.F. Buess, A. Arezzo, M.O. Schurr, F. Ulmer, H. Fisher, L. Gumb, T. Testa, and C. Nobman. A new remote-controlled endoscope positioning system for endoscopic solo surgery, the fips endoarm. *Surgical Endoscopy*, 14(4):395–399, April 2000. Springer-Verlag New York Inc.
- [25] G.C. Burdea. *Force and Touch Feedback for Virtual Reality*. John Wiley & Sons, Inc., 1996. ISBN 0-471-02141-5.
- [26] J.C. Byrn, S. Schluender, C.M. Divino, J. Conrad, B. Gurland, E. Schlasko, and A. Szold. Three-dimensional imaging improves surgical performance for both novice and experienced operators using the da vinci robot system. *The American Journal of Surgery*, 193(4):519–522, 2007.
- [27] W.D. Callister Jr. *Materials Science and Engineering, an introduction*. John Wiley & Sons Australia, sixth edition, 2003. ISBN 0-471-22471-5.
- [28] Cancerweg. *Medical Dictionary*. <http://cancerweg.ncl.ac.uk/omd/>, viewed April 2006.
- [29] M.C. Çavuşoğlu, F. Tendick, M. Cohn, and S. Shankar Sastry. A laparoscopic telesurgical workstation. In *IEEE transactions on robotics and automation*, volume 15, pages 728–739, August 1999.
- [30] M.C. Çavuşoğlu, W. Williams, F. Tendick, and S. Shankar Sastry. Robotics for telesurgery: Second generation berkeley/ucsf laparoscopic telesurgical workstation and looking towards the future applications. *Industrial Robot*, 30(1):22–29, January 2003. Special Issue on Medical Robotics.
- [31] J.K. Champion, J. Hunter, T. Trus, and W. Laycock. Teaching basic video skills as an aid in laparoscopic suturing. *Surgical Endoscopy*, 10(1):23–25, 1996.

- [32] J.Y.C. Chen, E.C. Haas, and M.B. Barnes. Human performance issues and user interface design for teleoperated robots. *IEEE Transactions on systems, man, and cybernetics - Part C: Applications and Reviews*, 37(6): 1231–1245, November 2007.
- [33] L. Crainich. Articulated medical instrument. Patent US 5549637 (A), Crainich, L., August 27 1996.
- [34] J. Danis. Theoretical basis for camera control in teleoperating. *Surgical Endoscopy*, 10(8):804–808, 1996.
- [35] G. De Gerssem. *Kinaesthetic feedback and enhanced sensitivity in robotic endoscopic telesurgery*. PhD thesis, Katholieke Universiteit Leuven, Belgium, 18 February 2005. ISBN 90-5682-582-8.
- [36] K.G.E. van Dijck. Design of a 4-dof minimally invasive instrument for haptic robotic surgery. Master’s thesis DCT 2008-148, Technische Universiteit Eindhoven, 2008.
- [37] J.J. van den Dobbelsteen, A. Schooleman, and J. Dankelman. Friction dynamics of trocars. *Surgical Endoscopy*, 21(8):1338–1343, August 2007.
- [38] F. Dubois, G. Berthelot, and H. Levard. Cholecystectomy par coelioscope. *Presse médicale*, 18(19):980–982, 1989.
- [39] A.V. Dubrowskij. Rotation joint, especially for medical instruments. Patent US 2003032948 (A1), Karl Storz GmbH & Co, February 13 2003.
- [40] M. Eto and S. Naito. *Endouroonology*, volume 6 of *Recent Advances in Endourology*, chapter Robotic Surgery Assisted by the ZEUS System, pages 39–48. Springer Tokyo, 2006.
- [41] R.T. Fenner. *Mechanics of Solids*, chapter 5: Bending of beams, page 194. CRC Press, Florida, 1993.
- [42] M. Ferre, R. Aracil, and M.A. Sánchez-Urán. Stereoscopic human interfaces, advanced telerobotic applications for telemanipulation. *IEEE Robotics and Automation Magazine*, 15(4):50–57, December 2008.
- [43] Formatec. *Formatec Technical Ceramics*. [www.formatec.nl](http://www.formatec.nl), 2009. viewed 2009.
- [44] Thomas Frede, Ahmed Hammadya, Jan Klein, Dogu Teber, Noriyuki Inaki, Masahiro Waseda, Gerhard Buess, and Jens Rassweiler. The radius surgical system a new device for complex minimally invasive procedures in urology? *European Urology*, 51:1015–1022, 2007.
- [45] Büro für angewandte Mineralogie. *High-Temperature-Coatings*. [www.a-m.de/eng/faq/zro2.html](http://www.a-m.de/eng/faq/zro2.html), April 2010.

- [46] J.M. Gilbert, S. Aiono, B. Soin, P.A. Finlay, and A. Gordon. Controlled trial of the introduction of a robotic camera assistant (endoassist) for laparoscopic cholecystectomy. In *Proceedings of 11th Annual Scientific Meeting of the Society for Minimally Invasive Therapy*, Boston, USA, September 1999.
- [47] J.C. Groen. Eerste metingen aan een robotframe (5dof) voor minimaal invasieve chirurgie. Bachelor Eind Project DCT-report 2009.070, Technische Universiteit Eindhoven, Eindhoven, 2009. in Dutch.
- [48] Crosby Group. Tackle block and sheave assembly. Warning, use & maintenance information, The Crosby Group, Inc., 2008.
- [49] G.S. Guthart and J.K. Salisbury. The intuitive telesurgery sytem: Overview and application. In *Proceedings of the 2000 IEEE International Conference on Robotics & Automation*, pages 618–621, 2000.
- [50] A.J.H. Haak. *De Menselijke Maat*. Number ISBN 90-407-2567-5. Delft University Press, P.O. Box 98, 2600 MG Delft, the Netherlands, completely revised edition, 2005.
- [51] D.W.P. van Haendel. Concept for an 8-dof per hand master with force feedback for control of a laparoscopic, thoracoscopic surgery robot. Free space project, Eindhoven University of Technology, 2010.
- [52] U. Hagn, M. Nickl, S. Jörg, G. Passig, T. Bahls, A. Nothhelfer, F. Hacker, L. Le-Tien, A. Albu-Schäffer, R. Konietschke, M. Grebenstein, R. Warpup, R. Haslinger, M. Frommberger, and G. Hirzinger. The dlr miro: a versatile lightweight robot for sugical application. *Industrial Robot: An International Journal*, 35(4):324–336, 2008.
- [53] U. Hagn, T. Ortmaier, R. Konietschke, B. Kübler, U. Seibold, A. Tobergte, M. Nickl, S. Jörg, and G. Hirzinger. Telemanipulator for remote minimally invasive surgery, requirements for a light-weight robot for both open and laparoscopic surgery. *IEEE Robotics and Automation Magazine*, 15(4):28–38, December 2008.
- [54] B. Hannaford. *Lecture Notes of the first European Summer School on Surgical Robotics*, chapter Experimental measurements for specification of surgical mechanisms and understanding of surgical skill. September 2003.
- [55] B. Hannaford and J. Rosen. Raven surgical robot: Overview. IIIrd Summer European University, February 2007.
- [56] C. Hasser. Force-reflecting anthropomorphic hand masters. 82 pp ALCF-TR-1995-0110, Armstrong Laboratory Technical Report, Wright-Patterson AFB, OH, 1995.
- [57] Armstrong Healthcare. *EndoAssist - total control at a glance*. [www.armstrong-healthcare.com](http://www.armstrong-healthcare.com), 2004.

- [58] R. Hendrix. *Design of a Haptic Master*. PhD thesis, Eindhoven University of Technology, 2010. to be published.
- [59] R. Hendrix, P.C.J.N. Rosielle, and H. Nijmeijer. Design of a haptic master interface for robotically assisted vitreo-retinal eye surgery. pages 1–6, München, Germany, 22–26 June 2009.
- [60] J. Himpens, G. Leman, and Cadiere G.B. Telesurgical laparoscopic cholecystectomy. *Surgical Endoscopy*, 12(8):1091, 1998. Letter.
- [61] D.E. Hoefig and F. Lei. Endoscope with variable direction of view. Patent US 2007055103 (A1), Karl Storz GmbH & Co, March 2007.
- [62] R. Howe and D. Kontarinis. Task performance with a dexterous teleoperated hand system. In *Proceedings of SPIE*, volume 1833, pages 199–207, Boston, MA, November 1992. SPIE.
- [63] *da Vinci Surgical System Brochure*. Intuitive Surgical Inc., Sunny Vale, CA, USA, 2005. [www.intuitivesurgical.com](http://www.intuitivesurgical.com).
- [64] Yoriko Iwamori, Jun Okamoto, and Masakatsu G. Fujie. Multi-dof forceps manipulator for an approach to the dorsal aspect of an organ. In *World Congress on Medical Physics and Biomedical Engineering 2006*, volume 14 of *IFMBE Proceedings*, pages 4164–4168. Springer Berlin Heidelberg, 2006.
- [65] J.E.N. Jaspers. *Simple Tools for Surgeons - Design and Evaluation of Mechanical Alternatives for "Robotic" Instruments for Minimally Invasive Surgery*. PhD thesis, Technische Universiteit Delft, Delft, the Netherlands, March 2006.
- [66] J.E.N. Jaspers and C.A. Grimbergen. Mechanical manipulator for intuitive control of endoscopic instruments with seven degrees of freedom. In *IEEE International Conference on Systems, Man and Cybernetics*, pages 2479–2484, 2004.
- [67] J.E.N. Jaspers, M. Bentala, J.L. Herder, B.A. de Mol, and C.A. Grimbergen. Mechanical manipulator for intuitive control of endoscopic instruments with seven degrees of freedom. *Minimally Invasive Therapy and Allied Technologies*, 13(3):191–198, 2004.
- [68] L.A. Jones. Kinesthetic sensing. In *Human and Machine Haptics*. MIT Press, 2000.
- [69] L.A. Jones and I.W. Hunter. Human operator perception of mechanical variables and their effects on tracking performance. *Advances in Robotics*, 42:49–53, 1992.
- [70] Yusuke Kamei and Chiharu Ishii. Passivity based bilateral control with motion scaling for robotic forceps teleoperation system with time delay. In *International Conference on Control, Automation and Systems*, volume xx, pages 1657–1662, Seoul, Korea, 2008.

- [71] Jin-Cheol Kim, Yong-Keun Lee, Bum-Son Lim, Sang-Hoon Rhee, and Hyeong-Cheol Yang. Comparison of tensile and knot security properties of surgical sutures. *Journal of Materials Science: Materials in Medicine*, 18 (12), 2007.
- [72] KISSsoft, *calculation programs for machine design*. KISSsoft, release 08-2009c edition, 2009. <http://www.kisssoft.ch>.
- [73] M. Kitagawa, D. Dokko, A.M. Okamura, and D.D. Yuh. Effect of sensory substitution on suture-manipulation forces for robotic surgical systems. *The Journal of Thoracic and Cardiovascular Surgery*, 129(1):151–158, 2005.
- [74] W.Way Lawrence, F.R.C.S. Sunil Bhojwala, and M. Toshiyuki. *Fundamentals of laparoscopic surgery*. New York, Churchill Livingstone Inc., 1995.
- [75] G.A.L. Leenknegt. Kaman sensor analysis: Accuracy, temperature and position dependence. Technical Report CST 2010.039, Technische Universiteit Eindhoven, July 2009.
- [76] G.A.L. Leenknegt. MIRS frf measurements. Measurement report CST 2010.037, Eindhoven University of Technology, 2010.
- [77] A. Linder. *WeBSurg*, chapter Video-assisted thoracoscopic surgery for the treatment of pneumothorax. [www.websurg.com](http://www.websurg.com), viewed June 2006.
- [78] Longman. *Longman, Dictionary of Contemporary English*. <http://www.ldoceonline.com/dictionary>.
- [79] M.J.H. Lum, D.C.W. Friedman, J. Rosen, G. Sankaranarayanan, H. King, K. Fodero, R. Leuschke, M.N. Sinanan, and B. Hannaford. The raven - design and validation of a telesurgery system. *International Journal of Robotics Research*, 28:1183–1197, 2009.
- [80] A.J. Madhani. *Design of Teleoperated Surgical Instruments for Minimally Invasive Surgery*. PhD thesis, Massachusetts Institute of Technology, USA, February 1998.
- [81] A.J. Madhani, G. Niemeyer, and J. Kenneth Salisbury Jr. The black falcon: A teleoperated surgical instrument for minimally invasive surgery. In *proceedings of the 1998 IEEE/RSJ International Conference on Intelligent Robots and Systems*, pages 936–944, Victoria, B.C., Canada, October 1998.
- [82] *Aktuellen Maedler-katalog (38)*. Maedler, 2009. [www.maedler.de](http://www.maedler.de).
- [83] J.G. Maessen. Cardiothoracic surgeon, private communication, academisch ziekenhuis maastricht, the netherlands, 2006–2008.
- [84] J.G. Maessen. Cardiothoracic surgeon, private communication, azm, July 31st 2006.

- [85] J. Marescaux, J. Leroy, F. Rubino, M. Smith, M. Vix, M. Simone, and D. Mutter. Transcontinental robot-assisted remote telesurgery: Feasibility and potential applications. *Annals of Surgery*, 235(4):487–492, 2002.
- [86] Hansen Medical. *Hansen Medical and Intuitive Surgical Cross-License Robotic Technologies*. <http://www.hansenmedical.com/newsroom/news-releases.aspx>, September 7 2005.
- [87] M.A. Minor and R. Mukherjee. Dexterous articulated linkage for surgical applications. Patent US6309403-B1, University of Michigan, October 30 2001.
- [88] H. Mohrmann-Lendla and A.G. Fleischer. The effect of a moving background on aimed hand movements. *Ergonomics*, 34(3):353–364, 1991.
- [89] Mondofacto. *Online Medical Dictionary*. [www.mondofacto.com/dictionary](http://www.mondofacto.com/dictionary), viewed March 2010.
- [90] R. Mukherjee and G. Song. Articulated manipulator for minimally invasive surgery (ammis). Patent US 5810716 (A), US Army, September 22 1998.
- [91] Z. Nawrat and P. Kostka. Polish cardio-robot ‘robin heart’. system description and technical evaluation. *The International Journal of Medical Robotics and Computer Assisted Surgery*, 2(1):36–44, 2006.
- [92] Z. Nawrat and P. Kostka. *Medical Robotics*, chapter Robin Heart - Perspectives of application of mini invasive tools in cardiac surgery, pages 265–290. I-Tech Education and Publishing, first edition, 2008.
- [93] O2view. *O2view, broad spectrum imaging*. [www.O2view.nl](http://www.O2view.nl), viewed December 2008.
- [94] T. Ortmaier. Concepts for an advanced (tele-) surgical robot system. In Lecture notes of the European Summer School on Surgical Robotics, September 2003. Montpellier, France.
- [95] T. Ortmaier, H. Weiss, and V. Falk. Design requirements for a new robot for minimally invasive surgery. *Industrial Robot: An International Journal*, 31(6):493–498, 2004.
- [96] T. Ortmaier, H. Weiss, and G. Hirzinger. A new robot for minimally invasive surgery. Lecture Notes in Computer Science on Medical Image Computing and Computer- Assisted Intervention, 2004.
- [97] W.J. Peine. Standard and metrology needs for surgical robotics. Presentation, Purdue University, Mechanical Engineering, November 2006. [http://www.isd.mel.nist.gov/medical.devices/Standard\\_and\\_Metrology\\_Needs\\_for\\_Surgical\\_Robotics](http://www.isd.mel.nist.gov/medical.devices/Standard_and_Metrology_Needs_for_Surgical_Robotics).

- [98] J. Peirs, J. Clijnen, D. Reynaerts, H. Van Brussel, P. Herijgers, B. Corteville, and S. Boone. A micro optical force sensor for force feedback during minimally invasive robotic surgery. *Sensors and Actuators A*, (115):447–455, 2004.
- [99] L. Podsedkowski. Robin heart 0, 1, and 3 mechanical construction development. *Bulletin of the Polish Academy of Sciences*, 53(1):79–85, 2005.
- [100] P.P. Pott, H.-P. Scharf, and M.L.R. Schwarz. Today’s state of the art in surgical robotics. *Computer Aided Surgery*, 10(2):101–132, 2005.
- [101] S.K. Ravensbergen. Assisted catheter steering for electrophysiological technology (accept). Master’s thesis, internal report DCT 2007.137, Technische Universiteit Eindhoven, 2007.
- [102] W. Reynolds Jr. the first laparoscopic cholecystectomy. *Journal of the Society of Laparoendoscopic Surgeons*, 5(1):89–94, January-March 2001.
- [103] P. Richard, G. Burdea, G. Birebent, D. Gomez, N. Langrana, and P. Coiffet. Effect of frame rate and force feedback on virtual object manipulation. *Presence-Teleoperators and Virtual Environments*, 5(1):95–108, 1996.
- [104] C.N. Riviera, R.S. Rader, and P.K. Khosla. Characteristics of hand motion of eye surgeons. In *Proceedings of the 19th International Conference of the IEEE Engineering in Medicine and Biology Society*, 30 October – 2 November 1997. Chicago.
- [105] L. Rosenberg. How to assess the quality of force-feedback systems. Technical report, Immersion Co., Santa Clara, CA, 1995.
- [106] P.C.J.N. Rosielle. Surgical robot. Patent WO/2007/133065, Eindhoven University of Technology, November 2007.
- [107] J.P. Ruurda. *Robot-assisted endoscopic surgery*. PhD thesis, University Utrecht, the Netherlands, 2003.
- [108] J.P. Ruurda, Th.J.M.V. van Vroonhoven, and I.A.M.J. Broeders. Robot-assisted surgical systems: a new era in laparoscopic surgery. *Annals of The Royal College of Surgeons of England*, 84(4):223–226, 2002.
- [109] R.M. Satava and S.R. Ellis. Human interface technology, an essential tool for the modern surgeon. *Surgical Endoscopy*, 8(7):817–820, 1994. Springer-Verlag New York Inc.
- [110] M.O. Schurr, A. Arezzo, B. Neisius, H. Rininsland, H.-U. Hilzinger, J. Dorn, K. Roth, and G.F. Buess. Trocar and instrument positioning system tiska, an assist device for endoscopic solo surgery. *Surgical Endoscopy*, 13:528–531, 1999. Springer-Verlag New York Inc.
- [111] M.O. Schurr, G. Buess, B. Neisius, and U. Voges. Robotics and telemanipulation technology for endoscopic surgery, a review of the artemis project. *Surgical Endoscopy*, 14(4):375–381, 2000. Springer-Verlag New York Inc.

- [112] *Stock Drive Products - Sterling Instrument*. SDP-SI, 2009. <http://www.sdp-si.com>.
- [113] U. Seibold, B. Kuebler, and G. Hirzinger. *Medical Robotics*, chapter Prototypic force feedback instrument for minimally invasive robotic surgery. I-Tech Education and Publishing, 2008.
- [114] K.B. Shimoga. A survey of perceptual feedback issues in dexterous telemanipulation: Part i. finger force feedback. In *Proceedings of the IEEE Virtual Reality Annual International Symposium*, pages 263–270, 1993.
- [115] C.M. Smith. Human factors in haptic interfaces. *ACM Crossroads Student Magazine*, 3(3):14–16, Spring 1997.
- [116] R. Solberg, K.-J. Zandsteeg, G.A.L. Leenknecht, and R. van der Aalst. Software description for the mirs master-slave robot. Technical Report CST 2010.034, Eindhoven University of Technology, 2009.
- [117] Intuitive Surgical. *Endowrist Instruments*. <http://www.intuitivesurgical.com/products/endowrist>. viewed at April 16th 2007.
- [118] H. Tan, X. Pang, and N. Durlach. Manual resolution of length, force, and compliance. In *Advances in Robotics* Burdea [25], pages 13–18.
- [119] H.Z. Tan, M.A. Srinivasan, B. Eberman, and B. Cheng. Human factors for the design of force-reflecting haptic interfaces. *ASME Journal of Dynamic Systems and Control*, 55(1):353–359, 1994.
- [120] R.H. Taylor and D. Stoianovici. Medical robotics in computer-integrated surgery. *IEEE Transactions on Robotics and Automation*, 19(5):765–781, October 2003.
- [121] M. van Veggel. *The Basic Angle Monitoring system: picometer stability with Silicon Carbide optics*. PhD thesis, Eindhoven University of Technology, March 2007.
- [122] C.A.M. Verbaan. Design of a weight compensation mechanism for an adjustable structure to support robots for minimal invasive surgery. Technical Report CST 2010.014, Eindhoven University of Technology, February 2010.
- [123] WeBSurg. *WeBSurg, World Electronic Book of Surgery*. [www.websurg.com](http://www.websurg.com), viewed 2006.
- [124] P. Wieneke and T. Lutze. Technologies for microendoscopies of the future: the minop project. *Minimally Invasive Therapy and Allied Technologies*, 7(3):223–239, 1998.
- [125] *Optical measurement setup with a nano-stepping piezo stage*. Xpress Precision Engineering, July 2009.
- [126] A.P.C. Yim and C. Ng. *WeBSurg*, chapter Video-assisted thoracic surgery: thymectomy for myasthenia gravis. [www.websurg.com](http://www.websurg.com), viewed June 2006.

## Appendix A

# Minimally Invasive Surgery

Minimally Invasive Surgery (MIS) is surgery performed through small incisions, with an endoscope and long and slender instruments. In general MIS comes with reduced postoperative pain, reduced hospital stay, equal result of the treatment, increased procedure time and increased costs per procedure [22]. Advantages of MIS mostly are for the patient's benefit (Section A.1), whereas the surgeon has to cope with the disadvantages when performing conventional MIS (Section A.2).

### A.1 Advantages of conventional MIS with respect to open surgery

Advantages include, but are not limited to:

- reduced trauma to the body. Organs are less subject to dehydration, because they are not in direct contact with air [19],
- reduced blood loss and need for transfusion. Bleeding is prevented as much as possible, because it absorbs light and reduces the view on the operating site,
- less risk of infection, because only small incisions are made,
- shorter hospital stay. In open surgery, trauma due to the access path typically is greater than trauma at the operating site [35],
- faster recovery and return to normal daily activities, reduced post-operative pain and stress reactions. A critical note in [22] states that some patients are disappointed in their recovery. The impact of the procedure within their abdomen can not be derived from the outside. In addition, patients

will hardly ever experience treatment of one disease with both open and minimally invasive surgery, which makes it hard to compare, and

- less scarring, reduced risk of rupture of the scar tissue [21] and improved cosmetics.

## A.2 Disadvantages of conventional MIS with respect to open surgery

The disadvantages are mainly due to the indirect way of manipulating instruments and obtaining information from the operative site. These are listed below in subsections.

### A.2.1 Reduced dexterity

Reduced dexterity caused by the necessity of using entry points and trocars in this technique. The accompanying fulcrum point results in a variable transmission ratio of in- and outgoing movements (and forces), tremor could be amplified even. Also, hand movements result in mirrored instrument tip-movements. Besides, in open surgery the surgeon has virtually indefinite ways to position and orient his/her instrument in its six (or seven) DoFs. A surgeon's arm provides seven DoFs and the hand over 20 DoFs to manipulate the tool and approach the tissue from an arbitrary orientation. But the incision decreases the six or seven DoFs of the instrument in space to four or five. This limitation of the surgeon's dexterity [22] is the most important disadvantage.

### A.2.2 Visual information obtained from the operative field

The second essential difference is the way the surgeon looks at the field of surgery [22]. Before 1987, the surgeon could see the surgical field through an endoscope with an eyepiece while performing MIS [74]. In 1987 the video camera was introduced so the surgical team could see the operative site too. The surgeon (and his team) has to interpret a 2D-image of the operative site. More specifically, depth perception is impeded by the lack of shadows in endoscopic camera pictures, the lack of stereovision and movement parallax, and misfits of accommodation and convergence can occur [18]. In addition, the image of the surgical space is degraded: dirt and vapor can accumulate on the endoscope lens and the image suffers reduced resolution, contrast and illumination [18]. High definition video-endoscopes improve these last points. Still, the instruments have to stay within the camera-field and the surgeon needs to be aware of the risk of loss of overview ([5, 31] mentioned in [18]). The viewpoint is directed by the camera assistant using a set of empirical rules and not by the surgeon. An unsteady camera

picture decreases the performance of aimed hand movements ([31, 34, 88] from [18]).

### **A.2.3 Haptic information obtained from the operative field**

The surgeon doesn't feel due to friction and instrument length. The tactile sensation is lost, surgeons would like to have kinesthetic and tactile feedback during MIS. In laparoscopic surgery, tactile feedback consists only of what can be sensed through a long rigid instrument. Friction in the cannulas (also caused by the air tight seal when it is used) further reduces the kinesthetic sense. The handle of most instruments is configured as a Roman scissors design, which further reduces tactile sensation, especially when a locking mechanism is in use [74].

### **A.2.4 Hand-eye coordination in MIS**

The surgeons view and movements do not coincide, which results in an unnatural pose. The natural axis of work is interrupted. There are three vectors: 1 viewing vector, 2 manipulation vector and 3 endoscope or image vector. The larger the angle between these vectors, the more difficult to carry out the job. Most of the time the screen is placed on top of the equipment tower. The screen in the middle of the tower would enhance the natural axis of work. There is proof that more surgeon's suffer from hernias in neck and back when they perform conventional MIS than performing conventional open surgery. A proper use of technology could extend the professional life time of a surgeon.

### **A.2.5 Required time**

Beside the intervention itself, preparation takes more time, because of the difficulties in tool-placement [74]. According to [18], the operative protocols of many procedures are still far from optimal, and it is difficult to transpose preoperative information from X-rays, Ultrasound, or MRI images onto the endoscopic camera pictures, which makes tool-placement difficult. Most surgeons will rather work with a non-optimal trocar position than adding an incision, since this reduces the benefit of MIS. Besides, it is a different technique, which takes time to get used to when one has to learn working with it.




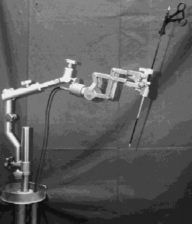
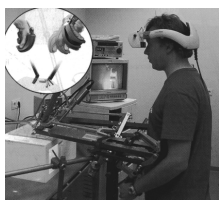

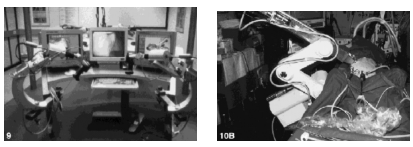

## Appendix B

# Existing Robotic MIS Systems and Instruments

Table B shows existing systems both commercial and in research. These systems are related and additional to the laparoscopic/thoracoscopic surgical systems presented in Chapter 1. In Table B.2 some instruments are shown with 1, 2 or 3 additional DoFs, additional to the instruments shown in Chapter 1. Figure B.1 shows a three-DoF sensor that can be integrated in a MIS instrument.

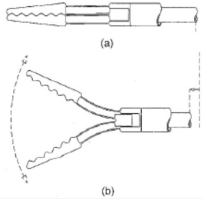
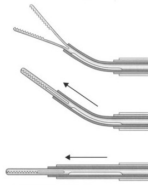
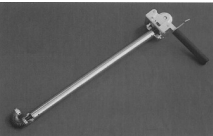
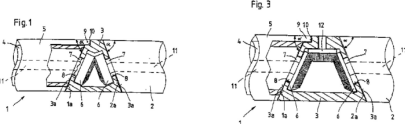
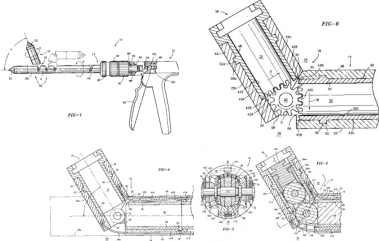
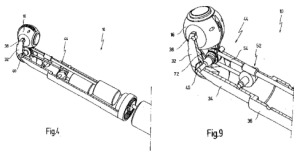
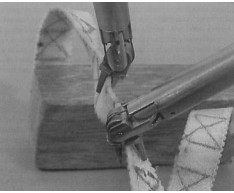
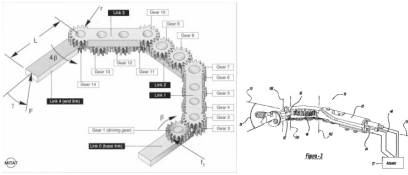
## B.1 Existing Systems

Table B.1: Pick from overview on robotic MIS systems

Commercially available: Laparoscopic / Thoracoscopic Assistant Devices	
 <p>Armstrong Healthcare (Great Britain), has the Endoassist, a robotic camera assistant [3, 46, 57].</p>	 <p>Karlsruhe Research Center (Germany), has the Tiska Endoarm, the Trocar and Instrument Positioning System Karlsruhe [110].</p>
Research Projects: Laparoscopic / Thoracoscopic Surgical Systems.	
 <p>Academical Medical Hospital (AMC) Amsterdam (the Netherlands), has the Minimal Invasive Manipulator [65–67]. It has force-feedback; is table mounted with two mechanical manipulators, 4+3 instrument DoFs each, and passively supports the instrument.</p>	 <p>Joseph Fourier University (France), has the compact cable driven manipulator [13].</p>
 <p>Karlsruhe Research Center (Germany), has the ARTEMIS, Advanced Robotic Telemanipulator for Minimally Invasive Surgery, with FIPS Endoarm integrated ([24, 111]).</p>	 <p>UC Berkeley (USA), has the Second Generation Berkeley/ UCSF Laparoscopic Telesurgical Workstation [29, 30]. It is floor mounted, has no force-feedback and 4+2 DoFs. The instrument is supported by the tissue.</p>

## B.2 Existing instrument-tips and accessories

Table B.2: Pick from overview on instruments with additional DoFs, different drive concepts. The overview is divided according to number of DoFs.

 <p>1-DoF elastic grasping forceps [7] from [17]. DLR (Germany).</p>	 <p>1-DoF deflectable nickel-titanium instrument for neurosurgery [124]. AESCULAP (Germany).</p>
 <p>1-DoF (pitch) cable driven Endo-Periscope I [15]. Technische Universiteit Delft (the Netherlands).</p>	 <p>1-DoF rotation joint, especially for medical instruments [39]. Karl Storz GmbH &amp; Co (Germany).</p>
 <p>2-DoF articulated medical instrument: roll and pitch [33].</p>	 <p>2-DoF endoscope with variable direction of view: roll and pitch [61]. Karl Storz GmbH &amp; Co (Germany).</p>
 <p>3-DoF cable actuated instrument: pitch, yaw and gripper [65, 67]. Operated with the Minimal Invasive Manipulator. Academic Medical Hospital Amsterdam (the Netherlands).</p>	 <p>3-DoF (pitch, roll, gripper) dexterous articulated linkage for surgical applications [87] (with the AMMIS, [90]) Michigan State University (USA).</p>

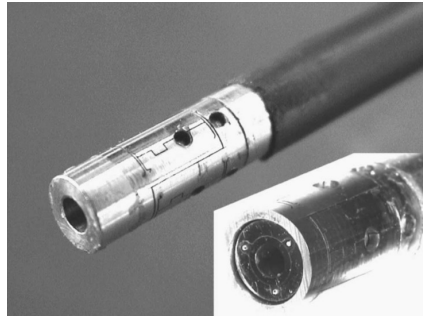


Figure B.1: Three-DoF optical force sensor for integration in MIS instruments [98].  
Katholieke Universiteit Leuven (Belgium).

## Appendix C

# Observed Procedures

A study on laparoscopic and thoracoscopic procedures has been performed to gain insight in the requirements of the robot [8]. The procedures considered were based on descriptions [123] and on (partially) comparable mainly laparoscopic observed procedures. An overview of the latter procedures can be found in this chapter. These were performed to a large extent by or under supervision of [20], either in the conventional manner or with the da Vinci telesurgery system [63]. The procedures have been subdivided in (lower and upper) abdominal procedures and thoracic procedures. Similar procedures presented (indicated with I, II) are performed (or supervised) by the same surgeon. Characteristics like: (i) patient and team (including robot) position, trocar positions and table orientation of the procedures are given in Table C.1, (ii) trocar placement (Table C.2), (iii) pre-surgical initial trocar orientation (Table C.3), (iv) and instrument movements (Table C.4) are displayed. Based on Table C.1 it is stated that conventional and robotic procedures are hard to compare on some levels, since generally both techniques are used for different procedures. Basically, conclusions on the conventional procedures will be used for general purposes regarding MIS procedures and robotic procedures for requirements regarding initial trocar set-up, instrument orientation etc. The characteristics presented form the basis of the requirements of the Slave.

Table C.1: Impression of some observed conventional and robotic MIS procedures [8], (I,II is the first or second procedure observed), with: The patient and the field of surgery (grey area), divided in surgery performed in the lower abdomen, upper abdomen and thorax. The trocars:  $\bigcirc$  endoscope trocar,  $\triangle$  robot instrument trocar,  $\square$  assistant instrument or retractor trocar  
The team position: surgeon (S), assistant 1,2 (A1,2), Robot (R); the anesthetologist, scrub-nurse and OR nurse are omitted  
The table orientation: (r)T (reverse) Trendelenburg rotation, L lateral rotation.

	Lower abdomen	Upper (middle) abdomen			Thorax
Conventional		<b>Cholecystectomy I</b> $rT:30^\circ, LL:10-20^\circ$ 	<b>Cholecystectomy II</b> $rT:20-30^\circ$ 	<b>Oesophageal resection (part a)</b> $rT:0-20^\circ, RL:0-18^\circ$ 	<b>Nissen fundoplication</b> $rT:30^\circ, L:0^\circ$ 
Robotic	<b>Rectopexy I,II</b> $T:30^\circ, L:0^\circ$ 	<b>Laparoscopic oesophageal myotomy I,II</b> $rT:30^\circ, L:0^\circ$ 	<b>Redo Nissen fundoplication</b> $rT:20^\circ, L:0^\circ$ 	<b>Hiatal hernia repair and Nissen fundoplication I,II</b> $rT:30^\circ; L:0^\circ$ 	<b>Oesophageal resection (part b)</b> $rT:10^\circ, RL:0^\circ$ , flexed 

Table C.2: Trocar positions of the instruments in observed procedures [8]. The robot instruments ( $R_{i1,i2}$ ) and assistant instruments ( $A_{i1,i2}$ ) trocar positions are given relative to the endoscope (E) trocar. The values displayed are estimates with an uncertainty of about 5 cm. With: r.a.l. right axillary line; l.m.l. left midclavicular line.

Procedure		$R_{i1}$	$R_{i2}$	$A_{i1}$	$A_{i2}$
<b>Robotic procedures in the lower middle abdomen</b>					
Rectopexy I	$x$	-5	-5	-5	-5
	$y$	-15	15	-10	10
Rectopexy II	$x$	-5	-5	-5	-5
	$y$	-15	15	-10	10
<b>Conventional procedures in the upper right abdomen</b>					
Oesophageal resection 1a: checking liver on metastases	$x$				
	$y$				
<b>Conventional procedures in the upper middle abdomen</b>					
Cholecystectomy I	$x$	-20–15	-10	-10	-
	$y$	0	l.m.l.	r.a.l.	-
Cholecystectomy II	$x$	-3	-12	-5	-
	$y$	-7–5	0	-14	-
Oesophageal resection 1b: mobilization of oesophagus and stomach	$x$	+5	+5	-5	-5
	$y$	-15–12	-5	r.a.l.	2
Nissen fundoplication	$x$	-5	-5	-5	-5
	$y$	-15	15	r.a.l.	7
<b>Robotic procedures in the upper middle abdomen</b>					
Laparoscopic oesophageal myotomy I	$x$	-5	-5	-15	-5
	$y$	-12	12	r.a.l.	7
Laparoscopic oesophageal myotomy II	$x$	-5	-5	-10	-5
	$y$	-10	15	r.a.l.	7
Redo Nissen fundoplication	$x$	-1	-1	-1	-1
	$y$	-7	15	r.a.l.	10
Hiatal hernia repair and Nissen fundoplication I	$x$	-5	-5	-5	-5
	$y$	-20–15	15–20	-25–20	10
Hiatal hernia repair and Nissen fundoplication II	$x$	-5	-5	-5	-5
	$y$	-15–10	10–15	r.a.l.	5–7.5
<b>Conventional procedures in the upper left abdomen</b>					
Oesophageal resection 1c: mobilization of stomach	$x$				
	$y$				
<b>Robotic procedures in the thorax</b>					
Oesophageal resection 2a: lower oesophageal resection	$x$				
	$y$				
Oesophageal resection 2b: higher oesophageal resection	$x$				
	$y$				

Table C.3: Initial trocar orientation [8] of the endoscope (E) and robot instruments ( $R_{i1,i2}$ ) [ $^{\circ}$ ]: the initial orientation  $\theta_{E,Ri}$  is the angle of the trocar pointing towards the target organ, relative to the global coordinate system (Figure 2.3) for the endoscope trocar and relative to the endoscope trocar for the robot instrument trocars. The initial orientation  $\psi$  of the endoscope or robot instruments is the rotation around its corresponding  $y$ -axis:  $y_E, y_{Ri}$  (Figure 2.3). Italic values indicate angles that are estimated afterwards. The procedures are subdivided in conventional and robotic MIS.

Procedure		Initial trocar orientation			
		E	$R_{i1}$	$R_{i2}$	$\theta_{Ri2} - \theta_{Ri1}$
<b>Conventional laparoscopic procedures</b>					
Oesophageal resection 1a: checking liver on metastases	$\theta$ [ $^{\circ}$ ]	45	-60	-30	30
	$\psi$ [ $^{\circ}$ ]	80	90	90	
Cholecystectomy I	$\theta$ [ $^{\circ}$ ]	15	40	75	35
	$\psi$ [ $^{\circ}$ ]				
Cholecystectomy II	$\theta$ [ $^{\circ}$ ]	20	-30	90	120
	$\psi$ [ $^{\circ}$ ]	60	40	10	
Oesophageal resection 1b: mobilization of oesophagus and stomach	$\theta$ [ $^{\circ}$ ]	0	-60	-30	30
	$\psi$ [ $^{\circ}$ ]	70	70	50	
Nissen fundoplication	$\theta$ [ $^{\circ}$ ]	-10	-30	30	60
	$\psi$ [ $^{\circ}$ ]				
Oesophageal resection 1c: mobilization of stomach	$\theta$ [ $^{\circ}$ ]	-30	-30	-15	15
	$\psi$ [ $^{\circ}$ ]	50	60	60	
<b>Robotic laparoscopic procedures</b>					
Rectopexy I	$\theta$ [ $^{\circ}$ ]	180	-75	75	150
	$\psi$ [ $^{\circ}$ ]				
Rectopexy II	$\theta$ [ $^{\circ}$ ]	180	-75	75	150
	$\psi$ [ $^{\circ}$ ]				
Laparoscopic oesophageal myotomy I	$\theta$ [ $^{\circ}$ ]	0	-15	15	30
	$\psi$ [ $^{\circ}$ ]	75	75	75	
Laparoscopic oesophageal myotomy II	$\theta$ [ $^{\circ}$ ]	0	-30	40	70
	$\psi$ [ $^{\circ}$ ]	65	65	65	
Redo Nissen fundoplication	$\theta$ [ $^{\circ}$ ]	0	-30	60	90
	$\psi$ [ $^{\circ}$ ]	60	60	50	
Hiatal hernia repair and Nissen fundoplication I	$\theta$ [ $^{\circ}$ ]	0	-30	30	60
	$\psi$ [ $^{\circ}$ ]				
Hiatal hernia repair and Nissen fundoplication II	$\theta$ [ $^{\circ}$ ]	0	-30	30	60
	$\psi$ [ $^{\circ}$ ]	60	50	50	
<b>Robotic thoracoscopic procedures</b>					
Oesophageal resection 2a: lower oesophageal resection	$\theta$ [ $^{\circ}$ ]	30	-30	30	60
	$\psi$ [ $^{\circ}$ ]	30	30	30	
Oesophageal resection 2b: higher oesophageal resection	$\theta$ [ $^{\circ}$ ]	15	-15	15	30
	$\psi$ [ $^{\circ}$ ]	75	75	75	

Table C.4: Instrument movements [8] of endoscope (E) and robot instruments ( $R_{i1,i2}$ ) [ $^\circ$ ]: the given angle describes the cone in which the endoscope or instrument remains during surgery with respect to its initial trocar orientation. With n.o.: not observed. The procedures are subdivided in conventional and robotic MIS.

Procedure	Instrument movements		
	E	$R_{i1}$	$R_{i2}$
<b>Conventional laparoscopic procedures</b>			
Oesophageal resection 1a: checking liver on metastases	$\pm 10$	45 up 10 down	45 up 10 down
Cholecystectomy I		10–20	
Cholecystectomy II	$\pm 15$	$\pm 20$ right: 40	$\pm 20$
Oesophageal resection 1b: mobilization of oesophagus and stomach	$\pm 90$	$\pm 90$	$\pm 90$
Nissen fundoplication	n.o.		
Oesophageal resection 1c: mobilization of oesophagus and stomach	$\pm 10$	80 up 30 down	$\pm 30$
<b>Robotic laparoscopic procedures</b>			
Rectopexy I	n.o.		
Rectopexy II	n.o.		
Oesophageal myotomy I		20	
Oesophageal myotomy II		20	
Redo Nissen fundoplication	$\pm 10$	$\pm 20$	$\pm 20$ right: 40
Hiatal hernia repair and Nissen fundoplication I	n.o.		
Hiatal hernia repair and Nissen fundoplication II	20	30	20
<b>Robotic thoracoscopic procedures</b>			
Oesophageal resection 2a: lower oesophageal resection	30	30	30
Oesophageal resection 2b: higher oesophageal resection	15	15	15



## Appendix D

# Pre-Surgical Set-up

This appendix provides information regarding the pre-surgical set-up of the Slave robot: its platform-adjustment and measurement equipment and set-ups used to test the platform-adjustment and manipulator-adjustment. Information on the platform-adjustment includes: concepts for its platform, the mass of its parts, calculations on clamp  $\Theta_1$  and its weight compensation mechanism.

### D.1 Concepts for the pre-surgical set-up platform

Concepts for the platform that holds (three) manipulator-adjustments with their connected manipulators, are shown in Figure D.1 on the next page.

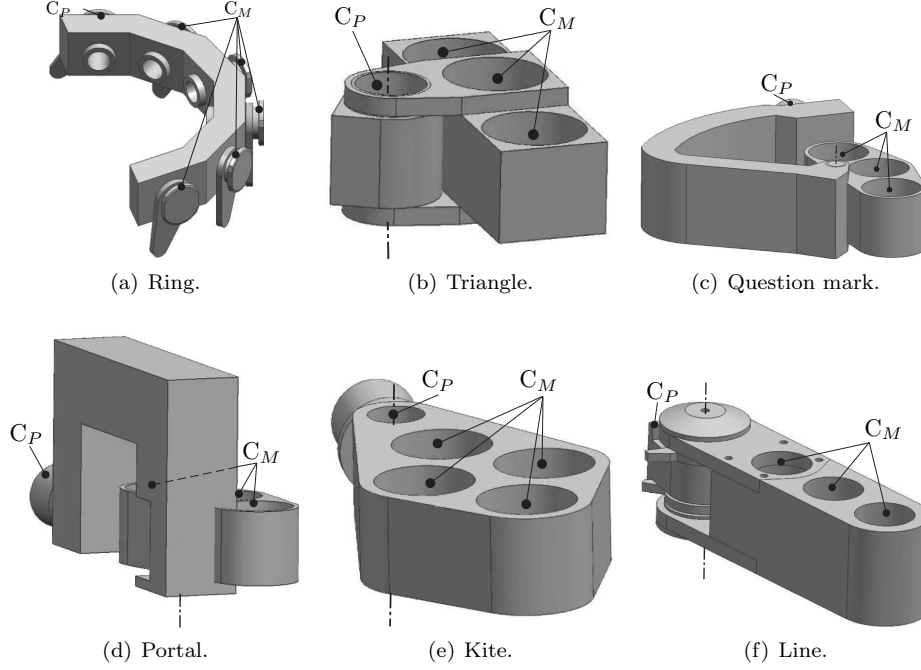


Figure D.1: Concepts for the platform connected at the platform-adjustment at  $C_P$ , holding (three) manipulator-adjustments at  $C_M$ . Each manipulator-adjustment has either an endoscope-manipulator or one of two instrument-manipulators connected.

## D.2 Mass of the platform-adjustment and platform

Table D.1: Mass of the platform-adjustment and platform (Figure 3.7), including the platform-inserts of the manipulator-adjustment.

Part	[kg]
Frame-a	25.5
Frame-b	10.4
Clamp $\Theta_1$	2.1
Link 1 plus clamp $\Psi_1$	8.2
Link 2	2.6
Link 3 plus clamp $\Psi_2$ and $\Psi_3$	4.2
Link 4 plus clamp $\Theta_2$ plus platform	4.8
Platform-inserts x3	0.9
<b>Sum</b>	<b>56</b>

## D.3 Clamp $\Theta_1$ of the platform-adjustment

### D.3.1 Required clamp and actuation force

Figure D.2 shows clamp  $\Theta_1$  of the platform-adjustment.

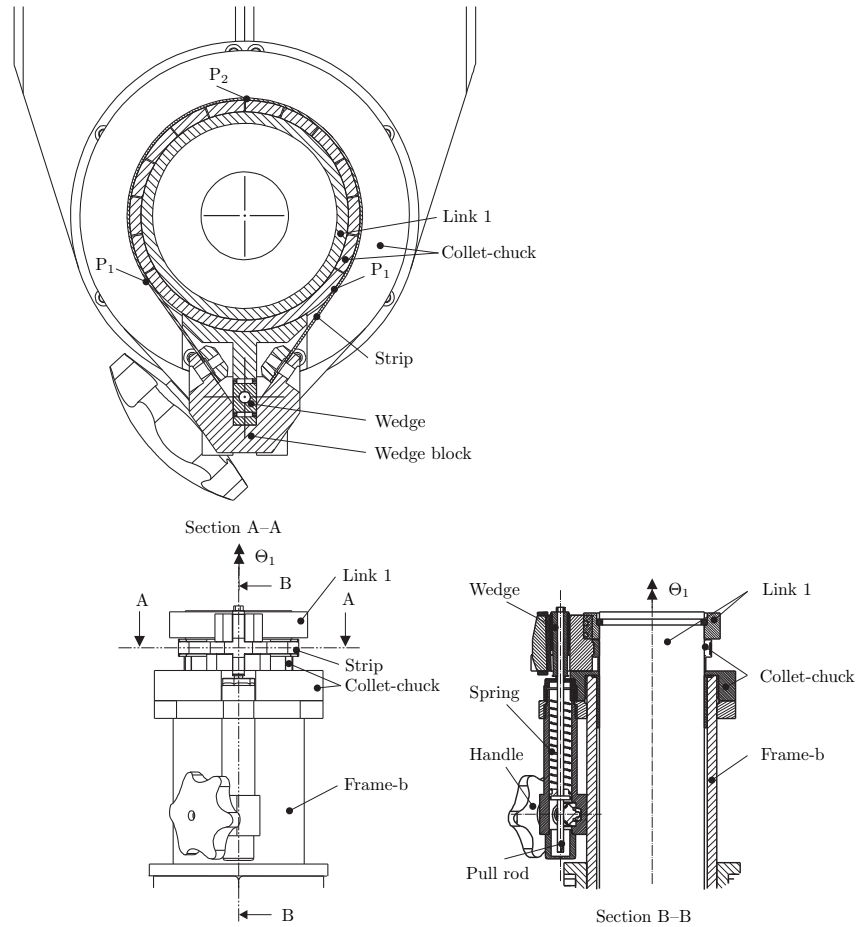


Figure D.2: Clamp  $\Theta_1$ .

Link 1 is locked in  $\Theta_1$  (and  $z$  when lifted) with this clamp by means of friction. Clamp  $\Theta_1$  is force-closed. Its main parts are a collet-chuck, a strip applying the normal force to the chuck and a wedge and spring to provide the required preload in the strip. This section presents the calculations on the required friction force between link 1 and the clamp, the required pretension in the strip to apply this friction force, the spring force to apply the pretension in the strip and the actuation force to open the clamp.

A (tangential) load applied at the platform, requires a friction force ( $F_{lock}=2250$  N, Equation D.1, see Table D.2) between link 1 of the platform-adjustment and the collet-chuck to keep the platform in its position. The collet-chuck is connected to frame-b and supports this friction force  $F_{lock}$ .

$$F_{lock} = F_p R_p S / R_c \quad (D.1)$$

This  $F_{lock}$  determines the required radial normal force ( $F_n \approx 11$  kN) between the chuck and link 1. This normal force applies between the strip and chuck as well, with a resulting friction force  $F_{strip-chuck}$ , calculated (Equation D.2) and shown in Table D.2.

$$F_{strip-chuck} = F_{lock} f_{lock} / f_{strip-chuck} \quad (D.2)$$

Table D.2: Clamp  $\Theta_1$  of the platform-adjustment,  $F_{lock}$  (Eq. D.1) and  $F_{strip-chuck}$  (Eq. D.2).

<b><math>F_{lock}</math>, required friction force of clamp <math>\Theta_1</math></b>	<b>[N]</b>	<b>2250</b>
$F_p$ , tangential force applied at the platform	[N]	300
$R_p$ the arm between $\Theta_1$ and the platform	[mm]	225
$S$ , the safety factor	[-]	1.5
$R_c$ , the internal radius of clamp $\Theta_1$ in contact with link 1	[mm]	45
<b><math>F_{strip-chuck}</math>, friction force between collet-chuck and strip</b>	<b>[N]</b>	<b>500</b>
$f_{lock}$ the friction coefficient in contact link 1 – chuck	[-]	0.2
$f_{strip-chuck}$ the friction coefficient (teflon) in contact strip – chuck	[-]	0.04

The steel strip wraps the chuck with  $\alpha=250^\circ$ . The required pretension in the strip is calculated with Equation D.3 and D.4:

$$S_2 = \frac{F_{strip-chuck}/2}{e^{f_{strip-chuck}(\alpha/2)} - 1} \quad (D.3)$$

$$S_1 = S_2 * e^{f_{strip-chuck}(\alpha/2)} \quad (D.4)$$

The force  $S_2$  in the strip (point P<sub>2</sub>, top of Figure D.2) determines the force  $S_1$  (point P<sub>1</sub>). This force prescribes the radial outward force  $F_{rad}$  (Equation D.5 and Table D.3) the wedge block needs to apply to the ends of the strip.

$$F_{rad} = 2S_1 \sin((360 - \alpha)/2) \quad (D.5)$$

The wedge ( $i=1:50$ ), supported with linear needle bearings, provides this force. It transforms its axial actuation force ( $F_a$  in Equation D.6 and Table D.3) to the radial preload force acting on the wedge-block.

$$F_a = F_{rad}(i + 2f_n) \quad (D.6)$$

The compression spring (stiffness  $c_{spring}$ ) applies the required axial preload force to the wedge. A handle rotation of  $90^\circ$  sets link 1 free. This increases the spring

compression, resulting in a maximum spring force  $F_{spring}$  (Table D.3) required to open the chuck. A double (calculated) tangential force  $F_{act}$  (Equation D.7) applied at a radius at the handle, provides the required actuation torque  $T_{handle}$  (Table D.3).

$$F_{act} = T_{handle}/(2R_{act}) = F_{spring}dR/(2R_{act}) \quad (D.7)$$

Table D.3: Clamp  $\Theta_1$  of the platform-adjustment,  $F_{act}$  (Eq. D.7).

<b><math>S_1</math>, required preload force in the strip at point P<sub>1</sub></b>	[kN]	<b>3.0</b>
$S_2$ , required preload force in the strip at point P <sub>2</sub>	[kN]	2.7
$\alpha$ , angle of the strip wrapping the chuck of the collet-chuck	[°]	250
<b><math>F_{rad}</math>, required radial outward preload of the wedge block</b>	[kN]	<b>4.9</b>
<b><math>F_a</math>, axial actuation force of the wedge</b>	[N]	<b>128</b>
$i$ , transmission ratio of the wedge	[-]	1:50
$f_n$ , the friction coefficient of needle bearings	[-]	0.003
<b><math>T_{act}</math>, required actuation torque at the handle</b>	[Nm]	<b>≈1.6</b>
$F_{spring}$ , maximum spring force when the clamp is opened	[N]	160
$c_{spring}$ , compression spring stiffness, preloading the wedge	[N/mm]	2.12
$dL_p$ , compression of the spring to apply the preload	[mm]	60
$\gamma$ , handle rotation to open the clamp	[°]	90
$dR$ , radial distance between handle axis and rod-axis	[mm]	10
$dL_o$ , additional compression length to open the clamp	[mm]	15.7
<b><math>F_{act}</math>, double (calculated) actuation force at the handle</b>	[N]	<b>27</b>
$R_{act}$ , radius of actuation at the handle	[mm]	30

Note: the radial stiffness of each elastic component of the chuck increases the required radial normal force in the chuck. The axial cross-section of these elastic components are assumed to approximate a rectangle. The radial bending stiffness (Equation D.9) of these elastic components on the chuck (*chuck components*), results in a change of the experienced normal force  $F_{dn}$  (Equation D.8, Table D.4) with  $c_{br}$  from Equation D.9.

$$F_{dn} = c_{br}dr \quad (D.8)$$

$$c_{br} = \frac{12EI}{L^3} = \frac{EHt^3}{L^3} \quad (D.9)$$

This can be neglected. The accompanying bending stress is calculated with Equation D.10, see Table D.4.

$$\sigma_{br} = \frac{3Ext}{L^2} \quad (D.10)$$

Table D.4: Clamp  $\Theta_1$  of the platform-adjustment, radial stiffness of its aluminium chuck components.

$c_{br}$ , <b>radial bending stiffness of the chuck components</b>	[N/mm]	<b>78</b>
$L$ , length of the chuck components	[mm]	12
$H$ , width of the chuck components	[mm]	15.5
$t$ , thickness of the chuck components	[mm]	0.5
$n$ , number of chuck components of the chuck	[-]	12
$F_{dn}$ , <b>change of the experienced normal force</b>	[N]	<b>8</b>
$\sigma_{br}$ , <b>bending stress in the chuck component</b>	[N/mm <sup>2</sup> ]	<b>73</b>
$dr$ , radial distance between open and closed chuck	[mm]	0.1

### D.3.2 Stiffness of clamp $\Theta_1$

The tangential stiffness ( $c_t$  in Equation D.11) of clamp  $\Theta_1$  is (among others) based on the shear-stiffness ( $c_s$  in Equation D.13) and bending-stiffness ( $c_b$  in Equation D.14) of each elastic component of the chuck. Calculations are performed with the axial cross-section approximated by a rectangle. Actually, the axial cross section of each elastic element is described by an arc. However, the straight line connecting the end-points of this arc is 97% of the arc length, which is the reason to use a rectangular cross section.

$$c_t = n \frac{c_s c_b}{c_s + c_b} \quad (D.11)$$

with  $n=12$  the number of elastic components of the chuck. The rotational stiffness  $k_t$  is calculated with Equation D.12.

$$k_t = c_t R_{chuck}^2 \quad (D.12)$$

$$c_s = \frac{GtH}{L} \quad (D.13)$$

$$c_b = \frac{12EI}{L^3} = \frac{EtH^3}{L^3} \quad (D.14)$$

Table D.5: Clamp  $\Theta_1$  of the platform-adjustment, stiffness of its chuck, with the dimensions of the chuck components from Table D.4.

$R_{chuck}$ , radial position of the elastic components	[mm]	45.75
$c_b$	[ $\cdot 10^4$ N/mm]	7.5
$c_s$	[ $\cdot 10^4$ N/mm]	1.7
$c_t$	[ $\cdot 10^5$ N/mm]	1.7
$k_t$	[ $\cdot 10^8$ Nmm/rad]	3.5

## D.4 Platform weight-compensation

The weight of the platform and platform-adjustment will be supported by a weight-compensation mechanism when the platform-adjustment clamps are released [122]. This improves the sense of freedom to manipulate the platform towards its required position and improves the safety for both the person manipulating the platform and the patient. The platform is intended to be setup, normally without the mounted manipulator-adjustments and manipulators. However, for safety reasons the weight-compensation mechanism is designed to compensate the weight of the the mounted manipulator-adjustments as well (see Table D.6). The weight-compensation mechanism presented here, consists of an external parallel link mechanism, to apply or obtain the orientation of the appropriate link (respectively left and middle in Figure D.3), and an energy storage system integrated in link 1 of the platform-adjustment (shown in Figure D.7). This safety system is completely passive.

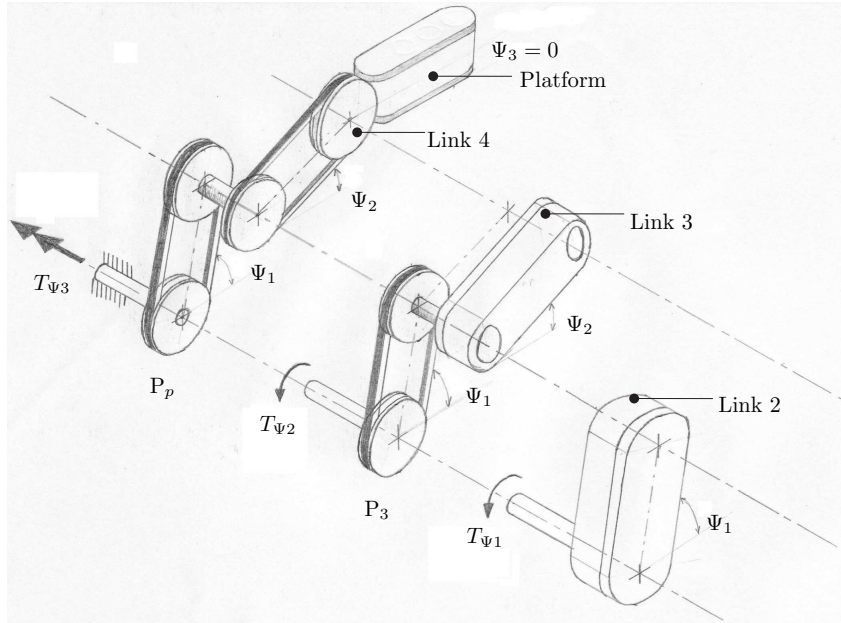


Figure D.3: The platform-adjustment with its platform and link 4 (left), link 3 (middle) and link 2 (right) and its weight-compensation mechanism are shown. Here,  $P_p$  and  $P_3$  are the parallel link mechanisms and  $T_{\Psi_3}$ ,  $T_{\Psi_2}$ ,  $T_{\Psi_1}$  are the required reaction torques of the weight-compensation mechanism.

Figure D.5 shows the parallel link mechanism added to the platform-adjustment. An integrated mechanism is proposed at the end of this section. Parallelogram  $P_p$  shown at the left of Figure D.3, keeps the platform parallel to the table-top ( $\Psi_3=0$ ) at all times and immovable if a single clamp is opened (releasing  $\Psi_1, \Psi_2, \Psi_3$ ) in-

advertently. In case more clamps are opened in the series  $\Psi_1, \Psi_2, \Psi_3$ , the mechanisms in the center and right of Figure D.3 take over. Parallel link mechanism  $P_3$  (Figure D.3 middle) copies the orientation of link 3 ( $\Psi_2$ ) to the energy storage system. The orientation of link 2 ( $\Psi_1$ ) is coupled directly.

The parallel orientation of the platform will be most common, however it can be made adjustable when required. It simplifies the weight-compensation mechanism. Now two energy storage systems are required instead of three. Both energy storage systems are integrated in link 1 of the platform-adjustment mechanism, see Figure D.7. This limits the inertia of, and reduces the modifications to the links of the platform-adjustment. The flat strip-like rods of the parallel link mechanism (Figure D.5) are loaded in tension only, since rods are better at handling tensile than at handling compressive load.

### Torques required to compensate weight loads

The loads on the joints of the platform-adjustment, shown in Table D.6, need to be compensated. Parallel link mechanism  $P_p$  fixates platform orientation  $\Psi_3$  and takes  $T_{\Psi_3}$  to the base. The weight of the platform then is accounted for by reaction force  $F_{\Psi_3}$  (Equation D.15) which is independent of  $\Psi_3$ . It is incorporated in the reaction torques  $T_{\Psi_2}$  and  $T_{\Psi_1}$  that need to be compensated, see Table D.6.

Table D.6: Static loads on the links and joints of the platform-adjustment. In light grey the applied loads, in dark grey the reaction force and torque of each specific part.

<p>Link 4 and platform:</p>	$F_{\Psi_3} = g(m_{i1} + m_{i2} + m_{i3} + m_p) \quad (D.15)$
	<p>with <math>m_{i1}=m_{i2}=m_{i3}\approx 8</math> kg and <math>m_p=5.35</math> kg</p>
	$T_{\Psi_3} = g(L_{i1}m_{i1} + L_{i2}m_{i2} + L_{i3}m_{i3} + L_p m_p) \quad (D.16)$
	<p>with <math>L_{i1}=160</math> mm, <math>L_{i2}=240</math> mm, <math>L_{i3}=320</math> mm and <math>L_p=125</math> mm</p>
<p>Link 3:</p>	$F_{\Psi_2} = g m_3 + F_{\Psi_3} \quad (D.17)$
	<p>with <math>m_3=3.2</math> kg</p>
	$T_{\Psi_2} = \cos(\Psi_2)(L_{m3} g m_3 + L_3 F_{\Psi_3}) \quad (D.18)$
	<p>with <math>L_{m3}=98.1</math> mm and <math>L_3=160</math> mm</p>
<p>Link 2:</p>	$F_{\Psi_1} = g m_2 + F_{\Psi_2} \quad (D.19)$
	<p>with <math>m_2=3.3</math> kg</p>
	$T_{\Psi_1} = \cos(\Psi_1)(L_{m2} g m_2 + L_2 F_{\Psi_2}) \quad (D.20)$
	<p>with <math>L_{m2}=100.8</math> mm and <math>L_2=160</math> mm</p>

Torque  $T_{\Psi_2}$  and  $T_{\Psi_1}$  are a function of respectively  $\Psi_2$  and  $\Psi_1$ , see Figure D.4. The energy storage system requires these angles to apply the appropriate compensation torque.

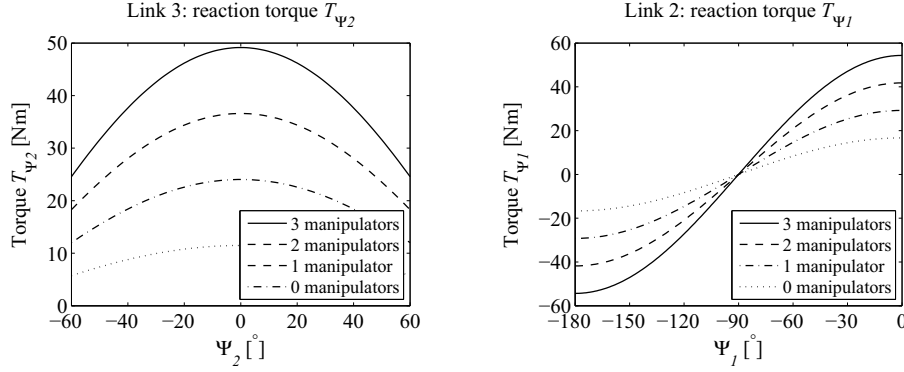


Figure D.4: Reaction torque  $T_{\Psi_2}$  and  $T_{\Psi_1}$ , with 0, 1, 2 or 3 manipulators mounted in the platform. These torques need to be compensated. For both cases the most extreme values are applicable, with all three manipulator-adjustments mounted into the platform.

The potential energy of the platform-adjustment changes with a change in orientation of the links. This energy needs to be stored in an element, such as a spring. Applying a counter mass would increase the mass of the platform-adjustment considerably as the stroke it may travel in link 1, is limited. A mechanical compression spring is used for compactness. An indication of the required volume  $V$  of the spring is obtained from a first estimate of this change in energy. This energy (Equation D.21) is a function of the torque required, just described:

$$U_p = \int_{\Psi_{min}}^{\Psi_{max}} T_{\Psi-max} \cos(\Psi) d\Psi \quad (D.21)$$

The potential energy stored in a spring is shown in Equation D.22.

$$U_{spring} = \frac{\mu V \tau^2}{2G} \quad (D.22)$$

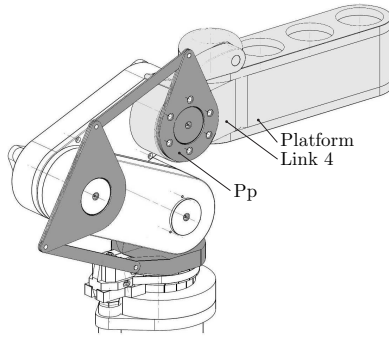
The spring volume and mass (Equation D.23) are derived from this:

$$m_{spring} = \rho_{steel} V = \rho_{steel} \frac{2U_{spring}G}{\mu\tau^2} = \rho_{steel} \frac{U_{spring}E}{(1+\nu)\mu\tau^2} \quad (D.23)$$

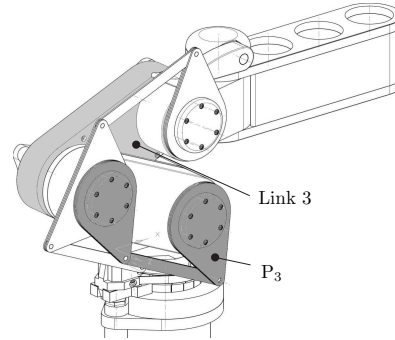
A spring with mass  $m_{spring} \approx 0.6$  kg is required to store the potential energy released from link 3 and the platform. A spring with mass  $m_{spring} \approx 0.4$  kg to store energy related to link 2 should be sufficient. These masses indicate the springs have far less mass than a counterweight system of which the stroke fits in link 1.

### Add-on parallel link mechanism of the weight-compensation

Parallelogram  $P_p$  (Figure D.5(a)) prescribes the orientation of the platform and supports reaction torque  $T_{\Psi_3}$ . Parallel link mechanism  $P_3$  (Figure D.6(b)) copies the orientation of link 3 ( $\Psi_2$ ) toward the energy storage system. It is internally connected to the energy storage system by means of a chain transmission through link 1.



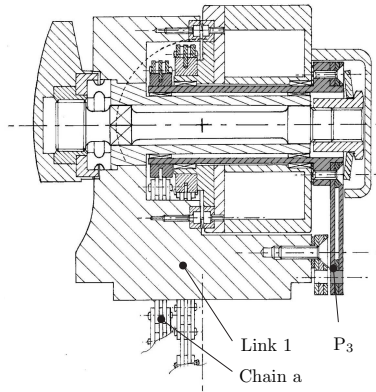
(a) Parallelogram  $P_p$  keeps the platform and link 4 parallel to the table-top.



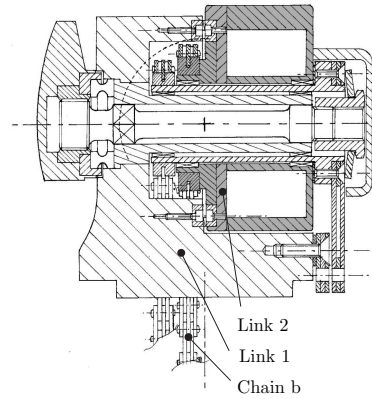
(b) Parallelogram  $P_3$  copies the orientation of link 3 to the energy storage system.

Figure D.5: Parallel link mechanisms.

This chain transmission can be seen in Figure D.6. Link 2 is directly coupled to the energy storage system by means of a similar chain transmission.



(a) Chain (a) transmission to couple link 3 by means of parallelogram  $P_3$  (Figure D.5(b)) to the energy storage system.



(b) Chain (b) transmission to couple link 2 to the energy storage system.

Figure D.6: The chain transmission copies the orientation of link 3 (a) and link 2 (b) to the energy storage system inside link 1, shown in Figure D.7.

### Energy storage system

Figure D.10 shows the energy storage system, or the system supplying a weight compensation torque. The potential energy of the platform-adjustment is stored when the spring is compressed, and released when the spring elongates again. A roller connected to the spring, rolling on a cam provides for the required compression and release of the spring. The shape of the cam creates Figure D.4. The

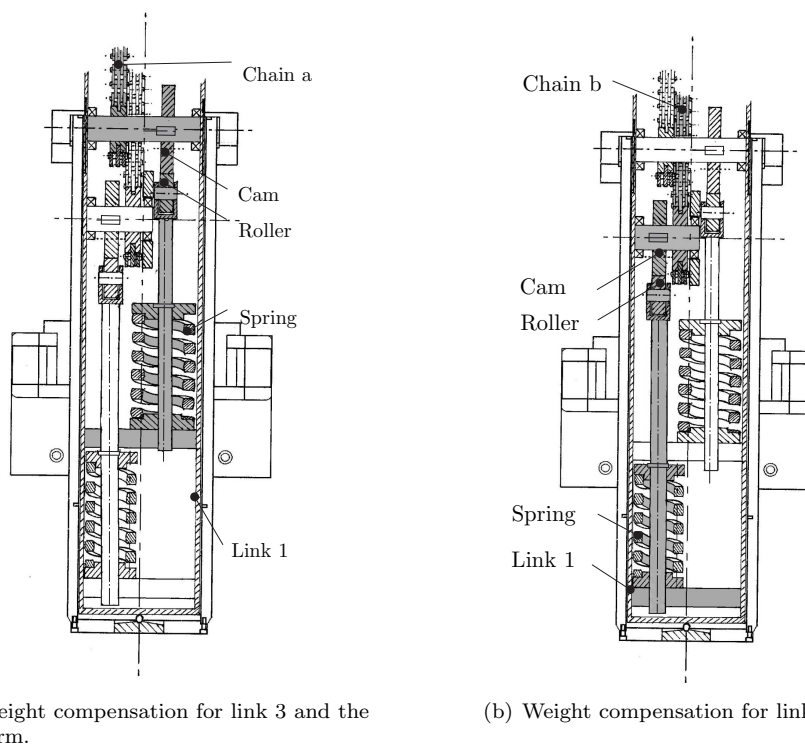


Figure D.7: The energy storage system consists of a spring connected to a roller. The roller runs on a cam connected to the links with the chains, compressing or releasing the spring. This stores and releases energy in a way corresponding to Figure D.4.

profile of the cam provides a change in radius which produces the required compensation torque. The figures used to derive the required cam profile are shown in Figure D.8.

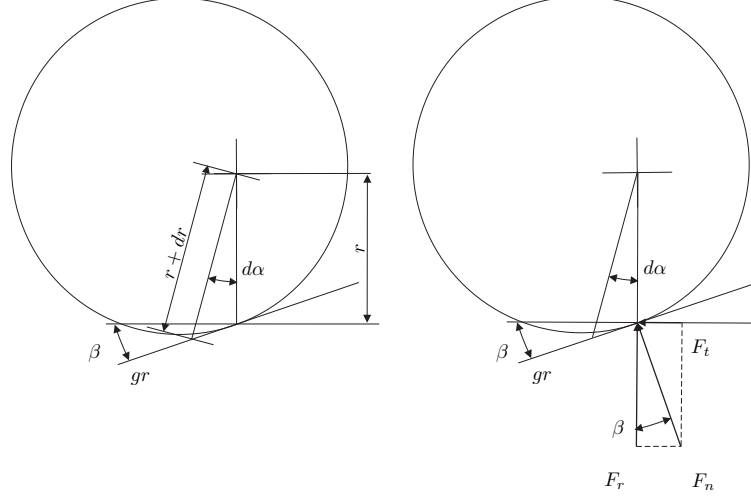


Figure D.8: The left of this figure shows the gradient on the cam-profile on which the roll runs. The right of this figure shows the forces acting on the cam.  $F_t$  is the force providing the compensation torque.

The gradient  $gr$  on the cam-profile at the local radius  $r$  with a very small change in angle  $d\alpha$  is shown in Equation D.24.

$$gr = \frac{dr}{rd\alpha} = \arctan \beta \quad (D.24)$$

The tangential force  $F_t$  (Equation D.25) at radius  $r$  applies the required compensation torque  $T_{comp}$  (Equation D.26).

$$F_t = F_r \tan \beta = F_{spring} \frac{dr}{rd\alpha} \quad (D.25)$$

$$T_{comp} = rF_t \quad (D.26)$$

with  $F_r$  shown in Equation D.27:

$$F_r = F_{spring} = F_0 + (r(\alpha) - r_0)c_{spring} \quad (D.27)$$

The torque  $T$  to be applied is  $T = A \cos \alpha$ . For link 3  $A_3 = L_{m3}gm_3 + L_3F_{\Psi3}$  and  $\alpha_3 = \Psi_2$  from Equation D.18; and for link 2  $A_2 = L_{m2}gm_2 + L_2F_{\Psi2}$  and  $\alpha_2 = \Psi_1$  from Equation D.20. This leads to the differential equation shown in Equation D.28.

$$\frac{dr}{d\alpha} = \frac{A \cos \alpha}{F_0 + (r(\alpha) - r_0)c_{spring}} \quad (D.28)$$

The cam profiles after solving this differential equation are shown in Figure D.9

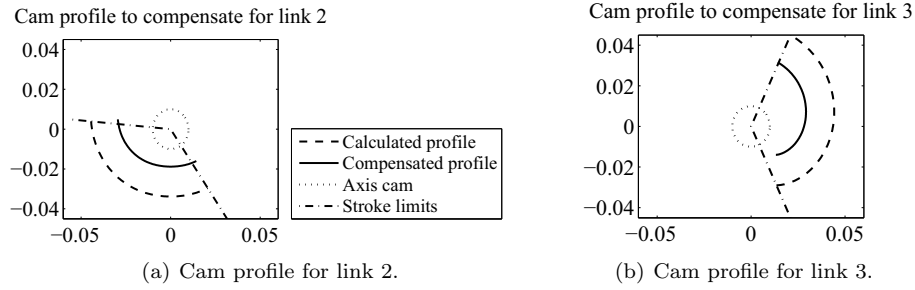


Figure D.9: Cam profiles resulting from the solved differential equation.

### Integrated weight-compensation mechanism

An alternative weight-compensation mechanism integrated inside the platform-adjustment (Figure D.10) also proposed by Verbaan [122] uses chains instead of flat strip rods, to copy the angle-information to the energy-storage mechanism inside link 1. These chains are integrated, by increasing the width of the links.

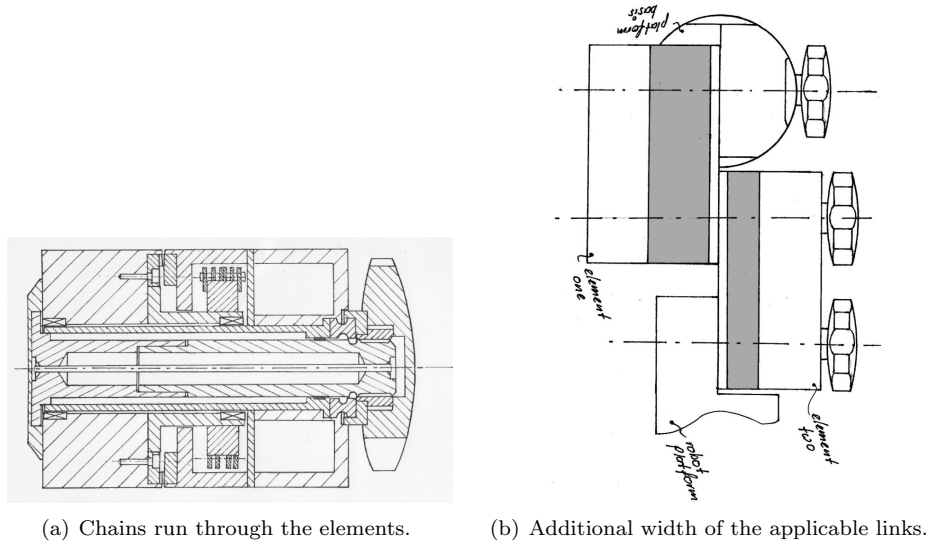


Figure D.10: Integrated weight-compensation mechanism, requires a more extensive modification of the existing platform-adjustment (not chosen).

## D.5 Measurement equipment used

Several measurements have been performed on the platform-adjustment and on the manipulator-adjustment. These measurements included (semi-)static measurements for stiffness and hysteresis and dynamic measurements to measure first natural frequencies of the pre-surgical set-up. The equipment used for these measurements is shown in Table D.7.

Table D.7: Equipment used for measurements on the pre-surgical set-up.

<b>Displacement sensor</b> used for stiffness, hysteresis and frequency measurements: Mahr Feinprüf millitron 1204 IC Mahr Feinprüf measurement-probe type 1300
<b>Force sensor</b> used for hysteresis measurements: AST Gruppe, force sensor KAP-E 2.0 mV/V, 1 kN Delta electronics Power Supply ES 030-5 Amplifier 500x
<b>Vibrometer</b> used to measure frequencies without contact: Polytec Vibrometer Controller OFV-5000 Polytec Fiber-optic Vibrometer Sensor Head OFV-551/-552
<b>Data-acquisition equipment</b> used for hysteresis and frequency measurements: National Instruments 6211 built-in interface Laptop with 'Meetpanel v6.0'

The hysteresis measurement on the platform and its platform-adjustment, was performed with the set-up schematically shown in Figure D.11.

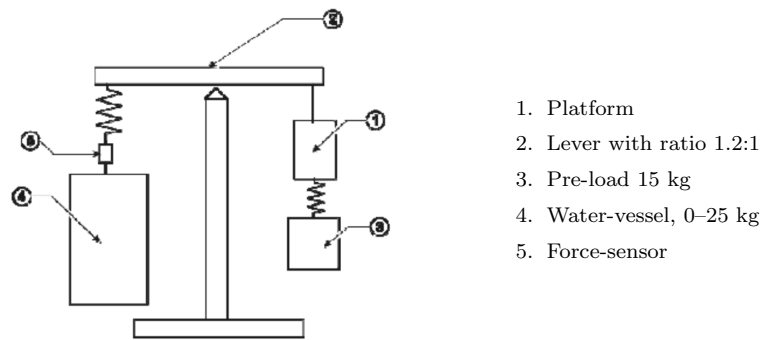


Figure D.11: Set-up for hysteresis measurement in  $z$ -direction of the platform-adjustment ( $F_z \pm 150$  N).

# Appendix E

## Manipulator

Additional information regarding the manipulator is given here. Section E.1 provides characteristics and details on the drive-train used for the  $\Phi$ ,  $\Psi$ ,  $\Theta$  and  $Z$ -DoFs. Section E.2 describes the components of the force-sensors and calibration results. Section E.3 and Section E.4 provide measurement results on respectively eigenmodes of the manipulator and open-loop and process information.

### E.1 Manipulator drive-train characteristics

The drive-train characteristics on hardware and calculated values based on the drive-train hardware are presented in respectively Table E.1 and E.2.

Table E.1: Hardware of the  $\Phi, \Psi, \Theta$  and Z-DoF drive-trains of the manipulator, for both worm-wormwheel and ball-screw layout. With transmission ratio  $i$  and efficiency  $\eta$ .

$\Phi$ :	
Motor	electronically commutated ECmax 22, 24 V, 25 Watt, type 283858
Motor transmission	Gysin GPL 22-1 stage, $i=1/4$ , $\eta \approx 0.96$ , reduced backlash $0.17^\circ$
Extra transmission	harmonic-drive CSF-8-100-2XH-F, $i=1/100$ , $\eta \approx 0.73$ , backlash $5 \cdot 10^{-3}$
Brake	AB 20 24 VDC, 0.1 Nm, type 301212
Encoder	500 cpt Scancon, type 2MCH
Potmeter	multiturn potmeter, Megatron AL1410P, with $i_{gears}=1/2.29$
$\Psi$ worm-wormwheel:	
Motor	electronically commutated EC 16, 32 V, 40 Watt, type 262862
Motor transmission	Gysin GPL22-2 stage, $i=1/20$ , $\eta \approx 0.9$ , reduced backlash $0.33^\circ$
Extra transmission	worm-wormwheel, $i=1/50$ , $\eta=0.75$
Encoder	512 cpt magnetic MR, 3 channel, line-driven, type 201940
Potmeter	single-turn Megatron MAB12A
$\Psi$ ball-screw:	
Motor	electronically commutated ECmax 16, 24 V, 8 Watt, type 283835
Motor transmission	Gysin GPL22-1 stage, $i=1/5$ , $\eta \approx 0.96$ , reduced backlash $0.17^\circ$
Extra transmission	screw lead=1.5 mm, $i_{screw}=0.24$ mm/rad, $i=\omega_{ins}/\omega_{nut}=1/215$ , $\eta \approx 0.99$
Encoder	128 cpt, magnetic MR, 3 channel, line driven, type 228177
Potmeter	single-turn Megatron MAB12A
$\Theta$ and Z:	
Motor	electronically commutated ECmax-16, 12 V, 5 Watt, type 283828
Motor transmission	three stage spur, $i=1/31$ , $\eta_{max} \approx 0.69$ , reduced backlash $0.25^\circ$
Gear-set $\Theta$	gear-pinion: $i=1/2.78$ , $\eta \approx 0.95$
Gear-set Z	bevel-bevel, planet-sun, gear-pinion: $i=1/2.78$ , $\eta \approx 0.72$
Encoder	256 cpt, magnetic MR, 3 channel, line driven, type 228182
End-switch	provided by instrument-wire guidance

Table E.2: Drive-train, calculated values. Various parameters for the four DoFs:  $\Phi, \Psi, \Theta$  and Z, with  $\Psi_W$ , the worm-wormwheel layout and  $\Psi_S$ , the ball-screw layout. With  $f_s$  the friction coefficient of the friction-wheels driving the instrument,  $D_o$  the outer diameter of the instrument-tube,  $D_{Fw}$  the friction-wheel diameter,  $T_{out}$  the output torque required to drive the instrument,  $i_{tot}$  and  $\eta_{tot}$  the transmission ratio and efficiency of the drive-train,  $T_{in}$  and  $n_{in}$  the ingoing torque and rotational speed (motor-side),  $d\alpha_{out-e}$  and  $d\beta_{out-mt}$  the smallest change in output angle that can be measured with the encoder and the output backlash of the motor and additional transmission.

DoF	$f_s$ [-]	$D_o$ [mm]	$T_{out}$ [Nmm]	$1/i_{tot}$ [-]	$\eta_{tot}$ [-]	$T_{in}$ [Nmm]	$n_{in}$ [rpm]	$d\alpha_{out-e}$ [ $^\circ$ ]	$d\beta_{out-mt}$ [ $^\circ$ ]
$\Phi$			$9 \cdot 10^3$	400	0.70	32	$1.3 \cdot 10^3$	$1.8 \cdot 10^{-3}$	$6.7 \cdot 10^{-3}$
$\Psi_W$			$9 \cdot 10^3$	1000	0.72	12.5	$3.2 \cdot 10^3$	$7.0 \cdot 10^{-4}$	$6.8 \cdot 10^{-3}$
$\Psi_S$			$9 \cdot 10^3$	1075	0.95	8.8	$3.3 \cdot 10^3$	$2.6 \cdot 10^{-3}$	$0.8 \cdot 10^{-3}$
$\Theta$	0.1 0.15	8.5	170 255	86.2	0.66	3.0 4.5	$3.4 \cdot 10^3$	$16 \cdot 10^{-3}$	$89 \cdot 10^{-3}$
	$f_s$ [-]	$D_{Fw}$ [mm]	$T_{out}$ [Nmm]	$1/i_{tot}$ [-]	$\eta_{tot}$ [-]	$T_{in}$ [Nmm]	$n_{in}$ [rpm]	$dz_{out-e}$ [mm]	$dz_{out-mt}$ [mm]
Z	0.1 0.15	13	130 195	86.2	0.50	3.0 4.5	$13 \cdot 10^3$	$1.9 \cdot 10^{-3}$	0.01

## E.2 Manipulator force sensors for $\Phi$ , $\Psi$ , $\Theta$ and $Z$

This section presents information on the hardware and calculated values of the force sensors applied in the manipulator, on the amplification circuit of the  $\Theta Z$  force sensors and on calibration results for the force-sensors.

### E.2.1 Hardware and characteristics of the force sensors

Hardware and accompanying components of the  $\Phi, \Psi, \Theta$  and  $Z$  force sensors are presented in Table E.3. Data on the  $\Phi$  and  $\Psi$  sensor of the manipulator with wormwheel-layout, on the  $\Phi$  and  $\Psi$  sensor of the manipulator with ball-screw layout and on the  $\Theta$  and  $Z$  force sensors is presented in respectively Tables E.4, E.5 and E.6.

Table E.3: Hardware of the force sensors and accompanying components, implemented in the manipulator.

$\Phi$ worm-wormwheel:	
Elastic element	rod: aluminium, $D=2.3$ mm, $L=14.5$ mm
Displacement sensor	SMU9000-2U Kaman eddy-current, offset 0.25 mm
End stop	steel pin-hole combination at $R=12$ mm
$\Psi$ worm-wormwheel:	
Elastic element	harmonic: aluminium, $H=28.4$ mm, $L=7.2$ mm, $t=7$ mm
Displacement sensor	SMU9000-2U Kaman eddy-current, offset 0.25 mm
End stop	steel hooked plates that allow 0.1 mm change of length
$\Theta Z$ force sensors:	
Pinion guidance	double leaf-spring: steel, leaf-spring $c=25$ N/mm
Force sensor	Honeywell FSG15N1A, compression, range 20 N, max deflection 30 $\mu$ m
Preload spring	compression, Amatec D11460

Table E.4: Details on the elastic elements and displacement sensors of the  $\Phi$  and  $\Psi$  force sensors in the worm-wormwheel layout. The range and resolution of the force sensors are given by the output torque of each drive-train  $T_{max}$  (based on maximum tip-load and mass of the manipulator) and  $T_{min}$ . Radius  $R_e$  is the radial position of the force sensor measured with respect to its DoF. Stiffness  $c$  is the stiffness of the elastic element as realized (based on  $k_t$  from Table 4.2, with ideally  $c=100k_t/R_e^2$ ), the rotational stiffness  $k=cR_e^2$  and the given displacement shows the maximum and minimum displacement measured by the displacement sensor.

DoF	Range	Resolution	Radius	Stiffness		Displacement	
	$T_{max}$ [Nm]	$T_{min}$ [Nm]	$R_e$ [mm]	$c$ [N/mm]	$k$ [Nmm/rad]	$dL_{max}$ [ $\mu$ m]	$dL_{min}$ [nm]
$\Phi$	9	$18 \cdot 10^{-3}$	30	$1.9 \cdot 10^4$	$1.7 \cdot 10^7$	16	31
$\Psi$	9	$18 \cdot 10^{-3}$	60	$3.9 \cdot 10^3$	$1.4 \cdot 10^7$	38	77

Table E.5: Details on the elastic element displacement sensor (strain gauge) of the  $\Phi$  force sensor and of the  $\Psi$  force sensor in the ball-screw layout. The range and resolution are not displayed, but equal to the range and resolution of Table E.4. The parameters given are similar to the parameters described in that table as well. Note that the rotational stiffness  $k \approx 25k_t$  here (with  $k_t$  from Table 4.2).

DoF	Radius	Stiffness		Displacement		Max load
	$R_e$ [mm]	$c$ [N/mm]	$k$ [Nmm/rad]	$dL_{max}$ [ $\mu$ m]	$dL_{min}$ [nm]	$F_{failure}$ [%]
$\Phi$	23.1	$9.3 \cdot 10^3$	$5.0 \cdot 10^6$	44	88	
$\Psi$	$70\cos(\Psi)$	$1 \cdot 10^3$	$4.9 \cdot 10^6$	100		200

Table E.6: Details on the  $\Theta$ Z force sensors integrated in the  $\Theta$ Z-manipulator. The range and resolution of the force sensors are given by the required output torque and force of each drive-train  $T, F_{max}$  and  $T, F_{min}$ . Radius  $R_{pinion}$  is the radius used to calculate reaction force that needs to be measured by the sensors.  $F_{max}$  and  $F_{min}$  are based on the range, resolution as well and on the transmission ratio  $i_{tot}$  and efficiency  $\eta_{tot}$  from Table E.1. The stiffness  $c$  is the stiffness of the integrated force-sensor.

DoF	Range	Resolution	Radius	Force		Stiffness
	$T_{out-max}$ [Nmm]	$T_{out-min}$ [Nmm]	$R_{pinion}$ [mm]	$F_{max}$ [N]	$F_{min}$ [N]	$c_{sensor}$ [N/mm]
$\Theta$	250	1.5	10.2	9.3	0.06	667
Z	$F_{out-max}$ [N]	$F_{out-min}$ [N]	$R_{pinion}$ [mm]	$F_{max}$ [N]	$F_{min}$ [N]	$c_{sensor}$ [N/mm]
	20	$60 \cdot 10^{-3}$	10.2	6.5	$20 \cdot 10^{-3}$	667

## E.2.2 Amplification circuit of the $\Theta$ Z force sensor

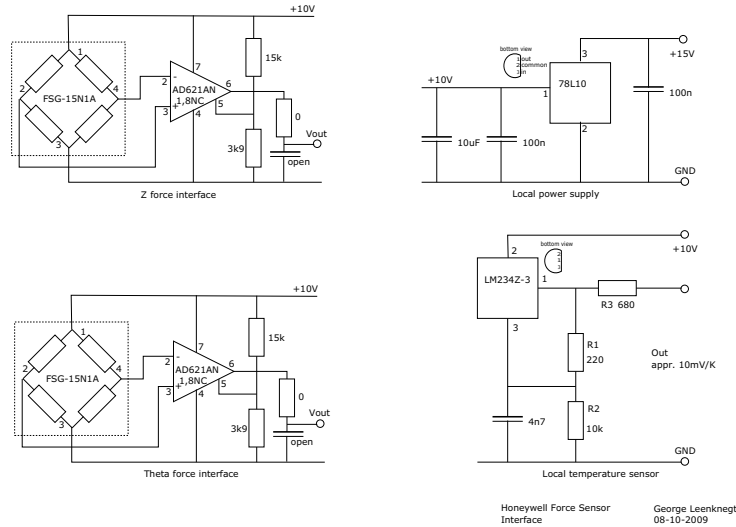
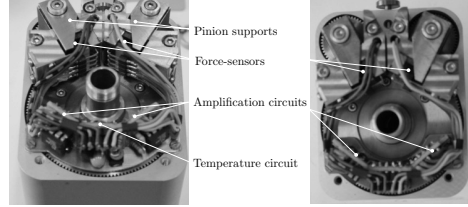
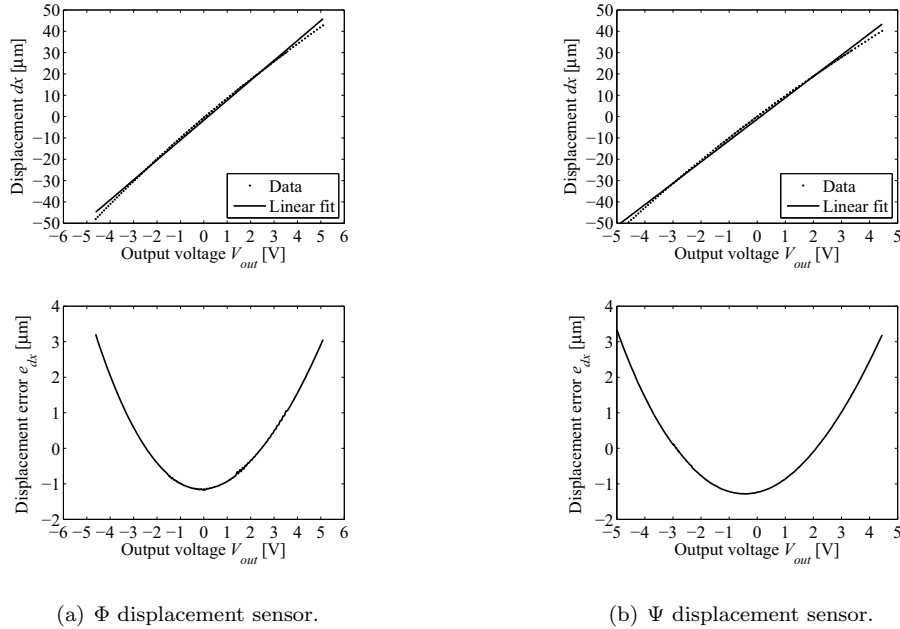


Figure E.1: Interface circuit for the  $\Theta$ Z force sensors, including temperature sensor and 10 V stabilized power supply.

Figure E.2: The circuits as realized built in the  $\Theta Z$ -manipulator, seen from below.

### E.2.3 Calibration and fit of the $\Phi$ and $\Psi$ displacement sensors

A calibration [75] of the sensors is executed using equipment from [125]. An optical measurement setup with a nano-stepping piezo stage is used to move the sensor. For all measurements, the sensor is moved along its range in steps of  $1\ \mu\text{m}$  with the piezo stage. Every point is measured four times in four consecutive scans. These measured four points are averaged in  $x$  and  $y$  to reduce measurement noise. A linear fit (top in Figure E.3) on both displacement sensors, gives a  $4.5\ \mu\text{m}$  error (bottom in Figure E.3). Since this error is asymmetric a second order fit would not be sufficient either.

Figure E.3:  $\Phi$  and  $\Psi$  displacement sensors measurement results and linear fit. Top: displacement data. Bottom: error of the calibration data when fit linearly.

For both sensors a fifth order polynomial (Equation E.1) is fit to the measurement data ( $n=140$ ).

$$p = a_5x^5 + a_4x^4 + a_3x^3 + a_2x^2 + a_1x + a_0[m] \quad (\text{E.1})$$

The coefficients of the polynomials of both sensors are given in Table E.7. The remaining errors are displayed in Figure 4.16(a) and 4.16(b).

Table E.7: Coefficients of the fifth order polynomial fit on the measurement data of the displacement sensors belonging to the  $\Phi$  and  $\Psi$  force sensors.

DoF	$a_5$	$a_4$	$a_3$	$a_2$	$a_1$	$a_0$
$\Phi$	$-8.44 \cdot 10^{-12}$	$2.63 \cdot 10^{-10}$	$5.98 \cdot 10^{-9}$	$-1.90 \cdot 10^{-7}$	$9.30 \cdot 10^{-6}$	$-5.51 \cdot 10^{-7}$
$\Psi$	$6.55 \cdot 10^{-11}$	$1.27 \cdot 10^{-10}$	$2.22 \cdot 10^{-9}$	$-2.02 \cdot 10^{-7}$	$9.83 \cdot 10^{-6}$	$2.33 \cdot 10^{-8}$

Table E.8: Range and output of the SMU9000-2U displacement sensors (serial number), used for the  $\Phi$  and  $\Psi$  force sensor after measurement and calibration. These sensors typically have an offset.

DoF	Serial number	Range measured	Range average	Resolution	Offset	Output
		[ $\mu\text{m}$ ]	[ $\mu\text{m}$ ]	[nm]	[ $\mu\text{m}$ ]	[V]
$\Phi$	1002041	-55 – 40	$\pm 47$	40	250	-5 – 4.4
$\Psi$	183950	-54 – 40	$\pm 47$	33	250	-5 – 4.4

## E.2.4 Calibration and fit of the $\Theta$ and Z force sensors

A quadratic fit (Equation E.2) suits best on a single ramp (Figure 4.30(a)). Due to hysteresis in the sensor and its setup, the increasing and decreasing ramp are not equal. The polynomials on both ramps of each run are averaged, the two polynomials of the second and third run are averaged once more resulting in:

$$F = (c_1U^2 + c_2U + c_3 = g \quad (\text{E.2})$$

[N]. Table E.9 shows its coefficients.

Table E.9: Coefficients of the quadratic polynomial fit on the measurement data of the  $\Theta$  and Z Honeywell FSG15N1A force sensor. One sensor has been evaluated, the behavior of other sensors is assumed to be similar.

sensor	$g$ [ $\text{m/s}^2$ ]	$c_1$ [-]	$c_2$ [-]	$c_3$ [-]
Honeywell FSG15N1A	9.81	$4.04 \cdot 10^{-3}$	$3.74 \cdot 10^{-1}$	-1.16

### E.3 Manipulator eigenmodes 2 and 3

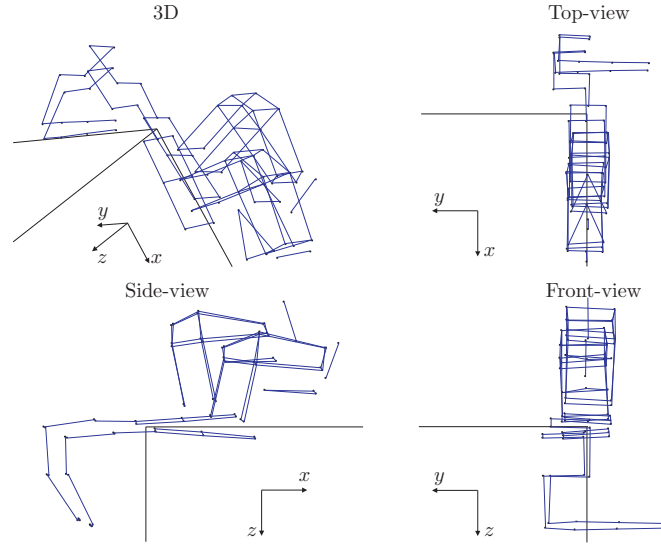


Figure E.4: Eigenmode 2 at 25 Hz, a rotation of the manipulator on the  $y$ -axis (the  $\Psi$ -DoF) best seen in the side-view.

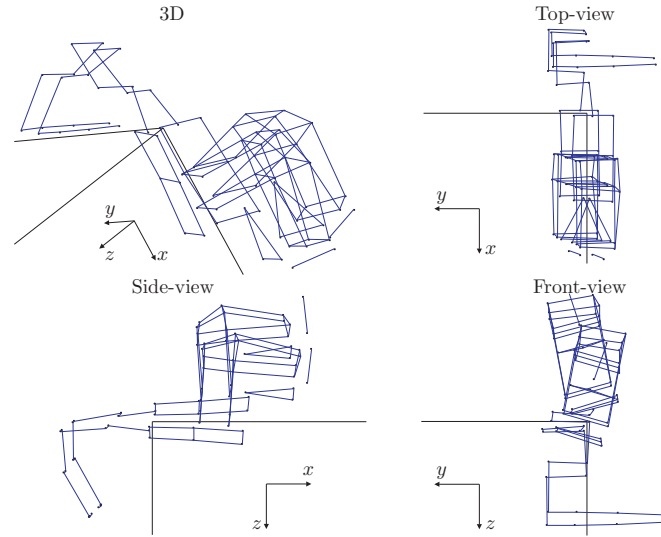


Figure E.5: Eigenmode 3 at 31 Hz, a rotation of the manipulator on the  $x$ -axis again (best seen in the front-view) with an additional rotation on the last  $y$ -axis ( $\Psi_3$  of the manipulator-adjustment, see Figure 3.16). This results in movement of the manipulator in  $z$ -direction.

## E.4 Manipulator identification measurement results

### E.4.1 Identification of the $\Phi$ -DoF: open-loop and process

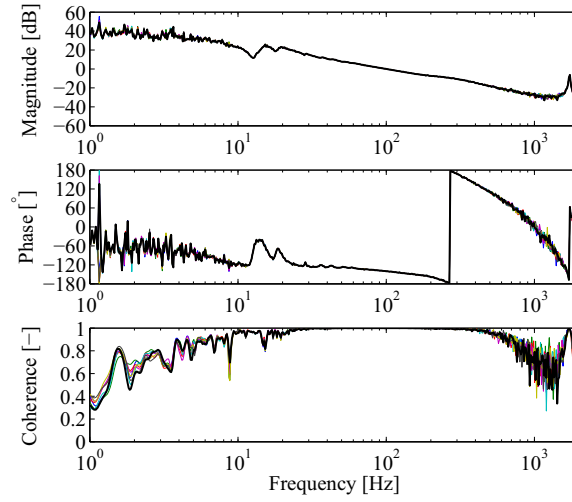


Figure E.6: Open-loop, resulting from measurement of the sensitivity and complementary sensitivity to identify the  $\Phi$ -DoF (at initial orientation  $\Phi_0=0^\circ$ ).

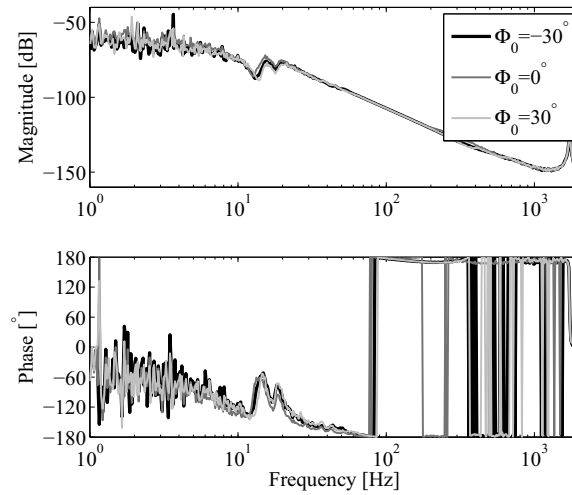


Figure E.7: Bode-plot of the  $\Phi$ -DoF (process), shown for an initial orientation  $\Phi_0=-30^\circ$ ,  $0^\circ$ ,  $30^\circ$ . The Bode-plot is shown without an instrument to display the behavior of the manipulator.

### E.4.2 Identification of the $\Theta$ and Z-DoFs: open-loop and MIMO process

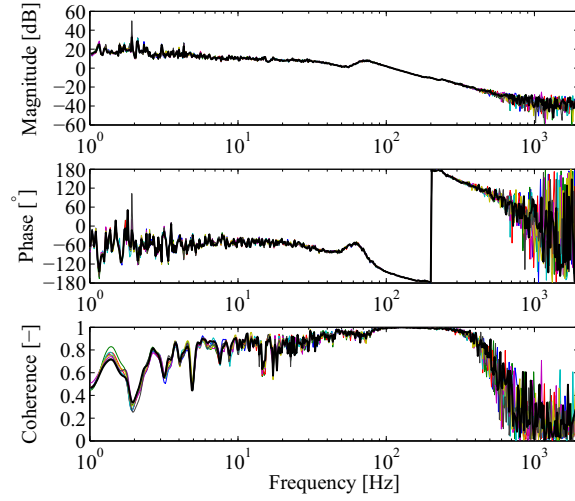


Figure E.8: Open loop, resulting from 8 measurements of the sensitivity and complementary sensitivity to identify the  $\Theta$ -DoF of the manipulator.

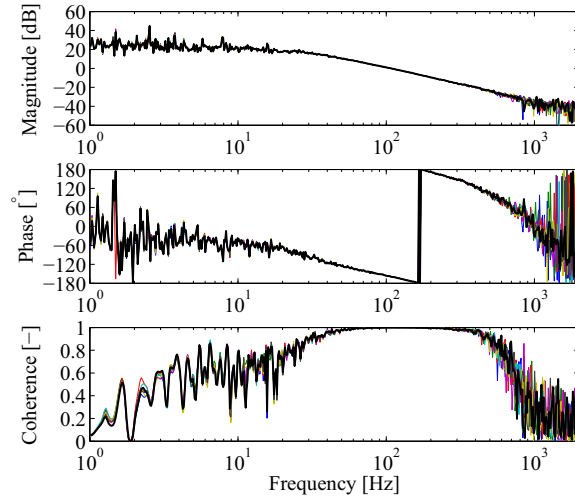


Figure E.9: Open loop, resulting from 8 measurements of the sensitivity and complementary sensitivity to identify the Z-DoF of the manipulator.

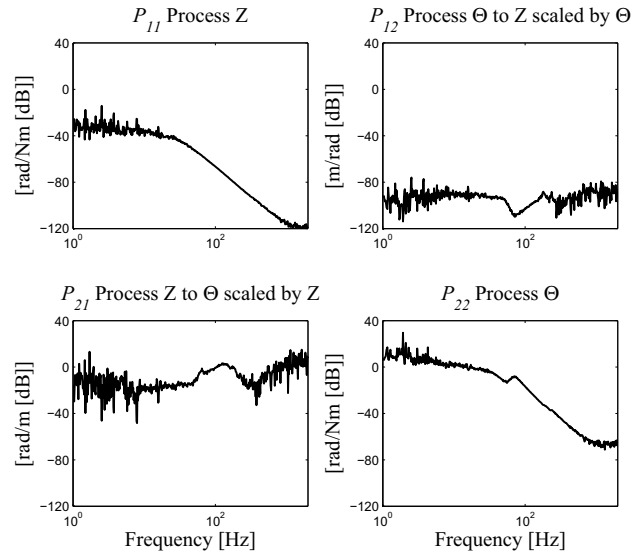


Figure E.10: MIMO bode magnitude diagram of the manipulator mechanics (scaled and amplitude only), with on the diagonal the  $\Theta$  and Z-DoFs.

## Appendix F

# Instrument

Several subjects regarding the instrument are presented. In Section F.1 calculations and details regarding the gears can be found. In Section F.3 characteristics and details on the drive-train used for the pitch, roll, pivot and close are shown.

### F.1 Calculations and data for the bevelgears used in the instrument-tip

The calculations on the bevelgears ([112] and mentioned references) are based on equations for spur gears. The factors  $Y_K$  and  $Z_K$  (respectively Table F.1 and F.2) transform the calculated values to allowable torque for bevelgears. The formulas used, hold for the situation where  $m=1-25$  mm, the pitch diameter is less than 1600 mm for straight bevelgears, the linear speed is less than 25 m/s and the rotating speed less than 3600 rpm. The first condition is not met, therefore the results are used as an indication. Generally, these formulas hold for linear elastic, homogeneous, isotropic material. Ceramic materials are linearly elastic homogeneous and isotropic in its elastic range. Its granule size (sub-micron [43]) is small compared to the end-product form details, which indicates that granule edges should not be noticed. The mechanical material properties are assumed to be constant at room temperature and slightly above, since a single phase is present and it is stabilized with  $Y_2O_3$  [45], which means it has a constant crystallographic structure. Furthermore, according to [121] and mentioned references therein, the given values for bending strength and tensile strength should be corrected for by means of Weibull flaw statistics. The variability in strength and lifetime due to flaws in the material can then be taken into account. As stated the results

are used as an indication for the allowable torque in the gears. The allowable torque depends on either the allowable bending stress  $\sigma_{bend}$  in the material or the allowable contact stress  $\sigma_{Hz}$ . In addition these torques depend on the factors  $K_b$  and  $K_c$ .

The maximally allowable torque on the bevelgear based on the bending stress is:

$$T_b = F_{tb}R_b = (Y_K \cos(\beta_m)(\sigma_{bend} K_{\sigma B})mb \frac{R_a - 0.5b}{R_a} K_b)R_b \quad (F.1)$$

with cone distance  $R_a = R_{a1} = R_{a2} = (D/2)/\sin(\delta)$ ,

$\delta = \arctan(\sin(\Sigma)/(z_2/z_1 + \cos(\Sigma)))$  and  $K_b$  calculated according to Equation F.2 and shown in Table F.1.

$$K_b = \frac{1}{Y_F Y_\epsilon Y_C} \frac{K_L K_{FX}}{K_M K_V K_O} \frac{1}{K_R} \quad (F.2)$$

Table F.1: Coefficients used to calculate the torque in the bevelgears as a function of bending strength, from [112]. The coefficients are merged into  $K_{bi}$ . With  $i=1$  the reference value, taken all factors equal to unity. The resulting allowable torques can be found by multiplying the found torques with the appropriate  $K_b$ . For  $i=2,3$  values are based on tables and figures from [112]. With 2 a mild variant and 3 a heavy case. Furthermore, the allowable bending stress at the tooth root should be taken as 2/3 of the given material value, to account for bidirectional load and equal load distribution on both sides of the tooth. The type of gear (bevelgear) is accounted for by factor  $Y_K=0.85$  (in Equation F.1).

Coefficient		i=2	i=3
$Y_F$	tooth profile factor	1	3
$Y_\epsilon$	load distribution factor	1	0.66
$Y_\beta$	spiral angle factor	1	1
$Y_C$	cutter diameter effect factor	1	1.15
$K_L$	life factor	1	1
$K_{FX}$	dimension factor	1	1
$K_M$	tooth flank load distribution factor	1	1.8
$K_V$	dynamic load factor	1	1
$K_O$	overload factor	1.25	1.25
$K_R$	reliability factor	1	1.2
$S_F$	safety factor for bending failure	1	1.2
$K_{bi}$	calculated according to Equation F.2	0.8	0.24

The maximally allowable torque on the bevelgear based on the contact stress  $\sigma_{Hz}$  is:

$$T_c = F_{tc}R_b = (Z_K \left(\frac{\sigma_{Hz}}{Z_M}\right)^2 \frac{D_b}{\cos(\delta_1)} \frac{R_a - 0.5b}{R_a} b \frac{u^2}{u^2 + 1} K_c)R_b \quad (F.3)$$

with the material factor  $Z_M$  (Equation F.4)

$$Z_M = \sqrt{\frac{1}{\pi \left( \frac{(1-\nu_1)^2}{E_1} + \frac{(1-\nu_2)^2}{E_2} \right)}} \quad (F.4)$$

and  $K_c$  calculated according to Equation F.5 and shown in Table F.2.

$$K_c = \left( \frac{K_{HL} Z_L Z_R Z_V Z_W K_{HX}}{Z_H Z_\epsilon Z_\beta} \right)^2 \frac{1}{K_{H\beta} K_V K_O} \frac{1}{C_R^2} \quad (\text{F.5})$$

Table F.2: Coefficients used to calculate the torque in the gears as a function of allowable Hertzian stress, from [112]. The coefficients are merged into  $K_c$ , which is calculated according to Equation F.5. The type of gear transmission (bevelgear) is accounted for by factor  $Z_K=1$  (in Equation F.3).

Coefficient		i=2	i=3
$Z_H$	zone factor	1	2.5
$Z_\epsilon$	contact ratio factor	1	1
$Z_\beta$	spiral angle factor	1	1
$K_{HL}$	life factor	1	1.5
$Z_L$	lubricant factor	1	1
$Z_R$	surface roughness factor	1	0.75
$Z_V$	sliding speed factor	1	0.95
$Z_W$	hardness ratio factor	1	1
$K_{HX}$	dimension factor of root stress	1	1
$K_{H\beta}$	load distribution factor	1	2.1
$K_V$	dynamic load factor, see previous table	1	1
$K_O$	overload factor, see previous table	1.25	1.25
$C_R$	reliability factor	1	1.15
$K_{ci}$	calculated according to Equation F.5	0.8	0.05

Table F.1 shows a dependence on variation of the factors for the outcome of  $K_{bi}$ . Table F.2 shows a stronger dependence for  $K_{ci}$  on variation in the factors. The contact stress determines the allowable torque for  $K_b=K_c$  and materials tungsten carbide/cobalt (further denoted as tungsten carbide) and stainless steel. For zirconia the bending stress prescribes the allowable torque.

Table F.3: Allowable torque ( $T$ ) on the bevelgears for pitch and roll, as a function of the allowable bending stress  $\sigma_{bend}$ , bending stress factor  $K_{b3}$  (Table F.1), Hertzian stress  $\sigma_{Hz}$ , Hertzian stress factor  $K_{c3}$  (Table F.2) and the maximum required torque  $T_{max}$ .

	$T_{max}$	$T(\sigma_{bend})$	$T(\sigma_{Hz})$	$T(\sigma_{Hz})/T_{max}$
	[Nmm]	$K_{b3}=0.24$ [Nmm]	$K_{c3}=0.05$ [Nmm]	[%]
Pitch	250	87	55	22
Roll	100	75	34	34

The torque values in Table F.3 with  $K_{b3}=0.24$  and  $K_{c3}=0.05$  are 22 and 34% of the required torque for respectively pitch and roll. These requirements are derived from literature, the forces are measured with conventional instruments. The forces required to manipulate needles and tissue with instruments that have additional DoFs at the its tip might be (much) smaller. These smaller forces can be provided by the gears.

## F.2 Cable-drive in the drive-box: gripper driven

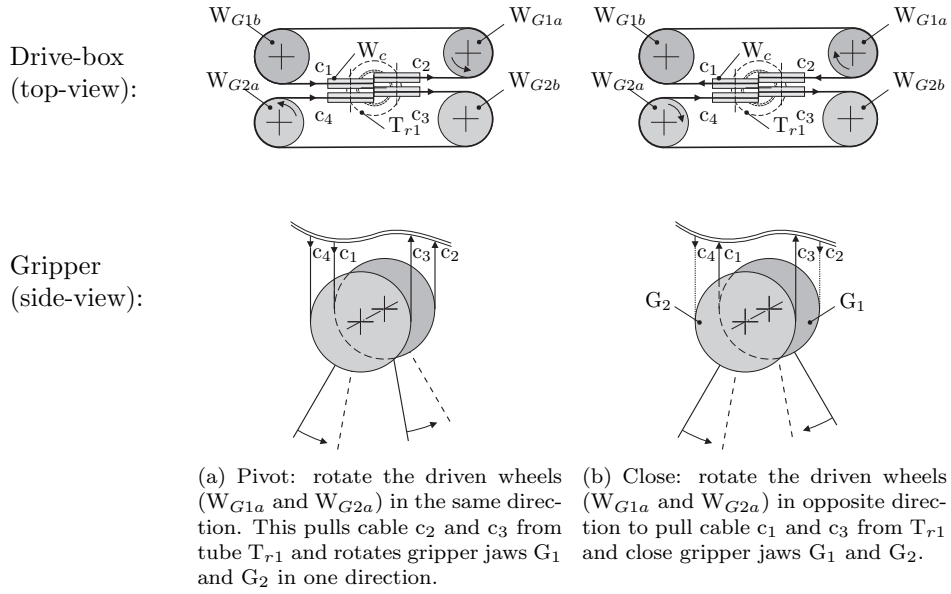


Figure F.1: Schematic representation of the cable-drive with each gripper-jaw driven by a motor. The motor is coupled to the wheel with the smallest diameter to reduce the motor torque required. The cables are rerouted to a plane perpendicular to the instrument, on wheels  $W_c$  that are oriented parallel and can therefore be easily assembled. Pretension of the cables can be applied by adjusting  $W_{G1b}$  and thereby the center distance of the wheel-set  $W_{G1a/b}$  and by adjusting  $W_{G2b}$  of wheel-set  $W_{G2a/b}$ .

### F.3 Drive-train characteristics

The drive-train characteristics and data are presented in tables per DoF.

#### Instrument drive-train

Table F.4: Hardware of the instrument-tip drive-train inside the instrument drive-box given per DoF, with pitch (p), roll (r), pivot (v), close (c), transmission ratio  $i$  and efficiency  $\eta$ .

Motor p, r, v and c	precious metal commutation, DC micromotor, 2232024SR, 24 V, 8.7 W,
Motor transmission p, r and v	-
Motor transmission c	planetary, type 20/1, $i=1/3.7$ , $\eta=0.88$
Additional transmission p	internal gear and spur pinion, $i=1/10$ , $\eta=0.99$
Additional transmission r	spur gear and pinion, $i=1/4.8$ , $\eta=0.99$
Additional transmission v	spur gear and pinion, $i=1/4.8$ , $\eta=0.99$
Additional transmission c	internal and spur gear and pinion, $i=1/5.9$ , $\eta=0.99$
Encoder p, r, v and c	IE2-512, 512 cpt, magnetic, 2 channels external line-driver

Table F.5: Calculated values of the instrument drive-train, with transmission  $i_{tot}$  and efficiency  $\eta_{tot}$  derived from Table F.4, and  $d\alpha_{out-e}$  the smallest change in angle that can be measured with the encoder defined at the output. The backlash at the output resulting from backlash of the gears and motor-transmission ( $d\alpha_{out-t}$ ) is to be measured.

DoF	$i_{tot}$ [-]	$\eta_{tot}$ [-]	$T_{in-nom}$ [Nmm]	$n_{in-max}$ [rpm]	$d\alpha_{out-e}$ [°]
Pitch	1/10	0.69	36	95	0.07
Roll	1/4.8	0.53	39	460	0.15
Pivot	1/4.8	0.80	26	460	0.15
Close	1/21.8	0.71	26	208	0.03



## Samenvatting

Het doel van een operatierobot voor minimaal invasieve chirurgie (MIS) is om de condities van de chirurg te verbeteren. In het ideale geval tot een vergelijkbaar niveau als dat van open operaties. Dit moet complexe procedures met behulp van MIS mogelijk maken. De chirurg wordt dan weer voorzien van tactiele terugkoppeling om gevoel te krijgen voor de krachten die hij uitoefent op bijvoorbeeld weefsel of hechtdraad. Ook biedt het de mogelijkheid om het doelorgaan van verschillende kanten te benaderen en de vrijheid om zo goed mogelijk de patient en het operatiegebied te bereiken. Deze eigenschappen worden toegevoegd aan die van het meest gangbare commercieel verkrijgbare systeem, de da Vinci. Dit systeem voorziet de chirurg van: (i) bewegingsvrijheid, (ii) natuurlijke oog-hand coördinatie, (iii) comfortabele lichaamshouding, (iv) intuïtief gebruik en (v) stereoscopisch '3D' visuele terugkoppeling van het operatiegebied.

Sofie (Surgeon's Operating Force-feedback Interface Eindhoven) wordt ontwikkeld om het verwachte voordeel dat zowel krachtterugkoppeling als de toegenomen mogelijkheden om patiënt en doelorgaan te benaderen, te evalueren. Sofie bestaat uit een master, een slave, electronica hardware en de benodigde control. Dit project focust op ontwerp en realisatie van een prototype van de Slave. Goede nauwkeurigheid en waardevolle krachtmetingen vereisen goed dynamisch gedrag en beperkte hysteresis van de Slave. De Slave heeft daarom een korte krachtlus tussen de instrument-tips en tussen tip en patiënt. De Slave voorziet het instrument van een passieve ondersteuning, door middel van een kinematisch vastgelegd draaipunt, het instrument steunt daardoor niet af op het weefsel van de incisie.

De Slave is direct bevestigd aan de operatietafel. Ze bestaat uit een stijf frame (*pre-surgical set-up*) met 20 graden van vrijheid (DoFs). Dit frame houdt drie 4-DoF manipulators op hun plaats gedurende de operatie. Een manipulator voor de endoscoop en twee voor verwisselbare 4-DoF instrumenten.

De pre-surgical set-up bestaat uit een 5-DoF platform instelmechanisme met een platform. Dit platform kan drie 5-DoF manipulator instelmechanismen herbergen. De pre-surgical set-up heeft een compacte layout om het team om de tafel zoveel mogelijk ruimte te geven en is volledig mechanisch en snel handmatig te bedienen.

Gedurende de operatie zijn de DoFs gefixeerd, wat resulteert in een stijf frame. Een gewichtscompensatie mechanisme is ontworpen. Metingen geven aan dat alle eerste eigen frequenties boven de 25 Hz liggen.

Elke manipulator beweegt het instrument of de endoscoop in 4 DoFs ( $\Phi$ ,  $\Psi$ ,  $\Theta$  en  $Z$ ) en biedt een passieve ondersteuning door middel van een parallellogram mechanisme. Dit mechanisme heeft een kinematisch vastgelegd draaipunt. Twee manipulators zijn opvolgend ontworpen. De eerste manipulator drijft  $\Psi$  aan met een worm-wormwiel overbrenging, de tweede maakt gebruik van een kogelomloopspindel. De tweede manipulator vermindert de optredende wrijving en heeft hierdoor o.a. een hogere coherentie bij lage frequenties. Deze zal gebruikt worden voor volgende versies van de manipulator. Het compacte  $\Theta Z$ -mechanisme bevat een trommel waarmee het instrument een beweging in  $\Theta$  krijgt. In de trommel bevinden zich wrijvingswielen voor een  $z$ -translatie. Deze trommel zal uiteindelijk verwisselbaar worden om te kunnen steriliseren. Deze manipulator layout zorgt voor een kleine bewegingsruimte en geeft zoveel mogelijk ruimte aan het team om de tafel. De krachten worden (in)direct gemeten met in de manipulator geïntegreerde krachtsensoren, zodat er geen elektrische signalen de patiënt ingaan. De krachtsensoren zelf functioneren goed. Geïntegreerd in de manipulator geven de  $\Phi$  en  $\Psi$  krachtsensoren een goede indicatie van de uitgeoefende kracht, maar laten ook wat hysteresis zien. Bij de  $\Theta Z$  krachtsensoren is de hysteresis groter. In beide gevallen ligt de oorzaak waarschijnlijk bij de bedrading van de manipulator.

Het instrument bestaat uit een drive-box, een buis en een 4-DoF tip. Dit zijn 3 DoFs extra ten opzichte van conventionele MIS instrumenten. Het zijn twee rotaties loodrecht op de instrument-buis, om het aantal naderingshoeken te vergroten (pitch en pivot) en een rol-DoF ten behoeve van het uitvoeren van hechttingen. Pitch en rol worden aangedreven met keramische kegeltandwielen en concentrische buizen. De pivot en close van het bekje worden aangedreven met kabels. Deze overbrengingen zijn backdriveable zodat ze uit de trocar verwijderd kunnen worden in een noodgeval. De theoretisch haalbare koppels voldoen vrijwel aan de vereiste koppels. Onderzoek zal uitwijzen of de in de praktijk behaalde koppels vergelijkbaar zijn en of de eisen aangepast kunnen worden voor dit instrument. De voorgestelde krachtsensoren kunnen ingebouwd worden.

Sofie bestaat momenteel uit de prototypes van de Master met twee 5-DoF haptic interfaces, de Slave en daarbij een electronicakast. De chirurg gebruikt de haptic interfaces om de manipulators en instrumenten van de Slave te bedienen. De chirurg voelt de krachten doordat de DoFs van de haptic interfaces voorzien zijn van motoren.

Een prototype Slave met geïntegreerde krachtsensoren, compact om de assistenten van ruimte te voorzien en met extra DoFs aan de instrument-tip om het doelorgaan beter te kunnen naderen, is het resultaat van dit project. Deze Slave en de Master zijn een goede basis om haptische controllers op te implementeren en de extra DoFs te evalueren. Als het systeem aan de verwachtingen voldoet zal het een waardevolle bijdrage leveren aan zowel de patient als de chirurg.

## Dankwoord

Een operatierobot voor minimaal invasieve chirurgie ontwerpen en realiseren. Een operatierobot waarbij de chirurg achter een obstakel kan opereren en zo mogelijk ook nog kan voelen hoe hard hij aan een hechtdraad trekt bijvoorbeeld. Daar zouden de chirurg en patient wel eens wat aan kunnen hebben. En voor mij: ik kon nog meer leren. Dit waren voor mij de twee belangrijkste drijfveren om te starten met dit promotie-onderzoek en door te knokken tot het eind. Het begon voor mij echt met het bezoeken van een congres waarbij ik Ivo Broeders (toen UMC Utrecht) een inspirerende presentatie zag geven over de OK van de toekomst. Tijdens een afspraak die volgde na de bewuste presentatie, bood hij mij aan om operaties bij te wonen, eerder 50 dan 5. Dus stond ik, als werktuigbouwer, in een grey's anatomy pak op de OK, te observeren wat een team en een robot (als daar sprake van was) kunnen. Vooral de eerste keer was spannend, zou ik blijven staan? Gelukkig bleek dat het geval. Bij kijkoperaties komt er weinig bloed vrij, wat helpt. Deze operaties en operaties die ik bij Jos Maessen (AZM) en anderen heb mogen observeren hebben mijn enthousiasme aangewakkerd.

Met (in het begin) een aantal chirurgen en een drietal werktuigbouwers staat er nog geen robot. Ik heb dit project dan ook zeker niet alleen gedaan en wil een aantal mensen heel hartelijk bedanken. Ik ben trots op de robot die we met z'n allen hebben neergezet. Mocht je je aangesproken voelen door deze uitspraak en (per ongeluk) niet zijn genoemd, voel je dan toch bedankt.

Nick Rosielle: voor je onuitputtelijke bron met nieuwe ideeën, je oplossingsgerichtheid in het geval van een technisch probleem, je kritische blik, je passie, je geduld om mij dingen uit te leggen.

Maarten Steinbuch: voor het promotie-onderwerp, voor het geloven in je medische projecten, voor je overzicht, je kunst om in korte tijd tot de kern van de zaak te komen, je kritische vragen, je passie, je warmte en de vrijheid die je me gaf.

Ivo Broeders en Jos Maessen: voor het kijkje achter de schermen in een voor mij nieuwe wereld, jullie tijd, gesprekken, advies en enthousiasme en jullie passie voor je vak en nieuwe dingen.

De mechanische afdeling van de GTD: dank je wel Meindert, Simon, Erwin, en alle mensen die jullie weer hebben geholpen met vonken, frezen etc. Meindert, ik heb ruim twee jaar met plezier met jou samengewerkt. Jij hebt veel ervaring, en bent creatief, erg goed in detailleren, problemen voorzien en mooi afgewerkt werkend tuig afleveren. Je staat altijd klaar om een helpende hand te bieden. Dank je wel. Simon, dank voor de samenwerking, de gesprekken, alle ideeën, detail tekeningen, zoekwerk en contacten die je hebt gelegd om tot dit instrument te komen.

De studenten die mij tijdens mijn project hebben geholpen door hun master dan wel stage project in het kader van de robot uit te voeren: Rien voor je werk aan de manipulator, Kevin voor je instrument-ontwerp, John voor je metingen, Kees voor je gewichtscompensatie en Dirk voor je 8-DoF master. Bedankt voor al jullie input, creativiteit en gezelligheid.

De electronica hardware en software mannen: Ramon, George, Ruud, Ruud, Kees-Jan en Dennis. Jullie hebben een enorme berg werk verzet om al die (electro)mechanica ook daadwerkelijk aan de praat te krijgen en de master en slave te kunnen koppelen. Daarnaast hebben jullie mij geholpen met het uitvoeren van veel metingen. Dank voor al jullie raad, daad en leuke gesprekken.

Alle mensen waarmee ik frequent overleg heb gehad: E-overleg onder leiding van Ramon met onder andere Jovita en Rinus (GTD), Dennis, Ron en Ruud. STW en de STW gebruikerscommissie, voor de (bijna) halfjaarlijkse meetings, waarbij ik weer eens alles op papier zette. Jullie kritische vragen gaven stof tot nadenken en enthousiasme gaven energie. De mensen, instanties en bedrijven die mij hebben geholpen met het volgende: STW voor subsidiëren van dit project, Cees Schot van het Catharina ziekenhuis en Jan van Beurden van Storz voor het optisch systeem dat we mogen lenen, Rob Jenneskens en Ronald Schneider van MI-Partners voor jullie instrument-ideeën, Xpress voor jullie hulp bij de sensor calibratie, Oswald Hermans en Ad Kuijpers van Formatec voor jullie hulp bij de realisatie van de tandwielen van het instrument, Etienne van den Heuvel van het AZM voor de operatietafel en het optisch systeem.

Collega's en studenten uit het lab, de gang (W-Hoog -1) en gerelateerde projecten en speciaal: Ron, Thijs, Simon, Mariëlle, Roger, Rens, Chris, Johan, Geert-Jan, Raimondo, Lennino, Eef, Kees, Gerrit en Dennis. Voor alle nuttige gesprekken en kletspraat die we hebben gehad. En natuurlijk Lia, Petra en Caroline, receptie W-Hoog en TNO, Bert en Peter.

Lieve pap & mam, Selma, Ralph & Otis, Mathijs & Manon, oma's, Frans & Fenny-An, Thijs & Ineke, vriendjes en vriendinnetjes. Dank voor jullie enthousiasme, luisterend oor, mening, jullie (in)directe hulp bij nalezen, de kaft en jullie gezelligheid, bbq's, borrels, fijne vakanties, uitjes en ga zo nog maar even door. Frans, dank je wel voor alles en dat is nogal wat. Je staat altijd voor mij klaar, maakt me aan het lachen en hebt regelmatig mijn radertjes weer aan het draaien gekregen, de ene keer subtiel de volgende met een stapresponsie :P. Je bent mijn olijke vrolijke lieve maatje.

## Curriculum Vitae

Linda van den Bedem was born on December 21, in 1978, Amersfoort, the Netherlands. She graduated from secondary school at 't Hooghe Landt of the Meridiaan College, Amersfoort, in 1997. In September 2000 she received her B.Sc. degree (cum laude) and in September 2004 her M.Sc. degree (with great appreciation), both in Mechanical Engineering at the Eindhoven University of Technology (TU/e), Eindhoven, the Netherlands. From October 2002 to February 2003 she performed her internship at the National Research Council, Institute of National Measurement Systems, Ottawa, Canada. At Philips Applied Technology, Eindhoven, she carried out her M.Sc. project in 2003-2004. Up to December 2005 she was appointed visiting scientist at TU/e, participated in teaching and research and wrote an STW subsidy proposal to design and realize a new slave robot for minimally invasive surgery (MIS). The subsidy was granted and she started performing research on this subject, as a Ph.D. student in the Control Systems Technology group of the Department of Mechanical Engineering at the TU/e in January 2006.